

***In vivo* metabolic studies in skeletal and cardiac muscle using ^{13}C magnetic resonance spectroscopy**

THÈSE N° 5969 (2013)

PRÉSENTÉE LE 25 OCTOBRE 2013

À LA FACULTÉ DES SCIENCES DE BASE

LABORATOIRE LEENAARDS-JEANTET D'IMAGERIE FONCTIONNELLE ET MÉTABOLIQUE

PROGRAMME DOCTORAL EN PHYSIQUE

ÉCOLE POLYTECHNIQUE FÉDÉRALE DE LAUSANNE

POUR L'OBTENTION DU GRADE DE DOCTEUR ÈS SCIENCES

PAR

Josefina Adriana Maria BASTIAANSEN

acceptée sur proposition du jury:

Prof. G. Meylan, président du jury
Prof. R. Gruetter, Prof. A. Comment, directeurs de thèse
Prof. J. Auwerx, rapporteur
Prof. M. Merritt, rapporteur
Prof. M. Stuber, rapporteur



ÉCOLE POLYTECHNIQUE
FÉDÉRALE DE LAUSANNE

Suisse
2013

Acknowledgements

It does not fit my personality to finish important matters well before the "due date", like this acknowledgement section. I always considered this as a challenge, which I should try to overcome, but now after all these years I accepted that this is simply the result of inspiration coming late... YES! As was the case with this section. Finally, my thesis has finished and it was such an amazing experience, to which so many people have contributed either personally, scientifically or both. It was a real challenge to put it down in words.

As confirmed by many PhD comics, which are on broad display in the cafeteria of the CIBM, a PhD experience comes with ups and downs. In retrospect, I think I have had all my downs in the first year. In that period it was very hard to imagine I would ever come to this point. I would not have continued this adventure if it were not because of the support of many, but especially of a handful of people, who gave me the confidence, motivation and patience to continue. Costas, Christine, Tian and Rolf, thank you so much.

I would like to thank Rolf for his supervision and for giving the freedom, encouragement and patience to explore my own interests. Above all, the group you created is truly special and a very pleasant and skilled working environment. The research was mainly muscle oriented, with many challenges to face, but you were always available for inspiring suggestions and advice, in any aspect.

Arnaud, thank you for your supervision and putting me on the "muscle" track, this was such an excellent idea! I must admit that I did not quite agree with that notion at the very start of my PhD... Your continuing and never ending enthusiasm made these projects work out really well. We kept on improving and improving, believing that it could always be better, stronger, higher, etc. I learned so much. Many thanks for all the support, the collaborations and letting me try out new ideas.

Tian, office mate, colleague, friend and above all, "Zen" master. I knew the word "patience" but never really knew the true meaning of it until I saw it in practice. It was great working with you, setting up the experiments and sharing the "Zen". I think I gained some years there. Yuhei, you replaced Tian in the office and showed yourself worthy of the "Zen" title too. I do not know if this is Asian wisdom, but I am happy I could share in it, and discuss with you. Andrea and Riccardo, "HELLO" (raising closed fingers), thanks for being a happy bunch, teaching me bad Italian, knowing hardware and making the occasional coffee. Hikari, "macro" king, sorry about that, I could not help it! It is great to work with and learn from you. I am so happy you joined this cardiac effort and made it more of a team challenge; it was and is very uplifting. Najat, for your positivity, humor and being down to earth. Also, for many French translations,

including my abstract! Emine for your creativity and kindness, and fruitful collaboration!! The public outreach of my thesis became much prettier!! Many thanks go to all my other DNP colleagues; our diversity makes us a good team.

Costas, I cannot thank you enough for your never ending support, belief and endless motivation throughout this entire thesis. You were a great mentor, made me feel confident about what I was doing and I am very fortunate that I could share this experience with you. I made it!

Joao, "senior", thanks for having such high standards and being hard to satisfy. I am not sarcastic, really, I did and do still appreciate it. In this manner you made me a better researcher, asking more thorough questions which led to improved understanding of what I was actually doing. You are an amazing researcher and I am lucky that I could work with you first hand and learn from you. You are also a great dancer and should do it more often. I quantified the data!

Hongxia, "no nonsense", I adore your honesty and appreciated all the times you walked into my experiments. Mostly, I learned a lot from these visits, though not the time you caught me drinking coffee... You are a lab by yourself, and multitasked. I was sure to ask you as much as possible in the first years, and still, and you were always ready to explain. Thank you.

Benoit, I can talk with you about anything, and besides a listening ear, you advise. You are such an uplifting spirit, even I would find motivation. Rajika, you tried to teach me verlan, what can I say? I am a bad student! Melanie, it is good to be done! I enjoyed chatting and sorry for bothering you with random questions. The four of us started together and I enjoyed sharing this phd adventure with you! Alia, "fluffy", we traveled to many places, and had so much fun. Thank you for steering me into the right direction, shape my thoughts, and being part of "decisive" me. I value your friendship a lot. Tobias, fellow show master! You set the tone in many endeavors! Dance moves, movies, it's great. You can keep the wig! Or not..? Bernard, "Bernardpedia", thanks for your explanations of modeling and sharing all your facts and figures. It's always a pleasure to discuss with you! Francisca, thanks for being a pleasant office mate and taking care of me when I was locked out. Masoumeh, my neighbour! You are "too funny". Thanks to Cedric for patiently saving me and my data many times.

Ruud, thanks for being there to introduce me to everybody when I arrived, and later on for interesting collaborations, good conversation, and for being from the south. You are so easygoing and down to earth; it is very refreshing and very much appreciated. Thanks for all your help with the heart movies!

Joao, "J", thank you for being there for me and for all your support in these last months. Also for being available to listen to all my plans and ideas. You qualify perfectly as a stand in P.T. and you made my thesis writing bearable!

The veterinary support in the lab, Hanne, Laure, Jackie, Mario, Corina, Anne. Without the patient help and support from you guys, I could not have performed any research.

All my other colleagues and friends who I have shared many great experiences with. Either lunches, running, hikes, aperos, barbecues, travels. Tom, Daniel, Florent, Wietske, Brammert, Daan, Lali, Jose, Sarah, Elise, Mayur, Diana, Kieran, Lijing, Nathalie, Nico.

I would like to thank my committee members for their time in taking part in the final steps and for their feedback and interesting discussions during the defense. Matthias Stuber,

Matthew Merritt, Johan Auwerx, Georges Meylan. Especially thanks to Matthias, for the collaboration we had and for making me feel so welcome in his group. Matt, thanks for working with us on the substrate competition project. Working with you was very inspiring to me and I enjoyed it a lot. This project I am the most proud of and without your input it would not have taken the shape it is in now.

My friends in The Netherlands who make me feel at home every time I return, even if we do not see each other much these days. It always feels like I never left.

Finally I would like to thank my family, who is always there for me, literally. My parents, sisters, aunts and uncles. They would drive to Switzerland without hesitation for anything. I cannot express how much your love and care is appreciated. I enjoy the times we spent here a lot, with ten people in one apartment!

Lausanne, October 2013

Jessica Bastiaansen

Abstract

Cardiac and skeletal muscle function relies on a continuous energy production via fatty acid metabolism and mitochondrial oxidation of pyruvate, with a fine balance between substrate delivery and utilization. Changes in metabolism are increasingly being implicated as playing an intrinsic role in many diseases, such as diabetes, cancer, and heart failure. Investigating and identifying fundamental metabolic processes are paramount to understanding pathologies.

Beyond morphology and functional information, magnetic resonance can provide insights at a metabolic level using spectroscopic techniques such as ^{13}C NMR. The low natural abundance and sensitivity of the ^{13}C nucleus makes ^{13}C NMR in biological systems challenging. In addressing this issue, hyperpolarized methods have emerged as a very promising tool, obtaining signal enhancements up to 10,000 fold. Spectra of hyperpolarized ^{13}C labeled substrates and their downstream metabolic products offer insight into metabolic processes occurring *in vivo* within seconds after the injection.

This thesis focused on the development of MR hyperpolarization methods and applications to study energy metabolism in cardiac and skeletal muscle *in vivo*. This ranged from development of the experimental frame work to mathematical tools to characterize the observed metabolic processes.

Methods were developed to visualize ^{13}C labeling kinetics of acetylcarnitine *in vivo* in resting skeletal muscle following the administration of hyperpolarized $[1-^{13}\text{C}]\text{acetate}$. Two different, novel mathematical models were constructed to quantify the kinetic rate constants. Although separated by two enzymatic reactions, the conversion of acetate to acetylcarnitine was uniquely defined by the enzymatic activity of acetylCoA synthetase (ACS).

A ^{13}C MRS protocol was developed and implemented for hyperpolarized studies in the heart, which included selecting appropriate cardiac triggers to align the measurements with the cardiac phase. The ^{13}C label propagation into acetylcarnitine and citrate could be measured in real time in the beating rat heart following the infusion of hyperpolarized $[1-^{13}\text{C}]\text{acetate}$, using a newly constructed ^{13}C RF coil which improved the detection sensitivity. The substantial spectral resolution at 9.4T and a triggered shimming and MR acquisition protocol allowed for the detection of citrate for the first time *in vivo* after injection of hyperpolarized $[1-^{13}\text{C}]\text{acetate}$. Mathematical models were successfully extended to include mitochondrial oxidation and analytical expressions were derived to interpret the dynamic ^{13}C labeling of citrate.

Cardiac dysfunction is often associated with a shift in substrate preference, while diagnostic methods such as PET provide only information on substrate uptake. The potential of hyperpolarized ^{13}C MRS to measure simultaneously lipid and carbohydrate oxidation was

demonstrated *in vivo*, and the sensitivity of the method to a metabolic perturbation was assessed. Hyperpolarized [1-¹³C]butyrate and [1-¹³C]pyruvate were used as representatives of carbohydrate and lipid oxidation. Fasting led to significant changes in preference for the injected substrates. The appearance of a cohort of downstream metabolites (bicarbonate, lactate, alanine, glutamate, citrate, acetylcarnitine, β-hydroxybutyrate and acetoacetate) allowed the independent and simultaneous monitoring of myocardial oxidation of both fatty acid and carbohydrates *in vivo* and is a sensitive indicator of metabolic shift.

Lactate is an important metabolic intermediate for mitochondrial oxidation. Carbohydrate metabolism in healthy rat skeletal muscle at rest was studied in different nutritional states using hyperpolarized [1-¹³C]lactate, which can be injected at physiological concentrations and leaves other oxidative processes undisturbed. A significant decrease in [1-¹³C]alanine and ¹³C bicarbonate were observed comparing both groups, attributed to a change in cellular alanine concentration and pyruvate dehydrogenase (PDH) flux. It was shown that lactate can be used to study carbohydrate oxidation in skeletal muscle at physiological levels and that the downstream metabolite signals are sensitive markers to probe metabolic changes.

Since the detection of [5-¹³C]citrate and [5-¹³C]glutamate in the heart is hindered by the close proximity of the [1-¹³C]acetate resonance, acetylcarnitine could be an interesting substrate for hyperpolarized MR. Acetylcarnitine crosses the mitochondrial membrane easily, while skipping a few metabolic steps needed for acetate to cross the membrane. Moreover, it does not interfere with the detection of [5-¹³C]glutamate and [5-¹³C]citrate. [1-¹³C]Acetylcarnitine was successfully hyperpolarized and despite its short T_1 it was possible to detect the formation of [5-¹³C]glutamate in the heart *in vivo*. Due to the absence of the [5-¹³C]citrate resonance, we hypothesized the existence of an intricate relationship between reaction, transport and relaxation rates in the choice of hyperpolarized substrates.

Acetylcarnitine has relatively small poolsizes and has only been observed using hyperpolarized ¹³C MRS techniques. Therefore, it has not been possible to obtain reliable quantification of the metabolic turnover of acetylcarnitine, which is an essential intermediate in the metabolism of acetate. Methods were implemented to measure the oxidation of [2-¹³C]acetate locally with increased sensitivity at high field (14.1T), using a ¹H-¹³C polarization transfer sequence. This allowed the observation of [2-¹³C]acetylcarnitine *in vivo* at 21.5 ppm, with a metabolic turnover time τ of 0.34 $\mu\text{mol/g/hr}$. The acetylcarnitine resonance assignment was confirmed by experiments infusing ¹³C labeled glucose. The measurement of the time courses of Glu C4 and C3 were also clearly observed, without lipid contamination.

To conclude, this work presents novel metabolic information about skeletal and cardiac energy metabolism using developed methods in hyperpolarized ¹³C MRS. The use of hyperpolarized ¹³C substrates to measure absolute flux through metabolic pathways *in vivo* would not only revolutionize clinical diagnostic imaging but also serve as an important tool to better understand diseased metabolism and the metabolic effects of new drugs aimed to combat diseases.

KEYWORDS: Metabolism, nuclear magnetic resonance (NMR), ¹³C magnetic resonance spectroscopy (MRS), skeletal muscle, cardiac muscle, hyperpolarization, dissolution dynamic nuclear polarization (DNP), enzyme kinetics, mathematical modeling, substrate competition

Résumé

La fonction musculaire cardiaque et squelettique repose sur la production constante d'énergie par l'intermédiaire du métabolisme des acides gras et l'oxydation mitochondriale du pyruvate, qui requièrent un équilibre subtil entre l'apport et l'utilisation du substrat. Les modifications du métabolisme sont de plus en plus considérées comme jouant un rôle intrinsèque majeur dans le cadre de nombreuses maladies telles que le diabète, le cancer et les défaillances cardiaques. L'étude et l'identification des processus métaboliques sont cruciaux pour comprendre avec précision et fiabilité ces pathologies.

Au delà des informations morphologiques et fonctionnelles, la résonance magnétique nucléaire (RMN) fournit également un aperçu au niveau métabolique en employant des techniques de spectroscopies telles que la RMN du ^{13}C . La faible abondance naturelle et sensibilité du noyau de ^{13}C fait de la RMN du ^{13}C un véritable défi. Afin de déjouer ces limitations, les méthodes d'hyperpolarisation apparaissent comme des outils prometteurs et procurent des augmentations de signal de l'ordre de 10 000. Les spectres provenant de substrats hyperpolarisés marqués au ^{13}C , ainsi que des produits métaboliques en découlant, permettent l'étude *in vivo* des processus métaboliques dans les premières secondes après l'injection du substrat.

Cette thèse porte sur le développement de méthodes RMN d'hyperpolarisation et d'applications permettant l'étude *in vivo* du métabolisme énergétique dans les muscles cardiaques et squelettiques. Ces développements s'étendent de la mise en place du cadre expérimental aux outils mathématiques pour la caractérisation des processus métaboliques observés.

Des méthodes ont été développées pour visualiser, *in vivo*, la cinétique du marquage en ^{13}C de l'acétylcarnitine dans le muscle squelettique au repos après l'administration de $[1-^{13}\text{C}]\text{acétate}$ hyperpolarisé. Deux nouveaux modèles mathématiques ont été développés afin de quantifier les constantes des vitesses de réaction. Bien que séparée par deux réactions enzymatiques, la conversion de l'acétate en acétylcarnitine a pu être exceptionnellement mesurée via l'activité enzymatique de l'acétylCoA synthétase (ACS).

Un protocole de spectroscopie RMN du ^{13}C a été développé et implémenté pour des études hyperpolarisées dans le coeur, ce qui inclut un choix pertinent de déclencheurs cardiaques qui font correspondre les mesures RMN avec la phase cardiaque. La propagation du marquage en ^{13}C vers l'acétylcarnitine et le citrate a pu être mesurée en temps réel dans le battement de coeur suivant l'infusion du $[1-^{13}\text{C}]\text{acétate}$ hyperpolarisé. Pour réaliser cette étude, une bobine RF a été ajustée à la fréquence du ^{13}C et a été construite sur mesure afin d'améliorer la sensibilité de la détection du signal RMN. La haute résolution spectrale à 9,4 T ainsi que le

shimming synchronisé avec le battement cardiaque et le protocole d'acquisition RMN ont permis la détection du citrate pour la première fois *in vivo* après injection de [1-¹³C]acétate hyperpolarisé. Les modèles mathématiques ont été complétés afin d'inclure l'oxydation mitochondriale et les expressions analytiques ont été dérivées dans le but d'analyser la cinétique de marquage du ¹³C du citrate.

Les défaillances cardiaques sont souvent associées à un changement de préférence du substrat, alors que les méthodes diagnostiques telles que le PET fournissent uniquement des informations sur la consommation du substrat. Le potentiel de la spectroscopie par RMN du ¹³C hyperpolarisé, qui mesure simultanément l'oxydation lipidique et des carbohydrate, a été démontré *in vivo*, et la sensibilité de la méthode à des perturbations métaboliques a été déterminée. Le [1-¹³C]butyrate et le [1-¹³C]pyruvate ont été utilisés comme des représentants de l'oxydation des carbohydrate et lipides. Le jeûne a induit des changements significatifs de préférence pour les substrats injectés. L'apparition d'une cohorte de métabolites secondaires (bicarbonate, lactate, alanine, glutamate, citrate, acétylcarnitine, β-hydroxybutyrate et acétoacétate) a permis le suivi indépendant et simultané de l'oxydation au niveau du myocarde à la fois des acides gras et des carbohydrate. Ce suivi *in vivo* est un indicateur sensible des changements métaboliques.

Le lactate est un intermédiaire métabolique important pour l'oxydation mitochondriale. Le métabolisme des carbohydrate dans le muscle squelettique du rat sain a été étudié dans deux états nutritionnels (nourris et à jeun) en utilisant le [1-¹³C]lactate, qui peut être injecté à des concentrations physiologiques n'influençant ainsi aucun autre processus oxydatif. Des diminutions significatives en [1-¹³C]alanine et ¹³C bicarbonate ont été observées entre les deux groupes. Ces diminutions sont attribuées à une modification de la concentration cellulaire d'alanine et du flux de la déshydrogénase du pyruvate (PDH). Il a été montré que le lactate peut être utilisé pour étudier l'oxydation des carbohydrate dans le muscle squelettique aux niveaux physiologiques et que les signaux des métabolites secondaires sont des marqueurs sensibles pour détecter les changements métaboliques.

La détection du [5-¹³C]citrate dans le coeur est difficile en raison de sa forte proximité avec la résonance du [5-¹³C]acétate, ce qui limite également la détection du [5-¹³C]glutamate. L'acétylcarnitine est un substrat intéressant pour la RMN hyperpolarisée compte tenu du fait que, contrairement à l'acétate, elle traverse facilement la membrane mitochondriale sans passer par certaines étapes métaboliques. De plus, elle n'interfère pas avec la détection du [5-¹³C]glutamate et du [5-¹³C]citrate. La [1-¹³C]acétylcarnitine a été hyperpolarisée avec succès et malgré son court T_1 , il a été possible de détecter la formation *in vivo* de [5-¹³C]glutamate dans le coeur. En raison de l'absence de la résonance du [5-¹³C]citrate, nous avons supposé qu'il existe une relation intriquée entre les taux de réaction, transport et relaxation dans le choix des substrats hyperpolarisés.

L'acétylcarnitine a des tailles de pool relativement petites et n'a pu être observée qu'en utilisant des techniques de spectroscopies RMN hyperpolarisées. Ainsi, il n'est pas possible d'obtenir une quantification robuste du taux de renouvellement de l'acétylcarnitine, qui est un intermédiaire essentiel du métabolisme de l'acétate. Des méthodes ont été implémentées, permettant de mesurer localement l'oxydation du [2-¹³C]acétate avec une meilleure

sensibilité à plus haut champ magnétique (14,1 T), en utilisant une séquence de transfert de polarisation ^1H - ^{13}C . Ceci a permis d'observer la [2- ^{13}C]acétylcarnitine *in vivo* à 21.5 ppm, avec un temps de renouvellement métabolique de 0,34 $\mu\text{mol/g/h}$. L'attribution de la résonance de l'acétylcarnitine a été confirmée en effectuant des expériences avec infusion de glucose marqué au ^{13}C . La mesure de la cinétique de Glu C4 et C3 a également été clairement observée, sans contamination des lipides.

Pour conclure, ce travail présente de nouvelles informations sur le métabolisme énergétique du muscle squelettique et cardiaque en utilisant des méthodes en développement de spectroscopie RMN hyperpolarisée du ^{13}C . L'utilisation de substrats hyperpolarisés marqués au ^{13}C pour mesurer *in vivo* le flux absolu à travers les chemins métaboliques permet de révolutionner l'imagerie diagnostique clinique. Elle fournit également un outil important pour mieux comprendre le métabolisme de certaines pathologies ainsi que les effets métaboliques de nouveaux traitements.

Mots-clés : Métabolisme, résonance magnétique nucléaire (RMN), spectroscopie par résonance magnétique du ^{13}C , muscle squelettique, muscle cardiaque, hyperpolarisation, polarisation dynamique nucléaire (DNP) par dissolution, cinétiques enzymatiques, modélisation mathématique, compétition de substrat

Contents

| | |
|--|--------------|
| Acknowledgements / Dankwoord | iii |
| Abstract (English/Français) | vii |
| Table of contents | xv |
| List of Figures | xix |
| List of Tables | xxi |
| List of Symbols and Abbreviations | xxiii |
| List of Publications and Conference Proceedings | xxv |
| Introduction and Outline of Thesis | 1 |
| 1 An introduction to NMR spectroscopy | 5 |
| 1.1 History of Magnetic Resonance | 6 |
| 1.2 Basic Principles of MR | 6 |
| 1.2.1 Nuclei in a magnetic field | 6 |
| 1.2.2 Polarization | 7 |
| 1.2.3 Magnetization | 8 |
| 1.2.4 Excitation and Bloch Equations | 10 |
| 1.2.5 Relaxation of the magnetization | 11 |
| 1.2.6 Detection of the MR signal - Fourier transform NMR | 14 |
| 1.2.7 Measurement of relaxation time constants | 16 |
| 1.2.8 Chemical Shift | 18 |
| 1.2.9 Nuclear coupling | 20 |
| 1.2.10 Localized spectroscopy | 22 |
| 1.3 Hyperpolarization | 25 |
| 1.3.1 Dynamic Nuclear Polarization | 25 |
| 1.3.2 Polarization mechanisms | 26 |
| 1.3.3 Dissolution DNP | 30 |
| 1.4 Radiofrequency Coils | 31 |
| 1.5 Dynamic ^{13}C NMR Spectroscopy | 33 |

| | | |
|----------|---|------------|
| 1.5.1 | Modeling biochemical processes using ^{13}C MRS | 36 |
| 2 | Enzymatic activity of acetylCoA synthetase revealed with hyperpolarized acetate | 43 |
| 2.1 | Introduction to acetate metabolism in skeletal muscle | 44 |
| 2.2 | Materials and Methods | 46 |
| 2.3 | Kinetic model of hyperpolarized acetate metabolism in skeletal muscle | 50 |
| 2.4 | Mathematical Derivation of the Signal Ratio | 54 |
| 2.5 | Results | 55 |
| 2.6 | Discussion | 61 |
| 2.7 | Incorporation of a substrate build-up in the kinetic model | 62 |
| 2.8 | Independence and sensitivity of fitting parameters k_{ACS} and R_A | 63 |
| 2.9 | Conclusion | 64 |
| 3 | In vivo real time cardiac metabolism using hyperpolarized acetate | 71 |
| 3.1 | Introduction | 72 |
| 3.2 | Methods | 73 |
| 3.2.1 | Cardiac triggering for MR imaging and spectroscopy | 73 |
| 3.2.2 | In vivo magnetic resonance spectroscopy | 76 |
| 3.3 | Kinetic model of hyperpolarized acetate metabolism in the heart | 80 |
| 3.4 | Results | 84 |
| 3.5 | Discussion | 85 |
| 4 | Myocardial substrate competition using hyperpolarized ^{13}C MR | 91 |
| 4.1 | Introduction | 92 |
| 4.2 | Materials and Methods | 94 |
| 4.3 | Results | 96 |
| 4.3.1 | Hyperpolarized $[1-^{13}\text{C}]$ pyruvate injection | 96 |
| 4.3.2 | Hyperpolarized $[1-^{13}\text{C}]$ butyrate injection | 97 |
| 4.3.3 | Hyperpolarized $[1-^{13}\text{C}]$ pyruvate and $[1-^{13}\text{C}]$ butyrate co-injection | 99 |
| 4.4 | Butyrate and Pyruvate Flux Analysis | 101 |
| 4.5 | Discussion | 103 |
| 4.5.1 | Pyruvate Injections | 103 |
| 4.5.2 | Butyrate Injections | 103 |
| 4.5.3 | Competition between pyruvate and butyrate | 105 |
| 5 | Hyperpolarized lactate metabolism in resting skeletal muscle in vivo | 113 |
| 5.1 | Introduction | 114 |
| 5.2 | Experimental Procedures | 116 |
| 5.3 | Results | 117 |
| 5.4 | Discussion | 121 |
| 5.5 | Metabolic flux analysis of alanine labeling | 124 |

| | | |
|----------|---|------------|
| 6 | Hyperpolarized acetylcarnitine as a probe for myocardial metabolism in vivo | 131 |
| 6.1 | Introduction | 132 |
| 6.2 | Methods | 133 |
| 6.3 | Results and Discussion | 134 |
| 7 | Acetylcarnitine turnover measurements in skeletal muscle in vivo using localized sensitivity enhanced ^{13}C MRS at 14.1 T | 139 |
| 7.1 | Introduction | 140 |
| 7.2 | Methods | 141 |
| 7.2.1 | Animal preparation | 141 |
| 7.2.2 | Saline and $[2\text{-}^{13}\text{C}]$ acetate infusion procedure | 141 |
| 7.2.3 | <i>In vivo</i> MR spectroscopy | 141 |
| 7.2.4 | <i>In vitro</i> MR spectroscopy | 142 |
| 7.2.5 | Fractional enrichments and turnover calculations | 143 |
| 7.3 | Results | 144 |
| 7.4 | Discussion | 148 |
| 8 | Conclusion and Outlook | 157 |
| A | Appendix | 161 |
| A.1 | RF coil design for hyperpolarized ^{13}C NMR studies | 161 |
| A.1.1 | Quadrature ^{13}C coil for cardiac muscle applications | 161 |
| A.1.2 | B_1 mapping | 163 |
| A.1.3 | Sensitivity comparison with a conventional design | 163 |
| A.2 | Adiabatic RF pulse calibrations and simulations | 163 |
| | Curriculum Vitae | 169 |

List of Figures

| | |
|---|----|
| 1.1 Spin energy as function of the magnetic field | 7 |
| 1.2 Precession and macroscopic magnetization | 9 |
| 1.3 Excitation of the magnetization vector | 11 |
| 1.4 Recovery of the magnetization after excitation | 14 |
| 1.5 T_1 measurement | 16 |
| 1.6 T_2 measurement - A spin echo experiment | 17 |
| 1.7 Chemical Shift | 19 |
| 1.8 Uncoupled and coupled spin system | 21 |
| 1.9 Effect of ^1H decoupling on the ^{13}C spectrum of $[1-^{13}\text{C}]\text{acetylcarnitine}$ | 22 |
| 1.10 Principle of slice selection | 23 |
| 1.11 ISIS sequence diagram | 24 |
| 1.12 General mechanism of dynamic nuclear polarization | 27 |
| 1.13 Energy levels and transitions of a two spin system consisting of a nucleus and an electron | 27 |
| 1.14 Linearly and circularly polarized magnetic fields | 32 |
| 1.15 Quadrature coil decoupling | 33 |
| 1.16 ^{13}C label flow through the TCA cycle following the metabolism of acetate, lactate and pyruvate. | 35 |
| 1.17 Glutamate multiplet patterns induced by ^{13}C - ^{13}C coupling | 36 |
| 2.1 Schematic of acetate metabolism in resting skeletal muscle <i>in vivo</i> | 44 |
| 2.2 Graphical scheme and timing of <i>in vivo</i> DNP experiments | 46 |
| 2.3 Picture of experimental settings for performing hyperpolarized ^{13}C experiments | 47 |
| 2.4 Influence of repeated RF excitation on longitudinal and transverse magnetizations | 47 |
| 2.5 Anatomical proton image of skeletal muscle and RF coil positioning | 49 |
| 2.6 Relaxivity of $[1-^{13}\text{C}]\text{pyruvate}$ and $[1-^{13}\text{C}]\text{pyruvate}$ in D_2O at 400 MHz | 50 |
| 2.7 Spectral time course of acetate and acetylcarnitine in skeletal muscle | 56 |
| 2.8 T_1 measurement of $[1-^{13}\text{C}]\text{acetylcarnitine}$ in plasma using a saturation recovery sequence | 57 |
| 2.9 Signal evolution and model fitting of hyperpolarized $[1-^{13}\text{C}]\text{acetate}$ metabolism | 58 |
| 2.10 Relation between reaction rates and acetate dosage | 59 |
| 2.11 Derivation of the kinetic rate constant k_{ACS} and initial reaction rate $v_{0,\text{ACS}}$ using two different approaches | 60 |

| | | |
|------|---|-----|
| 2.12 | Influence of the incorporation of an acetate build up on the estimation of k_{ACS} | 63 |
| 2.13 | Sensitivity of fitting parameters | 65 |
| 3.1 | Metabolism of hyperpolarized acetate in the heart | 74 |
| 3.2 | A Wiggers diagram, showing the cardiac cycle events occuring in the left ventricle | 75 |
| 3.3 | Double gating for cardiac ^{13}C MRS | 75 |
| 3.4 | Diagram of triggered gradient echo pulse sequence | 77 |
| 3.5 | Cinematographic MR image series of the rat heart for trigger planning | 78 |
| 3.6 | Cardiac positioning for hyperpolarized ^{13}C MRS | 79 |
| 3.7 | Voxel location for cardiac triggered shimming | 79 |
| 3.8 | Spectral time course of $[1-^{13}\text{C}]$ acetate metabolism in the heart <i>in vivo</i> | 84 |
| 3.9 | Spectrum sum revealing the presence of $[5-^{13}\text{C}]$ citrate | 85 |
| 3.10 | Integral time course of $[1-^{13}\text{C}]$ acetate and its metabolic products | 86 |
| 3.11 | Integral time course of $[1-^{13}\text{C}]$ acetylcarnitine and $[5-^{13}\text{C}]$ citrate | 86 |
| 4.1 | Metabolic pathways of pyruvate and butyrate metabolism in healthy myocardium. | 93 |
| 4.2 | Hyperpolarized ^{13}C MR spectra of the heart <i>in vivo</i> and and metabolite ratios following the metabolism of $[1-^{13}\text{C}]$ pyruvate | 97 |
| 4.3 | Hyperpolarized ^{13}C MR spectra of the heart <i>in vivo</i> and and metabolite ratios following the metabolism of $[1-^{13}\text{C}]$ butyrate | 98 |
| 4.4 | Time course of hyperpolarized ^{13}C MR spectra of the heart <i>in vivo</i> following the metabolism of $[1-^{13}\text{C}]$ pyruvate and $[1-^{13}\text{C}]$ butyrate simultaneously | 100 |
| 4.5 | Metabolite ratios normalized to pyruvate intensities | 101 |
| 4.6 | pH measurement in cardiac tissue <i>in vivo</i> using the spectral evolution of hyperpolarized ^{13}C bicarbonate and $^{13}\text{CO}_2$ | 104 |
| 5.1 | Pathways of lactate metabolism in skeletal muscle | 115 |
| 5.2 | ^{13}C spectra of lactate metabolism in skeletal muscle <i>in vivo</i> | 118 |
| 5.3 | Signal evolution of lactate and downstream metabolites. | 119 |
| 5.4 | Plasma lactate concentrations during a hyperpolarized experiments. | 120 |
| 5.5 | Signal ratios relative to alanine after lactate injection | 120 |
| 5.6 | Influence of repeated injections of lactate on muscle metabolism. | 121 |
| 5.7 | Pyruvate and bicarbonate ratios relative to alanine | 125 |
| 6.1 | Scheme of myocardial acetylcarnitine metabolism | 132 |
| 6.2 | Polarization buildup of $[1-^{13}\text{C}]$ acetylcarnitine and <i>in vitro</i> decay after dissolution | 135 |
| 6.3 | Integrated time course of cardiac metabolism following the infusion of hyperpolarized $[1-^{13}\text{C}]$ acetylcarnitine | 136 |
| 6.4 | <i>In vivo</i> cardiac ^{13}C NMR spectrum following the injection of hyperpolarized $[1-^{13}\text{C}]$ acetylcarnitine | 136 |
| 7.1 | Effect of OVS and ISIS on signal localization | 142 |
| 7.2 | Difference between unlocalized and localized ^{13}C MR spectra in skeletal muscle | 145 |
| 7.3 | Fractional enrichment of ^{13}C in acetate C2 in plasma | 146 |

| | | |
|-----|---|-----|
| 7.4 | Time course of [2- ^{13}C]acetate metabolism in skeletal muscle <i>in vivo</i> at 14.1T . . | 147 |
| 7.5 | Evolution of the fractional enrichment of glutamate C2 C3 and C4 in skeletal muscle <i>in vivo</i> after the infusion of [2- ^{13}C]acetate | 148 |
| 7.6 | Comparison of ^{13}C spectra of a ^{13}C labeled glucose and acetate infusion in brain and muscle respectively | 149 |
| 7.7 | Comparison of ^{13}C spectra of a ^{13}C labeled glucose and acetate infusion in skeletal muscle | 150 |
| 7.8 | Evolution of acetylcarnitine C2 concentration in skeletal muscle <i>in vivo</i> after the infusion of [2- ^{13}C]acetate | 151 |
| 7.9 | ^{13}C NMR of a skeletal muscle tissue extract | 151 |
| A.1 | Electrical circuit and image of ^{13}C coil in quadrature mode | 161 |
| A.2 | ^{23}Na MRI of a NaCl phantom | 162 |
| A.3 | ^{23}Na MRS for the measurement of the quadrature property in an RF coil | 162 |
| A.4 | Power calibration for adiabatic 90° pulses | 163 |
| A.5 | ^{13}C MRI of a ^{13}C labeled acetate phantom using a quadrature ^{13}C surface coil . | 164 |
| A.6 | B_1 maps of the quadrature ^{13}C surface coil | 164 |
| A.7 | Bloch simulations of magnetization vector | 165 |
| A.8 | NMR bandwidth calibrations for 10° pulses | 166 |
| A.9 | NMR bandwidth calibrations for 90° pulses | 167 |

List of Tables

| | | |
|-----|--|----|
| 1.1 | NMR properties of several nuclei | 8 |
| 1.2 | Polarization levels of nuclear and electron spins | 26 |
| 1.3 | T_1 of ^{13}C labeled metabolites of interest for <i>in vivo</i> DNP studies | 31 |
| 2.1 | T_1 of $[1-^{13}\text{C}]$ acetylcarnitine | 58 |
| 4.1 | Body weight and glucose levels after an overnight fast. | 95 |
| 4.2 | Chemical shifts of observed metabolites following the injection of hyperpolarized sodium $[1-^{13}\text{C}]$ butyrate and sodium $[1-^{13}\text{C}]$ pyruvate. | 96 |

List of Symbols and Abbreviations

| | |
|------------|---|
| δ | Chemical shift |
| γ | Gyromagnetic ratio |
| \hbar | Planck's constant divided by 2π |
| μ | Magnetic moment |
| ω_0 | Larmor frequency |
| E | Energy |
| k | Kinetic rate constant |
| k_B | Boltzmann constant |
| K_M | Michaelis constant |
| ν_0 | Initial reaction rate |
| V_{max} | Maximum reaction rate |
| B_0 | Main magnetic field strength or magnetic flux density |
| R_1 | Longitudinal relaxation rate equal to the reciprocal of T_1 |
| r_1 | Dipolar T_1 relaxivity of a contrast agent |
| R_2 | Transverse relaxation rate equal to the reciprocal of T_2 |
| r_2 | Dipolar T_2 relaxivity of a contrast agent |
| T_1 | Spin-lattice or longitudinal relaxation time |
| T_2 | Spin-spin or transverse relaxation time |
| T_2^* | Transverse relaxation time including macroscopic inhomogeneities |
| T_E | Echo time, the time between excitation pulse and peak echo formation |
| T_I | Inversion time, the time between an 180° inversion pulse and acquisition |
| T_R | Repetition time, the time between consecutive RF excitation pulses |
| AAT | acetoacetylCoA thiolase |
| Ace | Acetate |
| ACS | AcetylCoA synthetase |
| ALT | Alanine transaminase |
| ATL | Acetylcarnitine translocase |
| ATP | Adenosine triphosphate |
| BIR-4 | B_1 -insensitive rotation with 4 segments |
| CA | Carbonic anhydrase |
| CAT | Carnitine acetyltransferase |
| CoA | Coenzyme A |
| Cre | Creatine |

| | |
|---------|---|
| CS | Citrate synthase |
| DEPT | Distortionless enhancement by polarization transfer |
| DNP | Dynamic nuclear polarization |
| ECG | Electrocardiogram |
| emf | Electromotive force |
| FE | Fractional enrichment |
| FFA | Free fatty acid |
| FID | Free induction decay. |
| FID | Free induction decay |
| Glu | Glutamate |
| IR | Inversion recovery |
| ISIS | Image selected in vivo spectroscopy |
| Lac | Lactate |
| LCModel | Linear combination of model spectra |
| LDH | Lactate dehydrogenase |
| MCT | monocarboxylate transporter |
| MRI | Magnetic resonance imaging |
| MRS | Magnetic resonance spectroscopy |
| NMR | Nuclear magnetic resonance |
| NOE | Nuclear Overhauser effect |
| OAA | Oxaloacetate |
| OAT | 3-oxoacid CoA transferase |
| OVS | Outer volume suppression |
| PBS | Phosphate buffered saline |
| PDH | Pyruvate dehydrogenase |
| PET | Positron emission tomography |
| ppm | parts per million |
| PT | Pyruvate transporter |
| RF | Radio frequency |
| ROI | Region of interest |
| SD | Standard deviation |
| SEM | Standard error of the mean |
| SNR | Signal to noise ratio |
| SR | Saturation recovery |
| STEAM | Stimulated echo acquisition mode |
| Tau | Taurine |
| TCA | Tricarboxylic acid |
| TEMPO | 2,2,6,6-Tetramethylpiperidine-1-oxyl |
| VOI | Volume of interest |

Publications & Conference Proceedings

Journal Articles

- (1) **J.A.M. Bastiaansen**, T. Cheng, M. Mishkovsky, J.M.N. Duarte, A Comment, R. Gruetter. In vivo enzymatic activity of acetylCoA synthetase in skeletal muscle revealed by ^{13}C turnover from hyperpolarized $[1-^{13}\text{C}]$ acetate to $[1-^{13}\text{C}]$ acetylcarnitine. *Biochimica et Biophysica Acta*, vol. 1830, num. 8, p. 4171-4178 (2013)
- (2) T. Cheng, M. Mishkovsky, **J.A.M. Bastiaansen**, O. Ouari, P. Hautle, P. Tordo, B.v.d. Brandt, A. Comment, Method to minimize and monitor in situ the polarization losses in hyperpolarized biomolecules prior to in vivo MR experiments. *NMR in Biomedicine*, doi:10.1002/nbm.2993 (2013)
- (3) **J.A.M. Bastiaansen**, M.E. Merritt, A Comment. In vivo myocardial substrate competition using hyperpolarized ^{13}C magnetic resonance. Submitted, (2013)
- (4) **J.A.M. Bastiaansen**, H.A.I. Yoshihara, Y. Takado, R. Gruetter, A. Comment. Hyperpolarized ^{13}C lactate as substrate for in vivo metabolic studies in skeletal muscle. Submitted (2013)
- (5) **J.A.M. Bastiaansen**, T. Cheng, R. Gruetter, A. Comment. Mitochondrial cardiac metabolism of hyperpolarized acetate. Manuscript in preparation (2013)
- (6) **J.A.M. Bastiaansen**, T. Cheng, R. Gruetter, A. Comment. Hyperpolarized $[1-^{13}\text{C}]$ acetylcarnitine as a tracer for cardiac metabolism. Manuscript in preparation (2013)
- (7) **J.A.M. Bastiaansen**, J.M.N. Duarte, A. Comment, R. Gruetter. Acetylcarnitine turnover in rat skeletal muscle measured in vivo using localized ^{13}C NMR at 14.1 T. Manuscript in preparation (2013)
- (8) Y. Takado, T. Cheng, B. Lanz, **J.A.M. Bastiaansen**, M. Mishkovsky, R. Gruetter, A. Comment, Lactate brain metabolism in different mouse strains probed by hyperpolarized ^{13}C MRS. Manuscript in preparation (2013)

Conference Proceedings (Peer Reviewed)

- (1) **J.A.M. Bastiaansen**, Y. Takado, H. Yoshihara, T. Cheng, A. capozzi, R. Gruetter, A. comment, Hyperpolarized [1-¹³C]lactate metabolism in rat skeletal muscle in vivo. Fourth International Symposium on Dynamic Nuclear Polarization (2013), oral presentation
- (2) H. A. I. Yoshihara, **J. A. M. Bastiaansen**, C. Berthonneche, A. Comment, J. Schwitter, Energy metabolism in the ischemic rat heart assessed using hyperpolarized ¹³C Fourth International Symposium on Dynamic Nuclear Polarization (2013), poster
- (3) Y. Takado, T. Cheng, B. Lanz, **J.A.M. Bastiaansen**, M. Mishkovsky, R. Gruetter, A. Comment, Lactate brain metabolism in different mouse strains probed by hyperpolarized ¹³C MRS. Fourth International Symposium on Dynamic Nuclear Polarization (2013), poster
- (4) **J.A.M. Bastiaansen**, T. Cheng, R. Gruetter and A. Comment. Hyperpolarized [1-¹³C]acetyl-carnitine as a tracer for cardiac metabolism. Proc. Intl. Soc. Mag. Reson. Med. 21, 1936 (2013) poster
- (5) **J.A.M. Bastiaansen**, J.M.N. Duarte, A. Comment and R. Gruetter. Acetylcarnitine turnover in rat skeletal muscle measured in vivo using localized ¹³C NMR at 14.1 T. Proc. Intl. Soc. Mag. Reson. Med. 21, 0120 (2013) oral presentation
- (6) T. Cheng, M. Mishkovsky, **J.A.M. Bastiaansen**, O. Ouari and P. Hautle et al. Method to minimize polarization losses in hyperpolarized biomolecules prior to in vivo MR experiments. ESMRMB 29 (2012) poster
- (7) **J.A.M. Bastiaansen**, T. Cheng, JMN Duarte, M. Mishkovsky, A. Comment, R. Gruetter, Kinetic analysis of acetylCoA synthetase activity in skeletal muscle, ESMRMB 29 (2012) oral presentation
- (8) **J.A.M. Bastiaansen**, T. Cheng, R. Gruetter, A. Comment, In vivo real time cardiac metabolism using hyperpolarized acetate, Proc. Intl. Soc. Mag. Reson. Med. 20, 5137 (2012) electronic poster
- (9) **J.A.M. Bastiaansen**, Tian Cheng, Mor Mishkovsky, Arnaud Comment, Rolf Gruetter, In vivo enzymatic assay of carnitine acetyl transferase and acetylCoA synthetase using hyperpolarized acetate, Proc. Intl. Soc. Mag. Reson. Med. 20, 5117 (2012) electronic poster
- (10) E. Can, **J.A.M. Bastiaansen**, T. Cheng, N. Salameh, Y. Takado, M. Mishkovsky, R. Gruetter, A. Comment, BDPA as a polarizing agent for in vivo hyperpolarized MR experiment, Metaflux Meeting (2012) oral presentation
- (11) Y. Takado, T. Cheng, **J.A.M. Bastiaansen**, M. Mishkovsky, R. Gruetter, A. Comment, In vivo real-time metabolic studies of mice brain and skeletal muscle at 9.4T, Third International Symposium on Dynamic Nuclear Polarization (2011) poster
- (12) **J.A.M. Bastiaansen**, T. Cheng, M. Mishkovsky, A. Comment, R. Gruetter, The metabolic effect of hyperpolarized [1-¹³C]acetate dosage in vivo, Third International Symposium on Dynamic Nuclear Polarization (2011) poster

- (13) **J.A.M. Bastiaansen**, T. Cheng, R. Gruetter, A. Comment, Kinetics of hyperpolarized [1 - ^{13}C]acetate metabolism in cardiac muscle, Third International Symposium on Dynamic Nuclear Polarization (2011) poster
- (14) **J.A.M. Bastiaansen**, T. Cheng, M. Mishkovsky, A. Comment, R. Gruetter, Study of acetyl-carnitine kinetics in skeletal muscle in vivo using hyperpolarized [1- ^{13}C]acetate, Proc. Intl. Soc. Mag. Reson. Med. 19, 6795 (2011), electronic poster
- (15) **J.A.M. Bastiaansen**, T. Cheng, M. Mishkovsky, A. Comment, R. Gruetter, Hyperpolarized acetate as a metabolic tracer for skeletal and cardiac muscle energetics, TOPIM 2011, oral presentation

Previous work:

- (16) **J.A.M. Bastiaansen**, X. Zhang, D. Janvelyan, S. Fraser and R.E. Jacobs, Spatiotemporal connectivity in the mesolimbic system revealed by MEMRI, SSN (2010) poster
- (17) **J.A.M. Bastiaansen**, X. Zhang, D. Janvelyan, S. E. Fraser, R.E. Jacobs, Dynamics of Mn transport in the mesolimbic system reveal neural projections from the Nucleus Accumbens in vivo, Proc. Intl. Soc. Mag. Reson. Med. 18, 311 (2010) oral presentation
- (18) **J.A.M. Bastiaansen**, X. Zhang, R.E. Jacobs, Limits of Mn detection in vivo: Spatial segregation of relaxation behavior, Proc. Intl. Soc. Mag. Reson. Med. 18, 4502 (2010) electronic poster

Introduction and Outline of Thesis

Introduction

Beyond providing insight into tissue structure and functionality, nuclear magnetic resonance (NMR) is a powerful, non-invasive tool to study metabolism in cell cultures, perfused organs, animals and humans¹. The most bio-relevant NMR active nuclei which possess a nuclear magnetic moment are proton (^1H), phosphorus (^{31}P) and carbon (^{13}C). ^1H NMR allows the detection of important neurotransmitters² but, in addition to its small chemical shift range, it is hindered by the strong water signal. ^{31}P provides information about energetically important metabolites, intracellular pH and reaction fluxes, but its signal originates from a limited number of low molecular weight compounds³.

^{13}C NMR has become a well established technique to investigate *in vivo* metabolic processes and offers the possibility to study the fluxes through metabolic pathways⁴, and can be coupled with MR imaging techniques that give anatomical information. Since most metabolically relevant compounds contain carbon, it is possible to detect many metabolites with excellent spectral resolution. However, ^{13}C NMR only detects the ^{13}C isotope of carbon, which has a natural abundance of 1.11%. This sensitivity limitation can be overcome by infusing ^{13}C labeled molecules to study their metabolism *in vivo*. Although powerful, ^{13}C isotopomer methods, used to analyze relative fluxes, mostly require metabolic steady state conditions and sufficient sample to allow collection of ^{13}C NMR spectra over reasonable scan times. Contamination of the spectra by unwanted natural abundance ^{13}C lipid resonances poses additional challenges for applications in skeletal and cardiac muscle. Additionally, NMR suffers from an intrinsically low sensitivity due to a low spin polarization at thermal equilibrium. The most straightforward method to increase the sensitivity is to increase the external magnetic field, or employ the use of polarization transfer sequences. Improved RF coil design, increases the detection sensitivity and decreases the noise, but does not change the fundamental spin polarization.

Hyperpolarized techniques, such as dynamic nuclear polarization (DNP), have emerged as a means to enhance the sensitivity of MR tremendously, by increasing the nuclear spin polarization. The process of DNP itself is carried out on frozen solids, but the advent of dissolution DNP⁵ has enabled the preservation of the sensitivity increase at room temperature. This allows

for the measurement of low concentration metabolites as well as the observation of metabolic processes in real-time *in vivo* after infusion of hyperpolarized ^{13}C labeled biomolecules⁶. Dissolution DNP is a relatively young technique which opens the way for many interesting *in vivo* applications but the full scope of its potential remains to be investigated. Currently the technique is being used in the first human trials in the investigation of prostate cancer^{7;8}.

Of particular interest in this thesis are skeletal and cardiac muscle, which function relies on a continuous production of energy, mainly via the hydrolysis of adenosine triphosphate (ATP). The synthesis of ATP occurs via two metabolic pathways; aerobic and anaerobic combustion. Aerobic production of ATP is the predominant and most efficient pathway. It involves the chemical conversion of carbohydrates, lipids and proteins into carbon dioxide and water and requires a sufficient oxygen supply. Under normal physiological conditions, oxidative metabolism of nonesterified fatty acids provides 40-60% of the ATP used by the heart. Glucose is an important alternative fuel, and accounts for approximately 20-40% of the energy needs of the heart under fasting conditions⁹. The heart can use a variety of other substrates such as lactate and ketone bodies for energy production, but the low plasma concentrations of these substrates limit their usage. Skeletal muscle at rest oxidizes both carbohydrates and lipids, and a shift to carbohydrate oxidation is observed with increasing exercise levels.

The use of the fatty acid acetate as a substrate was of particular interest. Acetate is an important metabolic substrate which supplies 6-10% of the basal energy in humans¹⁰. Until recently, most studies were not able to obtain reliable quantification of the metabolic turnover of hyperpolarized acetate to acetylcarnitine¹¹. Carnitine plays an essential role in transferring long-chain fatty acids into the mitochondrial matrix for subsequent β -oxidation, and in the regulation of the mitochondrial acetylCoA/CoA ratio. Thus, carnitine regulates the balance between fatty acid and carbohydrate metabolism.

Since tissue metabolism is modified in many common disease states like cancer, diabetes, and heart failure, the use of hyperpolarized ^{13}C substrates to measure absolute flux through important pathways *in vivo* would not only revolutionize clinical diagnostic imaging but also serve as an important tool to better understand the metabolic effects of new drugs aimed to combat these diseases¹².

Aim

This work focused on the development of *in vivo* magnetic resonance techniques to investigate metabolism in skeletal and cardiac muscle, both using DNP hyperpolarized ^{13}C spectroscopy as well as conventional room temperature MR methods at high field.

Since *in vivo* DNP experiments by itself are challenging, initial experiments were conducted on skeletal muscle to establish a protocol for *in vivo* studies. Once these protocols were established, methods were adapted and further developed to enable hyperpolarized ^{13}C experiments in the heart.

Outline of thesis

Chapter 1 aims to provide a brief overview of the basics of NMR, ^{13}C spectroscopy *in vivo* and kinetic modeling which might be of aid in understanding the concepts used in this thesis.

Chapter 2 describes the experimental considerations and development of hyperpolarized ^{13}C experiments *in vivo* in skeletal muscle. A particular interest is given to acetate and its application for metabolic studies in resting skeletal muscle. Using hyperpolarized acetate, the ^{13}C labeling of acetylcarnitine was measured in real-time. A mathematical model was introduced to describe acetate metabolism in resting skeletal muscle, and two different analytical approaches were discussed to calculate enzymatic activity. It was shown that the labeling rate reflects the enzymatic activity of acetylCoA synthetase.

With the establishment of an *in vivo* protocol for hyperpolarized studies in skeletal muscle, the scope of experiments was extended to that of the beating heart. **Chapter 3** describes the development of cardiac ^{13}C MR experiments and appropriate cardiac triggering. Again, acetate was chosen as substrate based on its applicability as shown in Chapter 2, and our knowledge and experience in the past with its hyperpolarizable properties. Acetate metabolism was studied in the beating healthy heart, and the mathematical models were extended to include mitochondrial oxidation. Additionally, analytical expressions were derived to interpret the dynamic ^{13}C labeling in acetylcarnitine and citrate.

The heart is a highly metabolically active organ which uses a variety of substrates in a well-balanced manner to support its mechanical function. Often, metabolic alterations lie at the onset of diseases. **Chapter 4** presents the heart with a substrate challenge in order to gain insight into the preferred substrates for myocardial oxidation and the ability of hyperpolarized MR to use substrate competition as a potential diagnostic tool. To this end, two different metabolic compounds, the lipid butyrate and the carbohydrate pyruvate, were coinjected in animals divided in two different nutritional groups. The metabolic changes as a result of this competition, as well as the concept of cardiac pseudoketogenesis, are discussed.

Since pyruvate is commonly administered at supraphysiological concentrations, the use of the carbohydrate lactate was investigated as a tracer for carbohydrate metabolism. Lactate is not only a waste product, but also an oxidizable substrate in resting skeletal muscle, which does not interfere with other metabolic processes. **Chapter 5** investigated the use of hyperpolarized lactate as a substrate for skeletal muscle metabolism in fed and fasted rats. Furthermore, the implications of endogenous substrate concentration changes on observed metabolism are discussed.

The detection of citrate in chapter 3 was hindered by the close proximity of the acetate resonance, which also obscures the detection of glutamate. Acetylcarnitine could be an interesting substrate since it crosses the mitochondria easily, skipping a few metabolic steps, and does not interfere with the detection of glutamate and citrate. **Chapter 6** investigates the feasibility of hyperpolarized acetylcarnitine as a tracer for myocardial substrate oxidation.

The intrinsic insensitivity of the ^{13}C carbon nucleus can also be overcome by increasing the field and using polarization transfer sequences. **Chapter 7** presents acetate studies conducted in skeletal muscle at 14.1 T using a localized polarization transfer sequence. The influence of localization methods on lipid resonances is shown, as well as the quantification of ^{13}C labeled muscle metabolites. Furthermore, the applicability of this method to measure the turnover of acetylcarnitine is demonstrated.

Finally, in **Chapter 8**, the main achievements of this thesis are presented with an outlook to possible applications, and future directions based on the presented research are discussed.

References

- [1] R. de graaf. *NMR spectroscopy: Principles and Techniques*. Wiley, 2008.
- [2] J Pfeuffer, I Tkac, SW Provencher, and R Gruetter. Towards an *in vivo* neurochemical profile: quantification of 18 metabolites in short-echo time ^1H nmr spectra of the rat brain. *Journal of Magnetic Resonance*, 141:104–120, 1999.
- [3] Donald W McRobbie, Elizabeth A Moore, Marting J Graves, and Martin R Prince. *MRI From picture to proton*, chapter 12: Phosphorus Spectroscopy. Cambridge University Press, 2003.
- [4] R. Gruetter. In vivo c-13 nmr studies of compartmentalized cerebral carbohydrate metabolism. *Neurochemistry International*, 41(2-3):143–154, 2002.
- [5] J. H. Ardenkjaer-Larsen, B. Fridlund, A. Gram, G. Hansson, L. Hansson, M. H. Lerche, R. Servin, M. Thaning, and K. Golman. Increase in signal-to-noise ratio of $> 10,000$ times in liquid-state nmr. *Proc Natl Acad Sci U S A*, 100(18):10158–10163, 2003.
- [6] K. Golman, R. in't Zandt, and M. Thaning. Real-time metabolic imaging. *Proc Natl Acad Sci U S A*, 103(30):11270–11275, 2006.
- [7] J. Kurhanewicz, D. B. Vigneron, K. Brindle, E. Y. Chekmenev, A. Comment, C. H. Cunningham, R. J. DeBerardinis, G. G. Green, M. O. Leach, S. S. Rajan, R. R. Rizi, B. D. Ross, W. S. Warren, and C. R. Malloy. Analysis of cancer metabolism by imaging hyperpolarized nuclei: Prospects for translation to clinical research. *Neoplasia*, 13(2):81–97, 2011.
- [8] S. J. Nelson, J. Kurhanewicz, D. B. Vigneron, P E. Larson, A. L. Harzstark, M. Ferrone, M. van Criekinge, J. W. Chang, R. Bok, I. Park, G. Reed, L. Carvajal, E. J. Small, P. Munster, V. K. Weinberg, J. H. Ardenkjaer-Larsen, A. P. Chen, R. E. Hurd, L. I. Odegardstuen, F. J. Robb, J. Tropp, and J. A. Murray. Metabolic imaging of patients with prostate cancer using hyperpolarized $[1-^{13}\text{C}]$ pyruvate. *Sci Transl Med*, 5(198):198ra108, 2013.
- [9] Jeffrey J Brown, Scott A Mirowitz, John C Sandstrom, and William H. Perman. Mr spectroscopy of the heart. *American Journal of Roentgenology*, 155:1–11, 1990.
- [10] E Pouteau, H Piloquet, P Maugeais, M Champ, H Dumon, P Nguyen, and M Krempf. Kinetic aspects of acetate metabolism in healthy humans using $[1-^{13}\text{C}]$ acetate. *Am J Physiol Endocrinol Metab*, 271:E58–E64, 1996.
- [11] P. R. Jensen, T. Peitersen, M. Karlsson, R. In 't Zandt, A. Gisselsson, G. Hansson, S. Meier, and M. H. Lerche. Tissue-specific short chain fatty acid metabolism and slow metabolic recovery after ischemia from hyperpolarized nmr in vivo. *Journal of Biological Chemistry*, 284(52):36077–82, 2009.
- [12] C. R. Malloy, M. E. Merritt, and A. D. Sherry. Could (^{13}C) mri assist clinical decision-making for patients with heart disease? *Nmr in Biomedicine*, 24(8):973–979, 2011.

An introduction to NMR spectroscopy

1

Abstract

Nuclear magnetic resonance is a versatile and widely used technique, most commonly known for its applications in imaging (MRI). This thesis uses the phenomenon of NMR for its spectroscopic applications. Since nuclei with magnetic moments are detectable using MR spectroscopy, biomolecules containing these nuclei can be measured, each with their own frequency signature. The non-invasive nature of NMR spectroscopy allows for the measurement of biochemical reactions in living organisms to study metabolism. This chapter gives a brief overview of the principles of magnetic resonance spectroscopy *in vivo* and serves as background information for the remaining chapters.

1.1 History of Magnetic Resonance

The phenomenon that specific atomic nuclei are able to absorb and transmit electromagnetic energy was first observed in 1946 by E. Purcell¹ and F. Bloch², for which they were awarded the Nobel Prize in Physics. These so-called nuclear magnetic resonance (NMR) experiments were initially performed by physicists to determine the magnetic moments of nuclei. NMR typically uses radiofrequencies in the range of 10 - 800 MHz. Later it was discovered that nuclei within the same molecule absorb energy at different resonance frequencies and that these are influenced by the chemical environment of the nucleus, in addition to the applied magnetic field. This discovery, made by Proctor³ and Dickinson⁴ in 1950 led to an extension of the applicability of MR to study the structure and environment of different molecules. In the next decades after its discovery NMR was used to study living objects. A growing interest in defining and explaining the properties of water in biological tissues resulted in the observation that NMR properties of healthy tissue is significantly different from that of cancerous tissue⁵. In the mid 70's Lauterbur⁶, Mansfield⁷ and coworkers were able to reconstruct images from the NMR resonances using position dependent magnetic fields. This led to the establishment of one of the major applications of NMR as we know today, magnetic resonance imaging (MRI), and was awarded the Nobel price in Medicine in 2003. Over the last decades, NMR spectroscopy and imaging has evolved tremendously and became a widely used tool to study and analyze tissue structure, function, composition and dynamic metabolic processes in live subjects.

1.2 Basic Principles of MR

1.2.1 Nuclei in a magnetic field

Nuclei with a net spin angular momentum \vec{L} interact with a magnetic field^{8;9}. This interaction, known as nuclear magnetic resonance (NMR), is described by the linear relationship between the static magnetic field B_0 experienced by a nucleus and the resulting angular frequency of rotation ω_0 of the nuclear spin,

$$\omega_0 = \gamma B_0 \quad (1.1)$$

where γ is the gyromagnetic ratio, which is a unique constant for each nuclear isotope possessing a spin. The gyromagnetic ratio of several nuclei of interests are given in Table 1.1. The angular frequency ω_0 is also referred to as the Larmor frequency, and is identical to the frequency of the electromagnetic radiation associated with the possible spin energy transitions induced by the magnetic field B_0 .

Nuclei in a magnetic field have $(2I + 1)$ energy levels where I is the spin quantum number which is an integer or half-integer and determined by the combined spin of the protons and the neutrons inside the nucleus (Table 1.1). This energy splitting is called the Zeeman effect. Each nuclear spin is associated with a quantized magnetic dipole moment $\vec{\mu}$ which is related

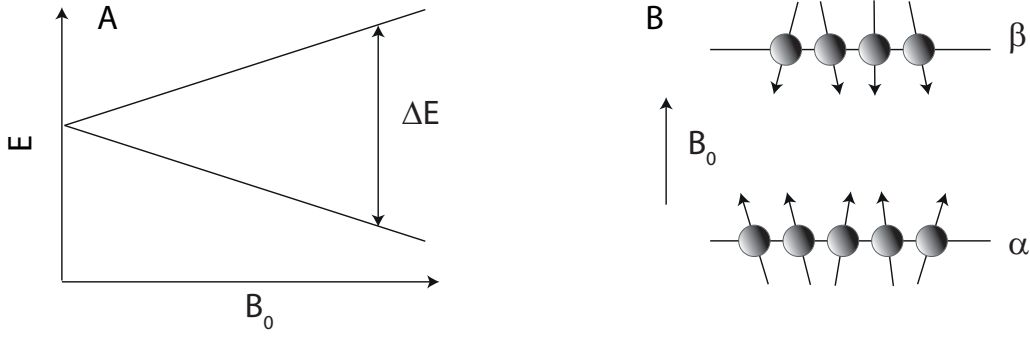


Figure 1.1: (A) The nuclear spin energy for a spin $\frac{1}{2}$ particle as function of the magnetic field strength B_0 . (B) The low energy level α corresponds to magnetic moments parallel with B_0 , while spins in the higher energy level β have an antiparallel alignment with B_0 .

to the angular momentum \vec{L} and given by:

$$\vec{\mu} = \gamma \vec{L} \quad (1.2)$$

The angular momentum of nuclei in the absence of a magnetic field are oriented randomly. When these spins are placed in a strong external magnetic field, their magnetic dipole moments tend to align with the field in either of the two states. For spin $I = \frac{1}{2}$ nuclei there are two possible energy levels in a magnetic field B_0 :

$$E = \pm \mu B_0 = \pm \frac{1}{2} \gamma \hbar B_0 \quad (1.3)$$

These two spin states are referred to as “up” and “down”, referring to a low (α) and a high (β) energy state (Figure 1.1). The energy difference ΔE between the two spin states is described as follows (Figure 1.1):

$$\Delta E = \gamma \hbar B_0 = \hbar \omega_0 \quad (1.4)$$

The energy needed to make transitions between energy levels increases with increasing magnetic field.

1.2.2 Polarization

The distribution of the spin states in a magnetic field is in thermal equilibrium and can be calculated using the Boltzmann equation:

$$\frac{n_\alpha}{n_\beta} = e^{\Delta E / k_B T} \quad (1.5)$$

Table 1.1: List of NMR properties of nuclei of interest in biomolecular applications

| Nucleus | Spin | Gyromagnetic ratio γ [MHz/T] | Natural abundance [%] |
|------------------|------|--|--------------------------|
| ^1H | 1/2 | 42.58 | 99.985 |
| ^2H | 1 | 6.54 | 0.015 |
| ^{12}C | 0 | - | 98.9 |
| ^{13}C | 1/2 | 10.71 | 1.1 |
| ^{31}P | 1/2 | 17.25 | 100 |
| ^{23}Na | 3/2 | 11.27 | 100 |
| ^{19}F | 1/2 | 40.08 | 100 |

where n_α and n_β denote the population in both the low and high energy state, k_B is the Boltzmann constant and T is the absolute temperature. The number of spins parallel to the magnetic field exceeds the number anti-parallel to that field, but this excess is very small. The polarization P is defined as the fraction of spins that are net aligned with the field and can be simplified to:

$$P = \frac{n_\alpha - n_\beta}{N} \simeq \frac{\hbar\omega_0}{2k_B T} \quad (1.6)$$

where $N = n_\alpha + n_\beta$ is the total number of spins. This means that at room temperature at low field the fraction of spins that are "up" is only one in a million. Considering the Avogadro number the amount of molecules in a small volume of sample that is in excess is such that it leads to measurable NMR effects.

For a sample at 37°C (310.15 K) and in a magnetic field of $B_0 = 9.4$ T, the ^{13}C ($\gamma=10.71$ MHz/T) spin polarization is only 8 ppm, 0.0008%

For a given amount of spins n the longitudinal equilibrium magnetization M_0 is determined by the magnetic moment component of each spin multiplied by the net amount of spins that are aligned and is described as follows:

$$M_0 = \frac{n\gamma^2\hbar^2}{4k_B T} B_0 \quad (1.7)$$

1.2.3 Magnetization

Although the NMR phenomenon is purely a quantum mechanical process, its macroscopic manifestation and interaction with external magnetic fields is, under most circumstances, well described by classical physics. In a classical description, the magnetic moment will experience a torque and starts to precess around an axis along the direction of the magnetic field with frequency ω_0 as illustrated in Figure 1.2A and this precession motion is described with the

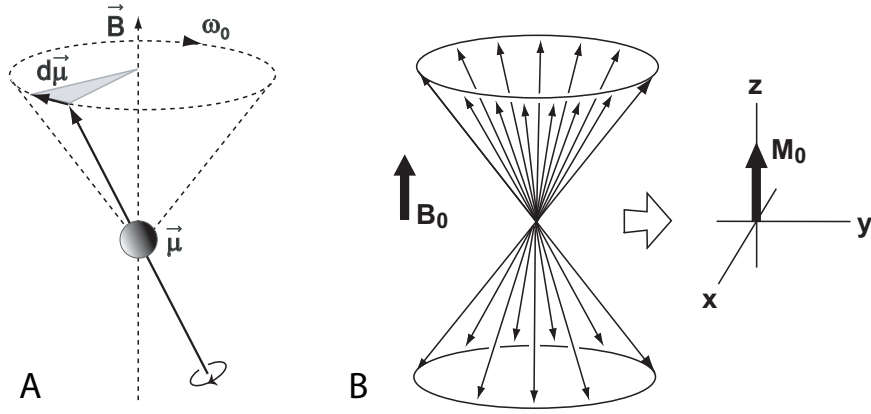


Figure 1.2: (A) The precession of a spin $\frac{1}{2}$ magnetic moment μ about a magnetic field B_0 according to a classical description. (B) The sum of all individual magnetic moments μ within a sample result in the net magnetization vector M_0 .

following equation:

$$\frac{d\vec{\mu}}{dt} = \gamma \vec{\mu} \times \vec{B} \quad (1.8)$$

In NMR, samples are studied which contain many individual spins. The spin angular momentum of all these spins are distributed on a cone (Figure 1.2B). Consider a volume V which is small enough that the external fields are constant but which contain a large number of nuclei. The total magnetization M in that voxel is the sum of the individual magnetic moments μ of the nuclei contained in that voxel (Figure 1.2B). This net magnetization vector is finite, observable and when the spin system is in a state of equilibrium this vector is parallel to the field,

$$\vec{M}_0 = \frac{1}{V} \sum_{\text{protons}} \vec{\mu}_i \quad (1.9)$$

A sum over the equation of motion for the individual spins yields the following description of the magnetization vector M :

$$\frac{d\vec{M}}{dt} = \gamma \vec{M} \times \vec{B} \quad (1.10)$$

This type of equation is known as the Bloch Equation^{2;10;11} and illustrates the interaction of spins with external magnetic fields.

1.2.4 Excitation and Bloch Equations

Magnetic resonance is based on the detection of the precessional motion of the magnetization vector. At thermal equilibrium the spins have no phase coherence in the transverse plane and the net longitudinal magnetization M_0 is a static vector (Figure 1.2B):

$$\frac{dM_z(t)}{dt} = 0 \quad (1.11)$$

No transversal components of \vec{M} exist at thermal equilibrium. To be able to measure the nuclear magnetization, M_0 needs to be moved away from its equilibrium. To be more specific, the M_0 needs to be rotated to the transverse plane. This is achieved by a second magnetic field, B_1 , which is a circularly polarized radio frequency (RF) field:

$$\vec{B}_1(t) = B_1 \cos \omega t + B_1 \sin \omega t \quad (1.12)$$

This second magnetic field B_1 is perpendicular to B_0 and oscillates in the xy -plane with the Larmor frequency ω_0 of the system. The longitudinal magnetization M_0 will experience a torque from the B_1 field, M_0 will then be tipped away from the z -axis towards the transversal plane. The magnetization vector will start to precess around the B_0 axis with ω_0 and around the B_1 axis with $\omega_1 = \gamma B_1$ (Figure 1.3A). The behavior of the macroscopic magnetization vector as a result of the magnetic interactions with B_1 and B_0 is described classically by the Bloch equation^{2,10,11}, which is given by,

$$\frac{d\vec{M}}{dt} = \gamma \vec{M} \times (\vec{B}_0 + \vec{B}_1) \quad (1.13)$$

Seen from a rotating frame of reference (1.3B), the magnetization vector experiences B_1 as a static field when B_1 is “on resonance”. oscillating with ω_0 . The angle of rotation α is determined by the duration t of the application of B_1 ,

$$\alpha = \gamma B_1 t \quad (1.14)$$

Typically, this angle α is referred to as the flip angle. Since the duration t needed to flip the magnetization by the required amount is typically very short, typically ranging from 100 μ s to a few ms, the applied B_1 -field is referred to as an RF pulse. The term excitation pulse is also used, reflecting the fact that the spin system will be in a higher energy state when the net magnetization of the system is moved away from its equilibrium orientation.

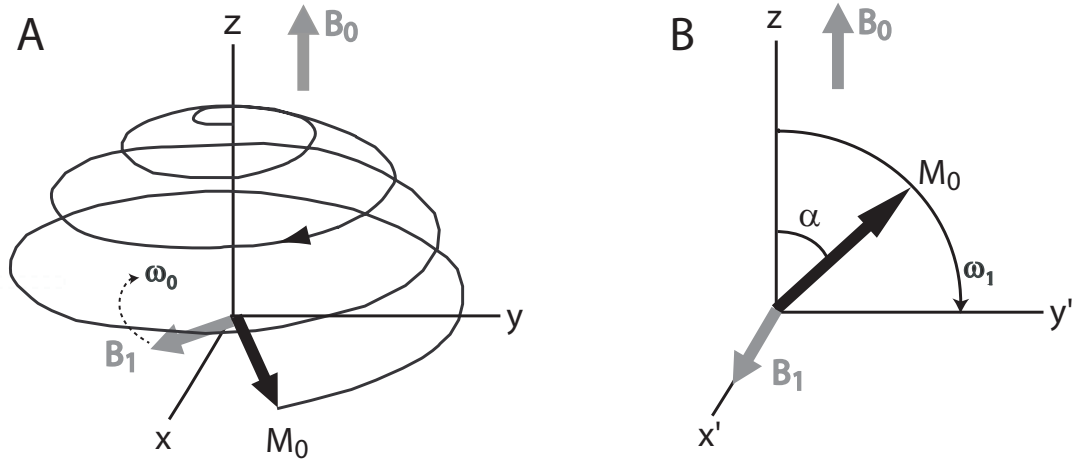


Figure 1.3: (A) The on-resonance trajectory of M_0 when an oscillating magnetic field B_1 is added to the static magnetic field B_0 in a laboratory frame xyz . The longitudinal magnetization M_0 will precess about the static magnetic field B_0 and the irradiating RF field B_1 in the transverse plane. (B) An identical situation is sketched in a rotating frame of reference where the x' and y' -axis are rotating about z with ω_0 .

1.2.5 Relaxation of the magnetization

During and after the application of the RF pulse, the magnetization vector consists of two components. The transversal magnetization M_{xy} which rotates about the z -axis and the longitudinal magnetization M_z . The oscillating nature of M_{xy} allows detecting induction of a current in a coil placed within this oscillating field. After application of the RF pulse, the measured NMR signal rapidly decays to zero. This process is generally referred to as relaxation, which describes the process of the magnetization returning to its thermal equilibrium. It is the result of several interactions and exchange and loss of the excitation energy. The Bloembergen Purcell Pound theory explains the relaxation mechanism by considering the motion and rotation of the spins influenced by its environment¹².

Two different relaxation processes occur with their own time constant, one is related to the decaying transversal magnetization M_{xy} , and one to the longitudinal magnetization M_z , and can be described by:

$$\frac{dM_{xy}(t)}{dt} = -\frac{M_{xy}(t)}{T_2} \quad (1.15)$$

$$\frac{dM_z(t)}{dt} = -\frac{M_z(t) - M_0}{T_1} \quad (1.16)$$

with T_1 the longitudinal relaxation time constant and T_2 is called the transversal relaxation time constant. The Bloch equations can be extended to incorporate relaxation as follows:

$$\frac{d\vec{M}}{dt} = \gamma \vec{M} \times \vec{B}_{ext} + \frac{1}{T_1}(\vec{M}_0 - \vec{M}_z) - \frac{1}{T_2} \vec{M}_{xy} \quad (1.17)$$

Spin longitudinal relaxation is also referred to as spin-lattice relaxation. This is caused by energy transfer from the spins to the surrounding 'lattice', which can be either solid or liquid. The rate of recovery of $M_z(0)$ to the thermal equilibrium value M_0 is described by a time constant T_1 as follows:

$$M_z(t) = M_z(0)e^{-t/T_1} + M_0(1 - e^{-t/T_1}) \quad (1.18)$$

where $M_z(0) = 0$ for a saturation recovery experiment using a 90° flip angle and $M_z(0) = -M_0$ for an inversion recovery experiment which rotates M_0 by 180° . The inverse of the longitudinal relaxation time, $1/T_1$, is referred to as the longitudinal relaxation rate, R_1 . The differences in T_1 in for example tissues, give rise to image contrast when using pulse sequences which are sensitive to variations in T_1 , referred to as T_1 -weighted sequences. In T_1 -weighted sequences, the repetition time T_R is short (compared to the longest T_1 observed) and tissues with short T_1 give more signal than tissues with a long T_1 since more magnetization is recovered.

The term transversal relaxation, also called spin-spin relaxation, is used to describe the decay of the transversal component M_{xy} . This is a result of local field inhomogeneities on a microscopic scale. The field variations are introduced by various shielding effects at the molecular level as well as macroscopic field inhomogeneities due to variations in the local susceptibility. This leads to different local precessional frequencies and dephasing of M_{xy} . The decay time of M_{xy} is described by T_2 as follows:

$$M_{xy}(t) = M_{xy}(0)e^{-t/T_2} \quad (1.19)$$

In practice, there is an additional dephasing of the magnetization. B_0 inhomogeneities will create a distribution of locally different B_0 magnetic fields across the sample which leads to a distribution of Larmor frequencies. This introduces an acceleration of loss of transverse magnetization after excitation. This additional loss can be described with the relaxation time constant T_2^* :

$$\frac{1}{T_2^*} = \frac{1}{T_2} + \gamma \Delta B_0 \quad (1.20)$$

where $\gamma \Delta B_0$ indicate the effect of static external field inhomogeneities. The loss of transverse magnetization due to T_2^* is recoverable. T_2^* dominates the dephasing of M_{xy} after excitation, but another pulse can be applied which rephases the spins.

Immediately following an excitation pulse all the protons in a voxel precess in phase and

their individual magnetic moments will collectively contribute to the transversal magnetization vector. However, the presence of field variations on a molecular level will introduce variations in the Larmor frequency with consequent loss of phase coherence among the spins in a voxel. The loss of phase coherence therefore causes M_{xy} to decay faster than M_z is recovering so that T_2 is always shorter than T_1 *in vivo*. Transversal relaxation times can vary significantly depending on tissue composition and local field homogeneity. T_2 is generally longer in fluids than in solids. In order to make a pulse sequence sensitive to T_2 differences, the repetition time T_R needs to be long and the echo time T_E should be sufficiently long to ensure that a large enough difference in the transversal magnetization has been established before the MR signal is acquired.

Fundamental understanding of both relaxation processes and their relation to molecular motion can be achieved by introducing a spectral density function $J(\omega)$, which gives a measure of the amount of motion at a frequency ω , and is described as follows:

$$J(\omega) = \frac{\tau_c}{1 + \omega^2 \tau_c^2} \quad (1.21)$$

where τ_c is the correlation time, which describes random motions. τ_c represents the average time it takes for a molecule to rotate by one radian. For example, small molecules have short τ_c relative to large molecules.

The relationship between the relaxation time and the spectral density was established by time-dependent perturbation theory¹². For a homonuclear spin 1/2 system, the two relaxation times can be described as:

$$\frac{1}{T_1} = K[J(\omega_0) + 4J(2\omega_0)] \quad (1.22)$$

$$\frac{1}{T_2} = \frac{K}{2}[3J(0) + 5J(\omega_0) + 2J(2\omega_0)] \quad (1.23)$$

where K represents the constant

$$K = \left(\frac{\mu_0}{4\pi}\right)^2 \cdot \frac{3}{10} \cdot \frac{\hbar^2 \gamma^4}{r^6} \quad (1.24)$$

where μ_0 is the magnetic constant and r the distance between the two spins. It can clearly be seen that T_2 relaxation contains the contribution from an additional low frequency component relative to T_1 relaxation. Therefore $T_2 \leq T_1$. When the molecule has a fast rotation and $\omega^2 \tau_c^2 \ll 1$, T_1 and T_2 tend to be similar. When the correlation time is long enough $\omega^2 \tau_c^2 \gg 1$, T_2 will be shorter than T_1 . Between these two conditions, there is a range of correlation time values for which T_1 reaches a minimum but T_2 will keep decreasing continuously. In the case of macromolecules, which have a slow rotational motion, the low frequency component is more expressed, resulting in a short T_2 and long T_1 . When τ_c increases T_1 values are changing,

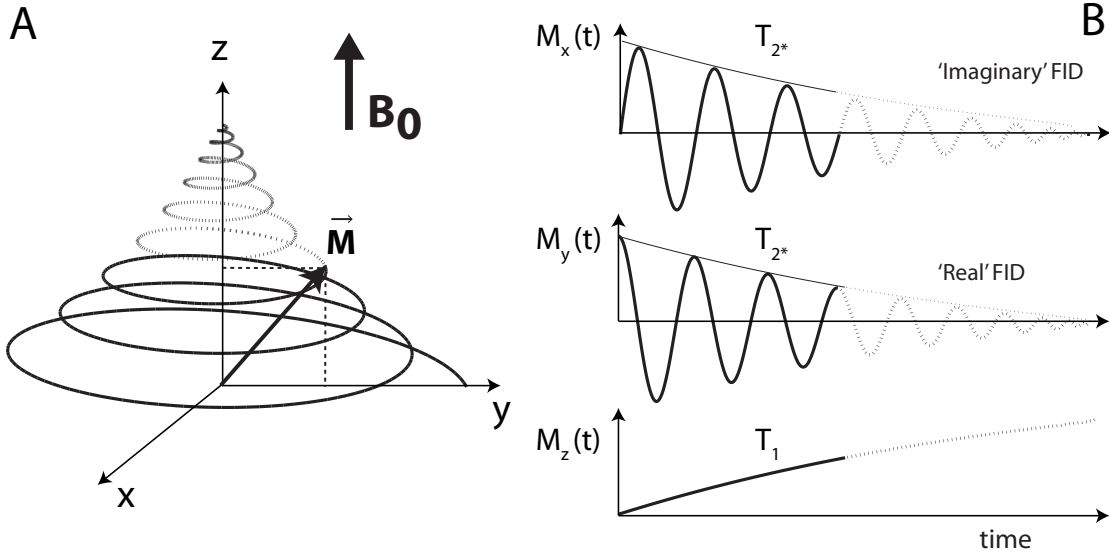


Figure 1.4: (A) The on-resonance trajectory of the magnetization \vec{M} after a 90° excitation in the laboratory frame. The magnetization undergoes precession and relaxation while it returns to its thermal equilibrium. (B) The magnetization components of \vec{M} are given in the x y and z direction. M_x and M_y both decay with T_2^* and M_z with T_1 .

indicated that T_1 is likely to be field dependent.

1.2.6 Detection of the MR signal - Fourier transform NMR

After the magnetization is perturbed by an RF pulse and rotated in the transverse plane, RF coils detect the oscillating magnetization as an induced emf. This oscillating NMR signal decreases as a function of time because of relaxation processes described in section 1.2.5 and is called a Free Induction Decay (FID). The FID is the sum of many oscillating waves of different frequencies, amplitudes and phases. It is usually detected using two orthogonal detection channels along the x and y axis, and known as quadrature detection (see Section 1.4). This allows for the simultaneous measurement of the x and y components of the FID. For each resonance, the two signals acquired are cosine and sine functions of the offset frequency $\Omega = \omega_0 - \omega$, decaying with T_2^* .

Consider the application of a short RF pulse with a 90° excitation, the magnetization components just after the pulse are obtained using the Bloch equation (Eq. 1.17) and given by:

$$\begin{aligned} M_x(0) &= 0 \\ M_y(0) &= M_0 \sin \theta \\ M_z(0) &= M_0 \cos \theta \end{aligned} \tag{1.25}$$

Right after the magnetization is precessing around B_0 and undergoes relaxation, therefore the magnetization components after an excitation can be described by (Figure 1.4):

$$\begin{aligned} M_x(t) &= M_0 \sin \theta \cos \Omega t e^{-t/T_2^*} \\ M_y(t) &= M_0 \sin \theta \sin \Omega t e^{-t/T_2^*} \\ M_z(t) &= M_0 \cos \theta e^{-t/T_1} + M_0(1 - e^{-t/T_1}) \end{aligned} \quad (1.26)$$

$M_x(t)$ and $M_y(t)$ can be regarded as a real and imaginary part of the signal $s(t)$ which, after a 90° excitation obtains the general form of:

$$s(t) \propto M_{xy}(t) = M_x(t) + i M_y(t) = M_0 [\cos \Omega t + i \sin \Omega t] e^{-t/T_2^*} \quad (1.27)$$

These can be converted into the frequency domain function $S(\omega)$ by Fourier transformation and is also called the spectrum

$$S(\omega) = \int s(t) e^{-i\omega t} dt \quad (1.28)$$

Fourier transformation of the time domain signal yields the real and imaginary frequency domain signals given by

$$R(\omega) = A(\omega) \cos \phi - i D(\omega) \sin \phi \quad (1.29)$$

$$I(\omega) = A(\omega) \sin \phi + i D(\omega) \cos \phi \quad (1.30)$$

where

$$A(\omega) = \frac{M_0 T_2^*}{1 + \Omega^2 T_2^{*2}} \quad (1.31)$$

$$D(\omega) = \frac{M_0 \Omega T_2^{*2}}{1 + \Omega^2 T_2^{*2}} \quad (1.32)$$

The real part $A(\Omega)$ is an absorptive Lorentzian curve, centered on frequency Ω with a full width at half height of $1/\pi T_2^*$ while the imaginary part, $D(\Omega)$, is the corresponding dispersive Lorentzian.

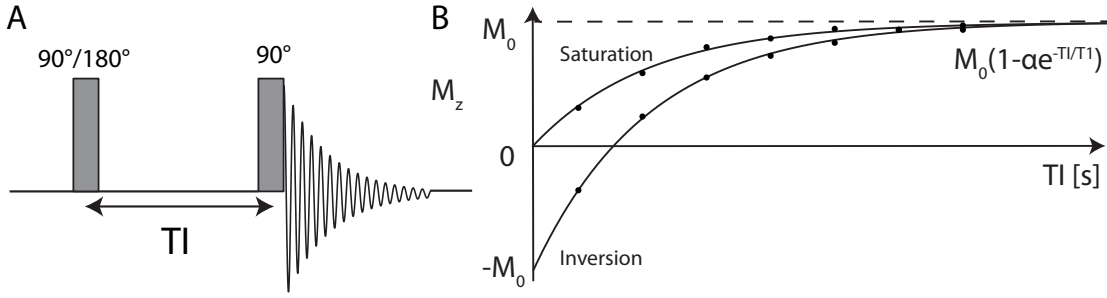


Figure 1.5: (A) T_1 relaxation can be measured using an inversion recovery ($180^\circ/90^\circ$, $\alpha=2$) or saturation recovery ($90^\circ/90^\circ$, $\alpha=1$) method. After the inversion of the magnetization it relaxes back to its thermal equilibrium value M_0 with time constant T_1 . (B) Using a variety of inversion times T_I the recovery of M_0 can be sampled and fitted to the expression for M_0 recovery (Eq. 1.33).

1.2.7 Measurement of relaxation time constants

In section 1.2.5 the return of the magnetization to its equilibrium state was introduced. The time constants T_1 and T_2 or T_2^* describe these relaxation phenomena and knowledge about them is essential, since they affect any magnetic resonance experiment. Knowledge about these time constants is important for signal quantification, chemical exchange and the design of timings for data acquisition.

In the case of hyperpolarized ^{13}C experiments, the T_1 value is one of the important factors determining the time during which data can be acquired, i.e. the measurement window.

T_1 measurements

To estimate T_1 one can consider a sequence with an initial excitation angle α and an inversion time T_I . Conventional methods to measure T_1 are the inversion recovery experiment with an initial 180° excitation and the saturation recovery experiment with a 90° excitation pulse (Figure 1.5). The inversion recovery sequence is the gold standard for the determination of T_1 relaxation times. The recovery of the longitudinal magnetization is given by:

$$M_z(t) = M_0(1 - \alpha e^{-t/T_1}) \quad (1.33)$$

where $\alpha = 2$ for an inversion recovery measurement or $\alpha=1$ for a saturation recovery measurement. By varying the parameter T_I several FIDs can be acquired and their signal intensities can be fitted using Eq. 1.33. The inversion recovery method is not optimal in terms of signal per unit of time since the majority of scan time is used to wait until M_z is fully recovered to M_0 before another excitation can be performed. In general the delay time between two consecutive excitations is $TR = 5T_1$.

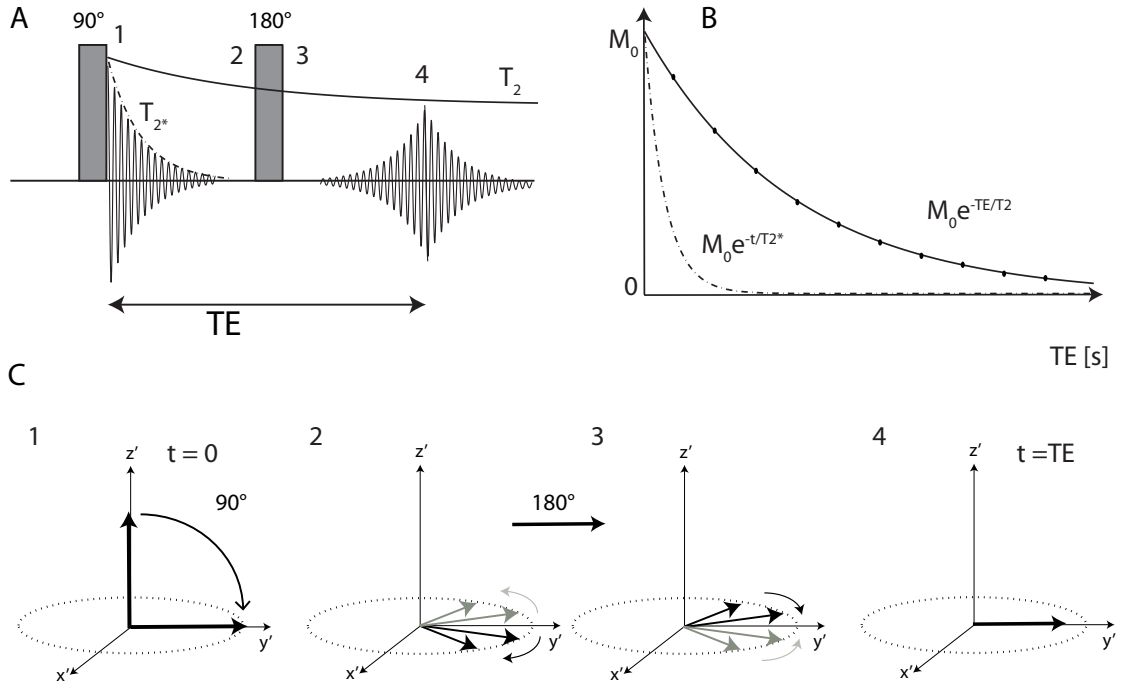


Figure 1.6: (A) A typical spin-echo experiment is sketched with the application of a 90° and 180° excitation pulse. (B) Measurement of T_2 relaxation is performed by obtaining the FIDs at different echo times and fitting the data to the expression for the decaying magnetization (Eq. 1.34). (C) First a 90° pulse excites the spins after which they dephase in the transverse plane during the first half of the echo time with a time constant T_2^* . As described in section 1.2.5 this is due to static and dynamic field inhomogeneities and frequency offsets. A 180° refocusing pulse mirrors all the magnetization vectors after which the spins rephase during the second half of the echo time due to the static magnetic field inhomogeneities and frequency offsets. At the echo time T_E , all spins have rephased and an echo is formed.

Since the saturation recovery experiment reduces the M_z to zero at time $t = 0$, it does not require a long repetition time. This significantly reduces the temporal resolution.

T_2 measurements

After RF excitation, spins in different positions will precess at slightly different Larmor frequencies due to the field inhomogeneities. This results in a loss of phase coherence and both effects are characterized by the time constant T_2^* , like described in Eq. 1.20. After a 90° pulse the T_2^* effect will obscure any information regarding T_2 , but during the generation of spin-echoes it is possible to separate the contribution of T_2 and magnetic field inhomogeneity¹³. In a spin echo sequence (Figure 1.6) the magnetization is tipped to the transverse plane by a 90° pulse. During the subsequent delay the magnetization starts to lose coherence because of the intrinsic T_2 relaxation and a range of B_0 magnetic fields, and precesses about z with a

variety of Larmor frequencies. After a delay of $T_E/2$ a 180° pulse is applied which causes a 180° rotation about y . During a second delay $T_E/2$ the spins precess again at their local Larmor frequencies and will be refocused at the end of the second delay to form a spin echo. The time between the 90° pulse and the time of the echo is called the echo time T_E . By varying the echo time in several experiments and measuring the signal, the T_2 relaxation time constant can be calculated by fitting the signal intensities as function of T_E to the following equation:

$$M_{xy}(t) = M_{xy}(0)e^{-T_E/T_2} \quad (1.34)$$

There are two additional dynamic dephasing terms which cannot be refocused during an 180° pulse and these are related to diffusion and exchange of the spins in the presence of local field inhomogeneities. By applying a train of 180° pulses instead of a single one, the measured T_2 relaxation time constant is closer to the intrinsic T_2 relaxation time constant^{14;15}.

1.2.8 Chemical Shift

The frequency of nuclei is not solely determined by the resonance condition $\omega_0 = \gamma B_0$. Nuclei of the same element in different molecules resonate at different frequencies. The frequency ω not only depends on the gyromagnetic ratio γ and the external field B_0 , but also to the chemical environment of the nucleus of interest³. This is referred to as chemical shift and is caused by shielding of nuclei from external magnetic field by electrons surrounding them (Figure 1.7).

The electrons will rotate about B_0 in an opposite sense to the proton spin recession. The static field B_0 induces currents in the orbital electrons, which in turn generate a local magnetic field that is several orders of magnitude times smaller than the main magnetic field. The electron magnetic moment opposes the primary applied magnetic field B_0 . This reduces the magnetic field that is sensed by the nucleus to

$$\vec{B} = \vec{B}_0(1 - \sigma) \quad (1.35)$$

where σ is the shielding constant, which is a dimensionless number expressed in parts per million (ppm). It depends on the chemical environment of the nucleus. The resonance condition for nuclei can be modified to

$$\nu_0 = \left(\frac{\gamma}{2\pi}\right)B_0(1 - \sigma) \quad (1.36)$$

with $\nu_0 = \omega_0/2\pi$. To make chemical shifts independent of magnetic field strength, they are not expressed in units of Hertz, but in terms of ppm. By convention this is defined as:

$$\delta = \frac{\nu - \nu_{ref}}{\nu_{ref}} \times 10^6 \quad (1.37)$$

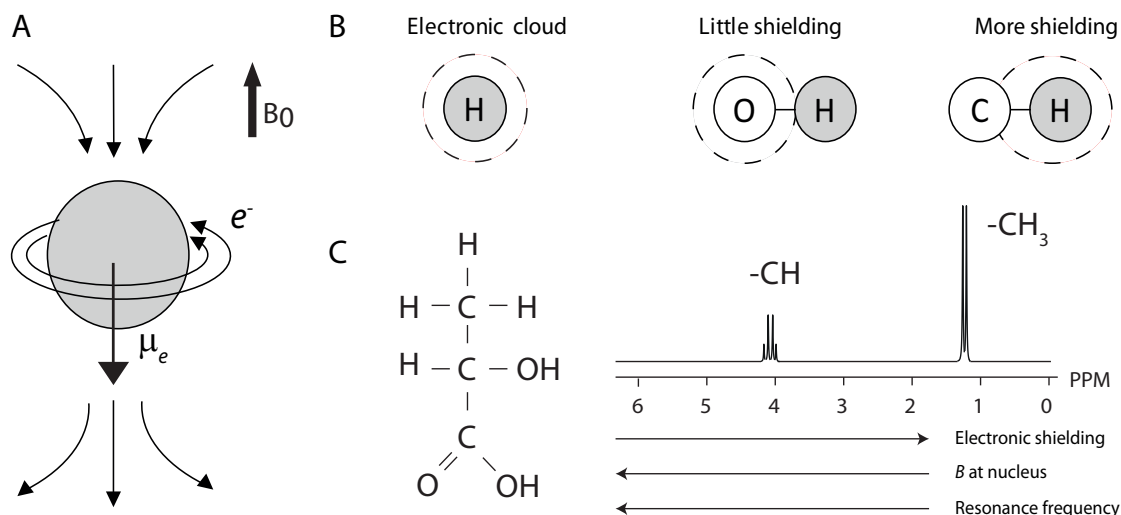


Figure 1.7: (A) Reorientation of the electron cloud in a magnetic field generates a magnetic moment μ_e at the nucleus. This magnetic moment opposes the external magnetic field B_0 , thereby reducing the effective magnetic field felt by the nucleus. This leads to a change in Larmor frequency and thus in chemical shift. This is called electronic shielding. (B) Nearby electronegative atoms attract electrons which lead to lower electron density and deshielding of nearby protons. Therefore the resonance frequency is higher in OH than in CH groups. (C) The electronegative oxygen atoms in lactate shift the electron density away from protons, leading to reduced electronic shielding and to a higher Larmor frequency. The proton NMR spectrum of lactate shows these shielding effects, the methine proton is closer to electronegative oxygen atoms than the three methyl protons. The resonance splitting is due to nuclear coupling (Section 1.2.9). The methine resonance splits into a quartet due to the neighbouring protons in the methyl group which induces 4 different energy level transitions in the methine proton. Conversely, the CH₃ resonance splits into a doublet due to the neighbouring methine proton.

where ν and ν_{ref} are the frequencies of the compound under investigation and of a reference compound. For *in vivo* NMR spectroscopy the reference compounds are usually biomolecules present in the tissue such as N-acetyl aspartate (2.01 ppm) for ^1H MRS. Typically, chemical shifts are spread over 10 ppm for proton spectroscopy and about 200 ppm for ^{13}C NMR spectroscopy.

1.2.9 Nuclear coupling

Besides the chemical environment of the nucleus which gives it a characteristic frequency known as chemical shift, nuclear spins are also affected by surrounding nuclear spins. This phenomenon results in the splitting of resonances into several smaller lines, and is called spin spin coupling. It originates from spins interacting through space (dipolar coupling) or through chemical bonds (scalar coupling). In a liquid the dipolar interactions normally average out due to rapid tumbling. However, interactions through the electrons of the chemical bonds do not average to zero and produce multiplets in spectra, as can be seen in the ^1H spectrum of lactate in Figure 1.7C. The frequency difference of the splitting is given by the J-coupling constant indicated in Hz.

Consider the spin-spin coupling between two spin 1/2 nuclei I (for example a proton) and S (a carbon-13). Spin I has two possible energy levels, related to the magnetic moment being parallel or anti-parallel to the main magnetic field B_0 . The S nucleus senses these two different states through the spin of electrons in the covalent $S - I$ chemical bond, which causes the energy levels to split in four (Figure 1.8). The energy of the levels depends on the J coupling constant relative to the absolute frequency difference between the two nuclei $|\nu_I - \nu_S|$. The J coupling constant is independent of the external magnetic field.

Typical J coupling constants are in the range of 1-15 Hz for ^1H - ^1H couplings, 100 - 200 Hz for ^1H - ^{13}C couplings and 30-80 Hz for ^{13}C - ^{13}C couplings. These J coupling constants are for one chemical bond, except for ^1H - ^1H interactions.

The J coupling property provides information about the structure of molecules. When more nuclei are coupled, spectral patterns can become complex, containing triplets, quadruplets or even doublet of quartets in the case of $[1-^{13}\text{C}]\text{acetylcarnitine}$ (Figure 1.9). The total area of a certain resonance is proportional to its magnetization and thus nuclear coupling will in fact reduce the SNR of each peak.

The appearance of ^{13}C NMR spectra is in general dominated by heteronuclear ^1H - ^{13}C coupling since most carbon nuclei are directly bonded to one, two or three protons. Crowded spectra also complicate the quantification of resonances. To increase the sensitivity and simplify the spectral appearance, the multiplets, originating from heteronuclear ^1H - ^{13}C coupling, are collapsed into singlets by applying ^1H decoupling during the ^{13}C MRS acquisition. To this end, a continuous RF field is applied at the Larmor frequency of the ^1H nucleus. This causes a continuous exchange between the energy levels of ^1H , which averages out the coupling

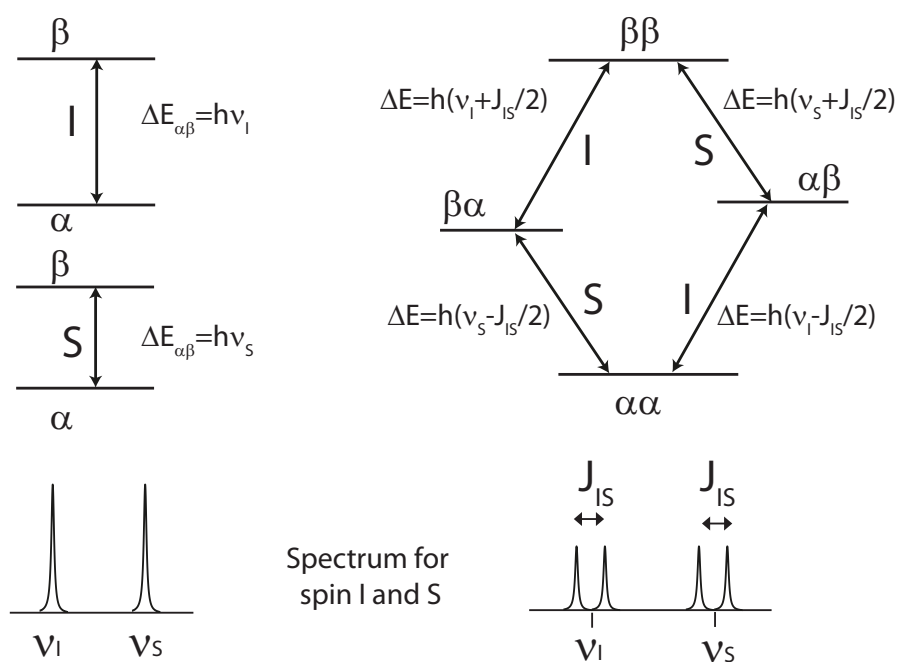


Figure 1.8: Energy diagrams and NMR spectra for an isolated (left) and a weakly coupled (right) two spin system of nuclei I and S. When the two nuclei are uncoupled the NMR spectrum show individual resonances for nucleus I and S with their frequencies ν_1 and ν_2 respectively. The coupling between the two nuclei result in a splitting of the resonances of I and S, since the energy level transition of each nucleus has two different frequencies.

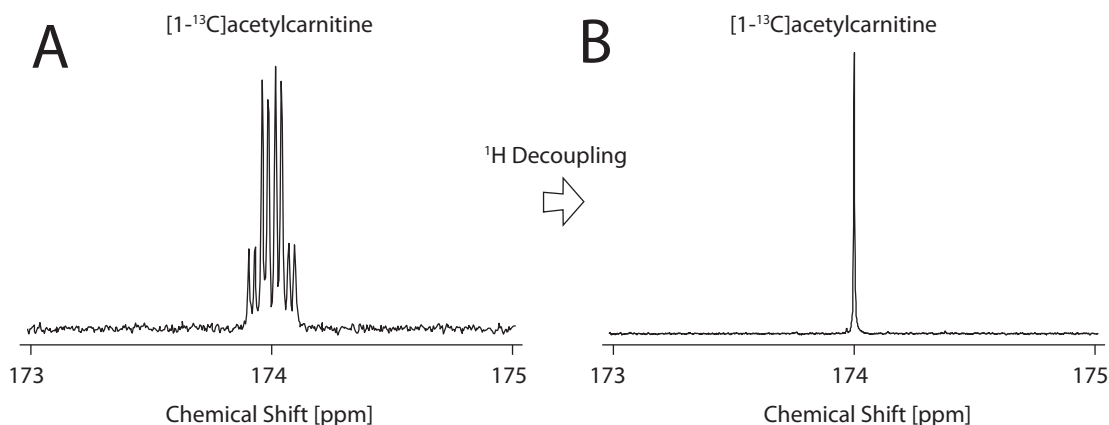


Figure 1.9: Effect of ^1H decoupling on the ^{13}C MRS spectrum of $[1-^{13}\text{C}]\text{acetylcarnitine}$, an intermediate metabolite detected after injecting hyperpolarized $[1-^{13}\text{C}]\text{acetate}$ 2. (A) ^{13}C spectrum of $[1-^{13}\text{C}]\text{acetylcarnitine}$ is a doublet of quartets as a result of ^1H - ^{13}C coupling with a neighbouring methyl (CH_3) and methine group (CH). (B) ^1H decoupled ^{13}C spectrum of $[1-^{13}\text{C}]\text{acetylcarnitine}$.

between the ^1H and ^{13}C nuclei, resulting in a singlet (Figure 1.9). In the case of heteronuclear decoupling of an entire ^{13}C spectrum, which contains a wide range of chemical shifts, broadband decoupling is usually applied. Broadband decoupling is performed by applying a series of composite pulses such as WALTZ-16¹⁶.

Because of the low probability of two adjacent ^{13}C isotopes, homonuclear ^{13}C - ^{13}C scalar couplings are usually not observed. However, in ^{13}C experiments where labeled ^{13}C compounds are infused multiple carbon positions will carry the ^{13}C label eventually and metabolite resonances will appear as multiplet structures due to the ^{13}C - ^{13}C homonuclear couplings. The appearance of such isotopomers allows isotopomer analysis and can provide information on the underlying metabolic pathways as discussed in Section 1.5.

1.2.10 Localized spectroscopy

So far we have considered macroscopic magnetizations which are excited to the transverse plane for MR detection. This restricts the data acquisition to a very large volume. The principle of localization is to obtain information from a particular location inside a tissue. Spatial localization of a volume of interest (VOI) is achieved by using a spatially varying magnetic field so that the Larmor frequencies become spatially-dependent. This additional field is also called a gradient which intensity is linearly varying in three orthogonal directions.

RF excitation can be performed for a particular range of frequencies, and thus the gradients can be adjusted so that the RF excitation affect a particular location in the sample. The position is then determined by the magnetic field gradient strength and the RF pulse frequency. A

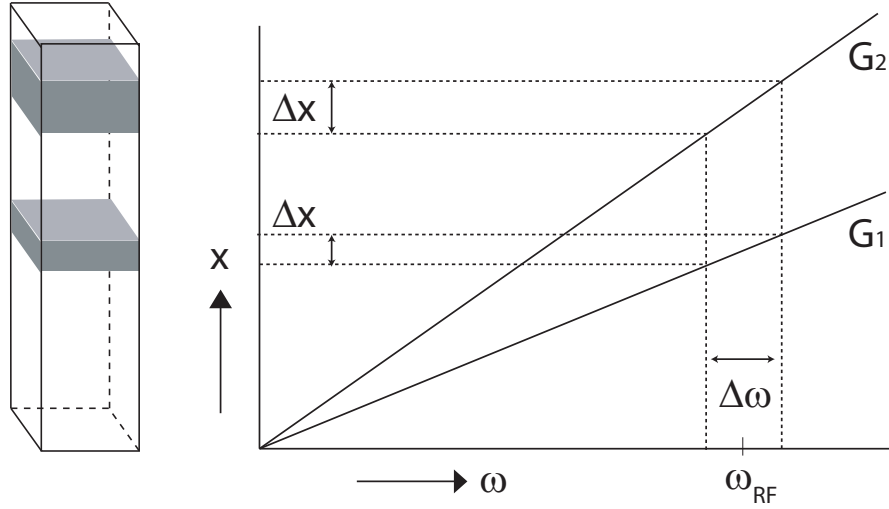


Figure 1.10: The principle of slice selection is illustrated. An RF pulse with carrier frequency ω_{RF} is applied in the presence of a gradient along the x direction. When the gradient strength is changed, slices are excited with different thickness Δx

proportional relationship exists between the spatial position x and the spin frequency when using simultaneously a frequency selective RF pulse with a linear gradient. The spin frequency ω of a given nucleus is depending on its position x in the sample as follows:

$$\omega(x) = \gamma(B_0 + G_x x) \quad (1.38)$$

where γB_0 is the Larmor frequency ω_0 . When a gradient is applied of amplitude G in a certain direction during an RF pulse, a slice perpendicular to the gradient direction will be selected. The width of the slice is determined by the magnetic field gradient strength and by the RF pulse bandwidth, and its position is given by the center frequency of the RF pulse (Figure 1.10). Now consider a certain bandwidth of frequencies $\Delta\omega$, the spatial displacement Δx of the acquired signal can be given by:

$$\Delta x = \frac{\Delta\omega}{\gamma G_x} \quad (1.39)$$

where G_x is a gradient along x . The application of gradients are used in many applications of MR spectroscopy and are the principal components in MR imaging.

Outer volume suppression

Outer volume suppression (OVS) leaves the magnetization in the VOI unperturbed during the localization and suppresses the external signals¹⁷. The application of a slice-selective 90° pulse is followed by crusher gradients that excite spins outside of the VOI and dephases them

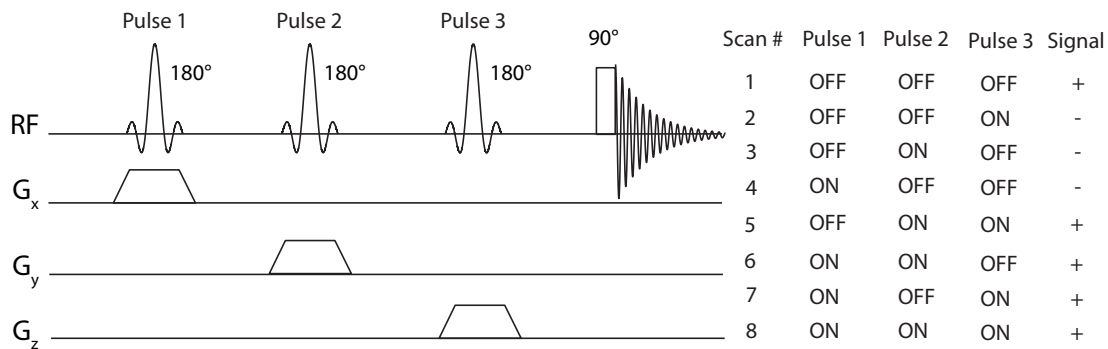


Figure 1.11: The ISIS sequence used for localization in NMR spectroscopy consists of three orthogonal slice selective 180° excitations followed by a 90° pulse for MR signal acquisition. 3D localization is achieved with the add and subtract scheme of 8 acquisitions, isolating signal from the VOI.

immediately after excitation in the transverse plane. The result of the dephasing is a zero net magnetization in the corresponding slices surrounding the VOI, while the signal from the VOI remains untouched. Thus, the OVS pulses selectively remove unwanted signal although it is limited by the T_1 recovery of the magnetization in the different slices before the actual acquisition starts.

ISIS

Image selected *in vivo* spectroscopy (ISIS) enables the excitation of magnetization in a VOI. In the MR sequence, the magnetization in the VOI is measured by successive excitations of three orthogonal slices which intersection corresponds to the VOI. ISIS relies on a set of longitudinal magnetization preparation 180° slice-selective inversion pulses in orthogonal directions followed by a 90° pulse for signal acquisition (Figure 1.11). Acquisitions are performed with the inversion pulses turned on and off in different combinations during successive scans. The acquired signals are added and subtracted following a specific procedure. The 1D ISIS requires two consecutive signal acquisitions. The first acquisition is a standard 90° excitation followed by the detection of the transverse magnetization. The second acquisition is identical, except that a slice selective 180° pulse inverts the magnetization prior to 90° pulse. The subtraction of the two acquisitions removes the signal from outside the slice. For the 3D ISIS sequence, a total of 8 scans acquisitions are combined to isolate the signal from the magnetization located in the VOI with a specific encoding scheme (Figure 1.11). As a consequence of this acquisition scheme with adding and subtracting, the final signal is particularly sensitive to physiological motion. An advantage of ISIS localization is that it can be used as a preparation module to any spectroscopic sequence.

1.3 Hyperpolarization

As seen in Section 1.2.2 Equation 1.6 the thermal equilibrium polarization depends on three factors, the gyromagnetic ratio γ , external magnetic field B_0 and the sample temperature T . Various methods have been proposed which enhance the nuclear spin polarization to a significant fraction. They create a polarization level which is far beyond the thermal equilibrium polarization and are collectively referred to as hyperpolarization techniques. These techniques have recently begun to show potential for *in vivo* applications. They include a "brute force" approach¹⁸, optical pumping of noble gases¹⁹, para-hydrogen induced polarization²⁰ and dynamic nuclear polarization (DNP)²¹. This studies conducted in this thesis employed dynamic nuclear polarization to obtain highly polarized biomolecules for subsequent metabolic studies.

1.3.1 Dynamic Nuclear Polarization

DNP hyperpolarization is achieved by transferring the electron spin polarization into a nuclear one. The process is usually carried out at temperatures below liquid helium temperature (1 ± 0.05 K), moderately high magnetic field (5 T) and on frozen glassy mixtures containing the target molecules and a small amount of radical. At these temperatures the electron spin polarization increases dramatically (95%) (Table 1.2). Continuous microwave irradiation at a frequency ω , which is close to the Larmor frequency of the electron spins ω_e , saturates the ESR line of the unpaired electrons of stable radicals which are added to the sample containing the nuclear spins of interest (Figure 1.12). Due to the out-of-resonance irradiation, the electrons start to interact with nuclei, through electron-nuclear spin flip-flop transitions, to compensate the energy offset. Now the electron spin polarization will be transferred via the dipolar-dipolar hyperfine coupling to its neighboring nuclear spins. The exchange of energy between the electron and the nuclear spins through electron-nuclear interactions typically involves one nuclear spin and one or more electron spins. Then, resonant mutual flips or transitions between two neighboring nuclear spins, also referred to as spin-diffusion, induce a polarization transfer to the nuclear spins in the bulk and the polarization will be build up as long as the nuclear T_1 permits. The spin diffusion mechanism involves both dipolar spin diffusion and, a faster, Zeeman spin diffusion^{22;23}

In DNP, the electron spins polarize the nuclear spins, but in the same fashion these paramagnetic centers also introduce a faster relaxation (Section 1.2.5). It is thus necessary for the polarized nuclear spins to be isolated from the electron spins, at least for a large part of the DNP experiment, and to carefully choose the ratio between nuclear and electron spin density. Typically the electron concentration is low (~ 0.001 electron spins per nuclear spin). on average N_e electron spins must polarize N_N/N_e nuclear spins and after each forced microwave-induced transition the electron spin must relax back into its thermal equilibrium before any of the N_N/N_e nuclear spins in its sphere of influence relax through a nuclear relaxation mechanism. The efficiency also depend on the ratio between the nuclear and electron spin longitudinal

Table 1.2: Polarization levels at several temperatures for electron spins and the nuclear spins of carbon-13 and proton

| Nucleus | Temperature [K] | Magnetic Field [Tesla] | Polarization [%] |
|-----------------|--------------------|---------------------------|---------------------|
| ^1H | 300 | 9.4 | 0.003 |
| ^{13}C | 300 | 9.4 | 0.0008 |
| ^1H | 1.2 | 3.35 | 0.3 |
| ^{13}C | 1.2 | 3.35 | 0.08 |
| e | 1.2 | 3.35 | 95 |

relaxation, which is highly influenced by the intensity of the applied magnetic field B_0 and the temperature of the sample. In order to effectively enhance the nuclear polarization of solid dielectric samples via DNP the following condition should be fulfilled²¹:

$$\frac{N_N}{N_e} \frac{T_{1e}}{T_{1N}} \ll 1 \quad (1.40)$$

where N_N and N_e are respectively the number of nuclear and electron spins in the sample. In other words, the total rate of spontaneous electron spin flips N_e/T_{1e} should considerably exceed the rate of spontaneous nuclear spin flips N_N/T_{1N} . If the nuclear relaxation is dominated by the hyperfine interaction with the electrons, then the condition will automatically hold.

There are three DNP mechanisms, the nuclear Overhauser effect (NOE) thermal mixing and the solid effect.

1.3.2 Polarization mechanisms

Overhauser Effect

In 1953 it was predicted that electron spins can polarize nuclear spins²⁴. Experimentally it was shown that not only metals²⁵, but also insulators in combination with paramagnetic impurities²⁶ are polarizable using DNP.

This Overhauser effect can be described by flip-flop transitions in two-spin systems consisting of an electron and a nuclear spin. The application of microwave irradiation, at the frequency of the electron spin resonance, saturates the ESR transitions (Figure 1.13). The electron spins are subject to relaxation, during which the nuclear spins will be polarized via an interaction referred to as hyperfine coupling.

By solving the rate equations established by Solomon²⁷, the NOE enhancement can be

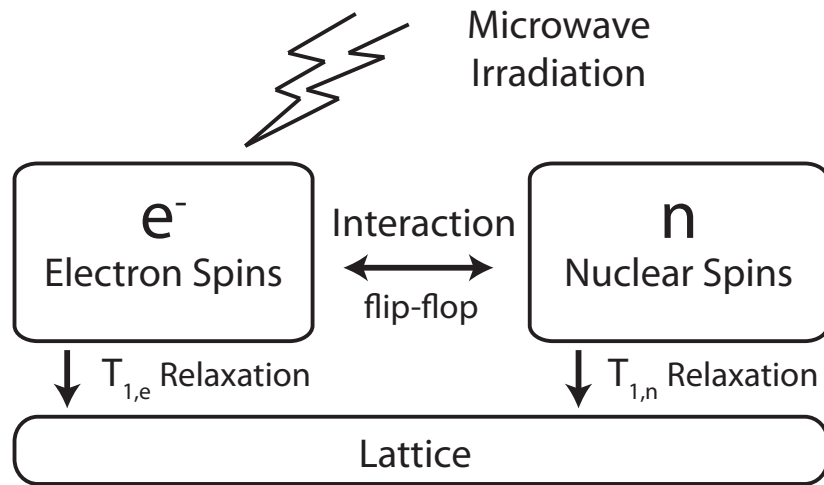


Figure 1.12: The transition of the electron spin resonance is saturated by a microwave source. The frequency of the source is close to ω_e . Through flip-flop electron-nuclear spin interactions the polarization is transferred from electron spin to nuclear spin. Due to the much faster electron spin relaxation processes, compared to that of the nuclei, the electron spins return to thermal equilibrium while the nuclear spin polarization builds up.

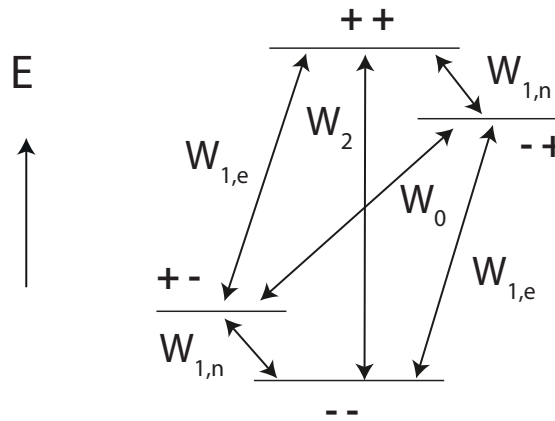


Figure 1.13: Energy levels and transitions of a coupled spin system consisting of a nuclear and an electron spin. The energy transitions of the electron spins are much larger than the transitions of the nuclear spins. W_0 and W_2 represent the zero quantum and double quantum transitions. The zero quantum transition, W_0 , is pumped by the microwave irradiation, with subsequent nuclear spin $W_{1,n}$ and electron spin relaxation, $W_{1,e}$

written as follows:

$$\epsilon = 1 - s\xi f \frac{|\gamma_s|}{\gamma_I} \quad (1.41)$$

where s represents the electron spin saturation level, ξ , a coupling factor which affects the efficiency of the microwave power saturation and f represents the leakage factor which is related to the paramagnetic relaxation time. ξ , the coupling factor, can be described expressed as follows:

$$\xi = \frac{W_2 - W_0}{W_0 + W_2 - 2W_{1,n}} \quad (1.42)$$

This coupling factor has a value depending on the interaction. The value can range from -1 in the case of pure scalar interactions, while it can be up to 0.5 in the case of pure dipolar interactions. The degree of electron spin saturation can be represented by the saturation parameter s , which can be described in terms of the component of the magnetization along the z axis as follows:

$$s = \frac{M_0 - \langle M_z \rangle}{M_0} \quad (1.43)$$

In case of a high power for the microwave irradiation, a full saturation can be achieved, $s = 1$. It is clear that in the case of microwave absence, the saturation becomes $s = 0$. The fraction of the nuclear polarization which is lost due to the presence of electron spins, the leakage factor f , can be expressed as follows:

$$f = \frac{W_2 + W_0 + 2W_{1,n}}{W_0 + W_2 + 2W_{1,n} + W_{1,e}} = 1 - \frac{T_{1n}^{+S}}{T_{1n}^{-S}} \quad (1.44)$$

where T_{1n}^{-S} is the relaxation time of the nucleus without the presence of electron spins, and T_{1n}^{+S} is the relaxation time of the nucleus in the presence of electron spins. When both s and f are equal to unity and $\xi = -1$, the enhancement factor from the Overhauser effect is proportional to the gyromagnetic ratio between the electron spin and nuclear spin. Resulting in a maximal theoretical enhancement factor of $\epsilon_H \approx 660$ for 1H and $\epsilon_C \approx 2630$ for ^{13}C .

Solid Effect

Like the Overhauser effect, the solid effect is also based on the interactions and transitions between an electron spin and a nuclear spin. However, unlike the Overhauser effect, the energy transitions of the spins take place at the same time as the microwave irradiation.

The frequency of the microwaves should equal the relative difference between the frequency of the electron resonance and the nuclear resonance frequency $\omega_{mw} = \omega_e \pm \omega_n$. This slight offset from the electron spin resonance frequency leads to a zero quantum transition, since it forces the simultaneous transition of the electron spin and the nuclear spin (Figure 1.13). This is referred to as a flip-flop transition if $\omega_{mw} = \omega_e - \omega_n$ or a flip-flip transition if $\omega_{mw} = \omega_e + \omega_n$.

The latter is a double quantum transition.

The polarization process at a frequency of $\omega_{mw} = \omega_e + \omega_n$ is referred to as negative DNP, since it forces the nuclear spins to populate the higher energy level, which leads to $P < 0$. On the other hand, when the polarization is carried out at a frequency $\omega_{mw} = \omega_e - \omega_n$ the process is referred to as positive DNP.

Thermal mixing

When the electron spin concentration is relatively large, the dipolar interaction between electron spins are non-negligible compared with the solid effect, and thermal mixing is the dominant DNP mechanism. The local magnetic field B_l which is induced by the dipolar field of the electron spins, causes that the width of the electron Zeeman energy levels becomes non-negligible as well. The probability of the existence of two electron spin ensembles, with a difference in Zeeman energy that matches the Zeeman energy of surrounding nuclear spins, becomes high.

Using a spin temperature formalism is necessary to understand the concept of thermal mixing. To this end, several thermal reservoirs are defined: The Electron Zeeman Reservoir (EZR), the Electron Dipolar Reservoir (EDR) and the Nuclear Zeeman reservoir (NZR).

EZR defines the Zeeman energy of the ensemble of electron spins and NZR that of nuclear spins. EDR includes the dipolar energy of the electron spins ensemble. Each reservoir can be defined by a spin temperature, which is T_Z for EZR, T_{SS} for EDR and T_I for NZR. At a thermal equilibrium $T_Z = T_{SS} = T_I = T_L$, resulting in all spin temperatures being equal to the temperature of the lattice.

The concept of thermal mixing can be understood as a two-step process. The first step consists of dynamic cooling and the second of thermal mixing proper^{21;28}. Dynamic cooling constitutes the lowering of the spin temperature of EDR, T_{SS} . The ultimate spin temperature can be estimated based on the intensity of the local magnetic field B_l as follows:

$$T_f \cong \frac{B_l}{B_i} T_i \quad (1.45)$$

where B_i is the initial magnetic field and, T_i defines the initial temperature of the system.

Using continuous RF irradiation at an off-resonance frequency ω , the effective local magnetic field B_{eff} can be reduced by a factor:

$$\frac{B_{eff}}{B_0} = \frac{\Delta}{\omega_0} \quad (1.46)$$

The spin temperature can be positive or negative, depending on the resonance offset, $\Delta =$

$\omega_0 - \omega$. The Zeeman spin temperature, T'_Z , is reduced by the same factor, under microwave irradiation, and is given by:

$$T'_Z = \frac{\Delta}{\omega_0} T_L \quad (1.47)$$

In this scenario, the electron Zeeman energy at a local magnetic field is decreased and comparable to the transition energy which is required for dipolar interaction. The energy exchange between EZR and EDR becomes possible and the EDR temperature is decreased.

The process of thermal mixing, through the thermal contact with the EDR, decreases the NZR spin temperature, thus increasing the nuclear spin polarization. This happens when the Larmor frequencies of electron spins are so dispersed that their difference is equal to the Larmor frequency of the nuclear spins. This thermal contact is inherent to the spin system and is depending on the radical concentration.

1.3.3 Dissolution DNP

The DNP process itself is carried out on a frozen sample. The invention of dissolution DNP²⁹ offered the possibilities to benefit from the the DNP signal enhancement for *in vivo* applications. The polarized solid material is brought into the liquid state by dissolution in an appropriate solvent while the nuclear polarization is preserved. Using this technique one can achieve signal to noise (SNR) enhancements of 10,000-fold for detection of ^{13}C metabolites *in vitro*²⁹. Because of the enormous sensitivity increase, it allows for detecting metabolites present at such low concentrations, that conventional MR is unable to detect³⁰. Additionally it enables the observation of fast metabolic processes in real-time *in vivo* after infusion of hyperpolarized ^{13}C labeled biomolecules³¹.

However, the hyperpolarized spin state has a short lifetime and the hyperpolarized ^{13}C substrates return to normal Boltzmann polarization levels with a time constant T_1 (Section 1.2.5). This T_1 limits the measurement time window and the amount of experiments which can be performed. It is favourable to use ^{13}C labeled carbonyl positions in biomolecules since the T_1 is about 30-50 seconds. Several T_1 times of biomolecules of interest are shown in Table 1.3.

Once a part of the hyperpolarized magnetization is brought to the transversal plane for detection, it will return to its thermal equilibrium, and not its initial hyperpolarized level. Therefore one can consider the amount of excited hyperpolarized magnetization as a loss of polarization. For this reason only a single 90° acquisition or multiple acquisitions with a low flip angle can be performed during one experiment following the DNP sample dissolution and subsequent infusion.

Table 1.3: Longitudinal relaxation times T_1 of ^{13}C labeled metabolites of interest for *in vivo* DNP studies. Adapted from³²

| Metabolite | T_1 [s] |
|---|-----------|
| [1- ^{13}C]acetate | 50 |
| [1- ^{13}C]alanine | 30 |
| [1- ^{13}C]aspartate | 29 |
| [1- ^{13}C]bicarbonate | 32 |
| [1- ^{13}C]pyruvic acid | 60 |
| [1- ^{13}C]butyric acid | 44 |
| [1,5- ^{13}C]citric acid | 25 |
| [1- ^{13}C]lactate | 46 |
| [1,3- ^{13}C 2] β -hydroxybutyrate | 31 |
| [1- ^{13}C]octanoate | 35 |
| [1,4- ^{13}C]fumarate | 35 |
| [1- ^{13}C]glutamate | 25 |
| [5- ^{13}C]glutamine | 26 |

1.4 Radiofrequency Coils

Radiofrequency coils are used for the excitation and detection of the MR signal and can be seen as an LCR circuit. The RF transmitter coil generates a transverse magnetic field which oscillates in the RF range and rotates the longitudinal magnetization into the transverse plane. The precessing transverse magnetization induces a voltage, or electromotive force (*emf*), in a nearby receiver coil according to Faradays law:

$$\xi = \oint_C \mathbf{E} \cdot d\mathbf{l} = - \int_S \frac{d\mathbf{B}}{dt} \cdot d\mathbf{S} \quad (1.48)$$

where ξ is the electromotive force induced across the loop C , \mathbf{E} is the electric field across a loop section $d\mathbf{l}$, \mathbf{B} is the magnetic field and \mathbf{S} is the loop area. The signal S from an MR experiment will depend on the square of the static magnetic field B_0 :

$$S \propto \frac{\gamma^3 B_0^2 \rho_0}{T} \quad (1.49)$$

where ρ_0 defines the number of spins per unit volume or "spin density".

There are many different types of RF coil designs that are being utilized for NMR spectroscopy *in vivo*.

A volume coil, for example a Helmholtz coil³³, provides a homogeneous B_1 field which can excite the spins uniformly in a large volume, but the large size and poor filling factor compromises their sensitivity for the acquisition. In situations where the total subject under

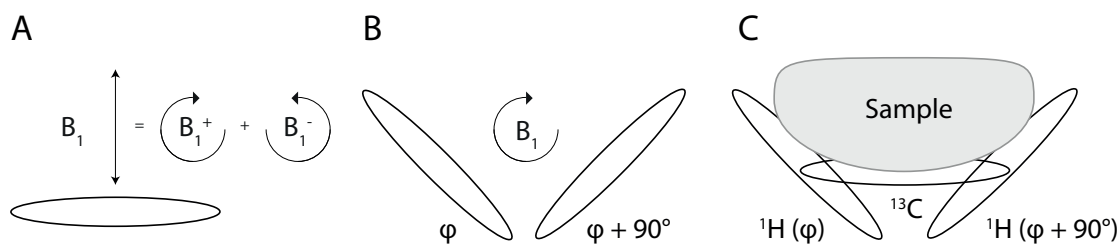


Figure 1.14: (A) A linearly polarized magnetic field generated by a single coil which can be decomposed into two counter rotating parts, from which only one interacts with the spins. (B) Two coils in quadrature mode generate a rotating magnetic field. (C) A typical coil set-up for ^1H decoupled ^{13}C NMR for *in vivo* applications.

investigation is much larger than the region of interest, an extensive amount of signals coming from surrounding tissue needs to be suppressed in order to achieve adequate localization.

Surface coils have a very good filling factor and a high sensitivity, since a surface coil can be placed adjacent to the region of interest and can often be reshaped to exactly fit the object under investigation³⁴. The downside of surface coils is that the B_1 field generated is far from homogeneous meaning that the excitation of the spins is dependent on the distance from the coil when using conventional RF pulses. However, this inhomogeneous excitation can be overcome using so-called adiabatic RF pulses, which can excite spins uniformly until a certain distance. The sensitive volume of a single loop coil approximately equals one coil radius and this sensitivity decreases with increasing distance from the coil. Roughly, the B_1 field along the coil axis can be described by:

$$B_{1,ax} \propto \frac{r^2}{(r^2 + y^2)^{3/2}} \quad (1.50)$$

The main advantage for surface coil reception is the high sensitivity that can be obtained immediately adjacent to the coil. This has made surface coils the primary choice for applications that are inherently sensitivity limited, like MRS. For almost all *in vivo* metabolic studies a double RF surface coil set-up is required. Besides the metabolic measurements which require MR probe to measure resonances from ^{31}P or ^{13}C nuclei, it is necessary to have an additional ^1H probe to obtain information about localization, perform shimming, decoupling and polarization transfer. The coil loops have typically a relatively small surface area, around 12-15 mm diameter for small animal applications, and often the same coil is used for both excitation and detection. Due to significant coil interactions and large RF power depositions during proton decoupling when both of the coils are placed in a co-planar arrangement, the ^1H RF coil is split into two surface coils driven in quadrature. Currently this is the most commonly used design and was described by³⁵ and shown in figure 1.14C.

A hybrid decoupler splits the incoming RF power evenly over the two ^1H coils, while simul-

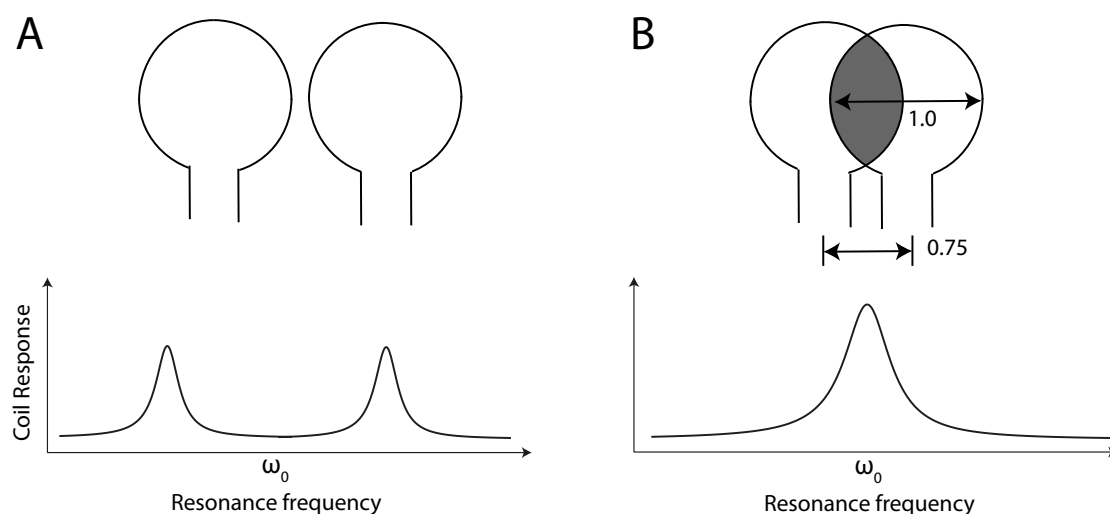


Figure 1.15: (A) Response of two adjacent surface coils tuned to the same frequency. The original resonances split into two resonances and the sensitivity of the coils at frequency ω_0 is reduced. (B) By separating the adjacent circular coils by 0.75 their diameter their mutual inductance is set to zero and splitting resonances are eliminated. The exact overlap is determined empirically.

taneously phase shifting the current by 90° for one of the ^1H coils. During reception the hybrid splitter combines the two out-of-phase NMR signals, such that one in-phase signal arrives at the pre-amplifier. This gives the quadrature design advantages in terms of RF power but also in the form of a more homogeneous excitation in the sensitive volume³⁶. The circularly polarized magnetic field that is produced is more efficient in exciting the spins compared to a linearly polarized field since one of its rotating components does not interact with the precessing spins (see Figure 1.14 A and B). Theoretically, an SNR enhancement of a factor of $\sqrt{2}$ is expected and only half of the transmitter RF power is required to rotate the nuclear magnetization as compared to the single loop arrangement³⁷.

When two identical resonance loops are in close proximity the oscillating current in one loop generates an oscillating magnetic field which induces a voltage across the second loop. This causes the resonance frequency to shift, for both coils in opposite directions and manifests itself as a splitting (see Figure 1.15 A). To reduce this coupling adjacent coils need to be overlapped to eliminate the mutual inductance (see Figure 1.15 B)³⁸.

For the studies conducted in this thesis two different kinds of surface coils were constructed which are described in Appendix A.1.

1.5 Dynamic ^{13}C NMR Spectroscopy

Almost all biologically relevant compounds contain carbon, making ^{13}C NMR spectroscopy capable of detecting many metabolites. ^{13}C NMR spectra are characterized by a large spectral

range, narrow line widths and low sensitivity because of the natural abundance of ^{13}C (1.1%). This can be overcome using averaging, polarization transfer, larger volumes and decoupling (Section 1.2.9). The spectrum can be divided into spectral ranges indicative of certain chemical groups. Chemical shift ranges above 150 ppm characterize carbonyl groups and is the region of interest in most hyperpolarized ^{13}C experiments. In conventional ^{13}C spectroscopy this region lies between 15-100 ppm, which contain carbons close to hydroxyl groups, such as glucose, resonating around 60-100 ppm. The CH, CH₂ and CH₃ groups, resonating around 45-60 ppm, 25-45 ppm and <25 ppm respectively. Lipid resonances dominate the spectrum around 20-50 ppm and are so abundant that natural abundance detection is possible in for example skeletal muscle. Two areas make ^{13}C NMR spectroscopy unique for *in vivo* applications: the detection of metabolic fluxes from ^{13}C labeled precursors and the detection of glycogen.

Most metabolites must become sufficiently enriched in ^{13}C for detection by NMR. This is accomplished by using ^{13}C labeled precursors. In general, resonances can only be observed in ^{13}C NMR spectra of intact tissues if their concentration exceeds a limit of 1 mM. Most intermediates are normally present in tissues below this concentration, and hence cannot be observed directly by NMR, even with a ^{13}C enrichment of unity, without excessively long periods of data accumulation.

As metabolism proceeds through particular pathways, the ^{13}C label transfers from one biomolecule to the other through many enzymatic transformations. Eventually, several carbon positions of TCA cycle intermediates will become ^{13}C labeled and neighboring ^{13}C nuclei will give rise to multiplet structures due to ^{13}C - ^{13}C scalar coupling (Section 1.2.9). Figure 1.16 shows an illustration of the ^{13}C label transfer from several ^{13}C labeled precursors after 4 turns of the TCA cycle. The resulting labeling patterns are dependent on the chemistry of the enzymatic reactions, the reaction rate and the pool sizes of the intermediates. The multiplet structure of the resonance of a certain carbon position, consisting of so called isotopomers (Figure 1.17), informs about the relative ^{13}C concentration of the neighbors of that carbon position. The fraction of a carbon position that is ^{13}C versus ^{13}C labeled is called the fractional enrichment:

$$FE = \frac{^{13}\text{C}}{^{13}\text{C} + ^{12}\text{C}} \quad (1.51)$$

The fractional enrichment of a neighbouring ^{13}C labeled carbon position can be determined by taking the ratio of the multiplet, induced by the ^{13}C - ^{13}C coupling of its neighbour, to the total carbon resonance area. Chapter 7 uses isotopomer analysis to determine the fractional enrichment of ^{13}C labeling in glutamate position C2, C3 and C4 after the infusion and metabolism of [2- ^{13}C]acetate in skeletal muscle. Consider the glutamate C4 resonance position. When glutamate is labeled at both C4 and C3, a doublet pattern will appear, when glutamate is only labeled at the C4 position, a singlet appears in the spectrum (Figure 1.17).

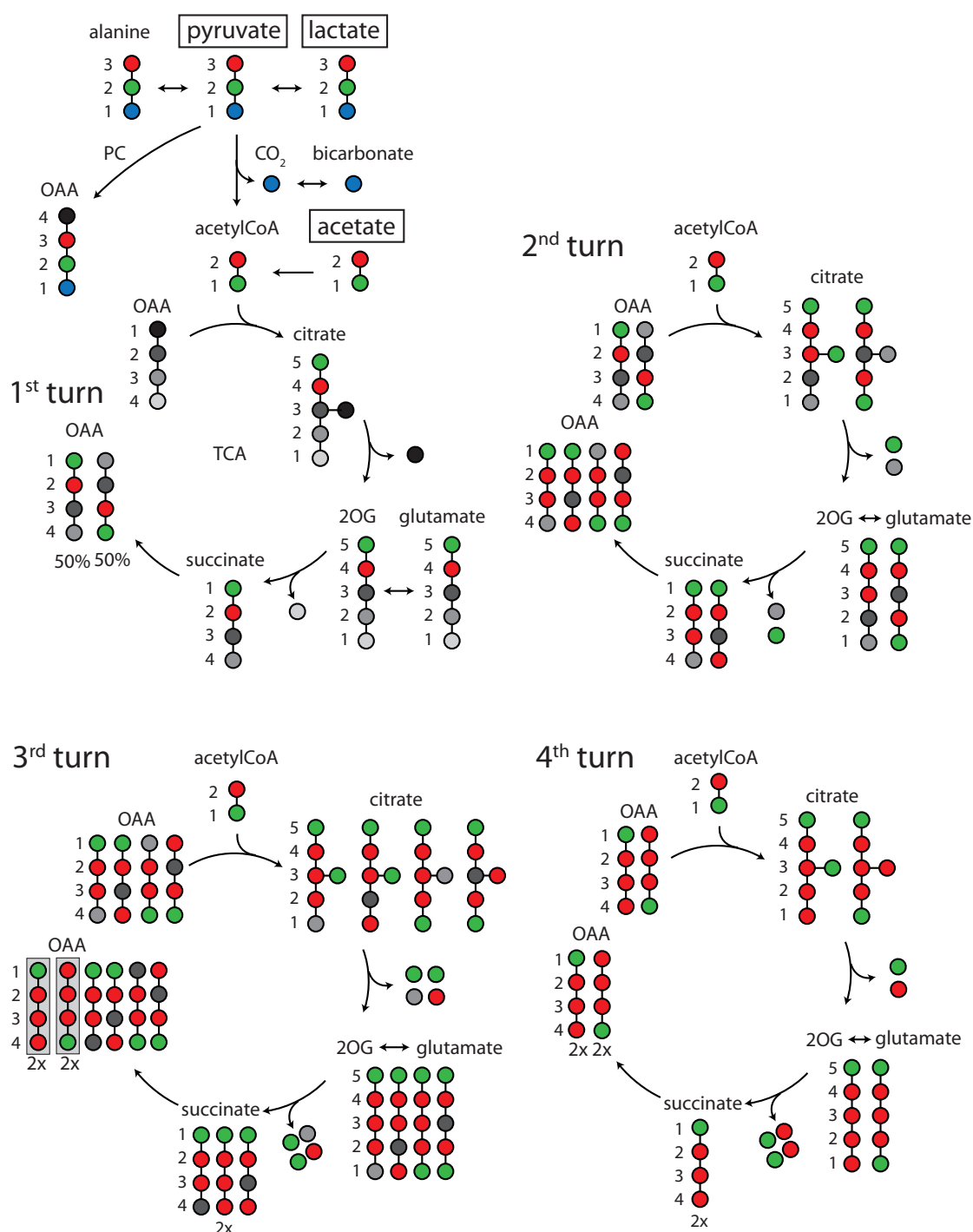


Figure 1.16: Illustration of the ^{13}C label transfer from the carbon positions C1, C2 and C3 of pyruvate, lactate and alanine and the C1 and C2 of acetate. The illustration shows the possible labeling patterns of several TCA cycle intermediates up to 4 cycles. In this scheme, pyruvate carboxylation (PC) and dilution of non-labeled acetylCoA are not taken into account. In the first cycle, the C1 and C2 of acetylCoA condenses with unlabeled oxaloacetate (OAA). The symmetry of the succinate molecule scrambles the labeling in oxaloacetate.

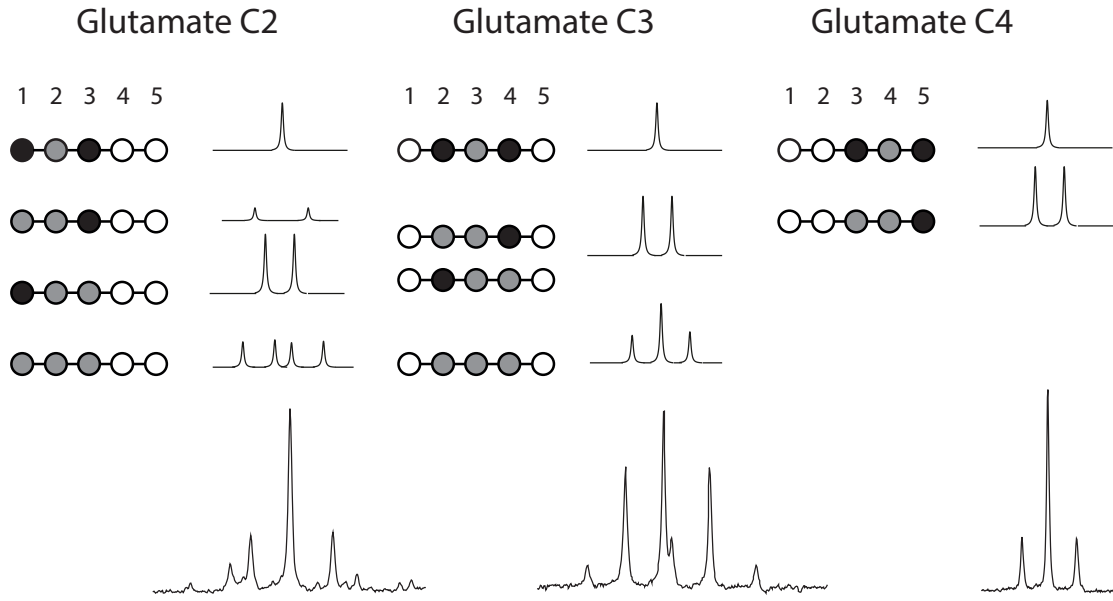


Figure 1.17: Illustration of ^{13}C spectra of glutamate C2, C3 and C4 labeled at several carbon positions. Neighbouring ^{13}C nuclei split the resonances in multiplets due to the ^{13}C - ^{13}C coupling. Grey spheres indicate ^{13}C nuclei, black spheres ^{12}C nuclei and white spheres could be ^{12}C or ^{13}C .

Therefore, the ratio of the doublet area to the total area of the C4 resonance,

$$\frac{C4D34}{C4} = FE_{\text{Glu},C3}, \quad (1.52)$$

is the fraction of glutamate molecules labeled at C4, which are also labeled at C3. This fraction represents in fact the fraction of glutamate labeled in C3, and thus, analyzing the multiplet pattern of glutamate C4 allows the calculation of the fractional enrichment of glutamate C3.

During dynamic ^{13}C experiments that typically run for several hours, a large set of metabolites will be labeled in this manner and give rise to so-called spectral time courses. These time courses can be modeled using differential equations that take into account current physiological and biochemical knowledge of the system.

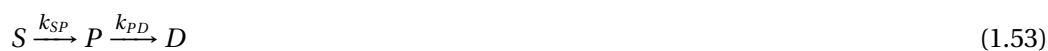
1.5.1 Modeling biochemical processes using ^{13}C MRS

^{13}C spectroscopy has the potential to measure dynamic processes, which for a comprehensive interpretation require mathematical treatment. Individual carbon resonances relative to the total intermediate present in tissues allows to determine the fractional enrichment of separate carbon atoms. The labeling pattern of carbon positions in different metabolites provides information on the pathway through which the metabolism proceeds. Also, changes

in the fractional ^{13}C enrichment of specific carbon atoms with time contain flux information concerning the state of activity of specific metabolic pathways. Flux information from the data can be obtained by using nonlinear least squares analysis of the differential equations describing the enzymatic pathways with the kinetic rate constants of fluxes as the unknown parameters. These parameters can be used to study differences in metabolism in pathological situations.

Irreversible Reactions

In living organisms there is a plethora of biochemical reactions happening to provide energy to maintain healthy functionality. Biochemical transformations are catalyzed by enzymes, which convert one molecule to the other. In a simple schematic of metabolism one can consider a simple three step biochemical reaction which starts with a substrate S and is converted to products P which is in turn converted to another downstream product D :



The conversion of substrate S to product P is characterized by a reaction rate k_{SP} which describes how fast one set of molecules is converted to the other and is expressed in s^{-1} . The amount of product P depends on the conversion rate of S to P and on the conversion rate of P to D . These three reactions can be described mathematically by the following differential equations:

$$\frac{dS(t)}{dt} = -k_{SP}S(t) \quad (1.54)$$

$$\frac{dP(t)}{dt} = k_{SP}S(t) - k_{PD}P(t) \quad (1.55)$$

$$\frac{dD(t)}{dt} = k_{PD}P(t) \quad (1.56)$$

This is an example of a non-reversible chemical reaction, i.e., the reaction goes in one direction only. The reaction rates k reflects the enzymatic conversion per unit of time and does not give information about chemical reactions quantitatively in terms of how much of a specific substrate is converted over time. Metabolic fluxes combine the kinetic rate constant with the amount of substrate available and are expressed in mM/s and can be described as follows:

$$V_{SP} = k_{SP}S \quad (1.57)$$

One can describe the concentration change of product P by the inflow from S and the

outflow towards D with the following mass-balance equation:

$$\frac{dP(t)}{dt} = V_{SP} - V_{PD} \quad (1.58)$$

In the case of a so-called metabolic steady state the concentration of metabolites does not change over time, making $dP/dt = 0$ and thus $V_{SP} = V_{PD}$. As long as the inflow is the same as the outflow, the concentration of P will not change. These types of equations are also known as mass-balance equations. Measuring the concentration of P over time will not give information about the kinetics which is involved in the formation and removal of P , i.e., will not give insight into the metabolic fluxes into and out of the poolsize of P . To be able to measure the rate of formation and degradation of P it is necessary to introduce some sort of label in the initial substrate P which can be followed over time while that label is being transferred into product P and further into downstream metabolite D . Since most reactions *in vivo* involve molecules with carbon backbones it is useful to label specific carbon atoms. One feature of carbon is that it naturally occurs in the ^{12}C isotope form which does not have a nuclear magnetic moment. The isotope ^{13}C does have a nuclear magnetic moment; it has a spin $1/2$, which allows it to be detected by NMR. The introduction of a ^{13}C labeled carbon in biomolecules does not have an effect on its metabolism. When incorporating ^{13}C labeled (*) biomolecules into the chemical reactions described before Equation 1.55 and 1.58 can be rewritten as follows:

$$\frac{dP^*(t)}{dt} = k_{SP}S^*(t) - k_{PD}P^*(t) \quad (1.59)$$

$$\frac{dP^*(t)}{dt} = V_{SP} \frac{S^*(t)}{S(t)} - \frac{P^*(t)}{P(t)} V_{PD} \quad (1.60)$$

The asterisk indicates a ^{13}C labeled compound which can be tracked using ^{13}C NMR spectroscopy. These type of equations are referred to as isotope-balance equations and the ratio of labeled versus unlabeled substrate is also referred to as the fractional enrichment of the metabolite pool. In conventional ^{13}C NMR studies performed under steady-state conditions, V_{SP} equals V_{PD} and the fractional enrichment of substrate S and the enrichment itself is constant over time. Therefore the time dependence of the ^{13}C labeling of P can be solved analytically:

$$P^*(t) = \frac{k_{SP}S^*}{k_{PD}}(1 - e^{-tk_{PD}}) \quad (1.61)$$

$$P^*(t) = \frac{PS^*}{S}(1 - e^{-t\frac{V_{PD}}{P}}) \quad (1.62)$$

In hyperpolarized studies a rapid injection is employed and the ^{13}C labeled substrate is not constant over time, resulting in a time-dependent fractional enrichment of the substrate S .

However, in these type of experiments the ^{13}C labeled molecule which is injected often exceeds the level of the non-labeled molecule making the fractional enrichment approaching unity, $S^*/S = 1$. When it is assumed that the labeled substrate is introduced at $t=0$. The analytical solution can be described as follows:

$$P^*(t) = \frac{k_{SP} S_0^* (e^{-t k_{SP}} - e^{-t k_{PD}})}{k_{SP} - k_{PD}} \quad (1.63)$$

$$P^*(t) = \frac{\frac{V_{SP}}{S} S_0^* (e^{-t \frac{V_{SP}}{S}} - e^{-t \frac{V_{PD}}{P}})}{\frac{V_{SP}}{S} - \frac{V_{PD}}{P}} \quad (1.64)$$

Reversible Reactions

Reactions can also be catalyzed by reversible enzymes, meaning that the reactions are going both in the forward and backward direction:



The differential equations describing enrichment in P are as follows:

$$\frac{dP^*(t)}{dt} = k_{SP} S^*(t) - k_{PS} P^*(t) \quad (1.66)$$

$$\frac{dP^*(t)}{dt} = \frac{S^*(t)}{S(t)} V_{SP} - \frac{P^*(t)}{P(t)} V_{PS} \quad (1.67)$$

Mass-balance and isotope-balance equations can be constructed for all metabolic pools, making up the metabolic model. For a full description of a set of metabolic pathways *in vivo*, such as after a $[2-^{13}\text{C}]$ acetate infusion in skeletal muscle (as described in Chapter 7), including multiple flows into a single pool and multiple metabolites, numerical approaches are used to solve the equations to obtain the metabolic flux parameters³⁹.

Bloch McConnell Equations

So far reactions kinetics were described which concern the ^{13}C label changes, concentration changes and pool sizes. In hyperpolarized NMR experiments the measured signal depends not only on the concentration of the ^{13}C labeled molecules but mainly on the polarization and the RF excitations:

In hyperpolarized NMR experiments concentrations changes of ^{13}C labeled metabolites are large and the measured signal is directly related to the polarization level. This is affected

by the initial polarization level of the injected substrate which decays with the longitudinal relaxation time T_1 . Additionally, the measured signal is affected by MR acquisitions since each acquisition results in additional signal losses⁴⁰.

The ^{13}C concentrations changes of the metabolites since this provides information about the reaction kinetics. To be able to do this one has to filter out the polarization effect and this can be done by taking into account the relaxation times of the observed metabolites. The magnetization of metabolites, which is the combination of the polarization levels and the concentration of the substance, can be described by the Bloch-McConnell equations⁴¹. Describing the magnetization levels of an injected substrate S and its product P in a reversible reaction process leads to the following expression:

$$\frac{dM_{P^*}(t)}{dt} = R_P [M_{P^*}(t) - M_{P^*,eq}] + k_{SP}M_{S^*}(t) - k_{PS}M_{P^*}(t) \quad (1.68)$$

where R_P is the longitudinal relaxation rate, $R_P = 1/T_{1,P}$, of the product P , $M_{P,eq}$ is the thermal equilibrium magnetization. In hyperpolarized experiments the ^{13}C signal is boosted over 10,000 fold and one can assume that the thermal equilibrium magnetization of product P approaches zero, $M_{P,eq} = 0$.

This description given here relies on several assumptions. The first is that the hyperpolarized substance is injected in the same compartment where it is also metabolized and does not take into account the transport from the plasma to the tissue compartment, whether this is concentration gradient mediated or enzymatic transport. In many situations, such as in cell cultures, it is fair to neglect this contribution since enzymatic transport is relatively fast compared to the reaction kinetics⁴². The second assumption is that the hyperpolarized product is quickly distributed to a homogeneous concentration in the plasma pool, "the well-mixed chamber" assumption. Often this is an acceptable assumption to make for organs, which are further downstream from the intravenous injection site.

References

- [1] E.M. Purcell, H. C. Torrey, and R.V. Pound. Resonance absorption by nuclear magnetic moments in a solid. *Phys Rev*, 69:37–38, 1946.
- [2] F Bloch, W W Hansen, and M E Packard. Nuclear induction. *Phys Rev*, 69:127, 1946.
- [3] W.G. Proctor and F. C. Yu. The dependence of a nuclear magnetic resonance frequency upon chemical compound. *Phys Rev*, 77:717, 1950.
- [4] W.C. Dickinson. Dependence of the f19 nuclear resonance position on chemical compound. *Phys Rev*, 77:736, 1950.
- [5] R Damadian. Tumor detection by nuclear magnetic resonance. *Science*, 171:1151–1153, 1971.
- [6] P.C. Lauterbur. Image formation by induced local interactions: examples employing nuclear magnetic resonance. *Nature*, 242:190–191, 1973.
- [7] P Mansfield and P. K. Grannell. Nmr diffraction in solids? *J Phys C; Solid State Phys*, 6:L422–L427, 1973.
- [8] E.M. Haacke, R. W. Brown, M. R. Thompson, and R. Venkatesan. *Magnetic Resonance Imaging: Physical Principles and Sequence Design*. Wiley-Liss, 1990.
- [9] R. de graaf. *NMR spectroscopy: Principles and Techniques*. Wiley, 2008.
- [10] F Bloch. Nuclear induction. *Phys Rev*, 70:460–473, 1946.
- [11] F Bloch, W W Hansen, and M E Packard. The nuclear induction experiment. *Phys Rev*, 70:474–485, 1946.
- [12] N Bloembergen, E M Purcell, and R V Pound. Relaxation effects in nuclear magnetic resonance absorption. *Physical Review*, 73:679–712, 1948.
- [13] E L Hahn. Spin echoes. *Phys Review*, 80:580–594, 1950.
- [14] HY Carr and EM Purcell. Effect of diffusion on free precession in nuclear magnetic resonance experiments. *Phys Rev*, 94:630–638, 1954.
- [15] S Meiboom and D Gill. Modified spin-echo method for measuring nuclear relaxation times. *Rev Scie Instrum*, 29:688–691, 1958.
- [16] A. J. Shaka, J. Keeler, and R. Freeman. Evaluation of a new broad-band decoupling sequence - waltz-16. *Journal of Magnetic Resonance*, 53(2):313–340, 1983.
- [17] R Sauter, S Mueller, and Weber H. Localization in in vivo 31p nmr spectroscopy by combining surface coils and slice selective saturation. *Journal of Magnetic Resonance*, 75:167–173, 1975.
- [18] RT Johnson, DN Paulson, RP Giffard, and JC Wheatley. Bulk nuclear polarization of solid ³he. *Journal of low temperature physics*, 10:35–58, 1973.
- [19] W Happer. Optical pumping. *Rev Mod Phys*, 44:169–249, 1972.
- [20] CR Bowers and DP Weitekamp. Parahydrogen and synthesis allow dramatically enhanced nuclear alignment. *J Am Chem Soc*, 109:5541, 1987.
- [21] A Abragam and M Goldman. Principles of dynamic nuclear polarization. *Rep Prog Phys*, 41:395–467, 1987.
- [22] W Zhang and DG Cory. First direct measurement of the spin diffusion rate in a homogeneous solid. *Physical Review Letters*, 80:1324–1327, 1998.
- [23] GS Boutis, D Greenbaum, H Cho, DG Cory, and C Ramanathan. Spin diffusion of correlated two-spin states in a dielectric crystal. *Physical Review Letters*, 92, 2004.

- [24] A.W. Overhauser. Polarization of nuclei in metals. *Physical Review*, 91:476, 1953.
- [25] T.R. Carver and C. P Slichter. Polarization of nuclear spins in metals. *Physical Review*, 92:212–213, 1953.
- [26] A Abragam. Overhauser effect in nonmetals. *Physical Review*, 98:1729–1735, 1955.
- [27] I Solomon. Relaxation processes in a system of 2 spins. *Physical Review*, 99:559–565, 1955.
- [28] M Goldman. Overview of spin temperature, thermal mixing and dynamic nuclear polarization. *Applied Magnetic Resonance*, 34:219–226, 2008.
- [29] J. H. Ardenkjaer-Larsen, B. Fridlund, A. Gram, G. Hansson, L. Hansson, M. H. Lerche, R. Servin, M. Thaning, and K. Golman. Increase in signal-to-noise ratio of > 10,000 times in liquid-state nmr. *Proc Natl Acad Sci U S A*, 100(18):10158–10163, 2003.
- [30] M. A. Schroeder, H. J. Atherton, L. E. Cochlin, K. Clarke, G. K. Radda, and D. J. Tyler. The effect of hyperpolarized tracer concentration on myocardial uptake and metabolism. *Magn Reson Med*, 61(5):1007–14, 2009.
- [31] K. Golman, R. in’t Zandt, and M. Thaning. Real-time metabolic imaging. *Proc Natl Acad Sci U S A*, 103(30):11270–11275, 2006.
- [32] M Karlsson, PR Jensen, J Duus, S Meier, and MH Lerche. Development of dissolution dnp-mr substrates for metabolic research. *Applied Magnetic Resonance*, 43:223–236, 2012.
- [33] J. Link. the design of resonator probes with homogenous radiofrequency fields. *NMR Basic Principles and Progress*, 26:3–31, 1992.
- [34] JL Evelhoch, MG Crowley, and JJH Ackerman. Signal-to-noise optimization and observed volume localization with circular surface coils. *J Magn Res*, 56:110–124, 1984.
- [35] G Adriany and R Gruetter. A half-volume coil for efficient proton decoupling in humans at 4 tesla. *J Magn Res*, 125:178–184, 1997.
- [36] DI Hoult, CN Chen, and VJ Sank. Quadrature detection in the laboratory frame. *Magnetic Resonance in Medicine*, 1:339–353, 1984.
- [37] CN Chen, VJ Sank, and DI Hoult. Quadrature detection coils - a further $\sqrt{2}$ improvement in sensitivity. *J Magn Res*, 54:324–327, 1983.
- [38] PB Roemer, WA Edelstein, CE Hayes, SP Souza, and OM Mueller. The nmr phased array. *Magnetic Resonance in Medicine*, 16:192–225, 1990.
- [39] R Gruetter, E.R. Seaquist, and K Ugurbil. A mathematical model of compartmentalized neurotransmitter metabolism in the human brain. *Am J Physiol Endocrinol Metab*, 281:E100–E112, 2001.
- [40] B. R. Patyal, J. H. Gao, R. F. Williams, J. Roby, B. Saam, B. A. Rockwell, R. J. Thomas, D. J. Stolarski, and P. T Fox. Longitudinal relaxation and diffusion measurements using magnetic resonance signals from laser-hyperpolarized ^{129}Xe nuclei. *Journal of Magnetic Resonance*, 126:58–65, 1997.
- [41] H. M. McConnell. Reaction rates by nuclear magnetic resonance. *Journal of Chemical Physics*, 28(3):430–431, 1958.
- [42] S. E. Day, M. I. Kettunen, F. A. Gallagher, D. E. Hu, M. Lerche, J. Wolber, K. Golman, J. H. Ardenkjaer-Larsen, and K. M. Brindle. Detecting tumor response to treatment using hyperpolarized (^{13}C) magnetic resonance imaging and spectroscopy. *Nat Med*, 13(11):1382–1387, 2007.

Enzymatic activity of acetylCoA synthetase revealed with hyperpolarized acetate

2

Abstract

Acetate metabolism in skeletal muscle is regulated by acetylCoA synthetase (ACS). The main function of ACS is to provide cells with acetylCoA, a key molecule for numerous metabolic pathways including fatty acid and cholesterol synthesis and the Krebs cycle. Hyperpolarized [1-¹³C]acetate prepared via dissolution dynamic nuclear polarization was injected intravenously at different concentrations into rats. The ¹³C magnetic resonance signals of [1-¹³C]acetate and [1-¹³C]acetylcarnitine were recorded *in vivo* for one minute.

The kinetic rate constants of the observed reactions were deduced from the 3s time resolution measurements using two analytical approaches, either mathematical modelling or relative metabolite ratios, both methods yielding similar results. The *in vivo* conversion rates from hyperpolarized acetate into acetylcarnitine were quantified, and, although separated by two enzymatic reactions, a kinetic analysis of the ¹³C label flow from [1-¹³C]acetate to [1-¹³C]acetylcarnitine led to a unique determination of the activity of ACS. The *in vivo* Michaelis constants for ACS were $K_M = 0.35 \pm 0.13$ mM and $V_{max} = 0.199 \pm 0.031$ μ mol/g/min.

This study demonstrates the feasibility of directly measuring ACS activity *in vivo* and, since the activity of ACS can be affected by various pathological states such as cancer or diabetes, the proposed method could be used to non-invasively probe metabolic signatures of ACS in diseased tissue.

Adapted and extended from

In vivo enzymatic activity of acetylCoA synthetase in skeletal muscle revealed by ¹³C turnover from hyperpolarized [1-¹³C]acetate to [1-¹³C]acetylcarnitine

Jessica AM Bastiaansen, Tian Cheng, Mor Mishkovsky, João MN Duarte, Arnaud Comment and Rolf Gruetter
Biochimica et Biophysica Acta 1830 Issue 8 August 2013 Pages 4171-4178

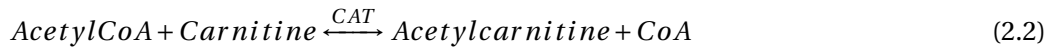
2.1 Introduction to acetate metabolism in skeletal muscle

Acetate plays an important role in human and rodent energy metabolism and it is readily taken up by skeletal muscle^{1–3} (see 2.1). Acetate is a pyruvate dehydrogenase (PDH) independent acetylator of tissue carnitine and free coenzyme A (CoA)¹ and is converted into acetylCoA via a reaction catalysed by the enzyme acetylCoA synthetase (ACS):



The main function of ACS is to provide the cell with acetylCoA, a key molecule for numerous metabolic pathways including fatty acid and cholesterol synthesis and the tricarboxylic acid (TCA) cycle. ACS has been previously shown to be the rate limiting enzyme in the metabolism of acetate^{4,5}. Pathological and substrate changes have an effect on the activity of ACS, which has been reported to be turned off faster than other CoA dependent enzymes during free CoA decrease⁶. Its activity increases together with insulin in response to a carbohydrate-rich diet to induce fatty acid synthesis⁷.

Carnitine acetyltransferase (CAT) converts acetylCoA to acetylcarnitine:



In skeletal muscle, carnitine plays two metabolic roles: on one hand it serves as a shuttle of acetyl groups and long chain fatty acids from the cytosol into mitochondria and thus enabling

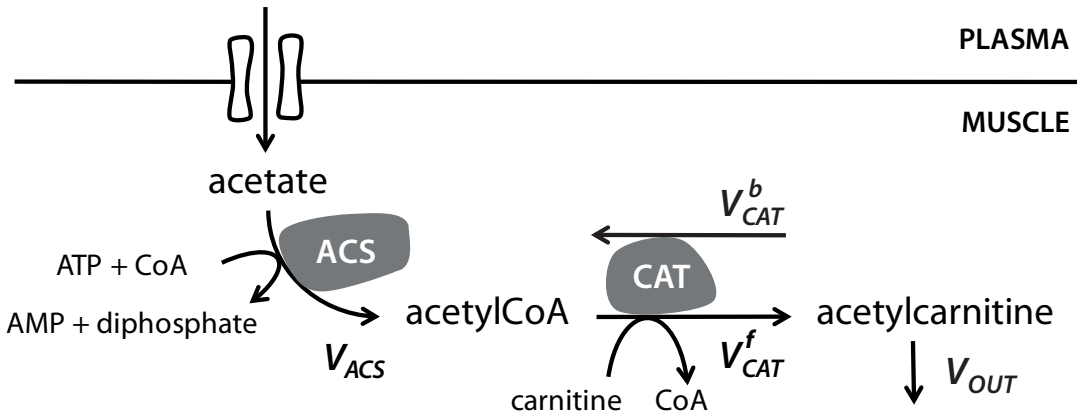


Figure 2.1: Schematic representation of the uptake and metabolism of acetate in rat skeletal muscle in vivo. Acetate diffusion into the muscle cell is facilitated by a concentration gradient. Via acetylCoA synthetase (ACS) it is transformed to acetylCoA in the cytosol. Carnitine acetyltransferase (CAT) converts acetylCoA to acetylcarnitine. Acetylcarnitine translocase (ATL) transports the acetylcarnitine to the mitochondrion where CAT converts acetylcarnitine back to acetylCoA for further utilization by the TCA cycle. In this study we measured cytosolic processes.

beta oxidation⁸⁻¹². On the other hand it can act as a buffer for excess acetylCoA when the rate of acetylCoA generation is greater than its entry into the TCA cycle. The reaction catalyzed by CAT has a well maintained equilibrium¹³ and despite different steady state concentrations of the reactants, the equilibrium constant is given by¹⁴:

$$K_{eq} = \frac{[AcetylCoA][Carnitine]}{[CoA][Acetylcarnitine]} = 0.6 \pm 0.06 \quad (2.3)$$

The general function of CAT is to balance rapid changes in the acetylCoA/CoA ratio in both the cytoplasmic and mitochondrial compartments¹⁰. In rat skeletal muscle, 98% to 99% of extra acetylCoA produced is buffered by acetylcarnitine¹⁵. Since the mitochondrial inner membrane is impermeable to acetylCoA, CAT is essential in the metabolism of acetate, as was shown in canine skeletal muscle¹⁶. After transformation to acetylcarnitine it traverses the inner mitochondrial membrane via acetylcarnitine translocase (ATL) where a mitochondrial CAT transfers the acetyl group back to CoA upon which acetylCoA can enter the TCA cycle.

Acetate, being a short chain fatty acid has a typical plasma concentration of 0.2 mM in rats which decreases during fasting and increases in a diabetic state⁵. Its oxidation has been deemed significant since it is rapidly cleared from the blood if injected *in vivo* or generated from precursors such as ethanol in the liver¹⁷. Acetate uptake by resting skeletal muscle is driven by a concentration gradient and is proportional to the plasma concentration^{18;19}. In a single passage of blood, half of the acetate presented to the tissue was removed by the muscle tissue indicating a high affinity for acetate⁵. In contracting skeletal muscle however, acetate oxidation decreased, indicating a shift of substrate preference compared to resting skeletal muscle²⁰.

To date, most of the information concerning these enzyme activities in rat has however been collected from cell cultures and tissue preparations^{5;21}. The ability to measure ACS and CAT activities *in vivo* is expected to provide valuable insight in normal and pathological conditions.

¹³C magnetic resonance spectroscopy (MRS) is a well-established technique to investigate *in vivo* metabolic processes²² and it can be coupled with standard MR imaging techniques that gives anatomical information. The advent of dissolution dynamic nuclear polarization (DNP) allows for the measurement of specific metabolic reactions in real-time, thanks to a sensitivity enhancement of several orders of magnitude^{23;24}, which is now being used in human trials in the investigation of prostate cancer²⁵.

The incorporation of ¹³C into acetylcarnitine has been reported after the infusion of hyperpolarized ¹³C acetate²⁶ and after the injection of [2-¹³C]pyruvate^{27;28}. The aim of the present study was to elucidate the enzyme kinetics involved in the *in vivo* transformation of acetate to acetylcarnitine in rat skeletal muscle *in vivo*, by extracting quantitative kinetic rate constants from the observed [1-¹³C]acetylcarnitine labeling dynamics following the infusion of different substrate concentrations of hyperpolarized [1-¹³C]acetate.

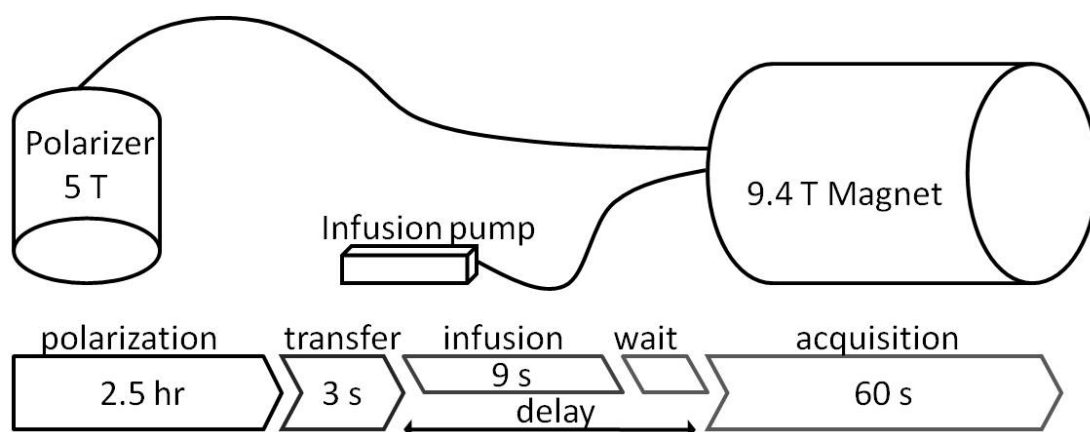


Figure 2.2: Graphical scheme of the setup and timing of *in vivo* DNP experiments described in this chapter. A metabolic precursor, in this case $[1-^{13}\text{C}]$ acetate, was dynamically polarized in a 5T magnet for 2.5 hours. This hyperpolarized sample is quickly dissolved in heated D_2O and automatically transferred to a separator-infusion pump located inside a 9.4T horizontal bore magnet. The hyperpolarized solution is injected within 5 seconds into a subject and the NMR acquisition is triggered automatically.

2.2 Materials and Methods

Sample preparation and hyperpolarization protocol of $[1-^{13}\text{C}]$ acetate

The hyperpolarized signal decays with time constant T_1 , which is one of the determining factors of the measurement window of the hyperpolarized *in vivo* experiment. Because of T_1 considerations, the acetate was ^{13}C labeled in position C1 which has a T_1 of 40 seconds compared to 3 seconds in the C2 position.

All chemicals were purchased from Sigma-Aldrich, Basel, Switzerland. $[1-^{13}\text{C}]$ sodium acetate was dissolved in a concentration ranging from 1.0 to 4.5 M in a 1:2 mixture of $\text{d}_6\text{-EtOD}/\text{D}_2\text{O}$ containing 33mM of TEMPO (2,2,6,6-Tetramethyl-1-piperidinyloxy) free radical. 300 μL of the resulting solution was rapidly frozen in liquid nitrogen to form 10 μL beads that were placed in a 5 T custom-designed DNP polarizer^{29;30}. The ^{13}C nuclear spins were dynamically polarized at 1.02 ± 0.03 K for 2 h using 30 mW of microwave power at 140.18 GHz. The sample was consecutively rapidly dissolved using 6.0 mL of superheated D_2O and transferred within 2 s to a separator/infusion pump located inside a 9.4 T horizontal bore magnet containing 0.6 mL of phosphate buffered saline and heparin. Subsequently, 1.0 mL of the room-temperature hyperpolarized acetate solution was automatically infused into the animal within 5 s (Figure 2.2). From *in vitro* measurements performed inside the separator/infusion pump, it was determined that the ^{13}C polarization at the time of injection was $13 \pm 2\%$ ³¹. No physiological changes were observed during the injection.

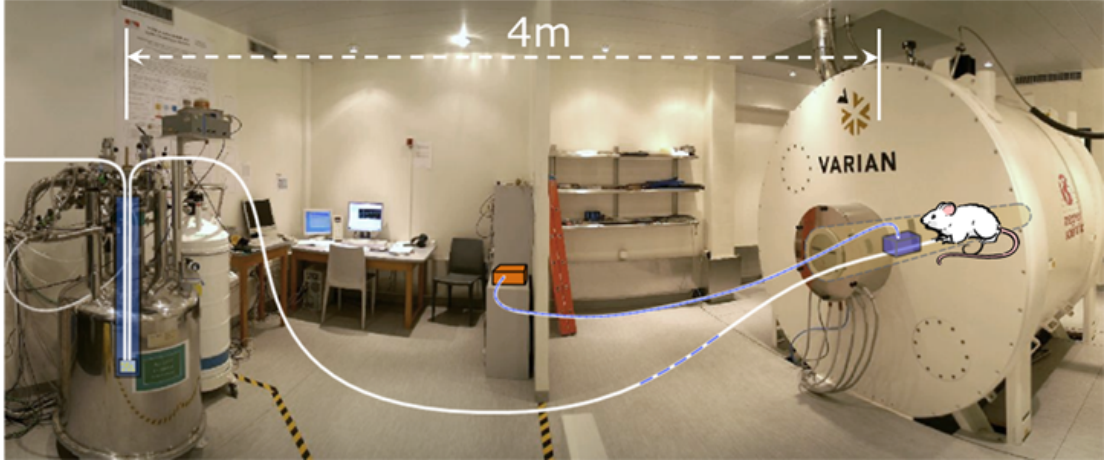


Figure 2.3: Picture of experimental set-up for performing hyperpolarized *in vivo* experiments. The polarizer magnet (left) is 4m apart from the animal imager (right). A detailed graphical depiction and timing of such experiments are shown in Figure 2.2.

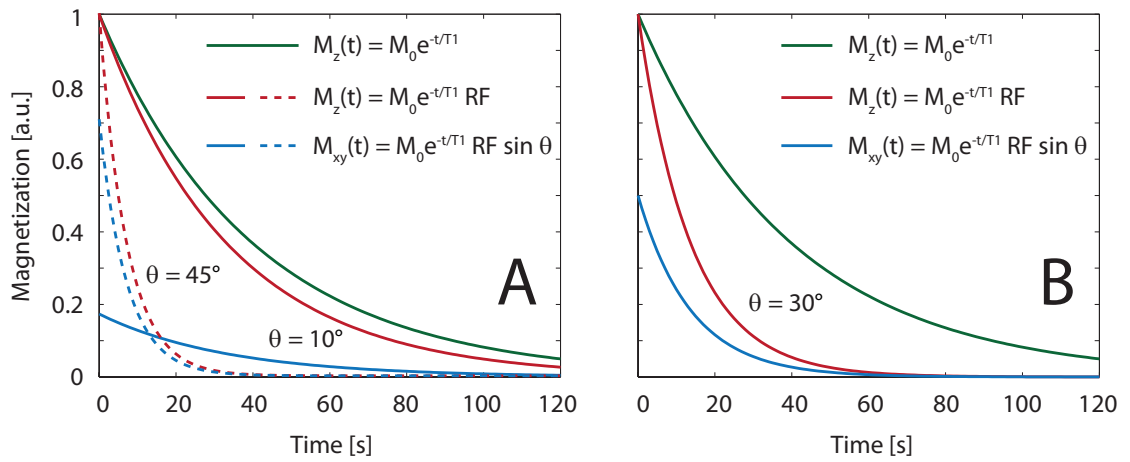


Figure 2.4: Influence of repeated RF excitations with flip angle θ on the longitudinal and transversal magnetization of $[1-^{13}\text{C}]\text{acetate}$. In these curves a T_1 of 40 seconds was assumed and a repetition time of 3 seconds. (A) Magnetization decay for a flip angle of 10° (solid lines), 45° (dotted lines), and (B) 30° . The decay of M_z without application of RF pulses is indicated with the green line.

Animals

All animal experiments were conducted according to federal ethical guidelines and were approved by the local regulatory body. Male Sprague Dawley rats (275 - 325 g) were anesthetized with 1.5% isoflurane in oxygen (n=19). A catheter was placed into the femoral vein for intravenous delivery of the hyperpolarized acetate solution. The respiration rate and temperature were monitored and maintained during the experiment.

Choice of flip angle and repetition time

The choice of flip angle and repetition time T_R needs to be carefully considered for each type of hyperpolarized *in vivo* experiment. With each 30° excitation pulse, the magnetization vector M will be tipped away by 30° from the z axis. The z component of the magnetization after excitation with flip angle θ equals $M_z = M \cos \theta$, resulting in a 13% polarization loss with each excitation. More generally, the initial magnetization M_0 will decay as a result of T_1 and n excitations with flip angle θ as follows:

$$M_z = M_0 e^{-t/T_1} \cos \theta^n \quad (2.4)$$

where $n = t/T_R$. Initial experiments were conducted with a 10° flip angle, resulting in a 2% polarization loss per excitation, however this was not sufficient to detect the metabolic products. Application of a 30° flip angle excites the acetylcarnitine to detectable levels while preserving the initial polarization levels long enough to obtain timecourses of both metabolites (Figure 2.4). Calibration measurements are described in Appendix A.2.

***In vivo* magnetic resonance spectroscopy**

All experiments were performed with a Direct Drive spectrometer (Agilent, Palo Alto, CA, USA) interfaced to an actively shielded 9.4 T magnet with a 31 cm horizontal bore (MagneX Scientific, Abingdon, UK). A home-built $^1\text{H}/^{13}\text{C}$ probe consisting of a pair of 10 mm diameter ^1H surface coils in quadrature and a 10 mm diameter ^{13}C surface coil was placed over the hind leg of the rat (Figure 2.5) to selectively excite and detect skeletal muscle tissue, more specifically, the gastrocnemius muscles.

A hollow glass sphere with a 3 mm inner diameter (WilmaD-LabGlass, NJ, USA) was filled with a 1 M [$1\text{-}^{13}\text{C}$]glucose solution and used to adjust the pulses power and set the reference frequency. Once the animal was positioned inside the magnet, ten axial 1 mm thick slices were acquired using a gradient echo sequence ($T_R = 50$ ms, $T_E = 3$ ms, field of view = 30 x 30 mm, matrix = 128 x 128, flip angle = 30°) from which the volume of interest was selected. The static magnetic field was homogenized in a 600 μL (6 mm x 10 mm x 10 mm) voxel to reduce the localized proton line width to 20 Hz using the FASTESTMAP shimming protocol³². Series of single-pulse ^{13}C acquisitions were sequentially recorded starting 12 s after dissolution using 30° adiabatic RF pulses (BIR4) applied every 3 s with ^1H decoupling during acquisition

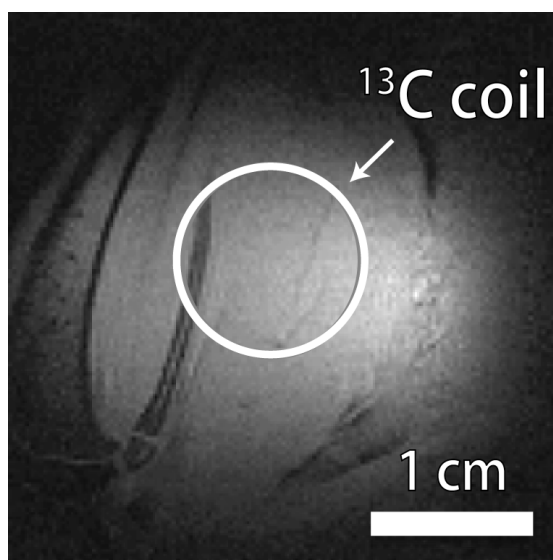


Figure 2.5: Anatomical scout image of the rat skeletal muscle showing the placement of the surface carbon coil.

(WALTZ). Decoupling is needed to remove the ^1H - ^{13}C scalar coupling induced splitting of the ^{13}C metabolite resonances. For example, the resonance of $[1\text{-}^{13}\text{C}]\text{acetylcarnitine}$ is a doublet of a quartet when not ^1H decoupled (Figure 1.9 in section 1.2.9). The adiabatic pulses offset and power was set such as to ensure a homogeneous 30° excitation of substrate and metabolite resonances in the entire volume of interest (for calibration measurements see Appendix A.2).

At the end of each *in vivo* experiment, 200 μL of the residual solution was collected from the infusion pump and the $[1\text{-}^{13}\text{C}]\text{acetate}$ concentration was measured in a high-resolution 400 MHz NMR spectrometer (Bruker BioSpin SA, Fallanden, Switzerland) by comparing the signal with a $[1\text{-}^{13}\text{C}]\text{pyruvate}$ reference sample of a known concentration. To reduce the T_1 of $[1\text{-}^{13}\text{C}]\text{acetate}$ and $[1\text{-}^{13}\text{C}]\text{pyruvate}$ and thus the measurement time, Omniscan was added to a final concentration of 1 mM, which reduced the T_1 about 15 fold (Figure 2.6). Measurements were performed using a pulse acquire experiment with a 90° flip angle, $T_R = 20\text{ s}$, ^1H decoupling and 12 scan averages.

The animals blood volume was calculated using the relation between total blood volume and body weight published by Lee and Blaufox³³ and the blood $[1\text{-}^{13}\text{C}]\text{acetate}$ concentration was obtained accordingly.

T_1 measurement of $[1\text{-}^{13}\text{C}]\text{acetylcarnitine}$

The *in vitro* spin-lattice relaxation times of $[1\text{-}^{13}\text{C}]\text{acetylcarnitine}$ were also measured at 400 MHz in D_2O and in freshly collected rat blood at 37°C using a saturation recovery sequence with proton decoupling during acquisition. The saturation recovery sequence used to measure

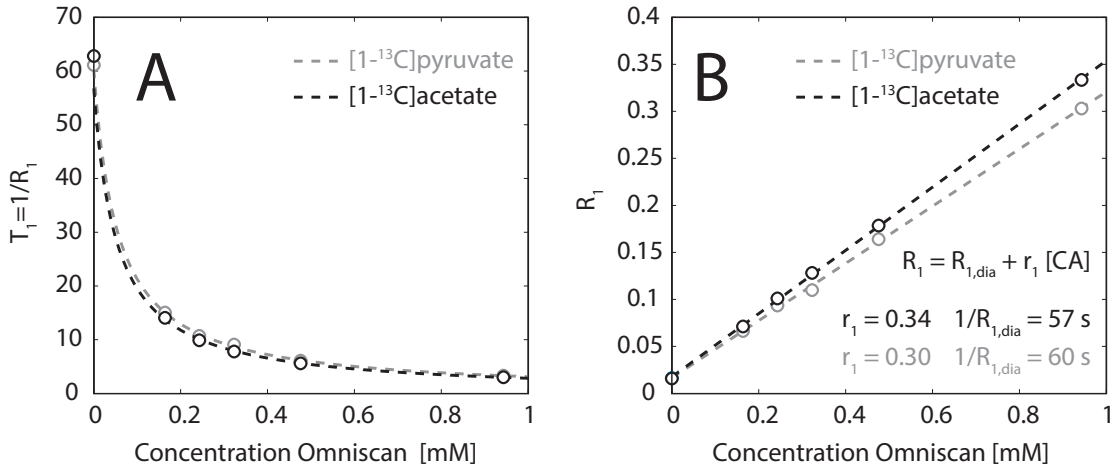


Figure 2.6: (A) Longitudinal relaxation time T_1 measurements of $[1-^{13}\text{C}]$ acetate and $[1-^{13}\text{C}]$ pyruvate in D_2O at 400 MHz at several concentrations of Omniscan. (B) The corresponding relaxation rate $R_1 = 1/T_1$ was calculated and used to determine the relaxivity r . These measurements were performed to determine the Omniscan concentration needed to reduce the T_1 's to such extent that reasonable T_R 's could be employed to measure the hyperpolarized $[1-^{13}\text{C}]$ acetate concentration in the separator infusion pump.

T_1 is described in section 1.2.7. This T_1 relaxation time is needed as an input value in the kinetic model of acetate metabolism in skeletal muscle as described in section 2.3. A small amount of heparin was added to the solution to avoid coagulation.

Data analysis

A non-linear least-squares quantification algorithm, AMARES, as implemented in the jMRUI software package³⁴, was used to fit the ^{13}C NMR data. The spectra were corrected for the phases and DC offset. Soft constraints were imposed to peak frequencies (182.55 - 182.65 ppm for acetate and 173.85 - 173.95 ppm for acetylcarnitine) and line widths (FWHM = 10 - 30 Hz) and the relative phases were fixed to zero. The acetylcarnitine peak areas were normalized to the maximum acetate signal in each experiment to account for varying polarization levels across experiments. The time courses of quantified peak areas were analyzed with the kinetic model described in section 2.3, implemented in Matlab (The MathWorks, Natick, MA, USA).

2.3 Kinetic model of hyperpolarized acetate metabolism in skeletal muscle

The uptake of acetate by skeletal muscle tissue as a function of the arterial concentration is described in^{18;19}. Acetate transport across the cellular membrane occurs by facilitated diffusion, and thus net transport of acetate between the plasma and the tissue depends on

the concentration gradient. We therefore assumed that the measured kinetic parameters are independent of processes related to membrane transport. As a result, the variations in conversion rates as a function of the injected concentration are expected to be directly correlated to ACS and CAT activity.

In the simplest model of a biochemical reaction, the conversion from substrate to product in a tissue can be described with a rate constant k that depends on substrate and enzyme concentrations. The assumption is that the enzyme concentration is not influenced by the substrate in the short time scale of the experiment, which is about 1 minute. Therefore, the ^{13}C (*) label flow between the substrate acetate (Ace) and the metabolites acetylCoA (A.CoA) and acetylcarnitine (A.Car) inside the cytosol of skeletal muscle can be described with the following equations:

$$\frac{d[Ace^*]}{dt} = -V_{ACS} \frac{[Ace^*]}{[Ace]} \quad (2.5)$$

$$\frac{d[A.CoA^*]}{dt} = V_{ACS} \frac{[Ace^*]}{[Ace]} - V_{CAT}^f \frac{[A.CoA^*]}{[A.CoA]} + V_{CAT}^b \frac{[A.Car^*]}{[A.Car]} \quad (2.6)$$

$$\frac{d[A.Car^*]}{dt} = V_{CAT}^f \frac{[A.CoA^*]}{[A.CoA]} - (V_{CAT}^b + V_{OUT}) \frac{[A.Car^*]}{[A.Car]} \quad (2.7)$$

where $[Ace]$, $[A.CoA]$, $[A.Car]$ represent total metabolites concentrations (sum of ^{13}C labeled and unlabeled molecules), $[Ace^*]$, $[A.CoA^*]$, $[A.Car^*]$ the ^{13}C labeled concentrations, V_{CAT}^f and V_{CAT}^b are the forward and the backward fluxes through CAT, respectively, V_{ACS} is the flux through ACS and V_{OUT} is the flux out of the acetylcarnitine pool into the mitochondrion (2.1). Since the physiological plasma acetate concentration is lower than 0.2 mM^5 , it can be assumed that the acetate blood pool was fully labeled following the bolus injection, i.e. $[Ace^*]/[Ace] \approx 1$. Summing Equation 2.6 and 2.7 leads to:

$$\frac{d[A.Car^*]}{dt} + \frac{d[A.CoA^*]}{dt} = V_{ACS} - V_{OUT} \frac{[A.Car^*]}{[A.Car]} \quad (2.8)$$

The acetylCoA pool size is well regulated and is typically more than 10 times smaller than the acetylcarnitine pool¹⁵, i.e. a small pool approximation^{35;36} can be used, therefore $d[A.CoA^*]/dt \ll d[A.Car^*]/dt$. The last term in Equation 2.8 can be neglected since, within the short experimental time frame, the acetylcarnitine pool is only partially labelled and thus a minute amount of ^{13}C label will reach the mitochondrial acetylCoA pool. This is further

supported by a previous study showing that the contribution of acetate to the TCA cycle in skeletal muscle was an order of magnitude smaller than our observed rate of acetylcarnitine formation³⁷. Condensing the previous statements, the ^{13}C flow from acetate to acetylcarnitine in the cytosolic compartment of skeletal muscle can be described by the following two equations:

$$\frac{d[Ace^*]}{dt} = -V_{ACS} = -k_{ACS}[Ace^*](t) \quad (2.9)$$

$$\frac{d[A.Car^*]}{dt} = V_{ACS} = k_{ACS}[Ace^*](t) \quad (2.10)$$

where the kinetic rate constant of ACS is introduced. Based on these conditions, it was concluded that the observed kinetic rate observed in these experiments corresponds to the enzymatic activity of ACS.

The acetate ^{13}C NMR signal measured in skeletal muscle tissue following the injection of hyperpolarized $[1-^{13}\text{C}]\text{acetate}$ decayed with time as a consequence of a combination of (a) the loss of spin polarization related to longitudinal relaxation and characterized by an exponential decay rate R_1 , (b) the loss of longitudinal magnetization due to radiofrequency excitations, and (c) the conversion of acetate into acetylcarnitine characterized by the kinetic rate constant k_{ACS} . The acetylcarnitine signal also decays because of (a) and (b), but (c) leads to an increase in signal. The time evolution of the carbonyl ^{13}C longitudinal magnetization of acetate, M_A , and acetylcarnitine, M_C , can thus be written as:

$$\frac{dM_A}{dt} = -R_A[M_A - M_{A,eq}] - k_{ACS}M_A \quad (2.11)$$

$$\frac{dM_C}{dt} = k_{ACS}M_A - R_{1,C}[M_C - M_{C,eq}] \quad (2.12)$$

where R_A , is the acetate signal decay comprising the carbonyl ^{13}C longitudinal relaxation rate $R_{1,A}$ as well as the potential $[1-^{13}\text{C}]\text{acetate}$ flow of signal in and out of the volume of interest; $R_{1,C}$ is the carbonyl ^{13}C longitudinal relaxation rate of acetylcarnitine: Finally, $M_{A,eq}$ and $M_{C,eq}$ are the thermal equilibrium magnetizations of the carbonyl sites of acetate and acetylcarnitine, respectively. The contributions of $M_{A,eq}$ and $M_{C,eq}$ to the acetate and acetylcarnitine signals can be neglected since $M_A \gg M_{A,eq}$ and $M_C \gg M_{C,eq}$ when the resonances are detectable. Equation 2.11 and 2.12 now become:

$$\frac{dM_A}{dt} = -R_A M_A - k_{ACS} M_A \quad (2.13)$$

$$\frac{dM_C}{dt} = k_{ACS} M_A - R_{1,C} M_C \quad (2.14)$$

These Bloch-McConnell differential equations³⁸ are identical to the ones derived for the one-compartment non steady-state metabolic model for one site exchange, which has already been shown to be applicable to hyperpolarized substrates³⁹. From the initial conditions $M_C(t=0) = 0$ and $M_A(t=0) = M_0$ and taking into account the signal losses due to RF excitations, the hyperpolarized acetate and acetylcarnitine signals, $S_A(t)$ and $S_C(t)$, measured at $t = nT_R$, T_R being the repetition time, are given by:

$$S_A(t) \propto M_A(t)(\cos\theta)^{t/T_R} = M_0 e^{(-k_{ACS}-R_A)t} (\cos\theta)^{t/T_R} \quad (2.15)$$

$$S_C(t) \propto M_C(t)(\cos\theta)^{t/T_R} = M_0 (b e^{(-k_{ACS}-R_A)t} - b e^{-R_{1,C}t}) (\cos\theta)^{t/T_R} \quad (2.16)$$

where

$$b = \frac{k_{ACS}}{-k_{ACS} - R_A + R_{1,C}},$$

and θ is the RF pulse flip angle. The time point of the first acetate observation, which also corresponds to the maximum acetate signal, was set to $t=0$ prior to fitting the data with the kinetic model. To relate the signals measured in the sensitive volume of the surface coil described by Equation 2.15 and 2.16 to the cytosolic concentrations described by Equation 2.8 and 2.9, it was assumed that the blood volume in the VOI was small enough to neglect its contribution to the measured ^{13}C acetate signal. This was supported by anatomical proton images taken prior to the injections and previous PET studies which determined a small blood volume in this area⁴⁰. This assumption is strengthened by a reported acetate removal of 50% by skeletal muscle in a single passage of blood⁵.

The dependence of the reaction kinetics on the hyperpolarized substrate concentration was analyzed using the standard Michaelis-Menten equation,

$$v_{0,ACS} = V_{max}[Ace]/(K_M + [Ace]) \quad (2.17)$$

where K_M and V_{max} are the Michaelis constant and the maximum reaction rate and the initial reaction rate v_0 is the product of the initial acetate concentration and the kinetic rate constant, i.e,

$$v_{0,ACS} = k_{ACS}[Ace]. \quad (2.18)$$

2.4 Mathematical Derivation of the Signal Ratio

It has been observed that there exists a linear relationship between the kinetic rate constants obtained using mathematical modelling and the ratio of the areas of acetylcarnitine and acetate, a linearity also observed in studies using hyperpolarized pyruvate⁴¹. This linearity in case of hyperpolarized acetate was investigated by analysing the system of coupled equations defined by Equation 2.15 and 2.16 which has only 3 free parameters, namely k_{ACS} , R_A and $R_{1,C}$.

The transient magnetization of hyperpolarized acetate and its metabolic product acetylcarnitine can be described as follows:

$$M_A(t) = M_0 e^{(-k_{ACS}-R_A)t} \quad (2.19)$$

$$M_C(t) = M_0 (b e^{(-k_{ACS}-R_A)t} - b e^{-R_{1,C}t}) \quad (2.20)$$

with $b = k_{ACS}/(-k_{ACS} - R_A + R_{1,C})$. Integration of both equations from $t=0$ to infinity results in the following: It is possible to eliminate R_A by integrating the two equations over from $t=0$ to infinity and by taking their relative ratio, yielding the following relationship between the signal ratio and the kinetic rate constant k_{ACS} :

$$\int_0^\infty M_A(t) dt = M_0 \int_0^\infty e^{(-k_{ACS}-R_A)t} dt = M_0 \frac{e^{(-k_{ACS}-R_A)t}}{-k_{ACS}-R_A} \Big|_0^\infty = -\frac{M_0}{k_{ACS} + R_A}$$

$$\int_0^\infty M_C(t) dt = b M_0 \int_0^\infty e^{(-k_{ACS}-R_A)t} dt - b M_0 \int_0^\infty e^{-R_{1,C}t} dt = -\frac{M_0 b}{k_{ACS} + R_A} + \frac{M_0 b}{R_{1,C}}$$

$$\begin{aligned}
\frac{\int_0^\infty M_C(t) dt}{\int_0^\infty M_A(t) dt} &= \frac{-\frac{M_0 b}{k_{ACS} + R_A} + \frac{M_0 b}{R_{1,C}}}{-\frac{M_0}{k_{ACS} + R_A}} = b \left(1 - \frac{k_{ACS}}{R_{1,C}} - \frac{R_A}{R_{1,C}} \right) = \\
&= \left(\frac{k_{ACS}}{-k_{ACS} - R_A + R_{1,C}} \right) \left(\frac{-k_{ACS} - R_A + R_{1,C}}{R_{1,C}} \right) = \frac{k_{ACS}}{R_{1,C}} \\
k_{ACS} &= R_{1,C} \frac{\int_0^\infty M_C(t) dt}{\int_0^\infty M_A(t) dt} \\
&\cong R_{1,C} \frac{\sum_{n=1}^N S_C((n-1)T_R) / \cos\theta^{(n-1)}}{\sum_{n=1}^N S_A((n-1)T_R) / \cos\theta^{(n-1)}} \quad (2.21)
\end{aligned}$$

where $S_C(nT_R)$ and $S_A(nT_R)$ are the signal intensity obtained at the n^{th} of the N acquisitions, corrected for the loss of signal due to the RF pulses for acetylcarnitine and acetate, respectively, by the term $\cos\theta^{(n-1)}$.

2.5 Results

The incorporation of hyperpolarized ^{13}C label into acetylcarnitine was detected in all animals ($n=19$). The average line width of the acetate resonance at 182.6 ppm was 21 ± 6 Hz and that of the acetylcarnitine resonance at 173.9 ppm was 6 ± 1 Hz (2.7).

The first acetate signal measured corresponds to the maximum observed signal which appeared 13.5 ± 2.3 s after the beginning of the injection and no progressive build-up of the signal was observed. The maximum acetylcarnitine signal was detected at a later time, 26.2 ± 3.9 s after the beginning of the injection. The maximal SNR of acetylcarnitine was 10 with zero line broadening and we imposed a minimum SNR threshold of 3 below which the signal was not taken into account for data analysis. In each experiment 1.0 mL of hyperpolarized acetate solution, with a concentration ranging from 40 to 290 mM was injected into the femoral vein. It was estimated that the injected hyperpolarized acetate doses resulted in a plasma acetate concentration ranging from 1.8 to 15.0 mM³³. Using a previously reported relation between plasma and tissue acetate concentration in rat skeletal muscle¹⁸, it was estimated that the tissue acetate concentration ranged from 0.12 to 1 mM.

To determine k_{ACS} from the system of coupled equations defined by Equation 2.11 and 2.12, the longitudinal relaxation time of $[1-^{13}\text{C}]$ acetylcarnitine was set to its *in vitro* value at 9.4 T,

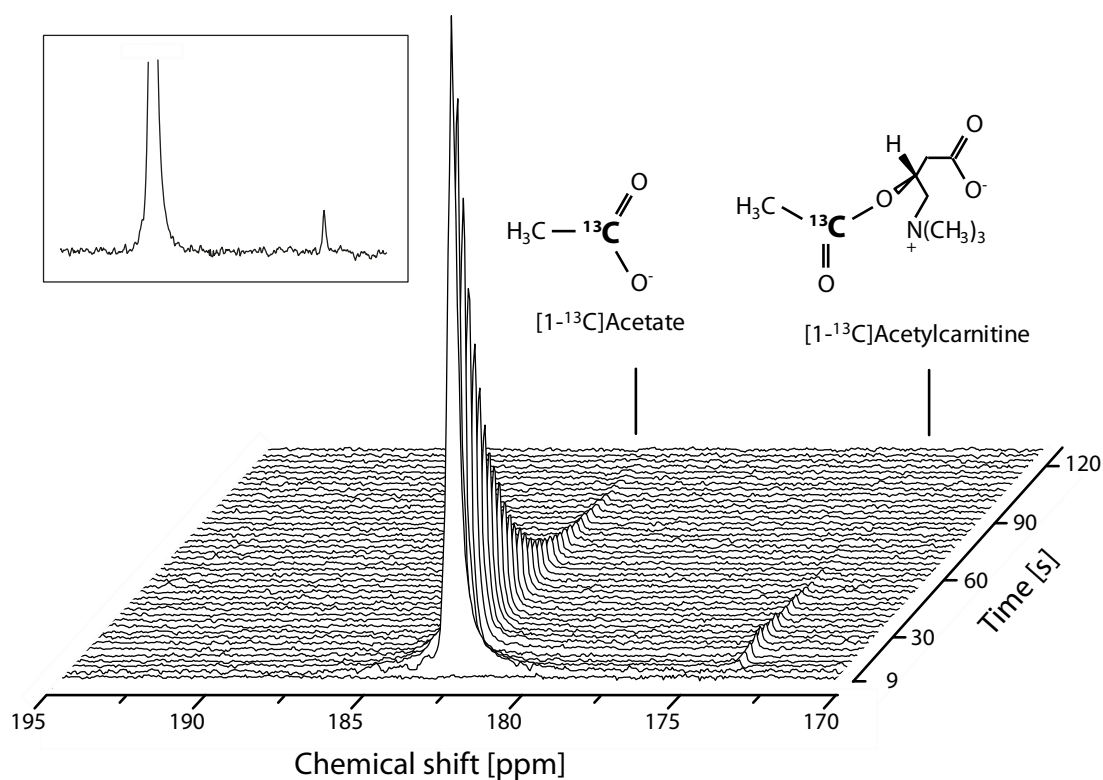


Figure 2.7: Transient ¹³C NMR spectra of hyperpolarized acetate (182.6 ppm) and its metabolic product acetylcarnitine (173.9 ppm) in healthy skeletal muscle in vivo. The transfer of the ¹³C label is catalyzed by the enzymes ACS and CAT. Spectra were acquired every 3 seconds using adiabatic 30° excitation pulses and ¹H decoupling during acquisition, a 1.0 mL solution of a 110 mM hyperpolarized acetate was injected. Inset: summation of the spectra as described in Equation 2.21 which was used to calculate the kinetic rate constants.

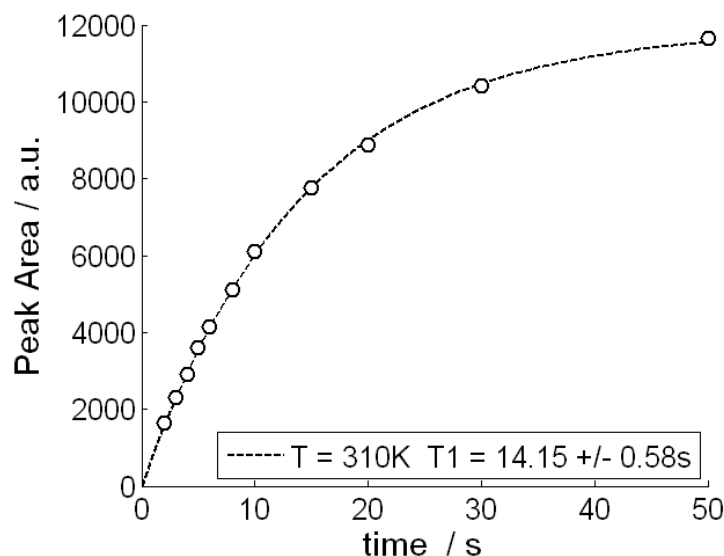


Figure 2.8: Signal integral of $[1-^{13}\text{C}]$ acetylcarnitine in plasma following a saturation recovery experiment. Data of a single measurement are shown.

$T_{1,C} = 1/R_{1,C}$ of 14.9 ± 0.7 s determined in blood at physiological temperature (310 K, 37°C) (Table 2.1, Figure 2.8). The T_1 of acetylcarnitine in D₂O had a value similar to the T_1 in plasma at 310 K. Its T_1 decreases with decreasing temperature (Table 2.1).

The kinetic rate constant k_{ACS} was determined by fitting Equation 2.15 and 2.16 to the time evolution of the acetate and acetylcarnitine signal integrals (Figure 2.9) yielding k_{ACS} and R_A . The observed decay of the acetate signal is mono exponential with a time constant of 16.2 ± 1.4 s. The values of k_{ACS} were determined as a function of the tissue acetate concentration deduced from the infused acetate dose and the animal weight (Figure 2.10). Yielding the initial reaction rates as a function of the tissue acetate concentration, used to derive the Michaelis-Menten kinetic parameters (Figure 2.10): The conversion of acetate into acetylcarnitine was characterized by a Michaelis constant $K_M = 0.35 \pm 0.13$ mM, as obtained with the model and a maximal reaction rate, V_{max} , of 0.199 ± 0.031 $\mu\text{mol/g/min}$. The summation approach estimated a $K_M = 0.32 \pm 0.12$ mM and V_{max} , of 0.190 ± 0.029 $\mu\text{mol/g/min}$.

To further demonstrate that the kinetic rate constant is uniquely determined if the relaxation rate of acetylcarnitine $R_{1,C}$ is fixed, k_{ACS} was calculated for all experiments using Equation 2.21 and plotted them against the kinetic rate constants obtained from the fitting procedure (Figure 2.11). The residual differences are most likely due to the fitting errors inherent to the limited signal-to-noise ratio.

Table 2.1: Longitudinal relaxation times of $[1-^{13}\text{C}]$ acetylcarnitine determined at a magnetic field strength of 9.4 T in plasma and D2O at different temperatures.

| Solvent | T_1 in seconds |
|-------------------------------|------------------|
| Blood T = 310 K (37C) (n = 4) | 14.9 ± 0.7 |
| D2O T=295 (n = 4) | 10.3 ± 0.4 |
| D2O T=305 K (n = 4) | 14.3 ± 0.5 |
| D2O T = 310 (n = 4) K | 15.5 ± 0.5 |

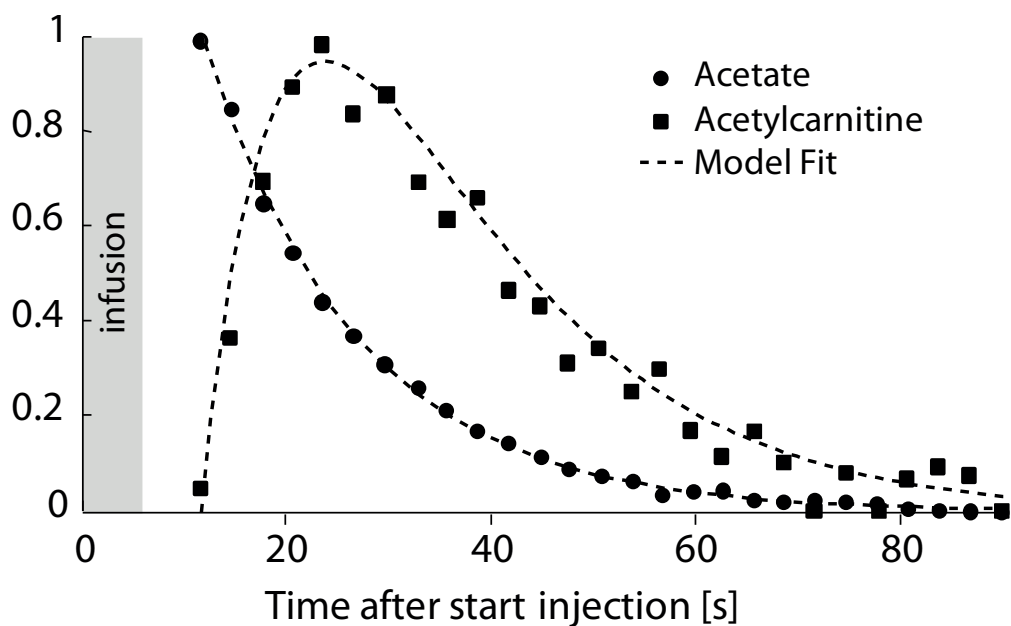


Figure 2.9: Time course of the normalized peak integrals of hyperpolarized acetate and its metabolic product acetylcarnitine. The kinetic model described with Equation 2.15 and 2.16 was used to fit (—) the hyperpolarized time courses to determine the kinetic rate constant k_{ACS} , and the decay rate of acetate R_A . The time courses were normalized to their maximum signal. In the data shown here 1.0 mL of a 110 mM hyperpolarized acetate solution was injected.

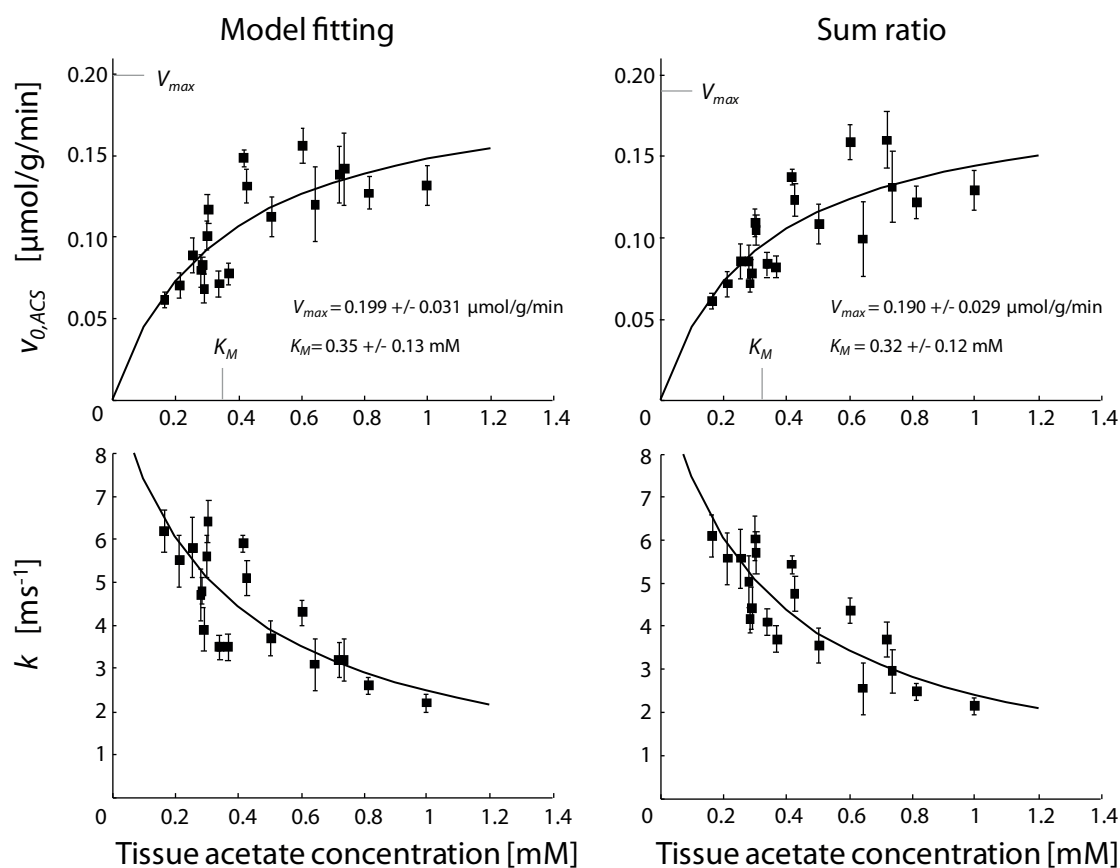


Figure 2.10: The relation between the initial reaction rates $v_{0,ACS}$ (top row) and kinetic rate constants k_{ACS} (bottom row) with the hyperpolarized $[1-^{13}\text{C}]$ acetate concentration. Every hyperpolarized experiment provided one kinetic rate constant k_{ACS} () and associated standard deviation as derived from the fit to the kinetic model (left column) or using the summation approach (right column). The initial reaction rate was obtained by multiplying the fitted kinetic rate constant k_{ACS} with the corresponding substrate concentration. Michaelis-Menten parameter fits are represented by the dashed line. Using model fitting a K_M of 0.35 ± 0.13 mM and V_{max} of 0.199 ± 0.031 $\mu\text{mol/g/min}$ were estimated. Using the summation approach a K_M of 0.32 ± 0.12 mM and V_{max} of 0.190 ± 0.029 $\mu\text{mol/g/min}$ was obtained.

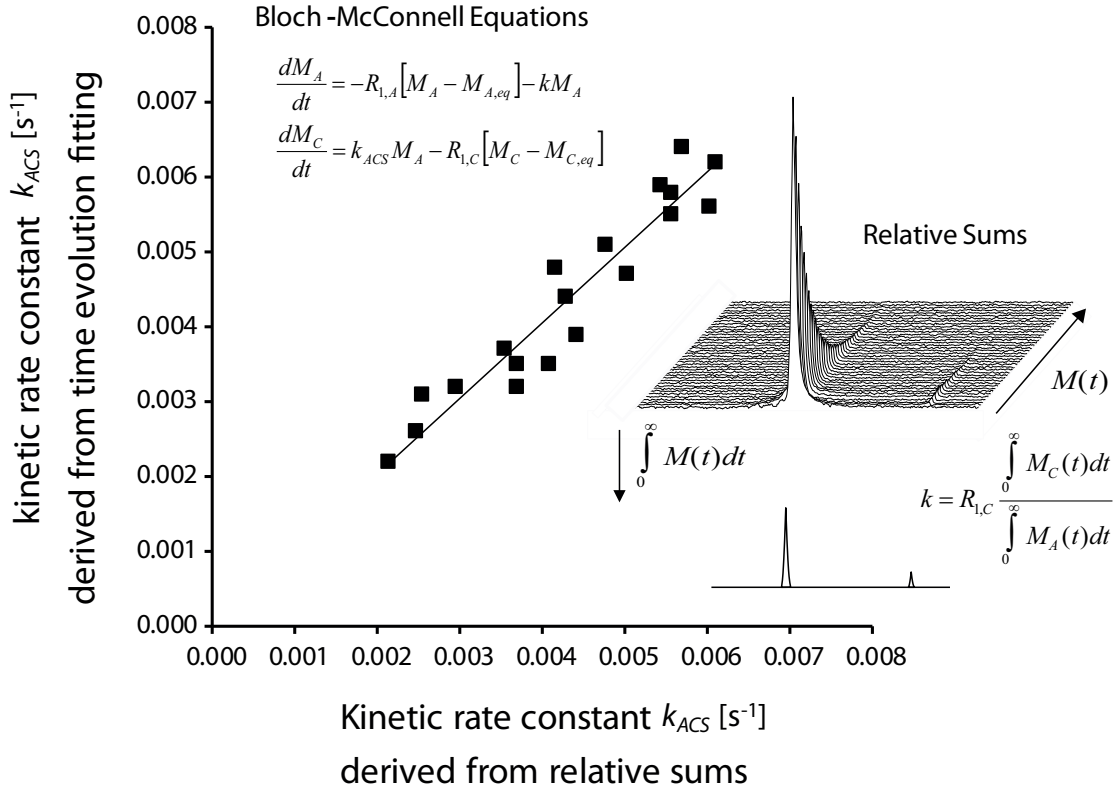


Figure 2.11: The linear relationship between the kinetic rate constants k_{ACS} obtained with mathematical modeling of the metabolite time courses and the ratio of the sum of RF corrected peak integrals of acetylcarnitine $C(t)$ and acetate $A(t)$ was used to calculate an integral derived kinetic rate constant (Equation 2.21). The integral derived kinetic rate constant equals the integral ratio times the longitudinal relaxation rate of acetylcarnitine $R_{1,C}$. The relationship between the kinetic rate constants derived from the metabolic model versus the kinetic rate constants derived using the relative areas of hyperpolarized acetylcarnitine and acetate are shown below.

2.6 Discussion

The present study demonstrates that kinetic rates for the conversion of acetate to acetylcarnitine can be derived from *in vivo* hyperpolarized magnetic resonance experiments and that these rates are in very good agreement with the ones determined in *in vitro* experiments. The plasma acetate concentrations used in the current study (1.8 - 15.1 mM) have been previously shown to linearly scale with the uptake of acetate in skeletal muscle tissue and thus with the cellular acetate concentration^{18;19}. This implies that the kinetic parameters extracted from the *in vivo* real-time measurements presented herein are independent of processes related to membrane transport since acetate uptake by resting skeletal muscle is proportional to the arterial concentration. Therefore, the variations in conversion rates as a function of the injected concentration are thus directly correlated to the biochemical transformations regulated by ACS and CAT in the cytosol. CAT also resides in the mitochondria where it converts acetylcarnitine back into acetylCoA followed by entry into the TCA cycle (2.1).

The tissue concentrations used in the present study (0.12 - 1.00 mM) were approximately an order of magnitude lower than those used to maximally acetylate free carnitine and CoA in canine skeletal muscle¹⁶ and human skeletal muscle at rest⁴²⁻⁴⁴. This indicates that the observed acetylcarnitine formation was not hindered by a decrease in carnitine availability to CAT. The observed kinetic rate constants range from 2 to 6 ms⁻¹, showing that substrate concentration is an important parameter to take into account while designing a study using hyperpolarized acetate as a metabolic tracer. It was also observed that this conversion is not saturated even at a tissue concentration of acetate as high as 1 mM.

Our analysis based on the assumption that, during the experimental time frame, the acetate pool is fully labeled and the time variation of the acetylCoA pool labeling is much smaller than the one of acetylcarnitine led to the conclusion that the kinetic rates corresponds to the conversion rate associated with the enzyme acetylCoA synthetase. This is further supported by the fact that the transformation catalyzed by ACS is the rate-limiting step in the transformation of acetate into acetylcarnitine⁴. It needs to be mentioned that the reaction through ACS is irreversible and there is no direct exchange between acetate and acetylcarnitine. Previous reported ACS activity suggested an *in vitro* K_M of 0.2 mM for acetate²¹. Following acetate infusions in rat and sheep, the Michaelis constant for acetate in the ACS reaction was between 0.28 and 0.39 mM, based on tissue extracts, with no marked differences between species, tissue or the intracellular location of the enzyme activity⁵. These values of K_M are in agreement with our observed Michaelis constant.

Based on the linear relationship between the ratio of signal integrals and the kinetic rate constants, two approaches were used to extract k_{ACS} from the data: One was based on time evolution fitting of the signal integrals (Equation 2.15 and 2.16) and the other on the relative ratio of the sum of both substrate and product (Equation 2.21). Note that, while the first requires the use of mathematical modeling, the summation approach is simpler but less accurate because each individual spectrum has to be divided by a factor of according to

Equation 2.21, where n is the acquisition number, leading to an increase in noise error propagation, whereas the fit of the time series takes into account the RF decay and only relies on raw data where the weight of the noise is not changed. Other approaches based on mathematical modeling of the metabolic time course were previously proposed to determine the conversion rates from hyperpolarized ^{13}C labeled pyruvate to its downstream metabolites^{39;45;46}.

Acetylcarnitine ^{13}C labeling in the heart has been previously reported following the infusion of hyperpolarized $[2-^{13}\text{C}]$ pyruvate^{27;28}, but unlike pyruvate, acetate is independent of PDH flux. The utilization of acetate by the TCA cycle is strictly aerobic and depending on the delivery of both acetate and oxygen⁵, the conversion rate constants are expected to be strongly dependent on the oxygenation of the tissue under investigation and TCA cycle activity: It was previously shown that intense muscle activity lead to an accumulation of acetylcarnitine¹⁰, and that a decreased exchange between acetylcarnitine and acetate was a relevant marker for ischemia²⁶. The possibility to monitor the acetylcarnitine kinetics *in vivo* in a measurement window of one minute in a non-invasive manner and the extraction of specific enzymatic activities can be expected to be a valuable tool for differentiating between healthy and pathological metabolism, in particular since the conversion rate regulated by ACS is implicated in disorders like diabetes⁴⁷ or cancer⁴⁸.

2.7 Incorporation of a substrate build-up in the kinetic model

All experimental observations in this chapter show a jump in the acetate signal from 0 to its maximum in a time frame consisting of one T_R , while its metabolic product, acetylcarnitine is observed at a later time point. Our metabolic modeling approach used in this study was chosen based on the assumption of an instantaneous distribution of the acetate and fitting of the the metabolic time courses started at the maximum observed acetate signal. This approach ignores a potential acetate build up within 3 s, one T_R , before the maximum is observed.

In this section was investigated whether the incorporation of an exponential substrate build-up influences the estimation of the kinetic rate constant k_{ACS} . More precisely, the model would incorporate an acetate signal increase from 0 to its maximum during a single T_R .

Metabolic time courses of acetate and acetylcarnitine were simulated for a range of exponential build up rates B and kinetic rate constants k_{ACS} . The differential equations for the build up and decay of both acetate and acetylcarnitine can be described by:

$$\frac{dM_A}{dt} = B e^{-Bt} - k_{ACS} M_A - R_A M_A \quad (2.22)$$

$$\frac{dM_C}{dt} = k_{ACS} M_A - R_{1,C} M_C \quad (2.23)$$

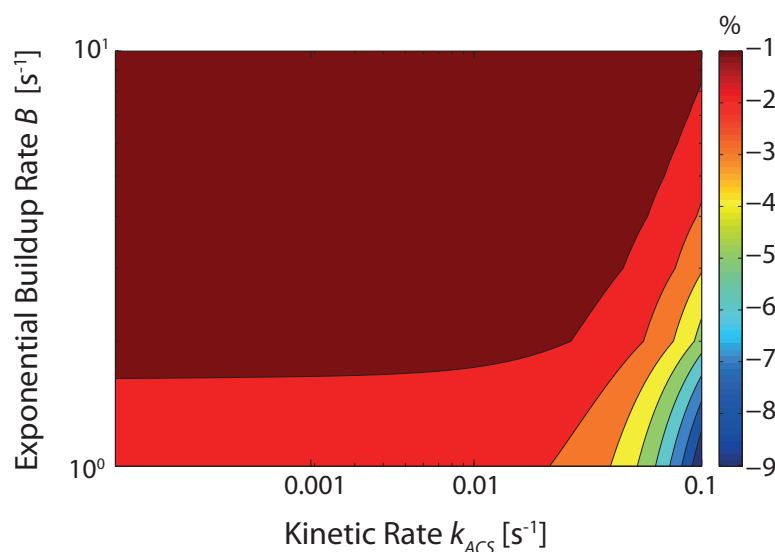


Figure 2.12: Influence of the incorporation of an acetate build up on the estimation of k_{ACS} . Simulations were performed for a range of kinetic rate constants k_{ACS} and build up rates B to determine the influence on the formation of acetylcarnitine and resulting fitting errors with the model described by Equation 2.16 which assumes an instant distribution of acetate.

Note that these are similar to Equations 2.13 and 2.14 with addition of an exponential build up B for acetate. During simulations the initial conditions were set to $M_C(t = 0) = 0$ and $M_A(t = 0) = 0$. The simulated data set of acetylcarnitine, $M_C(t)$, was subsequently fitted to the analytical solution of $M_C(t)$ (given by equation 2.16) which assumes an instant distribution of acetate. The error percentage between the simulated and fitted k_{ACS} was calculated for a range of build up rates and kinetic rate constants.

The simulation showed that in the range of our observed kinetic rate constants, between 0.01 and 0.001 ms^{-1} , the error on the estimation of k_{ACS} is about 1%. It can be seen that for substrates undergoing faster enzymatic conversion, i.e., larger kinetic rates, inclusion of a build up parameter is necessary to avoid errors in the estimation of the rate constant.

2.8 Independence and sensitivity of fitting parameters k_{ACS} and R_A

In order to characterize the enzymatic activity of ACS, a mathematical model with two free parameters, k_{ACS} and R_A , was used to fit the metabolite time courses of $[1-^{13}\text{C}]$ acetylcarnitine and $[1-^{13}\text{C}]$ acetate. Since the analytical solutions of both time courses consist of several exponentials and the rate constant R_A appears in both equations, there exists a correlation between the two parameters. By using correlation matrixes it can be investigated to what extend both parameters are dependent on each other. If both parameters are highly dependent, several combinations of k_{ACS} and R_A values can result in a good line fit of the data, meaning

that a change in one parameter will affect the other directly. Correlation matrices were calculated for all experiments and an average correlation between k_{ACS} and R_A was found to be 0.15.

Additionally, a sensitivity analysis was performed to investigate the sensitivity of each fitted parameter to the metabolite time courses. Such an analysis gives insight in how reliable and stable the fitted parameters are to changes in the metabolite time courses and to what extend the estimated values can be trusted.

After model fitting of the metabolite time courses, the estimated values of k_{ACS} and R_A were obtained. Simulations were performed using the same equations, the analytical solutions given earlier, as to which the data was fitted. In these simulations, one of the estimated parameters k_{ACS} or R_A were fixed while the other was varied stepwise to change from -50% to +50% the estimated value. The simulated metabolite time courses were overlain with the data and with the fit to the data for comparison (Figure 2.13).

It can be seen that the value of the kinetic rate constant k_{ACS} is very sensitive, meaning that small changes in its value affect the final time course of acetylcarnitine tremendously. This means that the fitting of k_{ACS} is relatively stable. On the other hand, a change in the decay rate of acetate R_A does not affect the simulated time course meaning that this parameter is very insensitive.

2.9 Conclusion

The conversion rates from hyperpolarized acetate into acetylcarnitine can be quantified *in vivo*, and although separated by two enzymatic reactions, these rates define uniquely the activity of acetylCoA synthetase. It was further shown that these rates can be obtained using either fitting of time courses, or an analysis based on time course integration, both approaches yielded similar enzymatic activity. This study showed the feasibility of measuring the activity of acetylCoA synthetase *in vivo*.

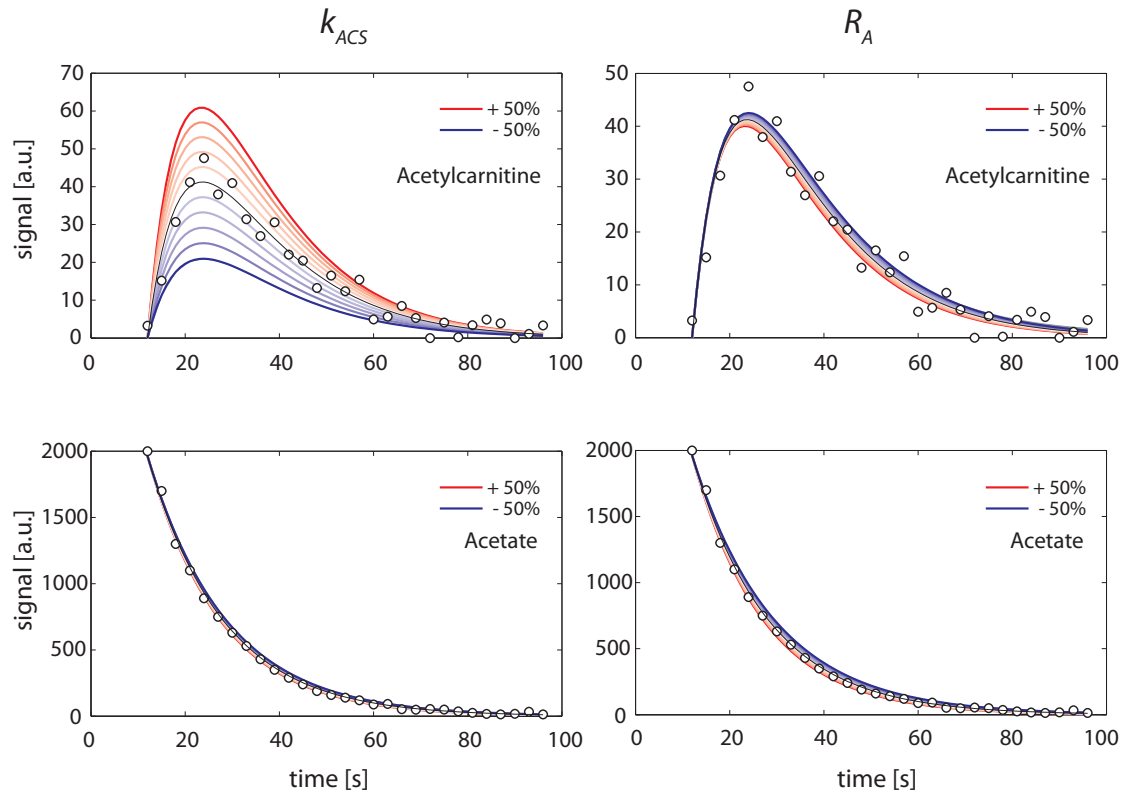


Figure 2.13: Simulation of the sensitivity of the fitting parameters k_{ACS} and R_A for changes in their estimated value. Time courses of the peak integrals of hyperpolarized acetate (bottom row) and its metabolic product acetylcarnitine (top row) are shown as function of time indicated with the circles. The fit to the metabolic model is shown with the black line. The two parameters which were fitted were changed up to 50% their estimated value (red) or less than 50% their estimated value (blue), and resulting time courses were simulated using the same equations.

References

- [1] E. N. Bergman. Energy contributions of volatile fatty acids from the gastrointestinal tract in various species. *Physiol Rev*, 70(2):567–90, 1990.
- [2] E. D. Mayfield, A. Bensadoun, and B. C. Johnson. Acetate metabolism in ruminant tissues. *J Nutr*, 89(2):189–96, 1966.
- [3] P. Vinay, M. Prud'Homme, B. Vinet, G. Cournoyer, P. Degoulet, M. Leville, A. Gougoux, G. St-Louis, L. Lapierre, and Y. Piette. Acetate metabolism and bicarbonate generation during hemodialysis: 10 years of observation. *Kidney Int*, 31(5):1194–204, 1987.
- [4] C. Barth, M. Sladek, and K. Decker. Dietary changes of cytoplasmic acetyl-coa synthetase in different rat tissues. *Biochimica Et Biophysica Acta*, 260(1):1–9, 1972.
- [5] S. E. Knowles, I. G. Jarrett, O. H. Filsell, and F. J. Ballard. Production and utilization of acetate in mammals. *Biochemical Journal*, 142(2):401–411, 1974.
- [6] P. M. L. Robitaille, D. P. Rath, A. M. Abduljalil, J. M. Odonnell, Z. C. Jiang, H. Z. Zhang, and R. L. Hamlin. Dynamic c-13 nmr analysis of oxidative-metabolism in the in-vivo canine myocardium. *Journal of Biological Chemistry*, 268(35):26296–26301, 1993.
- [7] H. Sone, L. Shimano, N. Inoue, Y. Sakakura, M. Amemiya, A. Takahashi, M. Osawa, A. Iwama, and N. Yamada. Acetyl-coenzyme a synthetase is a new lipogenic enzyme controlled by sterol regulatory element-binding proteins and influenced by diabetes. *Diabetes*, 50:A407–A407, 2001.
- [8] A. L. Carter, D. L. Lennon, and F. W. Stratman. Increased acetyl carnitine in rat skeletal muscle as a result of high-intensity short-duration exercise. implications in the control of pyruvate dehydrogenase activity. *FEBS Lett*, 126(1):21–4, 1981.
- [9] C. C. Childress, B. Sacktor, and D. R. Traynor. Function of carnitine in the fatty acid oxidase-deficient insect flight muscle. *Journal of Biological Chemistry*, 242(4):754–60, 1967.
- [10] F. B. Stephens, D. Constantin-Teodosiu, and P. L. Greenhaff. New insights concerning the role of carnitine in the regulation of fuel metabolism in skeletal muscle. *J Physiol*, 581(Pt 2):431–44, 2007.
- [11] R. R. Ramsay and V. A. Zammit. Carnitine acyltransferases and their influence on coa pools in health and disease. *Mol Aspects Med*, 25(5-6):475–93, 2004.
- [12] J. Bremer. Carnitine - metabolism and functions. *Physiological Reviews*, 63(4):1420–1480, 1983.
- [13] I. B. Fritz, S. K. Schultz, and P. A. Srere. Properties of partially purified carnitine acetyl-transferase. *Journal of Biological Chemistry*, 238(7):2509, 1963.
- [14] D. J. Pearson and P. K. Tubbs. Carnitine and derivatives in rat tissues. *Biochemical Journal*, 105(3):953–963, 1967.
- [15] L. L. Spriet, D. J. Dyck, G. Cederblad, and E. Hultman. Effects of fat availability on acetyl-coa and acetylcarnitine metabolism in rat skeletal muscle. *Am J Physiol*, 263(3 Pt 1):C653–9, 1992.
- [16] P. A. Roberts, S. J. G. Loxham, S. M. Poucher, D. Constantin-Teodosiu, and P. L. Greenhaff. Acetyl-coa provision and the acetyl group deficit at the onset of contraction in ischemic canine skeletal muscle. *American Journal of Physiology-Endocrinology and Metabolism*, 288(2):E327–E334, 2005.

-
- [17] E. Ciaranfi and A. Fonnesu. Time-course of injected acetate in normal and depancreatized dogs. *Biochemical Journal*, 57(1):171–175, 1954.
- [18] N. Karlsson, E. Fellenius, and K. H. Kiessling. The metabolism of acetate in the perfused hind-quarter of the rat. *Acta Physiol Scand*, 93(3):391–400, 1975.
- [19] B. Mittendorfer, L. S. Sidossis, E. Walser, D. L. Chinkes, and R. R. Wolfe. Regional acetate kinetics and oxidation in human volunteers. *American Journal of Physiology-Endocrinology and Metabolism*, 274(6):E978–E983, 1998.
- [20] L. A. Bertocci, J. G. Jones, C. R. Malloy, R. G. Victor, and G. D. Thomas. Oxidation of lactate and acetate in rat skeletal muscle: Analysis by c-13-nuclear magnetic resonance spectroscopy. *Journal of Applied Physiology*, 83(1):32–39, 1997.
- [21] Leslie T. Webster Jr. [58] *Acetyl-CoA synthetase*, volume Volume 13, pages 375–381. Academic Press, 1969.
- [22] R. Gruetter. In vivo c-13 nmr studies of compartmentalized cerebral carbohydrate metabolism. *Neurochemistry International*, 41(2-3):143–154, 2002.
- [23] J. H. Ardenkjaer-Larsen, B. Fridlund, A. Gram, G. Hansson, L. Hansson, M. H. Lerche, R. Servin, M. Thaning, and K. Golman. Increase in signal-to-noise ratio of > 10,000 times in liquid-state nmr. *Proc Natl Acad Sci U S A*, 100(18):10158–10163, 2003.
- [24] K. Golman, R. in't Zandt, and M. Thaning. Real-time metabolic imaging. *Proc Natl Acad Sci U S A*, 103(30):11270–11275, 2006.
- [25] J. Kurhanewicz, D. B. Vigneron, K. Brindle, E. Y. Chekmenev, A. Comment, C. H. Cunningham, R. J. DeBerardinis, G. G. Green, M. O. Leach, S. S. Rajan, R. R. Rizi, B. D. Ross, W. S. Warren, and C. R. Malloy. Analysis of cancer metabolism by imaging hyperpolarized nuclei: Prospects for translation to clinical research. *Neoplasia*, 13(2):81–97, 2011.
- [26] P. R. Jensen, T. Peitersen, M. Karlsson, R. In 't Zandt, A. Gisselsson, G. Hansson, S. Meier, and M. H. Lerche. Tissue-specific short chain fatty acid metabolism and slow metabolic recovery after ischemia from hyperpolarized nmr in vivo. *Journal of Biological Chemistry*, 284(52):36077–82, 2009.
- [27] H. J. Atherton, M. S. Dodd, L. C. Heather, M. A. Schroeder, J. L. Griffin, G. K. Radda, K. Clarke, and D. J. Tyler. Role of pyruvate dehydrogenase inhibition in the development of hypertrophy in the hyperthyroid rat heart a combined magnetic resonance imaging and hyperpolarized magnetic resonance spectroscopy study. *Circulation*, 123(22):2552–U134, 2011.
- [28] M. A. Schroeder, H. J. Atherton, M. S. Dodd, P. Lee, L. E. Cochlin, G. K. Radda, K. Clarke, and D. J. Tyler. The cycling of acetyl-coenzyme a through acetylcarnitine buffers cardiac substrate supply a hyperpolarized c-13 magnetic resonance study. *Circulation-Cardiovascular Imaging*, 5(2):201–U82, 2012.
- [29] A. Comment, B. van den Brandt, K. Uffmann, F. Kurdzesau, S. Jannin, J. A. Konter, P. Hautle, W. Th. Wenckebach, R. Gruetter, and J. J. van der Klink. Design and performance of a dnp prepolarizer coupled to a rodent mri scanner. *Concepts in Magnetic Resonance Part B: Magnetic Resonance Engineering*, 31B(4):255–269, 2007.
- [30] S. Jannin, A. Comment, F. Kurdzesau, J. A. Konter, P. Hautle, B. van den Brandt, and J. J. van der Klink. A 140 ghz prepolarizer for dissolution dynamic nuclear polarization. *J Chem Phys*, 128(24):241102, 2008.
- [31] Tian Cheng, Mor Mishkovsky, Jessica A. M. Bastiaansen, Olivier Ouari, Patrick Hautle, Paul Tordo, Ben van den Brandt, and Arnaud Comment. Method to minimize and monitor in situ the polarization losses in hyperpolarized biomolecules prior to in vivo mr

- experiments. *Nmr in Biomedicine - In Press*, 2013.
- [32] R. Gruetter and I. Tkac. Field mapping without reference scan using asymmetric echo-planar techniques. *Magnetic Resonance in Medicine*, 43(2):319–323, 2000.
 - [33] H. B. Lee and M. D. Blafox. Blood volume in the rat. *J Nucl Med*, 26(1):72–6, 1985.
 - [34] A. Naressi, C. Couturier, J. M. Devos, M. Janssen, C. Mangeat, R. de Beer, and D. Graveron-Demilly. Java-based graphical user interface for the mrui quantitation package. *MAGMA*, 12(2-3):141–52, 2001.
 - [35] K. Uffmann and R. Gruetter. Mathematical modeling of c-13 label incorporation of the tca cycle: The concept of composite precursor function. *Journal of Neuroscience Research*, 85(15):3304–3317, 2007.
 - [36] João M.N. Duarte, Bernard Lanz, and Rolf Gruetter. Compartmentalised cerebral metabolism of [1,6-13c]glucose determined by in vivo 13c nmr spectroscopy at 14.1 t. *Frontiers in Neuroenergetics*, 3, 2011.
 - [37] D. E. Befroy, K. F. Petersen, S. Dufour, G. F. Mason, R. A. de Graaf, D. L. Rothman, and G. I. Shulman. Impaired mitochondrial substrate oxidation in muscle of insulin-resistant offspring of type 2 diabetic patients. *Diabetes*, 56(5):1376–1381, 2007.
 - [38] H. M. McConnell. Reaction rates by nuclear magnetic resonance. *Journal of Chemical Physics*, 28(3):430–431, 1958.
 - [39] S. E. Day, M. I. Kettunen, F. A. Gallagher, D. E. Hu, M. Lerche, J. Wolber, K. Golman, J. H. Ardenkjaer-Larsen, and K. M. Brindle. Detecting tumor response to treatment using hyperpolarized (13)c magnetic resonance imaging and spectroscopy. *Nat Med*, 13(11):1382–1387, 2007.
 - [40] M. Mizuno, Y. Kimura, T. Iwakawa, K. Oda, K. Ishii, K. Ishiwata, Y. Nakamura, and I. Mu-raoka. Regional differences in blood volume and blood transit time in resting skeletal muscle. *Japanese Journal of Physiology*, 53(6):467–470, 2003.
 - [41] Deborah K. Hill, Erika Mariotti, Matthew R. Orton, Jessica K. R. Boulton, Yann Jamin, Simon P. Robinson, Nada M. S. Al-Saffar, Martin O. Leach, Yuen-Li, Chung, and Thomas R. Eykyn. Model free approach to kinetic analysis of real-time hyperpolarised 13c mrs data. In *Proc. Intl. Soc. Mag. Reson. Med.* 20, page 1738, 2012.
 - [42] M. K. Evans, I. Savasi, G. J. F. Heigenhauser, and L. L. Spriet. Effects of acetate infusion and hyperoxia on muscle substrate phosphorylation after onset of moderate exercise. *American Journal of Physiology-Endocrinology and Metabolism*, 281(6):E1144–E1150, 2001.
 - [43] R. A. Howlett, G. J. F. Heigenhauser, and L. L. Spriet. Skeletal muscle metabolism during high-intensity sprint exercise is unaffected by dichloroacetate or acetate infusion. *Journal of Applied Physiology*, 87(5):1747–1751, 1999.
 - [44] C. T. Putman, L. L. Spriet, E. Hultman, D. J. Dyck, and G. J. Heigenhauser. Skeletal muscle pyruvate dehydrogenase activity during acetate infusion in humans. *Am J Physiol*, 268(5 Pt 1):E1007–17, 1995.
 - [45] M. L. Zierhut, Y. F. Yen, A. P. Chen, R. Bok, M. J. Albers, V. Zhang, J. Tropp, I. Park, D. B. Vigneron, J. Kurhanewicz, R. E. Hurd, and S. J. Nelson. Kinetic modeling of hyperpolarized (13)c(1)-pyruvate metabolism in normal rats and tramp mice. *Journal of Magnetic Resonance*, 202(1):85–92, 2010.
 - [46] T. Xu, D. Mayer, M. Gu, Y. F. Yen, S. Josan, J. Tropp, A. Pfefferbaum, R. Hurd, and D. Spielman. Quantification of in vivo metabolic kinetics of hyperpolarized pyruvate in rat kidneys using dynamic c-13 mrsi. *Nmr in Biomedicine*, 24(8):997–1005, 2011.

- [47] Kornacker, M. and Lowenstein, J. M. Citrate and conversion of carbohydrate into fat - activities of citrate-cleavage enzyme and acetate thiokinase in livers of starved and re-fed rats. *Biochemical Journal*, 94(1):209–215, 1965.
- [48] Y. Yoshii, T. Furukawa, H. Yoshii, T. Mori, Y. Kiyono, A. Waki, M. Kobayashi, T. Tsujikawa, T. Kudo, H. Okazawa, Y. Yonekura, and Y. Fujibayashi. Cytosolic acetyl-coa synthetase affected tumor cell survival under hypoxia: the possible function in tumor acetyl-coa/acetate metabolism. *Cancer Science*, 100(5):821–827, 2009.

In vivo real time cardiac metabolism using hyperpolarized acetate

3

Abstract

The heart relies on continuous energy production via the Krebs cycle and imbalances herein impair cardiac functioning directly. Advances in hyperpolarized ^{13}C magnetic resonance have provided the means to measure normal and pathological metabolism in tissues in real-time. Unlike in skeletal muscle, fatty acids are the preferred substrates for oxidation in the myocardium. Since the heart has a large ventricular blood pool, substrate location impairs characterization of absolute rate constants. The aim of this study was to develop methods for hyperpolarized cardiac ^{13}C spectroscopy, investigate short chain fatty acid metabolism in the healthy heart *in vivo* and construct a kinetic modeling approach which is independent of the injected substrate.

In this study, $[1-^{13}\text{C}]$ acetate was dynamically polarized and injected intravenously in healthy animals. The propagation of ^{13}C label from the carboxyl groups of acetate, acetylcarnitine and citrate could be measured using hyperpolarized ^{13}C MRS *in vivo* in real time in the beating rat heart. The substantial spectral resolution at 9.4T and a triggered shimming and NMR acquisition protocol allowed for the detection of citrate for the first time *in vivo* after injection of hyperpolarized $[1-^{13}\text{C}]$ acetate.

Adapted from

In vivo real time cardiac metabolism using hyperpolarized acetate

Jessica AM Bastiaansen, Tian Cheng, Rolf Gruetter, Arnaud Comment

Presented at: Proc. Intl. Soc. Mag. Reson. Med. 20, 5137 (2012)

Manuscript in preparation

3.1 Introduction

Fatty acids are the preferred substrates for myocardial oxidation and fluxes in biochemical pathways in the heart are abnormal in many forms of heart disease. Acetate, with a 2C carbon chain is a short chain fatty acid and its uptake occurs by simple diffusion, and thus exchange of acetate between plasma and tissue only depends on the concentration gradient¹. This fatty acid is an effective oxidizable substrate and can be formed endogenously from acetylCoA via acetylCoA synthetase and acetylCoA hydrolase both present in cytosol and mitochondria, and also from ethanol². Acetate has been a successful tracer in assessing myocardial oxidative metabolism in PET³ and MRS^{4;5} and has been suggested as a marker of myocardial viability. Simultaneous uptake and release of acetate indicate rapid intracellular exchange of acetate with the intracellular acetylCoA pool, as seen in humans¹, dogs^{6;7} and rat livers⁸.

After extraction from plasma (Figure 3.1), acetate is activated to acetylCoA (Equation 2.1) which crosses the mitochondrial membrane as acetylcarnitine (Equation 2.2) through the carnitine shuttle complex after which it enters the TCA cycle as citrate via an irreversible condensation with oxaloacetate^{9;10} which is catalyzed by citrate synthase (CS):



After incorporation into different TCA cycle intermediates, ¹³C labeling equilibrates very rapidly with aspartate and glutamate¹¹. It was suggested that the shuttling of acetylcarnitine to the mitochondria, which is a carnitine/acetylcarnitine exchange process mediated by acetylcarnitine translocase (ATL) is not rate-limiting for carnitine promoted processes within the mitochondria^{12–14}.

The formation of acetylCoA and acetylcarnitine, an important shuttle and buffer of acetyl groups, was previously detected in vivo after the infusion of hyperpolarized acetate^{15;16}. The use of hyperpolarized acetate as a substrate for fatty acid metabolism in resting skeletal muscle studies is described in the previous chapter. It was shown that the rate of acetylcarnitine formation reflects that of the enzyme acetylCoA synthetase.

The dynamical aspect of ¹³C NMR in vivo and its chemical shift range provides additional capacity to obtain kinetic information compared with ¹H MRS. However, labeling of TCA cycle intermediates are rarely detected in vivo because of their inherent low concentrations. Therefore, intermediate metabolic reactions taking place before the ¹³C labeling of the glutamate pool are in general overlooked, since they cannot be measured. Glutamate is labeled through an isotopic exchange with the TCA cycle intermediate α -ketoglutarate. Nevertheless, the ¹³C labeling of glutamate is often used as a measure for the labeling of TCA cycle intermediates¹⁷, and an interpretation which is supported by the fact that the exchange rate between α -ketoglutarate and glutamate is equal to or higher than the TCA cycle rate¹¹. Based on these observations, glutamate ¹³C labeling is used as a marker for estimating TCA cycle rates.

Hyperpolarized ^{13}C MRS via dissolution DNP¹⁸ increases the sensitivity of the ^{13}C nucleus by several orders of magnitude and allows for the detection of intermediate reactions involving TCA cycle intermediates. Hyperpolarized ^{13}C MRS has provided unique insights into important questions regarding myocardial functioning and allows for the study of fast biochemical processes and enzymatic pathways and gives the ability to differentiate between normal and pathological metabolism in the heart^{15;19–21}.

Here we report the measurement of the ^{13}C label transfer from hyperpolarized $[1-^{13}\text{C}]\text{acetate}$ into $[1-^{13}\text{C}]\text{acetylcarnitine}$ and $[5-^{13}\text{C}]\text{citrate}$, a TCA cycle intermediate, in cardiac muscle *in vivo*. A kinetic analysis of the observed metabolic reactions was performed using a modeling approach which is independent of the injected substrate. The TCA cycle intermediate citrate could be detected at high field using gated shimming after injection of hyperpolarized acetate. The conversion of acetylcarnitine to citrate can be used as an estimate of the TCA cycle rate. Since particular conversion patterns were observed in diseased tissue, the proposed method may aid in targeting regions of pathology for biopsy or focal therapy and/or better characterize the extent or aggressiveness of disease present prior to or after treatment.

3.2 Methods

The sample preparation and hyperpolarization protocol of $[1-^{13}\text{C}]\text{acetate}$ is identical to the *in vivo* skeletal muscle studies performed earlier and are described in section 2.2.

3.2.1 Cardiac triggering for MR imaging and spectroscopy

In MR spectroscopy and imaging a homogeneous field and a steady sample is required. Motion of the sample or tissue during data-acquisition distorts the MR images and results in broader line widths in MR spectra. Heart muscle is in continuous motion which makes MR spectroscopy and imaging challenging. Shimming, used to obtain a homogeneous field needs to be well-timed at specific points in the cardiac cycle, as well as the MR measurements. Using sequences which are triggered at specific phases in the cardiac cycle aid in the measurement of the same time point and spatial location of the voxel of interest²². To measure the cardiac motion several physiological markers can be used (Figure 3.2).

Common techniques are the application of electrodes to measure the electrocardiogram (ECG) or measurement of the arterial blood pressure by insertion of a pressure sensor in the artery. The blood pressure is a more stable and reliable signal compared to ECG since experiments are performed at high magnetic fields which distort the ECG signal. Since experiments were performed in rats, the arterial blood pressure was chosen as a means to monitor the heart rate and generate a cardiac trigger signal. In mice, measurement of arterial blood pressure is challenging and ECG is the preferred method.

Besides the motion of the heart, the animals breathing results in a respiratory movement.

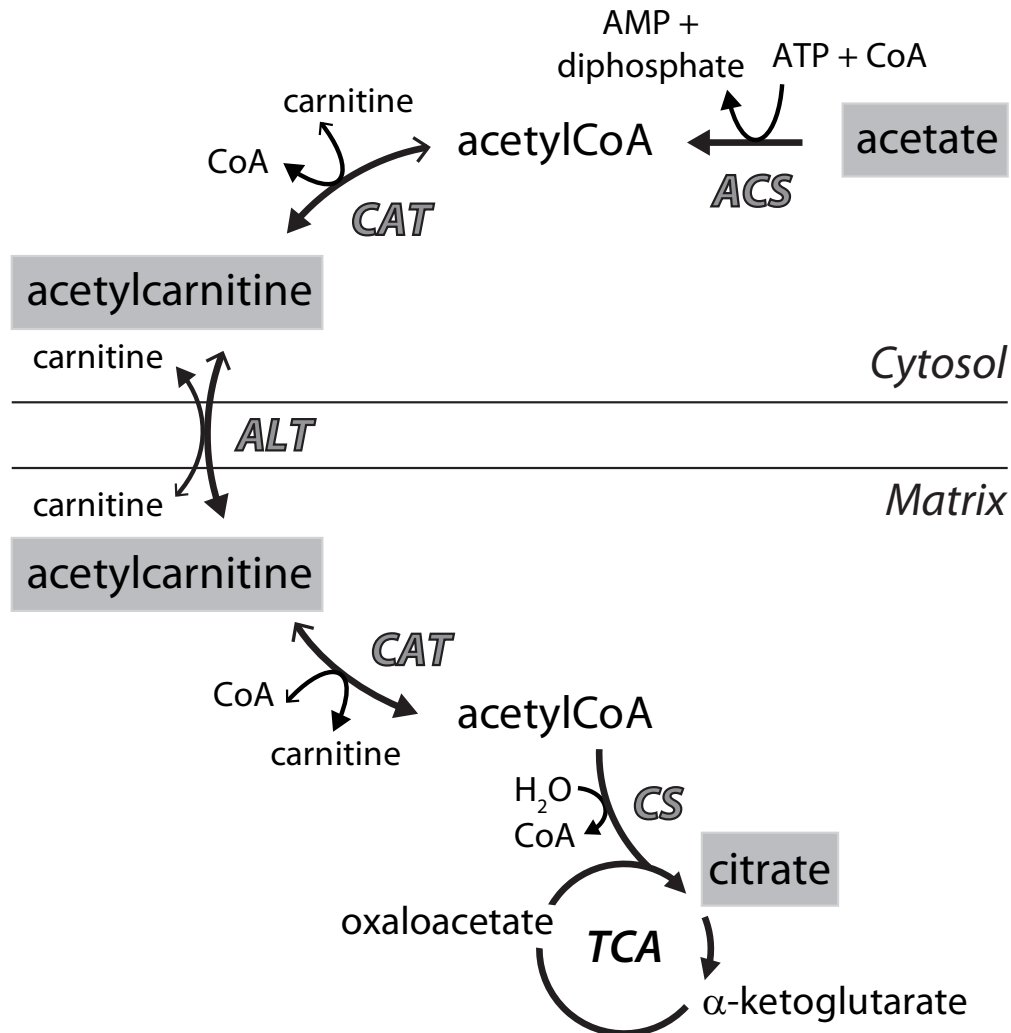


Figure 3.1: Scheme depicting the metabolism of acetate in healthy myocardium. Acetate diffuses freely into the cardiomyocyte, a process driven by a concentration gradient. Acetate is transformed via acetylCoA synthetase (ACS) to acetylCoA in the cytosol. Carnitine acetyltransferase (CAT) converts acetylCoA to acetylcarnitine. Acetylcarnitine translocase (ALT) transports the acetylcarnitine to the mitochondrion where CAT converts acetylcarnitine back to acetylCoA for further utilization by the TCA cycle. Citrate synthase (CS) condenses oxaloacetate with acetylCoA to form citrate. The grey boxes indicate the ^{13}C labeled metabolites which were detected in this study. Both cytosolic and mitochondrial processes are measured.

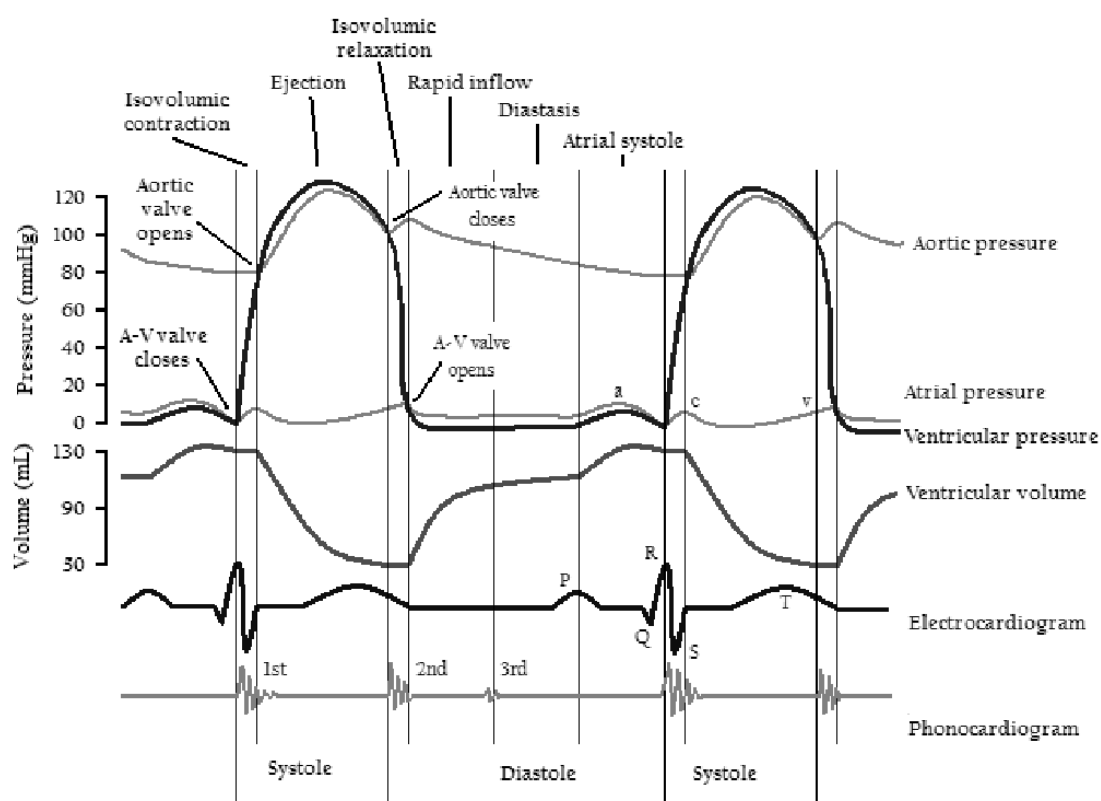


Figure 3.2: A Wiggers diagram, showing the cardiac cycle events occurring in the left ventricle. In the atrial pressure plot: wave "a" corresponds to atrial contraction, wave "c" corresponds to an increase in pressure from the closed mitral valve bulging into the atrium during ventricular systole, and wave "v" corresponds to passive atrial filling. In the electrocardiogram: wave "P" corresponds to the onset of atrial depolarization, waves "QRS" (aka QRS complex) correspond to the onset of ventricular depolarization, and wave "T" corresponds to ventricular repolarization. In the phonocardiogram: The sound labeled 1st contributes to the S1 heart sound and is the reverberation of blood from the sudden closure of the mitral valve (left A-V valve) and the sound labeled "2nd" contributes to the S2 heart sound and is the reverberation of blood from the sudden closure of the aortic valve. Adapted from²³

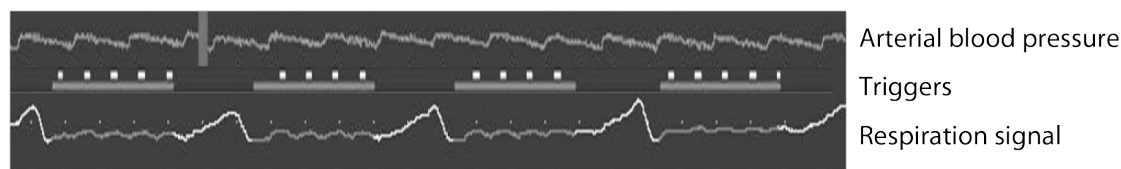


Figure 3.3: Physiological parameters monitored for MR triggering used in this study. The arterial blood pressure signal is shown on top (orange) and the respiration signal at the bottom (white). The respiration gate windows used in the cardiac¹³C MRS experiments described in this chapter are indicated with the green bars. Whenever the gating window overlaps with the desired cardiac phase, a 5V TTL pulse is sent to the MR console (white tick marks) which acts as a trigger signal.

This motion also has to be monitored and synchronized with the data acquisition, since it results in the same kind of artefact if not taken into account. Therefore, double gating setups are used in cardiac experiments, which is achieved by application of a respiratory gating window in combination with the cardiac trigger (Figure 3.3). A trigger signal is generated in form of a 5V TTL pulse and sent to the MR console when both the respiratory gating window and the selected cardiac phase overlap.

However, the arterial blood pressure signal is a pressure wave, and this introduces a time delay between the actual and the measured cardiac phase. Therefore it is not sufficient to select the trigger moment based on the arterial blood pressure signal alone. The delay time needs to be known to precisely select the desired cardiac phase for triggering. Initially the trigger is placed at the beginning of the downslope detection in the pressure signal and a series of cardiac images is acquired at evenly spaced time points in the entire cardiac cycle. These images were then evaluated for the maximum ventricular volume observed in the time series, a period also referred to as late diastole (Figure 3.5). The MR trigger was planned in the more or less steady part of the diastolic phase as indicated with the orange arrow (Figure 3.5). The diastolic phase is also used for cardiac triggering in ^1H NMR studies of the heart in small animals²⁴.

Modification of the GEMS sequence

To speed up the acquisition process of the cinematographic images, an existing gradient echo (GEMS) sequence was modified. A cardiac trigger module was placed after the phase encoding loop and before the slice encoding module, so that with each cardiac trigger a single k-space line is collected for each slice (Figure 3.4). When the repetition time T_R is set to the duration of one cardiac cycle and acquisitions are evenly distributed, the frame number of cinematographic images is determined by the number of slices.

3.2.2 In vivo magnetic resonance spectroscopy

All animal experiments were conducted according to federal ethical guidelines and were approved by the local regulatory body. Male Sprague Dawley rats (275 - 325 g) were anesthetized with 1.5% isoflurane in oxygen ($n = 5$). A catheter was placed into the femoral vein for intravenous delivery of the hyperpolarized acetate solution. A second catheter was placed in the artery to monitor the blood pressure. The respiration rate, cardiac rhythm, and temperature were monitored and maintained stable.

For cardiac ^{13}C NMR studies performed in this thesis, an RF coil was designed with two orthogonal receiving surface coils in quadrature mode. The design, construction and tests of this coil are described in Appendix A.1. This home-built $^{13}\text{C}/^1\text{H}$ probe consisted of a pair of 10 mm diameter ^{13}C surface coils in quadrature and a single 10 mm diameter ^1H surface coil. Since the heart of the rat is not located in the middle of the chest, the animal is slightly

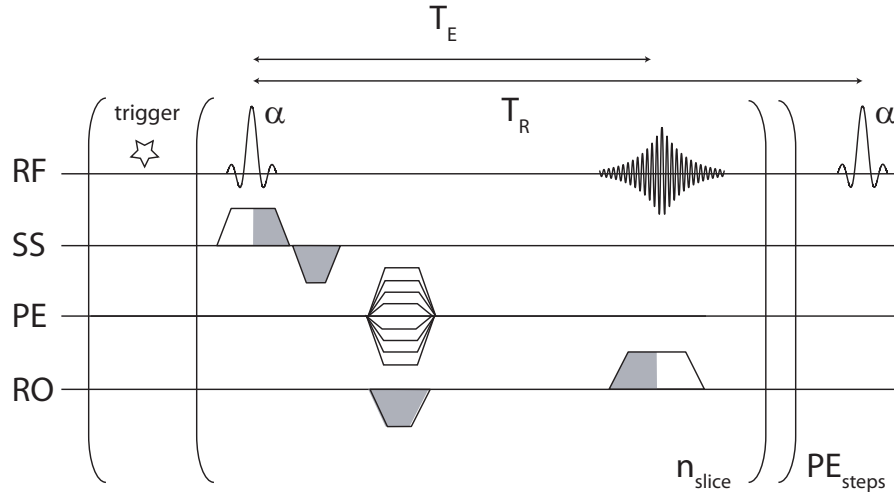


Figure 3.4: Pulse sequence diagram of a triggered gradient echo multi slice (GEMS) pulse sequence.

rotated. The RF coil is placed on top of the chest so that the left ventricle is located in the middle of both ^{13}C receiving coils (Figure 3.6), localizing signals from the cardiac muscle. A hollow glass sphere with a 3 mm inner diameter (Wilma-LabGlass, NJ, USA) was filled with an aqueous 1 M $[1-^{13}\text{C}]$ glucose solution and used to adjust the pulses power and set the reference frequency. All experiments were performed with a Direct Drive spectrometer (Agilent, Palo Alto, CA, USA) interfaced to an actively shielded 9.4 T magnet with a 31 cm horizontal bore (MagneX Scientific, Abingdon, UK).

Once the animal was positioned inside the magnet, ten axial 1 mm thick slices were acquired using a non-triggered gradient echo sequence ($TR = 50$ ms, $TE = 3$ ms, field of view = 30×30 mm, matrix = 128×128 , flip angle = 30° , number of averages = 8) from which the correct position of the animal was determined.

This was followed by a modified gradient echo sequence to confirm the timing of the cardiac trigger in the end-diastolic phase as described in section 3.2.1 (field of view = $40 \text{ mm} \times 40 \text{ mm}$, matrix = 256×256 , $TR = 140$ ms, $TE = 4.5$ ms, number of averages = 8, number of frames (slices) = 14, slice thickness = 1 mm). All scans were acquired using a cardiac trigger as indicated with the arrow in Figure 3.5. This trigger was typically sent 50 or 60 ms after the maximum blood pressure was observed by the SA Monitoring and Gating System (Model 1025, Small Animal Instruments, Stony Brook, NY).

With the selected cardiac trigger ten axial 1 mm thick slices were acquired using a triggered gradient echo sequence to select a voxel of interest. The static magnetic field was homogenized, generally, in a voxel of $4 \text{ mm} \times 5 \text{ mm} \times 5 \text{ mm}$, placed in the part of the myocardium closed to the RF coil, using the FASTESTMAP shimming protocol²⁵. The localized proton line width was reduced to 30 Hz acquired with a STEAM sequence and the unlocalized proton line width

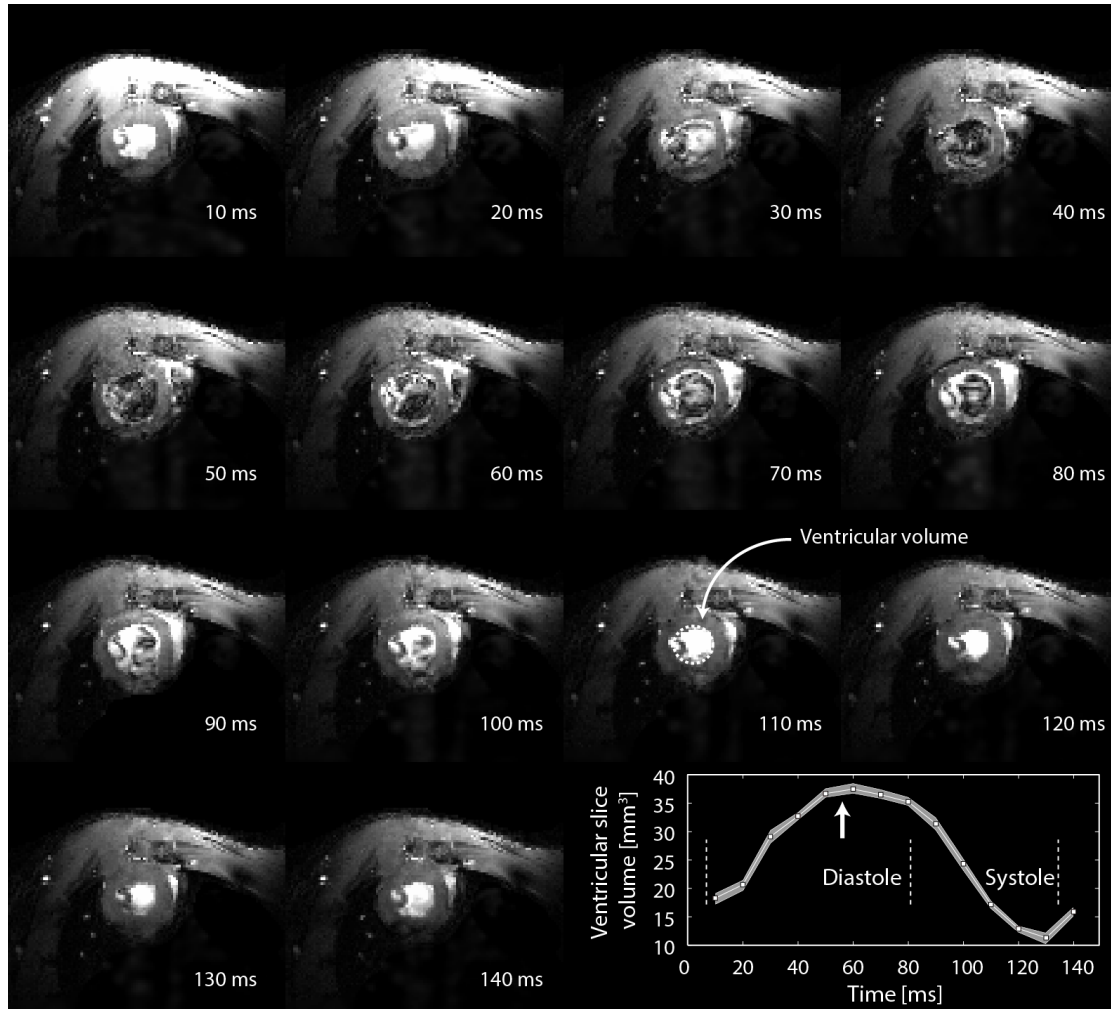


Figure 3.5: A gradient echo sequence was used to acquire cinematographic MR images of the cardiac cycle in a rat heart. Fourteen frames were acquired spaced by 10 ms in the cardiac cycle to plan the timing of the trigger. One complete cycle is illustrated and for each frame the ventricular volume was calculated. The cardiac trigger used for ^1H shimming and ^{13}C hyperpolarized MRS acquisitions is planned towards the end of the diastolic phase as indicated with the orange arrow.

Image parameters: field of view = 40 mm x 40 mm, matrix= 256 x 256, T_R = 140 ms, T_E = 4.5 ms, number of averages = 8, number of frames (slices) = 14, slice thickness = 1 mm, spectral width 5000 Hz, acquisition time 5.12 ms.

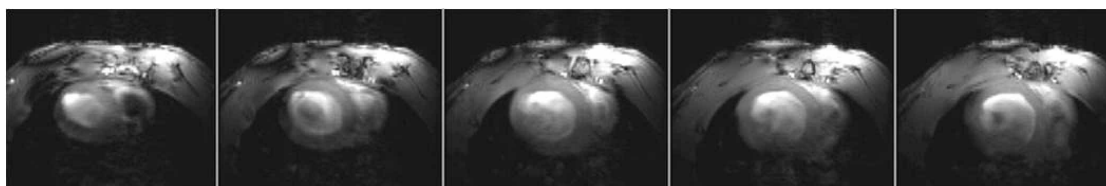


Figure 3.6: The animal is turned in the holder so that the left ventricle is located in the middle of both ^{13}C receiving coils.

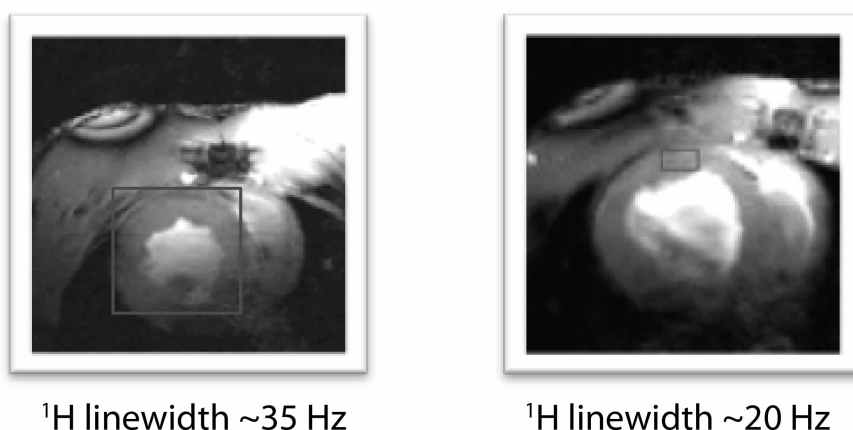


Figure 3.7: Several voxel positions, sizes and locations are used to optimize the localized and unlocalized ^1H linewidth.

to less than 100 Hz (Figure 3.7). The FASTESTMAP protocol as well as the STEAM sequence were cardiac gated.

Series of single-pulse ^{13}C acquisitions were sequentially recorded starting 6 s after dissolution using 30° adiabatic RF pulses (BIR4) applied every 3 s with ^1H decoupling during acquisition (WALTZ16). Decoupling is needed to remove the ^1H induced splitting of the ^{13}C metabolite resonances, for example, the resonance of $[1-^{13}\text{C}]\text{acetylcarnitine}$ is a quartet of doublets when not ^1H decoupled (Figure 1.9 in section 1.2.9). The adiabatic pulses offset and power were set such as to ensure a homogeneous 30° excitation of substrate and metabolite resonances in the entire volume of interest (for calibration measurements see Appendix A.2).

At the end of each *in vivo* experiment, 200 μL of the residual solution was collected and analysed as described in section 2.2.

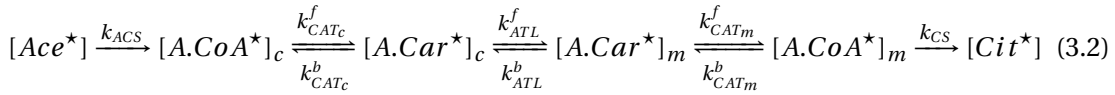
Data analysis

A non-linear least-squares quantification algorithm, AMARES, as implemented in the jMRUI software package²⁶, was used to fit the ^{13}C NMR data. The spectra were corrected for the

phases and DC offset. Soft constraints were imposed to peak frequencies (182.55 -182.65 ppm for acetate, 173.85 -173.95 ppm for acetylcarnitine and 179.65 - 179.75 ppm for citrate) and line widths (FWHM = 10 - 30 Hz) and the relative phases were fixed to zero. The acetylcarnitine and citrate peak areas were normalized to the maximum acetate signal in each experiment to account for varying polarization levels across experiments. The time courses of quantified peak areas were analyzed with the kinetic model described in section 3.3, implemented in Matlab (The MathWorks, Natick, MA, USA).

3.3 Kinetic model of hyperpolarized acetate metabolism in the heart

As discussed in section 2.3, it is assumed that measured kinetic parameters are independent of processes related to membrane transport of acetate. The assumption is that the enzyme concentration are not affected during the time frame of the experiment, which is about 1 minute. Therefore, the $^{13}\text{C}(\star)$ label flow between the substrate acetate (Ace) and the metabolites acetylCoA (A.CoA) and acetylcarnitine (A.Car) inside the cytosol (c) and mitochondria (m) of cardiac muscle, and citrate (Cit) in the mitochondria can be described with the following flow scheme:



These reactions can be described with the following differential equations:

$$\frac{d[Ace^*]}{dt} = -V_{ACS} \frac{[Ace^*]}{[Ace]} \quad (3.3)$$

$$\frac{d[A.CoA^*]_c}{dt} = V_{ACS} \frac{[Ace^*]}{[Ace]} - V_{CAT_c}^f \frac{[A.CoA^*]_c}{[A.CoA]_c} + V_{CAT_c}^b \frac{[A.Car^*]_c}{[A.Car]_c} \quad (3.4)$$

$$\frac{d[A.Car^*]_c}{dt} = V_{CAT_c}^f \frac{[A.CoA^*]_c}{[A.CoA]_c} - (V_{CAT_c}^b + V_{ATL}^f) \frac{[A.Car^*]_c}{[A.Car]_c} + V_{ATL}^b \frac{[A.Car^*]_m}{[A.Car]_m} \quad (3.5)$$

$$\frac{d[A.Car^*]_m}{dt} = V_{ATL}^f \frac{[A.Car^*]_c}{[A.Car]_c} - (V_{ATL}^b + V_{CAT_m}^f) \frac{[A.Car^*]_m}{[A.Car]_m} + V_{CAT_m}^b \frac{[A.CoA^*]_m}{[A.CoA]_m} \quad (3.6)$$

$$\frac{d[A.CoA^*]_m}{dt} = V_{CAT_m}^f \frac{[A.Car^*]_m}{[A.Car]_m} - V_{CAT_m}^b \frac{[A.CoA^*]_m}{[A.CoA]_m} - V_{CS} \frac{[A.CoA^*]_m}{[A.CoA]_m} \quad (3.7)$$

$$\frac{d[Cit^*]}{dt} = V_{CS} \frac{[A.CoA^*]_m}{[A.CoA]_m} \quad (3.8)$$

where $[Ace]$, $[A.CoA]$, $[A.Car]$, $[Cit]$ represent total (sum of ^{13}C labeled and unlabeled molecules) metabolites concentrations in the mitochondrial (m) or cytosolic (c) compartments, $[Ace^*]$, $[A.CoA^*]$, $[A.Car^*]$, $[Cit^*]$ the ^{13}C labeled concentrations, V_{CAT}^f and V_{CAT}^b are the forward and the backward fluxes through CAT, respectively, V_{ACS} is the flux through ACS, V_{ATL}^f and V_{ATL}^b are the backward and forward fluxes across the mitochondrial membrane, V_{CS} is the flux through CS. Here the forward fluxes indicate all reactions going towards the tricarboxylic acid cycle.

Since no distinction can be made between mitochondrial and cytosolic acetylcarnitine in ^{13}C MRS measurements, Equation 3.5 and 3.6 are combined to yield a description for total ^{13}C labeled acetylcarnitine:

$$\begin{aligned} \frac{d[A.Car^*]_{tot}}{dt} &= V_{CAT_c}^f \frac{[A.CoA^*]_c}{[A.CoA]_c} - V_{CAT_c}^b \frac{[A.Car^*]_c}{[A.Car]_c} \\ &\quad + V_{CAT_m}^b \frac{[A.CoA^*]_m}{[A.CoA]_m} - V_{CAT_m}^f \frac{[A.Car^*]_m}{[A.Car]_m} \end{aligned} \quad (3.9)$$

Summing this description with Equation 3.4 and 3.7 yields:

$$\frac{d[A.Car^*]_{tot}}{dt} = V_{ACS} \frac{[Ace^*]}{[Ace]} - \frac{d[A.CoA^*]_c}{dt} - V_{CS} \frac{[A.CoA^*]_m}{[A.CoA]_m} - \frac{d[A.CoA^*]_m}{dt} \quad (3.10)$$

Based on a small pool approximation^{27;28} as described in section 2.3 we can assume that $d[A.CoA^*]/dt \ll d[A.Car^*]/dt$. Since the physiological plasma acetate concentration is lower than 0.2 mM^2 , it can be assumed that the acetate blood pool was fully labeled following the bolus injection, i.e. $[Ace^*]/[Ace] \approx 1$. Condensing the previous statements, the ^{13}C flow from acetate to acetylcarnitine and citrate in the cytosolic and mitochondrial compartments of cardiac muscle can be described by the following equations:

$$\frac{d[Ace^*]}{dt} = -V_{ACS} \frac{[Ace^*]}{[Ace]} \quad (3.11)$$

$$\frac{d[A.Car^*]_{tot}}{dt} = V_{ACS} \frac{[Ace^*]}{[Ace]} - V_{CS} \frac{[A.CoA^*]_m}{[A.CoA]_m} \quad (3.12)$$

$$\frac{d[Cit^*]}{dt} = V_{CS} \frac{[A.CoA^*]_m}{[A.CoA]_m} \quad (3.13)$$

Since the labeled concentration of acetylCoA could not be measured, the term $\frac{[A.CoA^*]_m}{[A.CoA]_m}$ was eliminated via the following substitution derived from Equation 3.7:

$$\frac{[A.CoA^*]_m}{[A.CoA]_m} = \frac{V_{CAT_m}^f \frac{[A.Car^*]_m}{[A.Car]_m} - \frac{d[A.CoA^*]_m}{dt}}{V_{CAT_m}^b + V_{CS}} \quad (3.14)$$

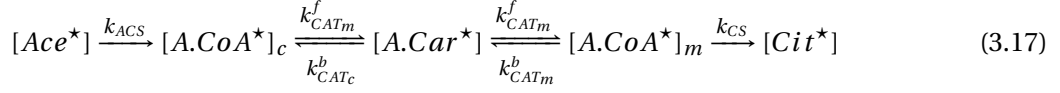
Using a small pool approximation and substituting Equation 3.14 in Equations 3.12 and 3.13 result in the following expressions:

$$\frac{d[A.Car^*]_{tot}}{dt} = V_{ACS} \frac{[Ace^*]}{[Ace]} - V_{CS} \frac{V_{CAT_m}^f}{V_{CAT_m}^b + V_{CS}} \frac{[A.Car^*]_m}{[A.Car]_m} \quad (3.15)$$

$$\frac{d[Cit^*]}{dt} = V_{CS} \frac{V_{CAT_m}^f}{V_{CAT_m}^b + V_{CS}} \frac{[A.Car^*]_m}{[A.Car]_m} \quad (3.16)$$

In these equations the mitochondrial fraction of labeled acetylcarnitine remain, however, the ^{13}C hyperpolarized experiments described here cannot distinguish between different cellular compartments. Since previous studies suggest that the shuttling of acetylcarnitine to the mitochondria via ATL is not rate-limiting for carnitine promoted processes within

the mitochondria^{12–14} a single cellular acetylcarnitine pool will be employed, yielding the following ¹³C label flow scheme:



The differential equations for ¹³C labeling in acetate, acetylcarnitine and citrate will be similar to respectively Equation 3.11, 3.15 and 3.16 with removal of the compartmentation suffix for acetylcarnitine. A flux V can be described as a kinetic rate constant k times the substrate concentration. Introducing kinetic rate constants yield the following expressions for the ¹³C labeling in observed metabolites:

$$\frac{d[Ace^*]}{dt} = -k_{ACS}[Ace] \frac{[Ace^*]}{[Ace]} = -k_{ACS}[Ace^*] \quad (3.18)$$

$$\begin{aligned} \frac{d[A.Car^*]}{dt} &= k_{ACS}[Ace^*] - k_{CS} \frac{[A.CoA]_m}{[A.Car]} \frac{V_{CAT_m}^f}{V_{CAT_m}^b + V_{CS}} [A.Car^*] \\ &= k_{ACS}[Ace^*] - k'_{CS}[A.Car^*] \end{aligned} \quad (3.19)$$

$$\frac{d[Cit^*]}{dt} = k'_{CS}[A.Car^*] \quad (3.20)$$

with k'_{CS} the apparent kinetic rate constant representing $k_{CS} \frac{[A.CoA]_m}{[A.Car]} \frac{V_{CAT_m}^f}{V_{CAT_m}^b + V_{CS}}$ and k_{ACS} the kinetic rate constant representing the enzyme ACS. Besides the influence of enzymatic reactions on the observed metabolite time courses as described above, the ¹³C NMR signals measured in the cardiac muscle tissue will decay as a consequence of relaxation processes and repeated RF excitations. The evolution of the magnetization of the carbonyl ¹³C in acetate, M_{Ace} , acetylcarnitine, $M_{A.Car}$, and citrate, M_{Cit} , can be described with the following differential equations:

$$\frac{dM_{Ace}}{dt} = -R_{Ace}M_{Ace} - k_{ACS}M_{Ace} + M_{Ace} \log \cos \theta / T_R \quad (3.21)$$

$$\frac{dM_{A.Car}}{dt} = k_{ACS}M_{Ace} - k'_{CS}M_{A.Car} - R_{1,A.Car}M_{A.Car} + M_{A.Car} \log \cos \theta / T_R \quad (3.22)$$

$$\frac{dM_{Cit}}{dt} = k'_{CS}M_{A.Car} - R_{1,Cit}M_{Cit} + M_{Cit} \log \cos \theta / T_R \quad (3.23)$$

where R_{Ace} is the acetate signal decay comprised of the longitudinal relaxation rate of the

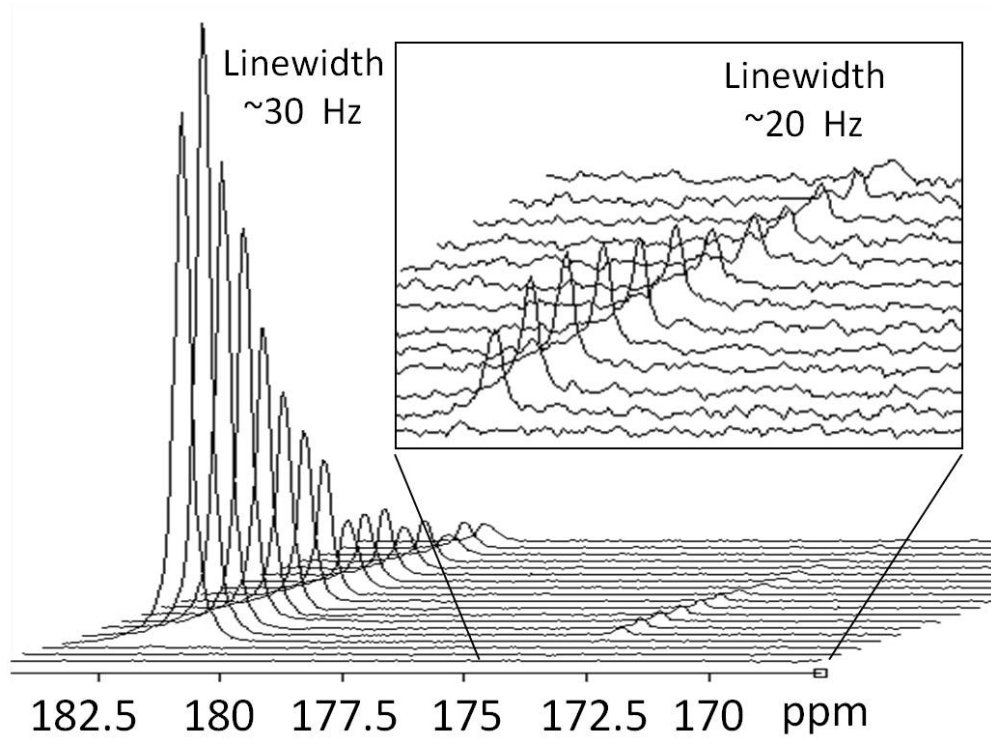


Figure 3.8: Spectral time course of hyperpolarized $[1-^{13}\text{C}]$ acetate (182.6 ppm) and acetylcarnitine (173.9 ppm) in the heart.

carbonyl ^{13}C acetate as well as the flow of signal in and out of the volume of interest; $R_{1,A.Car}$ is the longitudinal relaxation rate of acetylcarnitine. The thermal equilibrium magnetizations of the carbonyl sites of acetate, acetylcarnitine and citrate, respectively and can be neglected as described in section 2.3; The term $\log \cos \theta / T_R$ constitutes the decay rate of the magnetization as a result of repeated RF excitations with a repetition time T_R and flip angle θ . From the initial conditions $M_{A.Car}(t=0) = 0$, $M_{Cit}(t=0) = 0$ and $M_{Ace}(t=0) = M_0$ the analytical solutions to Equation 3.21, 3.22 and 3.23 can be obtained. These analytical solutions were used to fit the metabolic time courses where the time point of the first acetate observation, corresponding to the maximum acetate signal, was set to $t=0$ prior to fitting the data.

3.4 Results

The metabolic time courses of hyperpolarized acetate (182.6 ppm) and its metabolic products citrate (179.7 ppm) and acetylcarnitine (173.9 ppm) were recorded in healthy myocardium *in vivo* (Figure 3.8 and 3.9).

Using the FASTESTMAP shimming protocol, ^1H line widths of 20 to 30 Hz were obtained in a voxel size of $4 \times 6 \times 6 \text{ mm}^3$. The observed ^{13}C FWHM measured during the hyperpolarized

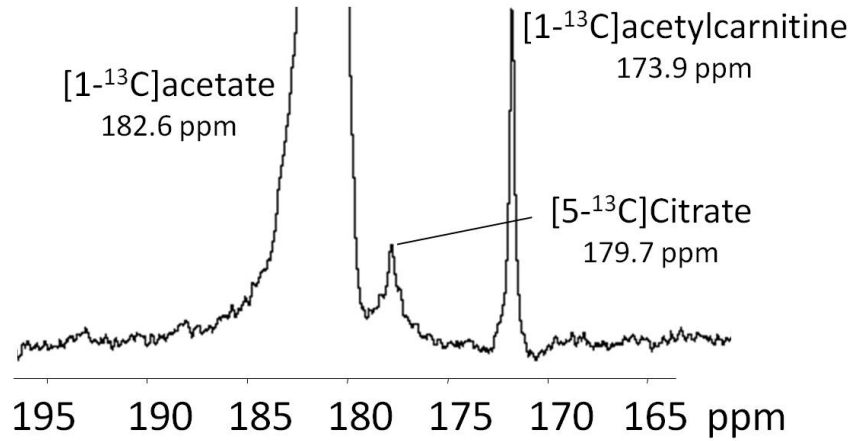


Figure 3.9: The spectral sum of ($t=21$ s to 30 s) reveals the presence of a third metabolite at 179.7 ppm. This spectrum is assigned to $[5-^{13}\text{C}]$ citrate.

MR experiments were between 30 and 40 Hz (localization achieved by placing the surface coil on top of the mouse heart). Peak areas were extracted using jMRUI to obtain metabolite time courses of acetate, acetylcarnitine and citrate (Figure 3.10 and 3.11). The observation of citrate is the first in vivo real time detection of $[1-^{13}\text{C}]$ citrate after using acetate as substrate.

The maximum peak integral of acetate was observed 9 s after the beginning of the infusion, the maximum acetylcarnitine about 12 s later and the maximum citrate approximately 6 s after acetylcarnitine. This observation supports the role of carnitine as a shuttle for acetyl groups across the mitochondrial membrane. A three-compartment non steadystate metabolic model was used to fit the metabolic time courses (Figure 3.10 and 3.11). This model takes into account the effect of repeated excitations and contains 4 free parameters (R_{Ace} , k_{ACS} , k'_{CS} , R_{Cit}). The kinetic rate constant k'_{CS} should be considered an apparent rate constant since it not only reflects the flux through the enzyme citrate synthase but also carnitine acetyltransferase, since

$$k'_{CS} = k_{CS} \frac{[A.CoA]_m}{[A.Car]} \frac{V_{CATm}^f}{V_{CATm}^b + V_{CS}}.$$

The kinetic rate constant k'_{CS} could be representative for TCA cycle activity and thus myocardial oxidation. The T_1 relaxation time of $[1-^{13}\text{C}]$ acetylcarnitine in blood was measured to be 14.9 s and used as a constant¹⁶. The kinetic parameters obtained from the fitting are $k_{ACS} = 1.5 \pm 0.2 \text{ ms}^{-1}$, $k'_{CS} = 21 \pm 4.5 \text{ ms}^{-1}$.

3.5 Discussion

In this study hyperpolarized acetate was used to probe short chain fatty acid metabolism in the rat heart *in vivo*. The detection of the citrate resonance showed that mitochondrial acetylCoA, ultimately derived from the injected acetate, continued into the TCA cycle and that acetate can be used as a metabolic probe for myocardial oxidation. When injected in

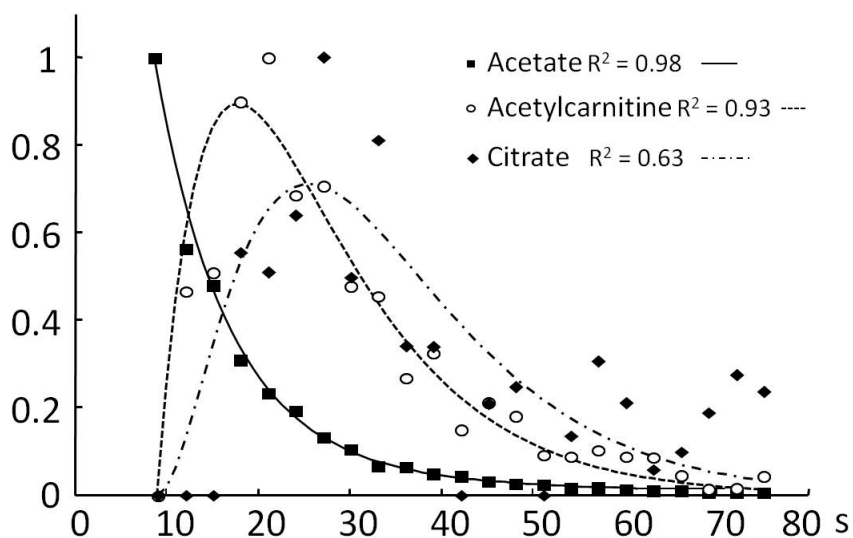


Figure 3.10: Time course of the peak integrals of the substrate $[1-^{13}\text{C}]$ acetate and its metabolic products $[1-^{13}\text{C}]$ acetylcarnitine and $[5-^{13}\text{C}]$ citrate. (---) The corresponding fit to the kinetic model.

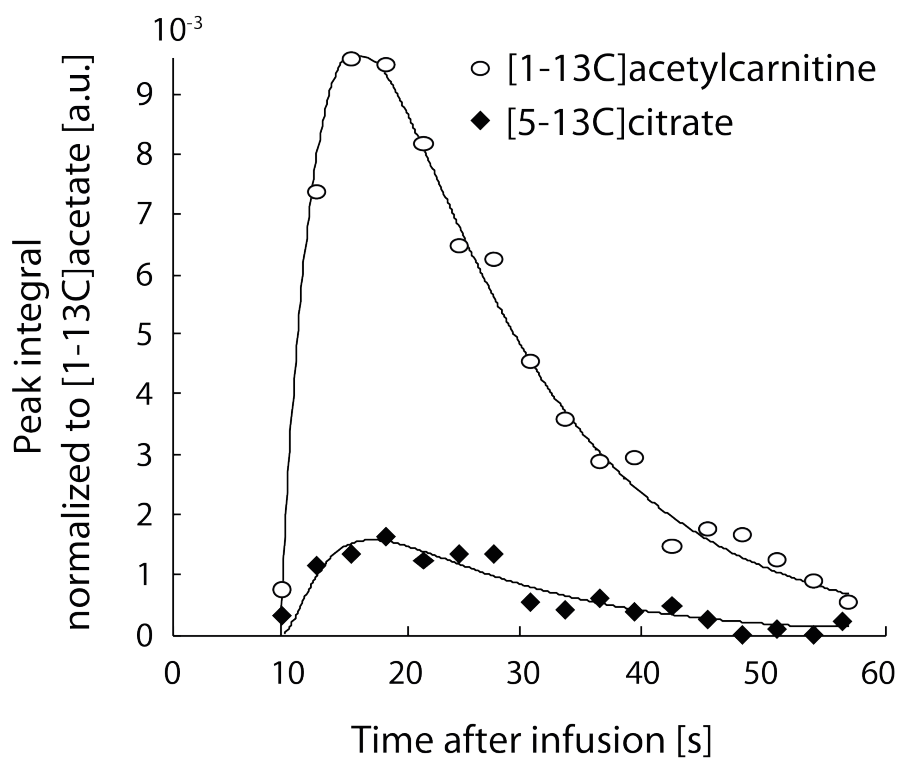


Figure 3.11: Time course of the peak integrals of the metabolic products $[1-^{13}\text{C}]$ acetylcarnitine and $[5-^{13}\text{C}]$ citrate and the corresponding fit (—) to the kinetic model.

resting rat skeletal muscle citrate was not detected¹⁶, which is related to the substantially higher activity of ACS in the heart²⁹ where acetate is oxidized at a much faster rate³⁰.

However, in skeletal muscle studies performed in this thesis (see results in Chapter 2, Figure 2.10), k_{ACS} values were ranging between 3 and 7 ms⁻¹, which appears much larger. This can be attributed to the location of the hyperpolarized substrate acetate, which resides mainly in the tissue compartment in the previous skeletal muscle study, and mainly in the ventricular compartment of the cardiac muscle study described here. The relatively lower value of k_{ACS} found in this study is resulting from the acetate signal being mainly located inside the ventricles.

The increased spectral resolution at 9.4 T allowed us to observe citrate compared to earlier investigations in cardiac muscle in mice at 2.35 T¹⁵. The aforementioned study reported the detection of the acetylCoA resonance at 202 ppm in mice heart and liver after a 90° excitation but was never detected in the experiments performed in this study. The use of adiabatic pulses which provides identical excitation for all metabolites enables observation of true ratios independent of their location in the myocardium.

The real-time kinetic measurements through citrate synthase, a measure of TCA cycle activity, as performed here does not depend on isotopic steady state, a necessity for thermal equilibrium ¹³C MRS. Hyperpolarized [1-¹³C]acetate can be used as a PDH independent metabolic probe for myocardial viability and elucidate changes in Krebs cycle metabolism during impaired heart function. Since both acetylcarnitine and citrate are located in the myocardium, both markers can be used as a direct indicator of TCA cycle activity.

Detectable quantities of ¹³C labeled glutamate were expected since 60% of the activity was found in glutamate 2 minutes after injection of ¹⁴C labeled acetate³¹, and only 8% in total labeled TCA cycle metabolites. However, due to overlapping resonances it was not possible to detect [5-¹³C]glutamate.

Conclusion

We conclude that by using hyperpolarized [1-¹³C]acetate it is possible to study the in vivo real-time formation of acetylcarnitine and TCA cycle intermediates and thus directly measure energy metabolism in healthy myocardium. This method could be applied to study models of cardiac ischemia-reperfusion.

References

- [1] B. Mittendorfer, L. S. Sidossis, E. Walser, D. L. Chinkes, and R. R. Wolfe. Regional acetate kinetics and oxidation in human volunteers. *American Journal of Physiology-Endocrinology and Metabolism*, 274(6):E978–E983, 1998.
- [2] S. E. Knowles, I. G. Jarrett, O. H. Filsell, and F. J. Ballard. Production and utilization of acetate in mammals. *Biochemical Journal*, 142(2):401–411, 1974.
- [3] R. Schulz, C. Kappeler, H. Coenen, A. Bockisch, and G. Heusch. Positron emission tomography analysis of [1-(11)c]acetate kinetics in short-term hibernating myocardium. *Circulation*, 97(10):1009–1016, 1998.
- [4] E. M. Chance, S. H. Seeholzer, K. Kobayashi, and J. R. Williamson. Mathematical-analysis of isotope labeling in the citric-acid cycle with applications to c-13 nmr-studies in perfused rat hearts. *Journal of Biological Chemistry*, 258(22):3785–3794, 1983.
- [5] Craig R Malloy, A. Dean Sherry, and F. Mark Jeffrey. Carbon flux through citric acid cycle pathways in perfused heart by 13c nmr spectroscopy. *FEBS Letters*, 212:58–62, 1987.
- [6] B. Bleiberg, T. R. Beers, M. Persson, and J. M. Miles. Systemic and regional acetate kinetics in dogs. *American Journal of Physiology*, 262(2):E197–E202, 1992.
- [7] B. Bleiberg, T. R. Beers, M. Persson, and J. M. Miles. Metabolism of triacetin-derived acetate in dogs. *American Journal of Clinical Nutrition*, 58(6):908–911, 1993.
- [8] L. Powers, M. K. Osborn, D. W. Yang, C. L. Kien, R. D. Murray, M. Beylot, and H. Brunen-graber. Assay of the concentration and stable-isotope enrichment of short-chain fatty-acids by gas-chromatography mass-spectrometry. *Journal of Mass Spectrometry*, 30(5):747–754, 1995.
- [9] P. A. Roberts, S. J. G. Loxham, S. M. Poucher, D. Constantin-Teodosiu, and P. L. Greenhaff. Acetyl-coa provision and the acetyl group deficit at the onset of contraction in ischemic canine skeletal muscle. *American Journal of Physiology-Endocrinology and Metabolism*, 288(2):E327–E334, 2005.
- [10] F. B. Stephens, D. Constantin-Teodosiu, and P. L. Greenhaff. New insights concerning the role of carnitine in the regulation of fuel metabolism in skeletal muscle. *J Physiol*, 581(Pt 2):431–44, 2007.
- [11] P. J. Randle, P. J. England, and R. M. Denton. Control of tricarboxylate cycle and its interactions with glycolysis during acetate utilization in rat heart. *Biochemical Journal*, 117(4):677–695, 1970.
- [12] K. F. Lanoue, Williams.Jr, and J. Bryla. Feedback interactions in control of citric-acid cycle activity in rat-heart mitochondria. *Journal of Biological Chemistry*, 247(3):667–679, 1972.
- [13] W. Lysiak, P. P. Toth, C. H. Suelter, and L. L. Bieber. Quantitation of the efflux of acylcarnitines from rat-heart, brain, and liver-mitochondria. *Journal of Biological Chemistry*, 261(29):3698–3703, 1986.
- [14] L. L. Bieber. Carnitine. *Annual Review of Biochemistry*, 57:261–283, 1988.
- [15] P. R. Jensen, T. Peitersen, M. Karlsson, R. In ’t Zandt, A. Gisselsson, G. Hansson, S. Meier, and M. H. Lerche. Tissue-specific short chain fatty acid metabolism and slow metabolic recovery after ischemia from hyperpolarized nmr in vivo. *Journal of Biological Chemistry*, 284(52):36077–82, 2009.
- [16] J. A. M. Bastiaansen, T. Cheng, M. Mishkovsky, J. M. N. Duarte, A. Comment, and R. Gruet-

- ter. In vivo enzymatic activity of acetylcoA synthetase in skeletal muscle revealed by ^{13}C turnover from hyperpolarized $[1-^{13}\text{C}]\text{acetate}$ to $[1-^{13}\text{C}]\text{acetylcarnitine}$. *Biochimica Et Biophysica Acta*, 1830(8):4171–4178, 2013.
- [17] X. Yu, L. T. White, C. Doumen, L. A. Damico, K. F. LaNoue, N. M. Alpert, and E. D. Lewandowski. Kinetic analysis of dynamic c- 13 nmr spectra: Metabolic flux, regulation, and compartmentation in hearts. *Biophysical Journal*, 69(5):2090–2102, 1995.
- [18] J. H. Ardenkjaer-Larsen, B. Fridlund, A. Gram, G. Hansson, L. Hansson, M. H. Lerche, R. Servin, M. Thaning, and K. Golman. Increase in signal-to-noise ratio of $> 10,000$ times in liquid-state nmr. *Proc Natl Acad Sci U S A*, 100(18):10158–10163, 2003.
- [19] M. E. Merritt, C. Harrison, C. Storey, F. M. Jeffrey, A. D. Sherry, and C. R. Malloy. Hyperpolarized ^{13}C allows a direct measure of flux through a single enzyme-catalyzed step by nmr. *Proc Natl Acad Sci U S A*, 104(50):19773–7, 2007.
- [20] K. Golman, J. S. Petersson, P. Magnusson, E. Johansson, P. Akesson, C. M. Chai, G. Hansson, and S. Mansson. Cardiac metabolism measured noninvasively by hyperpolarized c- 13 mri. *Magnetic Resonance in Medicine*, 59(5):1005–1013, 2008.
- [21] M. A. Schroeder, L. E. Cochlin, L. C. Heather, K. Clarke, G. K. Radda, D. J. Tyler, and R. G. Shulman. In vivo assessment of pyruvate dehydrogenase flux in the heart using hyperpolarized carbon- 13 magnetic resonance. *Proceedings of the National Academy of Sciences of the United States of America*, 105(33):12051–12056, 2008.
- [22] M.A. Bernstein, K.F. King, and X.J. Zho. *Handbook of MRI pulse sequences*. Elsevier, 2004.
- [23] Daniel Chang. Wiggers diagram. http://upload.wikimedia.org/wikipedia/commons/9/9a/Wiggers_Diagram.png, 2011.
- [24] Juergen E. Schneider, Damian J. Tyler, Michiel ten Hove, A. Elizabeth Sang, Paul J. Cassidy, Alexandra Fischer, Julie Wallis, Liam M. Sebag-Montefiore, Hugh Watkins, Dirk Isbrandt, Kieran Clarke, and Stefan Neubauer. In vivo cardiac 1h mrs in the mouse. *Magnetic resonance in medicine*, 52:1029–1035, 2004.
- [25] R. Gruetter and I. Tkac. Field mapping without reference scan using asymmetric echo-planar techniques. *Magnetic Resonance in Medicine*, 43(2):319–323, 2000.
- [26] A. Naressi, C. Couturier, J. M. Devos, M. Janssen, C. Mangeat, R. de Beer, and D. Graveron-Demilly. Java-based graphical user interface for the mrui quantitation package. *MAGMA*, 12(2-3):141–52, 2001.
- [27] K. Uffmann and R. Gruetter. Mathematical modeling of c- 13 label incorporation of the tca cycle: The concept of composite precursor function. *Journal of Neuroscience Research*, 85(15):3304–3317, 2007.
- [28] João M.N. Duarte, Bernard Lanz, and Rolf Gruetter. Compartmentalised cerebral metabolism of $[1,6-^{13}\text{C}]\text{glucose}$ determined by in vivo ^{13}C nmr spectroscopy at 14.1 t. *Frontiers in Neuroenergetics*, 3, 2011.
- [29] M. Aas. Organ and subcellular distribution of fatty acid activating enzymes in rat. *Biochimica Et Biophysica Acta*, 231(1):32–47, 1971.
- [30] J. R. Williamson. Effects of insulin + starvation on metabolism of acetate + pyruvate by perfused rat heart. *Biochemical Journal*, 93(1):97–106, 1964.
- [31] C. K. Ng, S. C. Huang, H. R. Schelbert, and D. B. Buxton. Validation of a model for $[1-^{13}\text{C}]\text{acetate}$ as a tracer of cardiac oxidative-metabolism. *American Journal of Physiology*, 266(4):H1304–H1315, 1994.

Myocardial substrate competition using hyperpolarized ^{13}C MR

4

Abstract

Cardiac energy is derived primarily from oxidation of fatty acids and to a lesser extent carbohydrates and ketone bodies. Cardiac dysfunction is often associated with a shift in substrate preference, for example in ventricular hypertrophy and heart failure where carbohydrate oxidation is upregulated. Diagnostic radiotracer methods such as ^{18}F FDG-PET provide information on substrate uptake and not directly about oxidation of either carbohydrates or alternative fuels. Hyperpolarization enables the metabolism of ^{13}C labeled substrates to be detected by magnetic resonance with high sensitivity and specificity. The aim here was to demonstrate the feasibility of simultaneously measuring lipid and carbohydrate competition *in vivo* using hyperpolarized magnetic resonance and to assess the sensitivity of the method to a metabolic perturbation. To study substrate competition in the rat heart *in vivo*, we injected hyperpolarized $[1-^{13}\text{C}]$ pyruvate ($n=10$), $[1-^{13}\text{C}]$ butyrate ($n=12$), or both ($n=14$) as representatives of carbohydrates and fatty acids respectively. The appearance of bicarbonate, lactate, alanine, glutamate, citrate, acetylcarnitine, β -hydroxybutyrate and acetoacetate could be assigned exclusively to pyruvate or butyrate oxidation, allowing for independent monitoring of their metabolism in a single experiment. The sensitivity of this method was tested by comparing the fed to the fasted state. Fasting led to significant changes in preference for the injected substrates in separate experiments as well as in co-injection. Combining hyperpolarized ^{13}C technology and co-administration of $[1-^{13}\text{C}]$ pyruvate and $[1-^{13}\text{C}]$ butyrate enables noninvasive and simultaneous monitoring of myocardial oxidation of both fatty acid and carbohydrates *in vivo* and is a sensitive indicator of metabolic shift.

Adapted from:

In vivo myocardial substrate competition using hyperpolarized ^{13}C magnetic resonance
Jessica AM Bastiaansen, Matthew E Merritt, Arnaud Comment

Submitted manuscript

4.1 Introduction

Cardiovascular disease is still the number one cause of death in the US and the industrialized world⁴¹. An emerging treatment avenue for ischemic heart disease is modulation of the substrate preference of the myocardium to improve the production of the ATP necessary for supporting continuous mechanical activity^{23;36}. The heart uses a variety of fuel sources to meet its energy requirements, namely fatty acids, ketone bodies, and carbohydrates; the consumption of the latter being up-regulated in the failing heart⁸. Since the complete oxidation of a single glucose molecule provides more molecules of ATP per mole of oxygen than any other substrate, including fatty acids or ketones²⁹, metabolic approaches for increasing cardiac efficiency include suppressing fatty acid oxidation and increasing glucose oxidation. Plasma substrate concentrations can vary dramatically depending on the physiological state of the body and as a result the myocardium modulates its substrate selection in order to maintain high levels of ATP⁴⁹. For instance, fasting leads to an increase of free fatty acids (FFA)³, an acceleration of lipid oxidation and a reduction of glycolysis²⁵, as well as an elevation of ketone body concentration, which eventually inhibit carbohydrate and fatty acid oxidation^{4;38}. Acetyl-CoA is the metabolite formed at the crossroads between lipid and carbohydrate metabolism and it is located at the entry of the tricarboxylic acid (TCA) cycle (Figure 4.1).

It is produced from fatty acids via β -oxidation and from carbohydrates through the glycolytic pathway, via the intramitochondrial pyruvate dehydrogenase (PDH) complex, which is the irreversible rate limiting step in carbohydrate oxidation. Substrate selection is regulated by many mechanisms, including the intramitochondrial acetylCoA to CoA ratio. An increased ratio results in the inhibition of PDH activity whereas a decreased ratio activates PDH. PDH is also modulated by the intramitochondrial NADH/NAD⁺ ratio as well as phosphorylation by pyruvate dehydrogenase kinase¹⁴. When acetyl groups are abundant they can be stored as acetylcarnitine, a reaction catalyzed by carnitine acetyl transferase (CAT).

Substrate selection is a clinically important variable that is known to vary with the severity of the myocardial pathology and is subject to manipulation by pharmacokinetic intervention²⁴. Upregulation of glucose metabolism should theoretically make the heart more efficient. The possibility of assaying substrate selection *in vivo* would constitute a fundamental advance in the diagnosis and treatment of heart failure and could help in correctly choosing the most effective intervention in a single patient, i.e., personalized healthcare. Positron emission tomography (PET) is widely used to study heart failure, both with ^{18}F FDG and ^{11}C labeled fatty acids^{22;48}, but the formulation of a protocol to measure substrate competition in a simultaneous sense is nearly impossible, since ^{18}F and ^{11}C both produce 511KeV electrons and their respective signals are thus indistinguishable. Using other radionuclides with different annihilation energies in addition to the ^{18}F and ^{11}C compounds would be cost prohibitive. Recent developments in hyperpolarized ^{13}C magnetic resonance (MR) allow the study of real-time metabolism of ^{13}C labeled pyruvate, providing a direct measurement of the flux through PDH by the formation of carbon dioxide and bicarbonate^{15;33;46}.

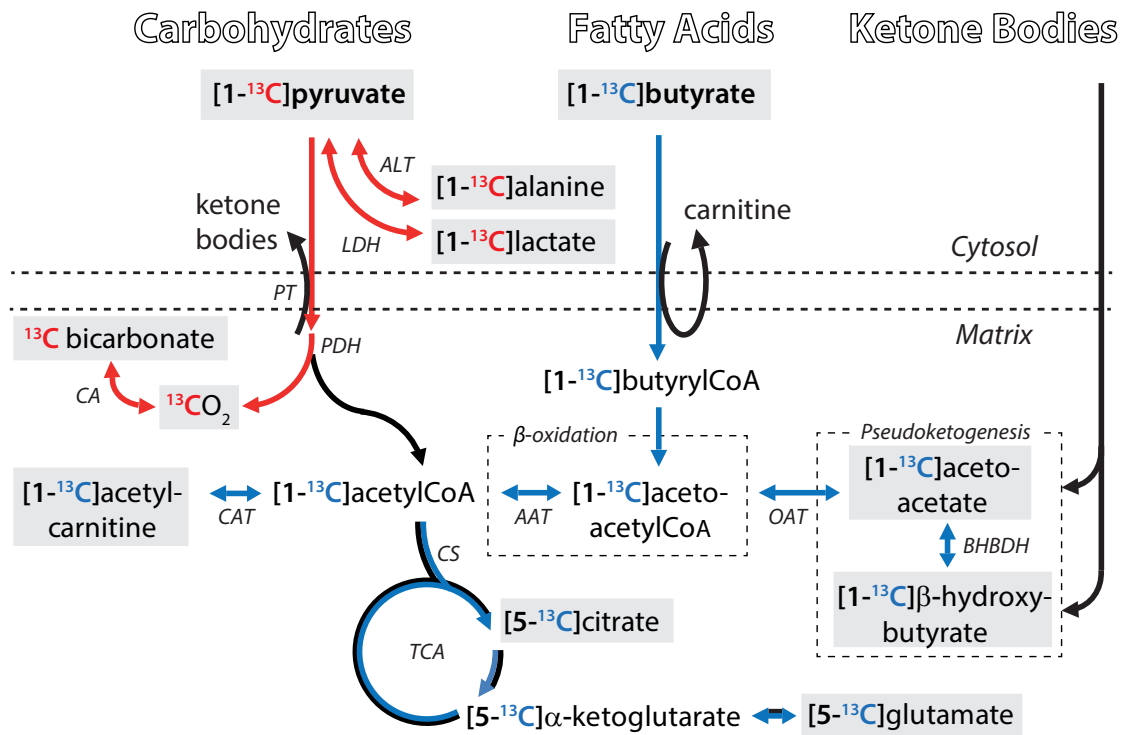


Figure 4.1: The metabolic pathways of $[1-^{13}\text{C}]$ pyruvate and $[1-^{13}\text{C}]$ butyrate in the myocardium in vivo. The propagation of the ^{13}C label from pyruvate to its downstream metabolites is indicated with red arrows and those of butyrate with blue arrows. The ^{13}C label of pyruvate will not enter the TCA cycle or dilute the acetyl-CoA pool. After an overnight fast ketone body uptake will increase the intracellular acetoacetate and β -hydroxybutyrate concentrations. CAT: carnitine acetyltransferase; AAT: acetoacetylCoA thiolase; OAT: 3-oxoacid CoA transferase; PT: pyruvate transporter; PDH: pyruvate dehydrogenase.

Hyperpolarized ^{13}C pyruvate alone, as a mimic of carbohydrate metabolism in general, has been used in promising pre-clinical investigations of myocardial metabolism in a perfused heart model of myocardial ischemia⁴⁷ and *in vivo*¹⁵. The effect of increased fatty acid availability on the metabolism of hyperpolarized pyruvate have been studied in perfused heart^{33;35}. Hyperpolarized [1- ^{13}C]butyrate was recently proposed as a substrate to study cardiac fatty acid metabolism². This short chain fatty acid does not need carnitine acyl transferase to enter the mitochondrion, unlike long chain fatty acids, and it effectively competes with long chain fatty acids for β -oxidation. Metabolism of hyperpolarized [1- ^{13}C]butyrate provides information about flux through the tricarboxylic acid (TCA) cycle via the formation of [5- ^{13}C]glutamate, the enzymatic activity of carnitine acetyl transferase (CAT) and pseudoketogenesis¹¹ via the formation of [1- ^{13}C] β -hydroxybutyrate (BHB) and [1- ^{13}C]acetoacetate (AcAc).

The considerable advantage of the hyperpolarized ^{13}C MR method over PET in the context of substrate competition is that chemical reactions are immediately detected, not simple uptake and export. To date, pyruvate, lactate and acetate are the only hyperpolarized substrates that have been used to probe real-time cardiac metabolism *in vivo*. The aim of the present study was to assess, *in vivo* and in real time, the competition between carbohydrate and fatty acid utilization in the fed and fasted metabolic states of the rat heart using hyperpolarized [1- ^{13}C]pyruvate and [1- ^{13}C]butyrate.

4.2 Materials and Methods

Samples preparation and hyperpolarization protocol

Sodium [1- ^{13}C]butyrate, sodium [1- ^{13}C]pyruvate and TEMPO (2,2,6,6-tetramethyl-1-piperidinyloxy) nitroxyl radicals were obtained from Sigma-Aldrich (Buchs, Switzerland). Sodium [1- ^{13}C]pyruvate was dissolved to a concentration of 3.0 M and sodium [1- ^{13}C]butyrate to a concentration of 4.5 M, both with a TEMPO concentration of 33 mM in a 1:2 mixture of $\text{d}_6\text{-EtOD}/\text{D}_2\text{O}$. The solutions were rapidly frozen in liquid nitrogen to form 10 μL beads that were inserted into a sample cup in a 2:3 butyrate/pyruvate mixture to have the same concentration of both substrates. The sample cup was further cooled to 1 ± 0.05 K in a 5 T custom-designed DNP polarizer¹⁰, where the ^{13}C nuclei were dynamically polarized for 2.5 h. Then, using an automated process⁹ the sample was rapidly dissolved using 6.0 mL of pressurized, heated D_2O and transferred within 2 s of dissolution to a separator/infusion pump, containing 0.6 mL of phosphate buffered saline and heparin, located inside a 9.4 T horizontal bore magnet. Subsequently, 1.0 mL of the hyperpolarized solution yielding physiological temperature and pH was automatically infused into the animal during 7 s. The polarization level was 12 ± 1 % in the liquid state at the time of the injection. Animals All animal studies conformed to institutional guidelines. Wild-type male Sprague Dawley rats (277 ± 26 g) were anesthetized with 1.5% isoflurane in oxygen. A catheter was placed into the femoral vein for intravenous delivery of the hyperpolarized solution. A second catheter was placed in the artery to monitor the blood pressure. The respiration rate, cardiac rhythm, and temperature were monitored

Table 4.1: Average glucose levels and body weight of all animals used in this study

| Parameter | Fed | Fasted |
|--------------------|---------------|---------------|
| Body weight [gram] | 288 \pm 18 | 265 \pm 22 |
| Glucose [mM] | 9.0 \pm 0.7 | 4.5 \pm 1.0 |

and maintained stable. Six groups of animals were studied and each animal was injected once. Each group was exposed to an injection of hyperpolarized butyrate ($n = 12$), pyruvate ($n = 10$) or both ($n = 14$) and the animals were either in a fed or fasted state. The animals were fasted overnight by placing them in a clean cage without food the day before the experiment at around 6 pm. All experiments on fasted animals were performed in the morning and the experiments on fed animals early in the afternoon. Glucose levels were measured to determine the levels of fasting and are displayed in table 4.1.

Animal physiology was not affected by the injections and body temperature as well as respiration and heart rates were stable through all experiments.

***in vivo* magnetic resonance spectroscopy**

Measurements were carried out on a 9.4 T / 31 cm actively shielded animal scanner (Varian/-Magnex). A custom-made radiofrequency (RF) hybrid probe consisting of a 10 mm diameter proton surface coil and a quadrature 10 mm diameter ^{13}C surface coil was positioned over the chest of the rat for transmission and reception, localizing the signals from the cardiac muscle (Appendix A.1). To generate an external reference signal, a small sphere filled with a water solution saturated with $[1-^{13}\text{C}]\text{glucose}$ was placed in the center of the carbon coil. Acquisition of gradient echo proton images confirmed the correct position of the heart. Shimming was performed to reduce the localized proton line width in a myocardial voxel of 4x5x5 mm to 20-30 Hz using FASTESTMAP¹⁶. The NMR console was triggered to start acquisition at the beginning of the automated injection process, 3 s after dissolution of the hyperpolarized sample. Series of single pulse acquisitions were recorded using 30 degree adiabatic RF pulses (BIR4) applied every 3 s with ^1H decoupling using WALTZ. Typically 40 - 60 FIDs were acquired with 4129 complex data points over a 20000 Hz bandwidth. All acquisitions were cardiac triggered and respiratory gated. The adiabatic pulse offset and power was calibrated to ensure a 30° excitation pulse for all observed metabolites in the entire tissue of interest. Following data acquisition, 200 μL liquid samples were extracted from the separator/infusion pump to precisely determine the infused $[1-^{13}\text{C}]\text{butyrate}$ and $[1-^{13}\text{C}]\text{pyruvate}$ concentration using a high resolution 400 MHz NMR spectrometer.

Table 4.2: Chemical shifts of observed metabolites following the injection of hyperpolarized sodium $[1-^{13}\text{C}]$ butyrate and sodium $[1-^{13}\text{C}]$ pyruvate.

| Metabolite | Chemical Shift (ppm) |
|---|----------------------|
| $[1-^{13}\text{C}]$ butyrate | 185.0 |
| $[1-^{13}\text{C}]$ lactate | 183.5 |
| $[5-^{13}\text{C}]$ glutamate | 182.45 |
| $[1-^{13}\text{C}]\beta$ -hydroxybutyrate | 181.6 |
| $[1-^{13}\text{C}]$ pyruvate hydrate | 179.8 |
| $[5-^{13}\text{C}]$ citrate | 179.7 |
| $[1-^{13}\text{C}]$ alanine | 177.0 |
| $[1-^{13}\text{C}]$ acetoacetate | 176.5-176.0 |
| $[1-^{13}\text{C}]$ acetylcarnitine | 173.9 |
| $[1-^{13}\text{C}]$ pyruvate | 171.4 |
| ^{13}C bicarbonate | 161.3 |
| $^{13}\text{CO}_2$ | 126 |

Data analysis

The ^{13}C NMR spectra of each time series were summed for the time period during which the hyperpolarized resonances were visible and the resulting summed spectra were fitted to Lorentzian line shapes using Bayesian analysis. The infused substrates and their corresponding metabolic products were assigned according to the chemical shifts reported in table 4.2.

The total integral of alanine was used as a reference for cardiac tissue specific metabolism, instead of pyruvate or butyrate, and has been shown to be a representative marker for intracellular pyruvate concentration. Statistical differences between the ratios of observed metabolites were calculated using a two-tailed t-test for unpaired data with equal variance. Error bars in figures and in the manuscript indicate \pm standard error of the mean (SEM).

4.3 Results

Substrate competition was studied in healthy rat hearts *in vivo* in the fed and fasted state. Fasting induces a shift from carbohydrate to fatty acid oxidation and blood glucose levels decrease⁴². In the present study, overnight fasting resulted in a 50% decrease in plasma glucose compared with animals which were fed *ad libitum* (Table 4.1).

4.3.1 Hyperpolarized $[1-^{13}\text{C}]$ pyruvate injection

Hyperpolarized $[1-^{13}\text{C}]$ pyruvate metabolism lead to the detection of $[1-^{13}\text{C}]$ lactate, $[1-^{13}\text{C}]$ alanine, $^{13}\text{CO}_2$, ^{13}C bicarbonate and the impurity pyruvate hydrate (Figure 4.2a, Table 4.2). The mea-

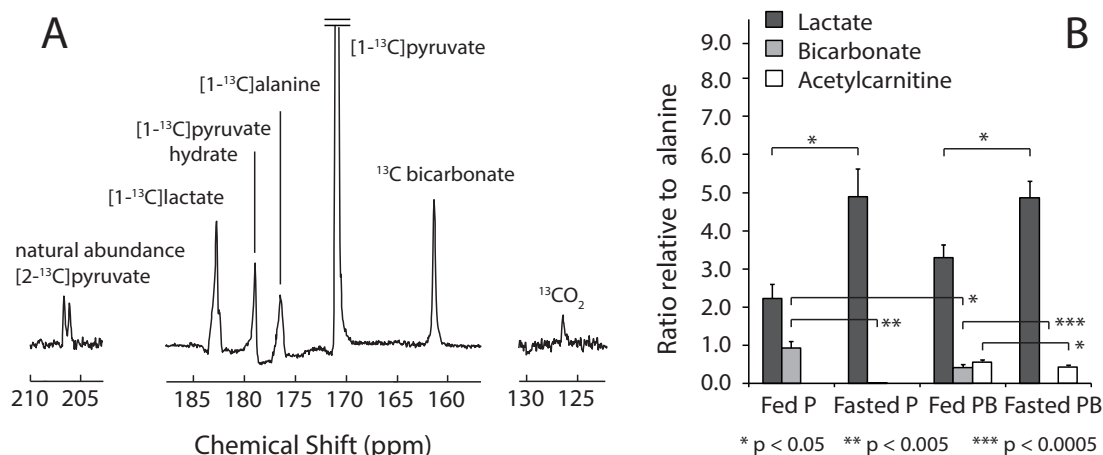


Figure 4.2: *In vivo* cardiac ¹³C spectrum recorded after the injection of hyperpolarized [1-¹³C]pyruvate (A). The following resonances were observed and are displayed using the same scale: [2-¹³C]pyruvate, [1-¹³C]lactate, [1-¹³C]pyruvate hydrate, [1-¹³C]alanine, [1-¹³C]pyruvate, ¹³C bicarbonate and ¹³CO₂. Signal ratios of lactate, bicarbonate and acetylcarnitine relative to alanine (B) in all 4 animal groups where hyperpolarized [1-¹³C]pyruvate was either injected separately (Fed pyruvate, P or Fast P) or co-injected with hyperpolarized [1-¹³C]butyrate (B) (Fed PB or Fast PB) in both fed and fasted animals. Asterisks denote statistical significant differences in metabolite ratios where *** $p < 0.00005$, ** $p < 0.005$, * $p < 0.05$. Significant changes were only reported between groups where one single condition was altered.

sured ratios between the total bicarbonate and pyruvate signal integrals (3%) were consistent with the *in vivo* data previously acquired in fed rat hearts^{19;46}. To avoid misinterpretations resulting from the ubiquitous [1-¹³C]pyruvate signal and its compartment specific downstream metabolites, metabolite signals were normalized to the total area of alanine. Alanine is preferred as a marker for intracellular pyruvate concentration occurring specifically in cardiac tissue²⁸. After an overnight fast, the ratio of bicarbonate to alanine was markedly reduced from 0.93 ± 0.18 to 0.00 ± 0.00 and a significant increase in the lactate to alanine ratio (2.23 ± 0.37 to 4.89 ± 0.72) associated with an increase in the NADH/NAD⁺ ratio was observed (Figure 4.2b). The fact that the bicarbonate signal decreased dramatically in fasted animals is due to a reduction in PDH flux, an observation made previously and confirmed in this study.

4.3.2 Hyperpolarized [1-¹³C]butyrate injection

[1-¹³C]butyrate was used to study cardiac short-chain fatty acid metabolism *in vivo*. The C1 of butyrate has a relatively long longitudinal relaxation time (T_1) compared with other fatty acids (25 s at 9.4 T), and its resonance signal does not overlap with that of [5-¹³C]glutamate like [1-¹³C]acetate does (Figure 4.3a).

The following metabolites were detected *in vivo*: [5-¹³C]glutamate, [1-¹³C]β-hydroxybutyrate,

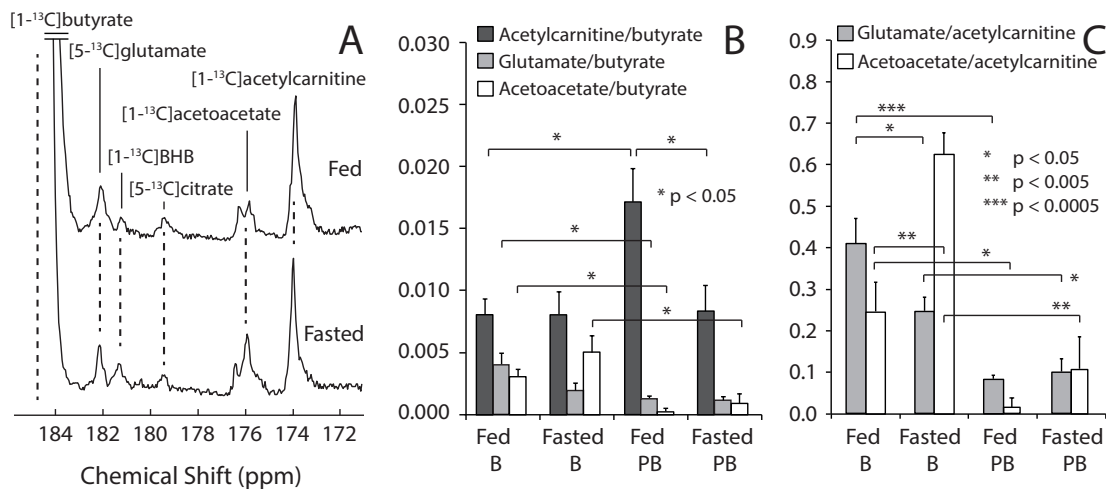


Figure 4.3: In vivo cardiac ^{13}C spectrum recorded after the injection of hyperpolarized $[1-^{13}\text{C}]$ butyrate in the fed and fasted state (A). The following metabolites were observed: $[1-^{13}\text{C}]$ butyrate, $[5-^{13}\text{C}]$ glutamate, $[1-^{13}\text{C}]\beta$ -hydroxybutyrate, $[5-^{13}\text{C}]$ citrate, $[1-^{13}\text{C}]$ acetoacetate and $[1-^{13}\text{C}]$ acetylcarnitine. The relative signal ratios of acetylcarnitine, glutamate and acetoacetate to their precursor butyrate (B) and glutamate and acetoacetate relative to acetylcarnitine (C) in all 4 animal groups following a hyperpolarized $[1-^{13}\text{C}]$ butyrate injection (Fed B or Fast B) and coinjection with hyperpolarized $[1-^{13}\text{C}]$ pyruvate (Fed BP or Fast BP) in both fed and fasted animals. Asterisks denote statistical significant differences between metabolite ratios where *** $p < 0.0005$, ** $p < 0.005$, * $p < 0.05$. Significant changes were only reported between groups where one single condition was altered.

[5-¹³C]citrate, [1-¹³C]acetoacetate, and [1-¹³C]acetylcarnitine. The signal-to-noise ratio (SNR) of glutamate, acetoacetate and acetylcarnitine was sufficient to be reliably detected in all the hyperpolarized butyrate injections. This is the first observation of TCA cycle intermediates following fatty acid oxidation *in vivo*. In terms of absolute flux into glutamate, it should be noted that the appearance of label at the 5-position undercounts butyrate oxidation by half, since the 3-position of butyrate is not enriched. Butyrate β -oxidation produces two units of acetylCoA, only one of which is labeled and hyperpolarized.

Since butyrate, like pyruvate, is not uniquely located in the myocardium, acetylcarnitine was additionally used as an internal reference. It was observed that the glutamate to acetylcarnitine ratio was significantly lower in fasted animals compared to fed animals, from 0.41 ± 0.06 to 0.25 ± 0.03 (Figure 4.3c). Additionally, a significant increase (0.24 ± 0.07 to 0.63 ± 0.05) of the ketone body acetoacetate relative to acetylcarnitine was observed (4.3c). The ratio of acetylcarnitine relative to butyrate did not show a significant difference (Figure 4.3b).

4.3.3 Hyperpolarized [1-¹³C]pyruvate and [1-¹³C]butyrate co-injection

The third type of experiment aimed at studying the competition between carbohydrates and fatty acids by co-injecting both [1-¹³C]pyruvate and [1-¹³C]butyrate as substrates. All metabolites observed in the separate injections could be detected since the carbon line widths were narrow enough to avoid overlaps with the exception of [5-¹³C]citrate, which overlaps with the [1-¹³C]pyruvate hydrate peak (Figure 4.4b).

The hyperpolarized solutions were prepared such as to inject an equal amount of both substrates. Injected pyruvate and butyrate concentrations were determined via high-resolution NMR following the *in vivo* experiments. The average concentration ratio was 0.98 ± 0.08 , and thus assumed equal.

The number of significant differences between the fed and fasted animals generated by the dual injection approach is large, and choice of the order of presentation was made by first looking at carbohydrate metabolism, followed by fatty acid metabolism.

From the data obtained in the fed state with and without co-injection of butyrate, it appears that its transport is not sufficiently fast to completely out-compete pyruvate for the production of acetylCoA. All data was analyzed in terms of ratios to the alanine signal (see Figure 2). The results reveal significant changes in the lactate to alanine ratio between the fed and fasted state during co-injection, 3.30 ± 0.33 to 4.87 ± 0.43 ($p=0.02$), as well as in the ratio of acetylcarnitine to alanine ($p=0.05$, Figure 4.3b) and highly significant changes in bicarbonate to alanine ratios ($p=0.00005$).

As a result of the co-injection with the fatty acid butyrate in fed animals, the relative bicarbonate to alanine ratio decreases as one would expect ($p=0.01$), and marginally significant changes in the lactate to alanine ratio were noted, 2.23 ± 0.38 to 3.30 ± 0.33 ($p=0.07$).

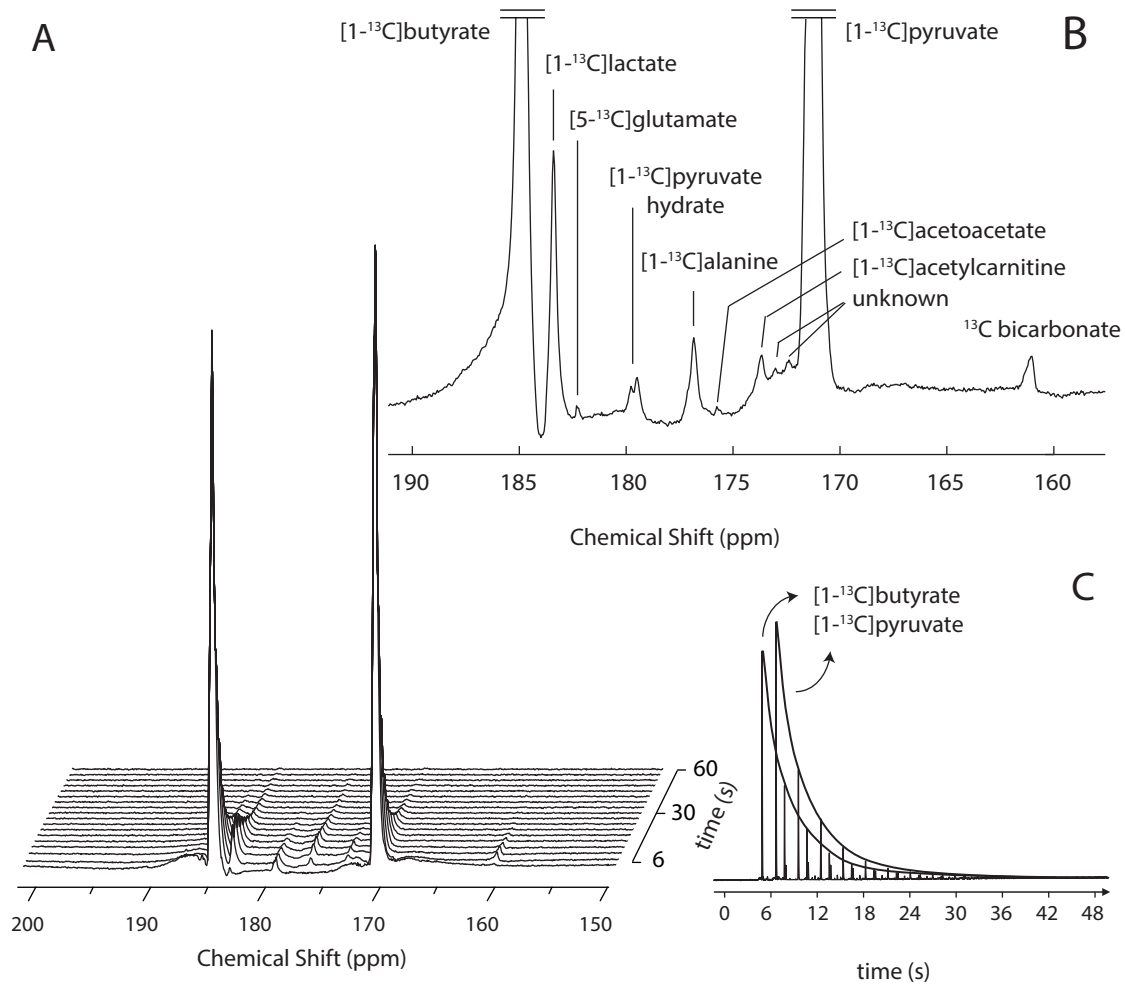


Figure 4.4: Spectral time course of myocardial metabolism *in vivo* following the co-injection of hyperpolarized $[1-^{13}\text{C}]$ butyrate and $[1-^{13}\text{C}]$ pyruvate (A). The acquisition started simultaneous with the co-injection with a time interval of 3 s. The first two spectra were omitted since no metabolites were observed. A spectral sum is shown in (B) revealing the detection of $[1-^{13}\text{C}]$ butyrate, $[1-^{13}\text{C}]$ lactate, $[5-^{13}\text{C}]$ glutamate, $[1-^{13}\text{C}]$ pyruvate hydrate, $[1-^{13}\text{C}]$ alanine, $[1-^{13}\text{C}]$ acetoacetate, and $[1-^{13}\text{C}]$ acetylcarnitine, unidentified $[2-^{13}\text{C}]$ pyruvate and ^{13}C bicarbonate. Horizontal time course of the hyperpolarized signals showing similar decay and acute substrate delivery (C).

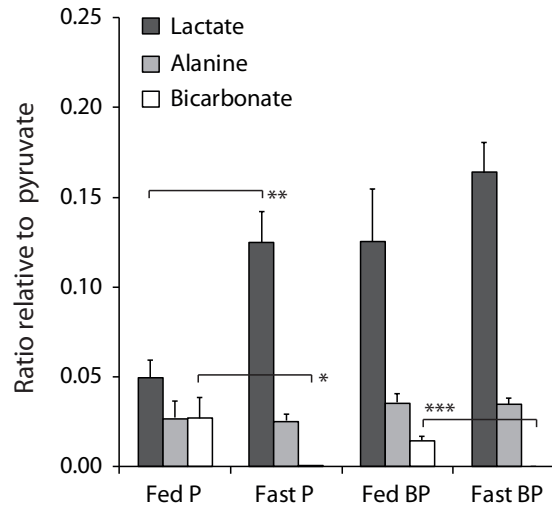


Figure 4.5: Signal ratios of lactate, alanine and bicarbonate relative to hyperpolarized [1-¹³C]pyruvate in all 4 animal groups where pyruvate was either injected uniquely (Fed P or Fast P) or co-injected with hyperpolarized [1-¹³C]butyrate (Fed BP or Fast BP) in both fed and fasted animals. Asterisks denote statistical significant differences in metabolite ratios where *** $p < 0.00005$, ** $p < 0.05$, * $p < 0.5$. Significant changes were only reported between groups where one condition was altered.

From the perspective of butyrate metabolism, the co-injection of pyruvate decreases the glutamate to acetylcarnitine ratio (both metabolites derived exclusively from butyrate) significantly in both fed and fasted states (Figure 4.3c). Taking into consideration the acetylcarnitine to butyrate ratio (Figure 4.3b) in the fed state, which increases significantly from 0.008 ± 0.001 to 0.017 ± 0.003 , the change in glutamate to acetylcarnitine ratio (Figure 4.3c) decreased significantly upon introduction of pyruvate. Additionally, the presence of pyruvate completely quenches the appearance of acetoacetate derived from butyrate.

4.4 Butyrate and Pyruvate Flux Analysis

In this section is briefly described how to interpret the signal ratios following the injection of hyperpolarized [1-¹³C]butyrate. This was done by looking at the isotope balance equations and the corresponding metabolic fluxes.

The ¹³C labeling in acetylCoA (A.CoA), acetylcarnitine (A.Car) and glutamate (Glu) can be described with the following equations after the injection of hyperpolarized [1-¹³C]butyrate, where * refers to the ¹³C labeled metabolite and otherwise its total pool size:

$$\frac{d[A.CoA^*]}{dt} = V_{Beta} \frac{[Ac.Ac.CoA^*]}{[Ac.Ac.CoA]} \quad (4.1)$$

$$+ V_{CAT} \frac{[A.Car^*]}{[A.Car]} - V_{CAT} \frac{[A.CoA^*]}{[A.CoA]} - V_{TCA} \frac{[A.CoA^*]}{[A.CoA]}$$

$$\frac{d[A.Car^*]}{dt} = V_{CAT} \frac{[A.CoA^*]}{[A.CoA]} - V_{CAT} \frac{[A.Car^*]}{[A.Car]} \quad (4.2)$$

$$\frac{d[Glu^*]}{dt} = V_{TCA} \frac{[A.CoA^*]}{[A.CoA]} \quad (4.3)$$

Where V_{Beta} refers to the β -oxidation flux, V_{CAT} the flux through carnitine acetyl transferase and V_{TCA} the flux through the tricarboxylic acid cycle. Combining the first 2 equations leads to:

$$\frac{d[A.Car^*]}{dt} + \frac{d[A.CoA^*]}{dt} = V_{Beta} \frac{[Ac.Ac.CoA^*]}{[Ac.Ac.CoA]} - V_{TCA} \frac{[A.CoA^*]}{[A.CoA]} \quad (4.4)$$

Combining Eq 3 and 4:

$$\frac{d[A.Car^*]}{dt} + \frac{d[A.CoA^*]}{dt} = V_{Beta} \frac{[Ac.Ac.CoA^*]}{[Ac.Ac.CoA]} - \frac{d[Glu^*]}{dt} \quad (4.5)$$

Based on small pool size approximation, $d[A.CoA]/dt \ll d[A.Car]/dt$ we can neglect changes in the acetylCoA pool and Eq. 5 becomes

$$\frac{d[A.Car^*]}{dt} = V_{Beta} \frac{[Ac.Ac.CoA^*]}{[Ac.Ac.CoA]} - \frac{d[Glu^*]}{dt} \quad (4.6)$$

Note that V_{Beta} constitutes the flux through the acetoacetylCoA thiolase reaction, the last enzymatic reaction in the β -oxidation pathway. The flux V_{Beta} should not be affected by fasting and is therefore constant. However, fasting would increase the unlabeled acetoacetylCoA pool and simultaneous pyruvate oxidation increases the unlabeled acetylCoA pool. Therefore our results can be explained using Eq. 4 and 6. The glutamate to acetylcarnitine ratio can be

described as follows:

$$\frac{[Glu^*]}{[A.Car^*]} = \frac{V_{TCA} \frac{[A.CoA^*]}{[A.CoA]}}{V_{Beta} \frac{[Ac.Ac.CoA^*]}{[Ac.Ac.CoA]} - V_{TCA} \frac{[Ac.CoA^*]}{[Ac.CoA]}} \quad (4.7)$$

Given that V_{Beta} and V_{TCA} remain constant the ratio of $[A.CoA^*]/[A.CoA]$ must decrease, in order to decrease the ratio of glutamate to acetylcarnitine. Meaning that the ratio of detected glutamate to acetylcarnitine is related to the ratio of labeled to unlabeled acetylCoA.

4.5 Discussion

4.5.1 Pyruvate Injections

The pyruvate doses in this study were well below the level at which perturbations in cardiac metabolism were previously reported^{1;35;44}. The detection of both bicarbonate and carbon dioxide in the fed animals with the injection of hyperpolarized pyruvate allowed us to determine the pH applying the Henderson-Hasselbach equation¹³.

Tissue pH can be determined from the concentration ratio of endogenous ^{13}C labeled bicarbonate and $^{13}CO_2$ as follows:

$$pH = pK_a + \log_{10} \frac{[HCO_3^-]}{[CO_2]} \quad (4.8)$$

where pK_a is the acid dissociation constant of CO_2 , which was assumed to be 6.15⁴³.

A stable value of 7.3 ± 0.1 was observed and demonstrated that the injections did not significantly disturb the body's pH during the experiment (Figure 4.6). The reduction of the bicarbonate intensity after overnight fasting was more pronounced in our experiments (declined 50%) compared to an earlier study⁴⁶ where the plasma glucose concentration only dropped 30%. It can be inferred that FFA's were higher in the current rats, which would explain the decreased bicarbonate signal. Significant changes in lactate to alanine ratios were observed, as reported in the liver^{18;32}. In summary, the $[1-^{13}C]$ pyruvate injections produced exactly the responses that would be expected given previous work in the literature.

4.5.2 Butyrate Injections

The heart is not a ketogenic organ. The ^{13}C labeling observed in β -hydroxybutyrate and acetoacetate is not a result of hepatic ketogenesis followed by shunting of ketone bodies to the

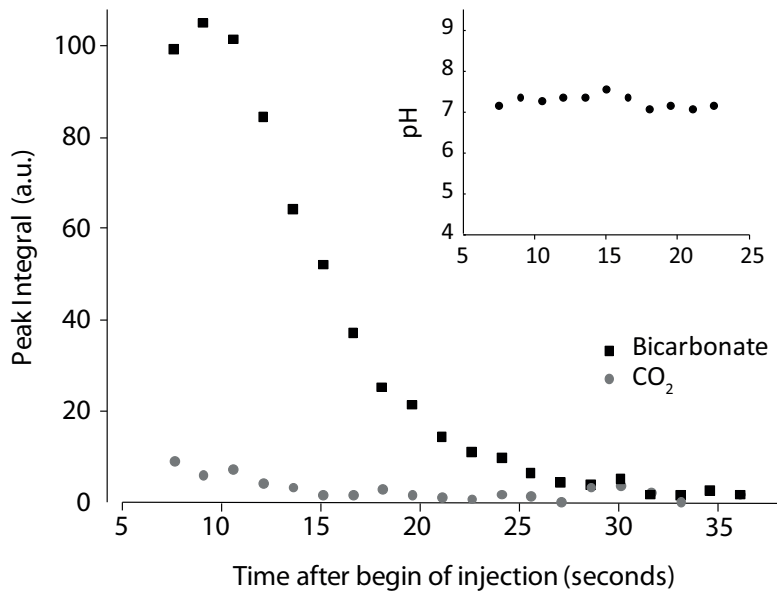


Figure 4.6: Time course of the ^{13}C labeled bicarbonate and carbon dioxide signal integrals. The point by point ratio of these biomolecules were used to calculate the pH using equation 4.8.

heart, but due to exchange between acetoacetylCoA and free, unlabeled acetoacetate in the heart itself¹¹. This is supported by the myocardial activity of 3-oxo-acidCoA transferase, which is 60 times greater than the net myocardial uptake of ketone bodies⁶. Also, these ketone bodies were observed *in vitro* in a perfused heart injected with hyperpolarized $[1-^{13}\text{C}]$ butyrate². Finally, the line shape of the observed ketone bodies resembles that of metabolites present in the myocardium and not in the ventricular blood pool. These observations suggest that the observed ketone bodies are formed in the myocardium. The exchange between acetoacetate and acetoacetylCoA is a mitochondrial process since both β -hydroxybutyrate dehydrogenase and 3-oxoacid CoA transferase are exclusively present in the mitochondrial space. AcetoacetylCoA thiolase can be found in both cytosolic and mitochondrial compartments but since the mitochondrial activity is much larger it was assumed in this report that all three pseudoketogenic enzymatic reactions are of mitochondrial nature.

The pulse bandwidth and power used here is in principle sufficient to excite the resonance of $[3-^{13}\text{C}]$ acetoacetate at 209 ppm³⁴ but was not present in detectable amounts in this study. The absence of the $[3-^{13}\text{C}]$ acetoacetate resonance suggest that during the timeframe of our experiment the label scrambling due to acetyl group circulation through the acetylCoA pool is negligible, and thus no flux from acetylCoA to acetoacetate via acetoacetylCoA is observable. In previous studies using hyperpolarized acetate, which is not β -oxidized, ketone body formation from acetylCoA in cardiac and skeletal muscle was also absent^{5;20}. This indicates that acetoacetylCoA, a product of β -oxidation, is a key metabolite to the formation of the observable ketone bodies (Figure 1).

Comparing fed versus fasted state, the glutamate to acetylcarnitine ratio is lower while the acetylcarnitine to butyrate ratio remains unchanged, indicating a decrease in labeling of glutamate. Also, the levels of acetylcarnitine and acetylCoA change only moderately. Since cardiac glutamate pool sizes remain unchanged over a fasting period for up to 48h in cardiac⁴⁹ and skeletal muscle²¹, and the ratio of acetylcarnitine to free carnitine remains unchanged after 48h of fasting⁷, it is most likely that the observed decrease in glutamate labeling is not a result of a change in pool size (See the section about the flux analysis). Conversely, the acetoacetate resonances are more intense in fasted animals. The formation of ketone bodies from butyrate is positively stimulated with increasing ketone body concentrations⁵⁰, as is the case during fasting since the pool sizes of acetoacetate and β -hydroxybutyrate increase 5 fold after 24h of fasting²⁵. Increases in ketone body concentrations are accompanied by an increase in the acetoacetylCoA concentration, which was observed during acetoacetate infusion in perfused hearts³¹. In summary, it is believed that the presence of additional intracellular unlabeled acetoacetate contributes to an increase in ketone body labeling from hyperpolarized butyrate via pseudoketogenesis, which constitutes an isotopic exchange with acetoacetylCoA and not a net formation of ketone bodies¹¹. The amount of label flow through β -oxidation in both nutritional states seems to be unchanged since the sum of ^{13}C label from acetylcarnitine, glutamate and acetoacetate relative to butyrate is constant (Figure 4.3b), an indication that the rate of butyrate oxidation is not affected after overnight fasting. This means that in both nutritional states the same amount of label ends up in acetoacetylCoA, but the label propagation from there onwards is changed as a consequence of competition with unlabeled ketone bodies, FFA's, and the larger unlabeled acetoacetylCoA pool during fasting.

Based on comparisons relative to the butyrate signal, acetylcarnitine is not significantly changed and the fluxes maintaining the acetylcarnitine pool acting as storage for excess mitochondrial acetylCoA does not seem to be affected. Therefore, the glutamate to acetylcarnitine ratio is meaningful for assessing the flow of acetylCoA derived from butyrate through the TCA cycle as opposed to that which is deposited in the cellular energy reserve of acetylcarnitine. Because both acetylcarnitine and glutamate are generated from the same pool of 2-carbon acetyl-subunits, the relative ratios should not have to be scaled for the 1 to 2 conversion of butyrate to acetylCoA. It was clearly observed that this ratio is substantially reduced in fasted animals (Figure 4.3c), indicative of the competition between the injected butyrate and the increased, unlabeled ketones and FFA's present in the fasted state. The increased signal associated with the hyperpolarized acetoacetate upon fasting is a further indication of the increased concentration of ketones available for pseudoketogenesis; pseudoketogenesis from $[1-^{13}\text{C}]$ butyrate is facilitated by the higher concentration of acetoacetate in the fasted state.

4.5.3 Competition between pyruvate and butyrate

Competition between butyrate and pyruvate in the fed animals caused a reduction in the observed $[^{13}\text{C}]$ bicarbonate signal ($p=0.01$, Figure 4.2b), $[5-^{13}\text{C}]$ glutamate signal ($p=0.02$ relative to butyrate and $p=0.0001$ relative to acetylcarnitine, Figure 4.3b), a nearly absent $[1-$

^{13}C]acetoacetate signal ($p=0.03$ relative to butyrate and $p=0.01$ relative to acetylcarnitine, Figure 4.3b,c), an increase in the $[1-^{13}\text{C}]$ acetylcarnitine signal ($p=0.02$ relative to butyrate, Figure 4.3a), and in the $[1-^{13}\text{C}]$ lactate signal that did not quite reach statistical significance ($p=0.07$, Figure 4.2b). In fasted animals, co-injection resulted in a decrease in the acetylcarnitine to alanine ratio ($p=0.05$). All of these observations fit into a detailed narrative of substrate competition in the myocardium.

It is known that the presence of medium chain fatty acids can severely restrict the entry of pyruvate into the TCA cycle as well as increase the lactate pool size in perfused hearts³³. These results are largely duplicated *in vivo*, with the caveat that the pyruvate and butyrate co-injection did not take place over a period long enough to establish a metabolic steady state. High concentrations of pyruvate (5 mM) can partially overcome PDH inhibition by high fatty acid concentrations³⁷. Assuming an instantaneous distribution of the hyperpolarized substrate, the maximum attainable plasma concentration of pyruvate was on the order of 4 mM. Hence, the production of $[^{13}\text{C}]$ bicarbonate was only halved as opposed to abolished when butyrate was also present, and lactate pool size changed only marginally. Nevertheless these results indicate an almost instantaneous adaptation of myocardial substrate utilization.

These changes are also a direct reflection of butyrate uptake in the myocardium. In a conjugate sense, the increase in $[1-^{13}\text{C}]$ acetylcarnitine and the decrease of the $[5-^{13}\text{C}]$ glutamate and $[1-^{13}\text{C}]$ acetoacetate signals, all derived initially from butyrate metabolism, are modulations due to competition from pyruvate for the limited number of CoA units in the mitochondria. Acetylcarnitine serves as a buffer for extra acetyl units that exceed the capacity of the TCA cycle for oxidation and this circulation of acetyl groups is a fast, well equilibrated process^{12;40;45}. When pyruvate is co-injected, it is surmised that free CoA is rapidly reacted to acetylCoA, and the extra acetyl units derived from butyrate oxidation are stored by reaction with carnitine, resulting in the increased observed acetylcarnitine. The lowering of the $[5-^{13}\text{C}]$ glutamate signal is a result of the same phenomena. Note that entry of pyruvate into the TCA cycle results in removal of the hyperpolarized $[1-^{13}\text{C}]$ label and subsequent oxidation of the unlabeled C2 and C3 positions, which cannot produce labeling in the C5 of glutamate, hence the lower total glutamate signal. In the case of fasting, co-injection results in a decrease in ^{13}C labeling in acetylcarnitine because of reduced flux of ^{13}C label from butyrate into acetylCoA, another example of the real-time effect of substrate competition.

The phenomenon of pseudoketogenesis in the myocardium seems the most likely explanation for the appearance of acetoacetate and β -hydroxybutyrate when hyperpolarized $[1-^{13}\text{C}]$ butyrate is injected¹¹. Understanding the mechanism of pseudoketogenesis (Figure 4.1) reveals why it is subject to manipulation by the presence of supra-physiological concentrations of pyruvate. Following transformation of $[1-^{13}\text{C}]$ butyrate to acetoacetylCoA, pseudoketogenesis results in the exchange of free acetoacetate in the mitochondria with the labeled acetoacetylCoA²⁷, giving rise to the ketone signals observed when only butyrate is injected (Figure 3). However, an explanation for the complete lack of ketone signal when butyrate is co-injected with pyruvate is more complicated. Pyruvate transport into the mitochondria can

actually be mediated not only by the antiporting of hydroxide but also by a variety of other compounds^{17;39}. One compound that is particularly effective in this function is acetoacetate. It is hypothesized that the injection of pyruvate not only competes with butyrate for oxidation, but also results in a depletion of unlabeled acetoacetate from the mitochondria during the mitochondrial pyruvate transport process. The consequent lack of a free unlabeled acetoacetate for exchange with the hyperpolarized acetoacetylCoA dramatically reduces the concentration of free, hyperpolarized ketones. Further experiments, for example blocking the mitochondrial pyruvate transporter, would be required to confirm this hypothesis.

These experiments demonstrate that the chemical selectivity inherent to magnetic resonance, when paired with the sensitivity enhancement of hyperpolarization, can be harnessed to produce a protocol that assesses substrate competition in real time, *in vivo*, in the functioning heart. A simple modification of substrate availability via fasting produced significant changes in pyruvate and butyrate metabolism, both when administered separately and in competition. Butyrate metabolism appears to be subject to the phenomenon of pseudoketogenesis, over a time period of seconds. Interestingly, co-administration of pyruvate with butyrate appeared to block this phenomenon, most likely due to acetoacetate anti-transport caused by the bolus of pyruvate. The clinical potential of the use of ¹³C hyperpolarized magnetic resonance techniques to probe *in vivo* metabolism has been recently discussed and the first trials in humans for application in cancer monitoring and diagnosis has already started²⁶. Applications in cardiology also seem at least as promising, and are expected to affect both preclinical and clinical practice³⁰. The protocol suggested here should augment the usefulness of hyperpolarized imaging further.

References

- [1] H. J. Atherton, M. A. Schroeder, M. S. Dodd, L. C. Heather, E. E. Carter, L. E. Cochlin, S. Nagel, N. R. Sibson, G. K. Radda, K. Clarke, and D. J. Tyler. Validation of the in vivo assessment of pyruvate dehydrogenase activity using hyperpolarised c-13 mrs. *Nmr in Biomedicine*, 24(2):201–208, 2011.
- [2] D. Ball, B. Rowlands, M. Dodd, L. Le Page, V. Ball, C. Carr, K. Clarke, and D. Tyler. Validation of the in vivo assessment of pyruvate dehydrogenase activity using hyperpolarised c-13 mrs. *Magnetic Resonance in Medicine*, 2013.
- [3] A. M. Barrett. Adventitious factors affecting concentration of free fatty acids in plasma of rats. *British Journal of Pharmacology and Chemotherapy*, 22(3):577–584, 1964.
- [4] E. Bassenge, V. E. Wendt, Schollme.P, G. Blumchen, Gudbjarn.S, and R. J. Bing. Effect of ketone bodies on cardiac metabolism. *American Journal of Physiology*, 208(1):162–168, 1965.
- [5] J. A. M. Bastiaansen, T. Cheng, M. Mishkovsky, J. M. N. Duarte, A. Comment, and R. Gruetter. In vivo enzymatic activity of acetylcoA synthetase in skeletal muscle revealed by ^{13}C turnover from hyperpolarized [1- ^{13}C]acetate to [1- ^{13}C]acetylcarnitine. *Biochimica Et Biophysica Acta*, 1830(8):4171–4178, 2013.
- [6] A. Beis, V. A. Zammit, and E. A. Newsholme. Activities of 3-hydroxybutyrate dehydrogenase, 3-oxoacid coa-transferase and acetoacetyl-coa thiolase in relation to ketone-body utilization in muscles from vertebrates and invertebrates. *European Journal of Biochemistry*, 104(1):209–215, 1980.
- [7] T. Bohmer, K. R. Norum, and J. Bremer. Relative amounts of long-chain acylcarnitine acetylcarnitine and free carnitine in organs of rats in different nutritional states and with alloxan diabetes. *Biochimica Et Biophysica Acta*, 125(2):244–251, 1966.
- [8] K. Carvajal and R. Moreno-Sanchez. Heart metabolic disturbances in cardiovascular diseases. *Arch Med Res*, 34(2):89–99, 2003.
- [9] T. Cheng, M. Mishkovsky, J. A. M. Bastiaansen, O. Ouari, P. Hautle, P. Tordo, B. v. d. Brandt, and A. Comment. Method to minimize and monitor in situ the polarization losses in hyperpolarized biomolecules prior to in vivo mr experiments. *Nmr in Biomedicine - In Press*, 2013.
- [10] A. Comment, B. van den Brandt, K. Uffmann, F. Kurdzesau, S. Jannin, J. A. Konter, P. Hautle, W. T. Wenckebach, R. Gruetter, and J. J. van der Klink. Design and performance of a dnp prepolarizer coupled to a rodent mri scanner. *Concepts in Magnetic Resonance Part B: Magnetic Resonance Engineering*, 31B(4):255–269, 2007.
- [11] G. Fink, S. Desrochers, C. Desrosiers, M. Garneau, F. David, T. Daloze, B. R. Landau, and H. Brunengraber. Pseudoketogenesis in the perfused rat-heart. *Journal of Biological Chemistry*, 263(34):18036–18042, 1988.
- [12] I. B. Fritz, S. K. Schultz, and P. A. Srere. Properties of partially purified carnitine acetyltransferase. *Journal of Biological Chemistry*, 238(7):2509, 1963.
- [13] F. A. Gallagher, M. I. Kettunen, S. E. Day, D. E. Hu, J. H. Ardenkjaer-Larsen, R. in't Zandt, P. R. Jensen, M. Karlsson, K. Golman, M. H. Lerche, and K. M. Brindle. Magnetic resonance imaging of ph in vivo using hyperpolarized (^{13}C)-labelled bicarbonate. *Nature*, 453(7197):940–U73, 2008.

-
- [14] D. M. Gibson and R. A. Harris. *Metabolic Regulation in Mammals*. Taylor and Francis, London, 2002.
- [15] K. Golman, J. S. Petersson, P. Magnusson, E. Johansson, P. Akeson, C. M. Chai, G. Hansson, and S. Mansson. Cardiac metabolism measured noninvasively by hyperpolarized c-13 mri. *Magnetic Resonance in Medicine*, 59(5):1005–1013, 2008.
- [16] R. Gruetter and I. Tkac. Field mapping without reference scan using asymmetric echo-planar techniques. *Magnetic Resonance in Medicine*, 43(2):319–323, 2000.
- [17] A. P. Halestrap. Pyruvate and ketone-body transport across the mitochondrial membrane. exchange properties, ph-dependence and mechanism of the carrier. *Biochemical Journal*, 172(3):377–387, 1978.
- [18] S. Hu, A. P. Chen, M. L. Zierhut, R. Bok, Y. F. Yen, M. A. Schroeder, R. E. Hurd, S. J. Nelson, J. Kurhanewicz, and D. B. Vigneron. In vivo carbon-13 dynamic mrs and mrsi of normal and fasted rat liver with hyperpolarized c-13-pyruvate. *Molecular Imaging and Biology*, 11(6):399–407, 2009.
- [19] M. A. Janich, M. I. Menzel, F. Wiesinger, E. Weidl, O. Khagai, J. H. Ardenkjaer-Larsen, S. J. Glaser, A. Haase, R. F. Schulte, and M. Schwaiger. Effects of pyruvate dose on in vivo metabolism and quantification of hyperpolarized (13) c spectra. *Nmr in Biomedicine*, 25(1):142–51, 2012.
- [20] P. R. Jensen, T. Peitersen, M. Karlsson, R. In 't Zandt, A. Gisselsson, G. Hansson, S. Meier, and M. H. Lerche. Tissue-specific short chain fatty acid metabolism and slow metabolic recovery after ischemia from hyperpolarized nmr in vivo. *Journal of Biological Chemistry*, 284(52):36077–82, 2009.
- [21] B. M. Jucker, J. M. Ren, S. Dufour, X. Y. Cao, S. F. Previs, K. S. Cadman, and G. I. Shulman. C-13/p-31 nmr assessment of mitochondrial energy coupling in skeletal muscle of awake fed and fasted rats - relationship with uncoupling protein 3 expression. *Journal of Biological Chemistry*, 275(50):39279–39286, 2000.
- [22] A. Kadkhodayan, A. Coggan, and L. Peterson. A pet area of interest: myocardial metabolism in human systolic heart failure. *Heart Failure Reviews*, pages 1–8, 2012.
- [23] B. S. Kalra and V. Roy. Efficacy of metabolic modulators in ischemic heart disease: An overview. *The Journal of Clinical Pharmacology*, 52(3):292–305, 2012.
- [24] P. F. Kantor, A. Lucien, R. Kozak, and G. D. Lopaschuk. The antianginal drug trimetazidine shifts cardiac energy metabolism from fatty acid oxidation to glucose oxidation by inhibiting mitochondrial long-chain 3-ketoacyl coenzyme a thiolase. *Circulation Research*, 86(5):580–588, 2000.
- [25] O. Kraupp, Adlerkas.L, H. Niessner, and B. Plank. Effects of starvation and of acute and chronic alloxan diabetes on myocardial substrate levels and on liver glycogen in rat in vivo. *European Journal of Biochemistry*, 2(2):197–214, 1967.
- [26] J. Kurhanewicz, D. B. Vigneron, K. Brindle, E. Y. Chekmenev, A. Comment, C. H. Cunningham, R. J. DeBerardinis, G. G. Green, M. O. Leach, S. S. Rajan, R. R. Rizi, B. D. Ross, W. S. Warren, and C. R. Malloy. Analysis of cancer metabolism by imaging hyperpolarized nuclei: Prospects for translation to clinical research. *Neoplasia*, 13(2):81–97, 2011.
- [27] B. R. Landau. Reply. *Metabolism*, 42(2):260–262, 1993.
- [28] P. M. Latipaa, K. J. Peuhkurinen, J. Hiltunen, and I. Hassinen. Regulation of pyruvate dehydrogenase during infusion of fatty acids of varying chain lengths in the perfused rat heart. *Journal of Molecular Cell Cardiology*, 17:1161–1171, 1985.
- [29] C. R. Malloy, J. G. Jones, F. M. H. Jeffrey, M. E. Jessen, and A. D. Sherry. Contribution

- of various substrates to total citric acid cycle flux and anaplerosis by ^{13}C isotopomer analysis and O_2 consumption in the heart. *MAGMA*, 4:35–46, 1996.
- [30] C. R. Malloy, M. E. Merritt, and A. D. Sherry. Could (^{13}C) mri assist clinical decision-making for patients with heart disease? *Nmr in Biomedicine*, 24(8):973–979, 2011.
- [31] L. A. Menahan and W. T. Hron. Regulation of acetoacetyl-coa in isolated perfused rat hearts. *European Journal of Biochemistry*, 119(2):295–299, 1981.
- [32] M. E. Merritt, C. Harrison, A. D. Sherry, C. R. Malloy, and S. C. Burgess. Flux through hepatic pyruvate carboxylase and phosphoenolpyruvate carboxykinase detected by hyperpolarized c-^{13} magnetic resonance. *Proceedings of the National Academy of Sciences of the United States of America*, 108(47):19084–19089, 2011.
- [33] M. E. Merritt, C. Harrison, C. Storey, F. M. Jeffrey, A. D. Sherry, and C. R. Malloy. Hyperpolarized ^{13}C allows a direct measure of flux through a single enzyme-catalyzed step by nmr. *Proc Natl Acad Sci U S A*, 104(50):19773–7, 2007.
- [34] R. Miura, Y. Nishina, S. Fujii, and K. Shiga. C-^{13} -nmr study on the interaction of medium-chain acyl-coa dehydrogenase with acetoacetyl-coa. *Journal of Biochemistry*, 119(3):512–519, 1996.
- [35] K. X. Moreno, S. M. Sabelhaus, M. E. Merritt, A. D. Sherry, and C. R. Malloy. Competition of pyruvate with physiological substrates for oxidation by the heart: implications for studies with hyperpolarized $[1-(^{13}\text{C})]$ pyruvate. *American Journal of Physiology-Heart and Circulatory Physiology*, 298(5):H1556–H1563, 2010.
- [36] T. Nagoshi, M. Yoshimura, G. M. C. Rosano, G. D. Lopaschuk, and S. Mochizuki. Optimization of cardiac metabolism in heart failure. *Current Pharmaceutical Design*, 17(35):3846–3853, 2011.
- [37] M. S. Olson, S. C. Dennis, M. S. Debuysere, and A. Padma. Regulation of pyruvate-dehydrogenase in isolated perfused rat-heart. *Journal of Biological Chemistry*, 253(20):7369–7375, 1978.
- [38] R. E. Olson. Effect of pyruvate and acetoacetate on metabolism of fatty acids by perfused rat heart. *Nature*, 195(4841):597–599, 1962.
- [39] G. Paradies. Interaction of α -cyano-cinnamate- c-^{14} with the mitochondrial pyruvate translocator. *Biochimica Et Biophysica Acta*, 766(2):446–450, 1984.
- [40] D. J. Pearson and P. K. Tubbs. Carnitine and derivatives in rat tissues. *Biochemical Journal*, 105(3):953–963, 1967.
- [41] C. f. D. C. Prevention and Prevention. Leading causes of death, 2010.
- [42] C. Robertson, J. C. Goodman, R. G. Grossman, M. Claypool, and A. White. Dietary nonprotein calories and cerebral infarction size in rats. *Stroke*, 23(4):564–568, 1992.
- [43] M. Schroeder, P. Swietach, H. J. Atherton, F. Gallagher, P. Lee, G. K. Radda, K. Clarke, and T. D. J. Measuring intracellular ph in the heart using hyperpolarized carbon dioxide and bicarbonate: a ^{13}C and ^{31}P magnetic resonance spectroscopy study. *Cardiovascular Research*, 86:82–91, 2010.
- [44] M. A. Schroeder, H. J. Atherton, L. E. Cochlin, K. Clarke, G. K. Radda, and D. J. Tyler. The effect of hyperpolarized tracer concentration on myocardial uptake and metabolism. *Magn Reson Med*, 61(5):1007–14, 2009.
- [45] M. A. Schroeder, H. J. Atherton, M. S. Dodd, P. Lee, L. E. Cochlin, G. K. Radda, K. Clarke, and D. J. Tyler. The cycling of acetyl-coenzyme a through acetylcarnitine buffers cardiac substrate supply a hyperpolarized c-^{13} magnetic resonance study. *Circulation-Cardiovascular Imaging*, 5(2):201–U82, 2012.

-
- [46] M. A. Schroeder, L. E. Cochlin, L. C. Heather, K. Clarke, G. K. Radda, D. J. Tyler, and R. G. Shulman. In vivo assessment of pyruvate dehydrogenase flux in the heart using hyperpolarized carbon-13 magnetic resonance. *Proceedings of the National Academy of Sciences of the United States of America*, 105(33):12051–12056, 2008.
 - [47] M. A. Schroeder, A. Z. Lau, A. P. Chen, Y. Gu, J. Nagendran, J. Barry, X. Hu, J. R. Dyck, D. J. Tyler, K. Clarke, K. A. Connelly, G. A. Wright, and C. H. Cunningham. Hyperpolarized ^{13}C magnetic resonance reveals early- and late-onset changes to in vivo pyruvate metabolism in the failing heart. *European Journal of Heart Failure*, 15(2):130–140, 2013.
 - [48] J. Sorensen, S. Valind, and L. G. Andersson. Simultaneous quantification of myocardial perfusion, oxidative metabolism, cardiac efficiency and pump function at rest and during supine bicycle exercise using ^1H - ^{13}C acetate pet - a pilot study. *Clinical Physiology and Functional Imaging*, 30(4):279–284, 2010.
 - [49] H. Taegtmeyer. 6 blind men explore an elephant - aspects of fuel metabolism and the control of tricarboxylic-acid cycle activity in heart-muscle. *Basic Research in Cardiology*, 79(3):322–336, 1984.
 - [50] Weideman.Mj and H. A. Krebs. Fuel of respiration of rat kidney cortex. *Biochemical Journal*, 112(2):149–166, 1969.

Hyperpolarized lactate metabolism in resting skeletal muscle in vivo

5

Abstract

Resting skeletal muscle has a preference for the oxidation of lipids compared to carbohydrates and a shift towards carbohydrate oxidation is observed with increasing exercise. Lactate is not only an end product in skeletal muscle but also an important metabolic intermediate for mitochondrial oxidation. Carbohydrate metabolism in healthy rat skeletal muscle at rest was studied in different nutritional states using hyperpolarized [1- ^{13}C]lactate, a substrate that can be injected at physiological concentrations and leaves other oxidative processes undisturbed. ^{13}C label incorporation from lactate into bicarbonate in fed animals was observed within seconds but was absent after an overnight fast, representing inhibition of the metabolic flux through pyruvate dehydrogenase. A significant decrease in ^{13}C labeling of alanine was observed comparing the fed and fasted group, and was attributed to a change in cellular alanine concentration and not a decrease in enzymatic flux through alanine transaminase. We conclude that lactate can be used to study carbohydrate oxidation in resting skeletal muscle at physiological levels and that the observed pyruvate, alanine, and bicarbonate signals are sensitive markers to probe changes in metabolism as demonstrated by the observed effect of a simple alteration of the nutritional state

Adapted from

Hyperpolarized [1- ^{13}C]lactate metabolism in skeletal muscle

Jessica AM Bastiaansen, Hikari Yoshihara, Yuhei Takado, Rolf Gruetter and Arnaud Comment

Submitted manuscript

5.1 Introduction

To meet its energy demands resting skeletal muscle has a preference for the oxidation of lipids compared to that of carbohydrates^{1;2}. With increasing exercise intensity, a fuel shift is observed from lipid towards carbohydrate utilization and during intense exercise nearly 100% of oxidative capacity is used for the oxidation of carbohydrates^{1;2}. Lactate concentrations in skeletal muscle and plasma are known to increase during exercise, and skeletal muscle is a major producer of lactic acid in the body. However, lactate is not only the product of anaerobic metabolism but also a source of pyruvate, and resting skeletal muscle is even viewed as the most likely primary consumer of lactic acid as a respiratory fuel³⁻⁵. Lactate enters the cell via monocarboxylate transporters and by free diffusion at higher concentrations (>10mM)^{6;7}. Changes in cellular lactate concentrations are affected by the cytosolic redox potential, thus affecting production and utilization of pyruvate. In the cytosol it is transformed into pyruvate by lactate dehydrogenase (LDH) and pyruvate is converted to alanine via alanine transaminase (ALT) (Figure 5.1). Pyruvate is shuttled into the mitochondria and transformed via pyruvate dehydrogenase (PDH) into acetylCoA, a key entry molecule for the tricarboxylic acid cycle. The flux through PDH also results in the formation of CO₂ which equilibrates with bicarbonate.

These aforementioned metabolic pathways can be studied using ¹³C magnetic resonance spectroscopy (MRS), and lactate, being a simple carbohydrate, has previously been used as a substrate for carbohydrate metabolism in resting skeletal muscle and was shown to be readily oxidized^{8;9}. Only the most abundant metabolites can be detected by conventional ¹³C MRS. Recent developments in hyperpolarized ¹³C MRS allow for the detection of less abundant metabolites by increasing the signal-to-noise ratio by several orders of magnitude¹⁰. However, pyruvate, which has been the most widely used substrate for hyperpolarized ¹³C studies of carbohydrate metabolism, has some disadvantages in the applicability to skeletal muscle. Hyperpolarized pyruvate administration results in supraphysiological levels and pyruvate also influences the oxidation of other metabolic substrates. Excess pyruvate of 10mM inhibits the oxidation of palmitate as well as lactate. Conversely, 10mM excess lactate fails to inhibit the oxidation of palmitate and pyruvate¹¹ and does not influence the uptake of glucose, alanine output, or the glycogen store up to 30 mM¹². Lactate does not influence the metabolism of other substrates, and endogenous lactate exceeds cytosolic pyruvate concentrations by an order of magnitude. Another benefit of using lactate as a hyperpolarized ¹³C substrate is that the formation and detection of the pyruvate resonance can be used directly as a marker of its intracellular concentration. This can be used as an intracellular reference for scaling the signals of the downstream metabolites alanine and bicarbonate, and for metabolic modeling studies. The applicability of hyperpolarized [1-¹³C]lactate as a metabolic substrate has recently been demonstrated¹³ and was used to measure the activity of LDH in tumors¹⁴, dichloroacetate modulated changes in PDH flux in hearts¹⁵ and in the brain¹⁶.

The aim of this study was to explore the use of hyperpolarized [1-¹³C]lactate as a suitable probe for investigating carbohydrate oxidation in skeletal muscle in vivo. To determine the sensitivity of hyperpolarized lactate metabolism to metabolic changes, two nutritional

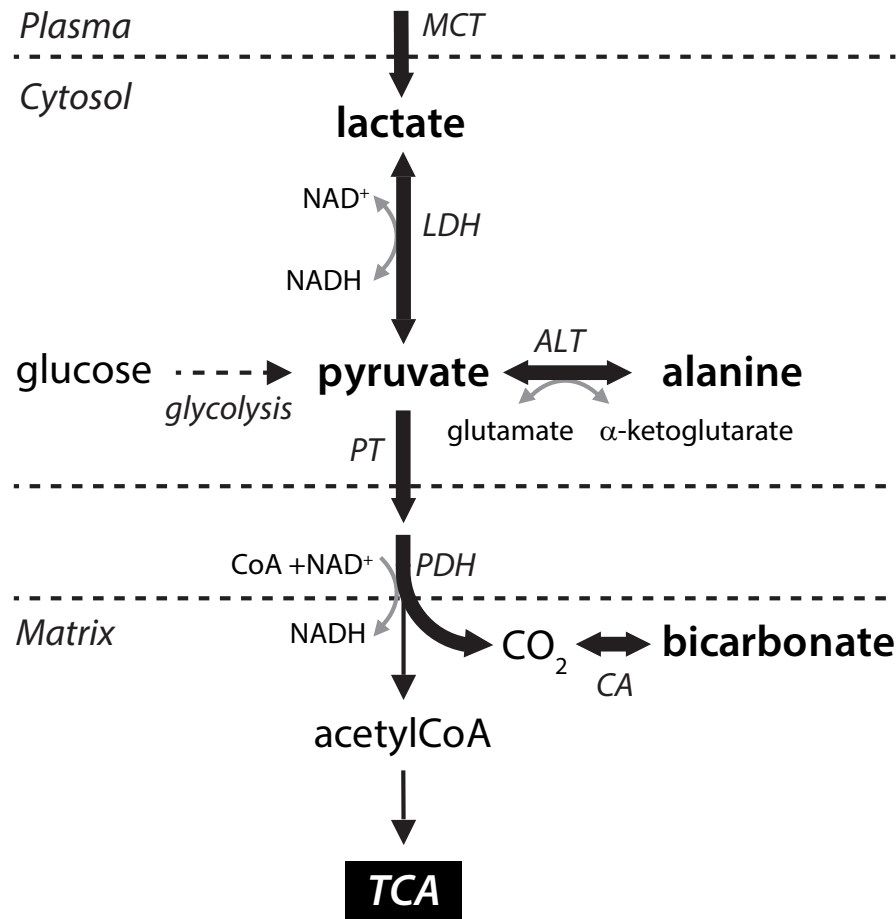


Figure 5.1: Scheme of $[1-^{13}\text{C}]$ lactate metabolism in rat skeletal muscle in vivo. The ^{13}C label propagation is indicated by the fat arrows and metabolites observed following $[1-^{13}\text{C}]$ lactate oxidation are in bold typeface. Lactate enters the cell through MCT transporters and is converted to pyruvate by LDH. Via a reversible transaminase reaction via ALT pyruvate is transformed to alanine. Pyruvate in turn can enter the mitochondria via an irreversible reaction catalyzed by PDH resulting in acetylCoA and bicarbonate. ALT: Alanine transaminase; LDH: lactate dehydrogenase; PDH: pyruvate dehydrogenase; TCA: tricarboxylic acid cycle; MCT: monocarboxylate transporter; CA: carbonic anhydrase.

situations were studied: the fed and fasted states.

5.2 Experimental Procedures

Sample preparation and hyperpolarization protocol

Sodium [$1\text{-}^{13}\text{C}$]lactate and TEMPOL nitroxyl radicals were obtained from Sigma Aldrich (Buchs, Switzerland). Sodium [$1\text{-}^{13}\text{C}$]lactate was mixed with d8-glycerol in a 2:1 weight ratio to a concentration of around 4.0 M with a final radical concentration of 50 mM. The solutions were rapidly frozen in liquid nitrogen to form 10 μL beads that were inserted into a sample which was further cooled to 1 ± 0.05 K in a 7 T custom-designed DNP polarizer¹⁷, where the ^{13}C nuclei were dynamically polarized with microwave irradiation (197.25 MHz and 55 mW) for 90 min, with a buildup time of 60 min. Using an automated process, the sample was rapidly dissolved using 6.0 mL of pressurized, heated D₂O and transferred within 2 s following dissolution to a separator/infusion pump, containing 0.6 mL of PBS and heparin, located inside a 9.4 T horizontal bore magnet^{17;18}. Subsequently, 1.5 mL of the hyperpolarized solution at physiological temperature and pH was automatically infused into the animal during 8 s. The ^{13}C polarization level at the time of the injection was 17 ± 2 %.

Animals

All animal studies conformed to institutional guidelines. Wild type male Sprague Dawley rats (293 ± 19 g) were anesthetized with 1.5% isoflurane in oxygen. A catheter was placed into the femoral vein for intravenous delivery of the hyperpolarized solution. A second catheter was placed in the artery to monitor the blood pressure and to measure plasma glucose and lactate concentrations. The respiration rate and temperature were monitored and maintained during the experiment. Two groups of animals were studied, fed animals ($n = 5$) and fasted animals ($n = 5$). The animals were fasted overnight in case of a fasted state study, by placing them in a clean cage without food the day before the experiment at around 5 pm. All animals were measured in the morning. Each animal was injected three times with hyperpolarized lactate. Animal physiology was not disturbed by the injections and the respiration and heart rates were stable through all experiments.

In vivo magnetic resonance spectroscopy

Measurements were carried out on a 9.4 T / 31 cm actively shielded animal scanner (Varian/-Magnex). A custom-made radiofrequency (RF) hybrid probe consisting of a 10 mm diameter carbon surface coil and a quadrature 10 mm diameter ^1H surface coil was positioned over the hind leg of the rat for transmission and reception, localizing the signals from the skeletal muscle. Acquisition of gradient echo proton images confirmed the correct position of the muscle tissue. Shimming was performed to reduce the localized proton line width in a voxel

of 6x10x10 mm to 20-30 Hz using FASTESTMAP¹⁹. The NMR console was triggered to start acquisition at the beginning of the automated injection process, 6 s after dissolution of the hyperpolarized sample. Series of single pulse acquisitions were recorded using 30° adiabatic RF pulses (BIR4) applied every 3 s with ¹H decoupling using WALTZ-16. Typically 40 to 60 FIDs were acquired with 4129 complex data points over a 20000 Hz bandwidth. The adiabatic pulse offset and power was calibrated to ensure a 30° excitation pulse for all observed metabolites in the entire tissue of interest. Following data acquisition, 200 µL liquid samples were extracted from the separator/infusion pump to precisely determine the infused [1-¹³C]lactate concentration using a high resolution 400 MHz NMR spectrometer.

Data analysis

The infused substrates and their corresponding metabolic products were assigned according to the chemical shifts. ¹³C NMR time courses were summed for the time period during which the hyperpolarized lactate resonance had a signal to noise ratio higher than 5, typically 15 spectra satisfied that criterion. The resulting summed spectra were fitted to Lorentzian line shapes using Bayesian analysis. These summed integrals were used to determine the ratios of one substrate relative to the other. Metabolite time courses were obtained by applying a 10 Hz line broadening on the raw data, followed by fitting in jMRUI. Statistical differences between the ratios of observed metabolites were calculated using a two-tailed t-test for unpaired data with equal variance. Error bars in figures and in the manuscript indicate ± standard error of the mean (SEM).

5.3 Results

Carbohydrate metabolism was studied in healthy resting skeletal muscle in vivo in fed and fasted animals using hyperpolarized [1-¹³C]lactate. Overnight fasting resulted in a 30% decrease in plasma glucose and a 41% decrease in plasma lactate compared with animals which were fed ad libitum. Lactate metabolism was detected in the skeletal muscle of healthy rats in vivo (n = 10) and the following metabolite resonances were observed: [1-¹³C]pyruvate (171.2 ppm), [1-¹³C]alanine (177.0 ppm) and ¹³C bicarbonate (161.3 ppm). The spectral time courses of fed animals injected with hyperpolarized [1-¹³C]lactate showed (Figure 5.2A) that within seconds, lactate was transformed into pyruvate in the cytosol. The observation of bicarbonate in summed spectra (Figure 5.2B) indicates the transport of pyruvate into the mitochondrion for subsequent oxidation in the tricarboxylic acid (TCA) cycle.

The time evolution of the signal integrals of lactate, alanine, pyruvate and bicarbonate (Figure 5.3) show that alanine attained higher signal intensities compared to pyruvate but the maximum was reached at a later time point compared with pyruvate in all experiments. On average, alanine reached its maximum at 28 ± 4 s and pyruvate at 22 ± 4 s in the fed state (\pm standard deviation). In the fasted state, the maximum for alanine was reached at 28 ± 3 s and for pyruvate at 22 ± 2 s. There were no significant differences in the time to maximum for

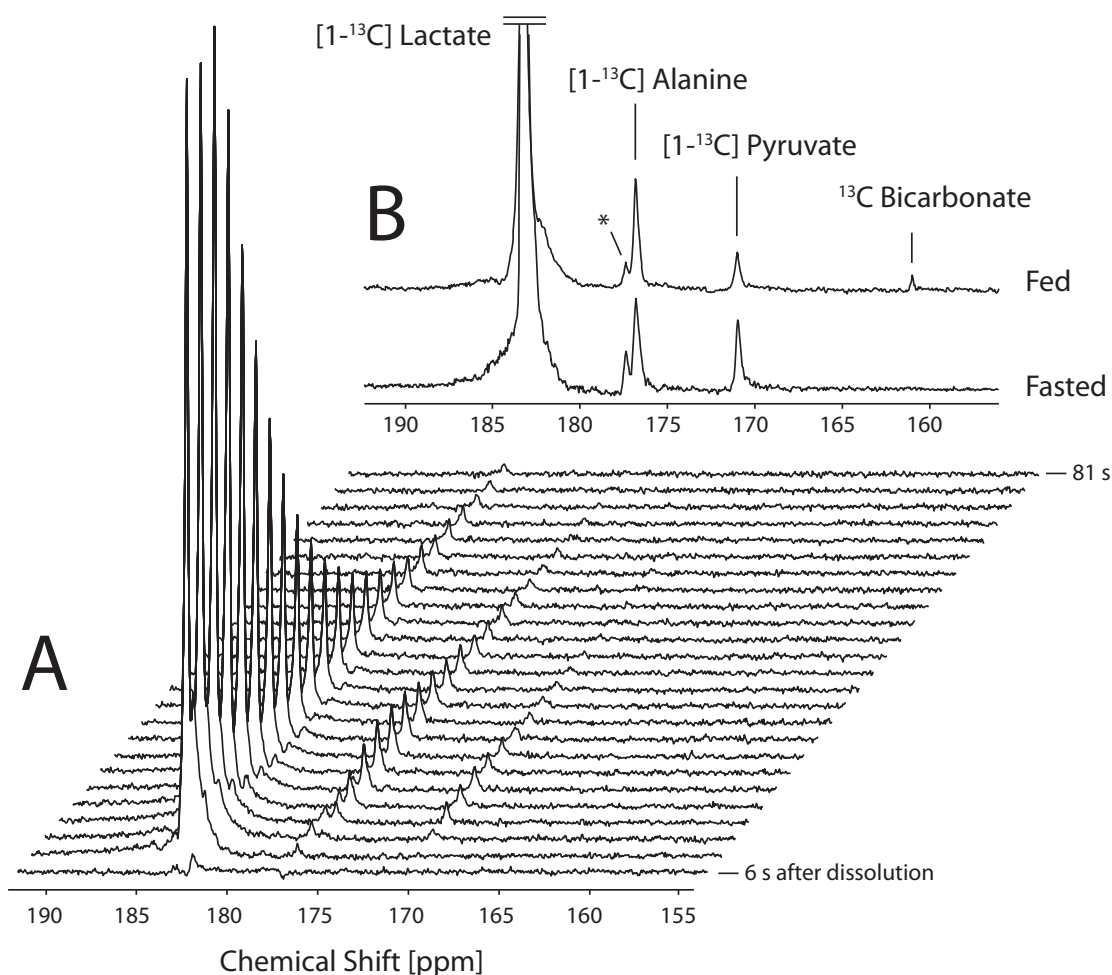


Figure 5.2: Transient spectra acquired from the rat skeletal muscle using 30° adiabatic pulses applied every 3 s after the injection of hyperpolarized $[1-^{13}\text{C}]$ lactate show the formation of $[1-^{13}\text{C}]$ alanine, $[1-^{13}\text{C}]$ pyruvate and ^{13}C bicarbonate. Spectra shown here were line broadened with 10 Hz (A). Representative summed spectrum acquired from rat skeletal muscle in vivo after hyperpolarized $[1-^{13}\text{C}]$ lactate injection in a fed (top) and fasted (bottom) animal. Fifteen spectra were summed and are displayed using a 5 Hz line broadening. *The resonance on the shoulder of alanine observed at 177.5 ppm is due to an impurity in the $[1-^{13}\text{C}]$ lactate solution (B).

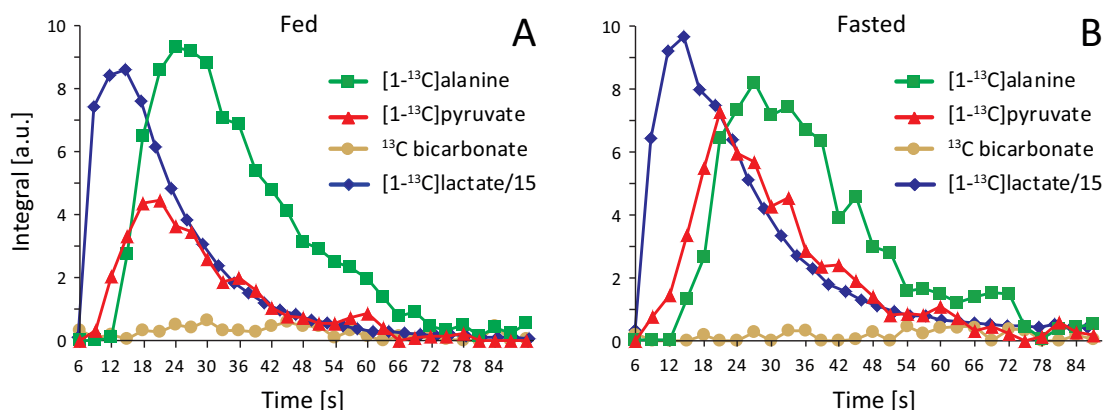


Figure 5.3: Timecourses of integrated spectra showing the evolution of the injected hyperpolarized substrate [1-¹³C]lactate and its downstream metabolites pyruvate, alanine and bicarbonate in a fed (left) and a fasted (right) animal. The hyperpolarized lactate integrals were scaled by a factor of 1/15. Spectral acquisition started 6 s after the dissolution process with a repetition time of 3 seconds.

both metabolites in both metabolic states. The linewidths of detected ¹³C resonances were on average 22 Hz.

The injected lactate concentration was between 100 and 250 mM. After a rapid elevation to 8.2 ± 1.5 mM following the delivery of the hyperpolarized solution, the arterial lactate concentration returned to its baseline level within 20 minutes (Figure 5.4). The resonance of ¹³C bicarbonate was absent in animals which were fasted overnight ($n = 5$). In the fed group ($n = 5$), bicarbonate was only detected in nine out of fifteen experiments because of the low SNR in experiments with lower lactate dose. In both groups, the same relationship was observed between the SNR of the lactate signal and the injected dose.

The signals were also expressed relative to the two other intracellular ¹³C enriched metabolites, namely [1-¹³C]pyruvate and [1-¹³C]alanine. These ratios are independent of variations in the initial polarization level of [1-¹³C]lactate. Comparing fed and fasted, the bicarbonate signal was undetectable in the fasted group ($p < 0.0005$), whereas the ratio of bicarbonate to lactate in the fed group was 0.003 ± 0.000 , the ratio relative to pyruvate was 0.10 ± 0.00 and the ratio relative to alanine 0.04 ± 0.00 . The ratio of pyruvate to lactate increased marginally from 0.030 ± 0.000 to 0.034 ± 0.001 ($p < 0.2$) and alanine decreased significantly from 0.072 ± 0.001 to 0.058 ± 0.001 when comparing fed with fasted animals ($p < 0.05$). The ratio of pyruvate to alanine increased significantly ($p < 0.005$) by 42% from 0.43 ± 0.01 to 0.61 ± 0.01 (Figure 5.5).

The influence of the injected lactate dose on the formation of bicarbonate, alanine and pyruvate was also investigated: The metabolite ratios were compared to the administered lactate dose and no relationship was observed (Figure 5.7). There was no influence of repeated lactate injections in the same animal on the ratio of alanine and bicarbonate relative to

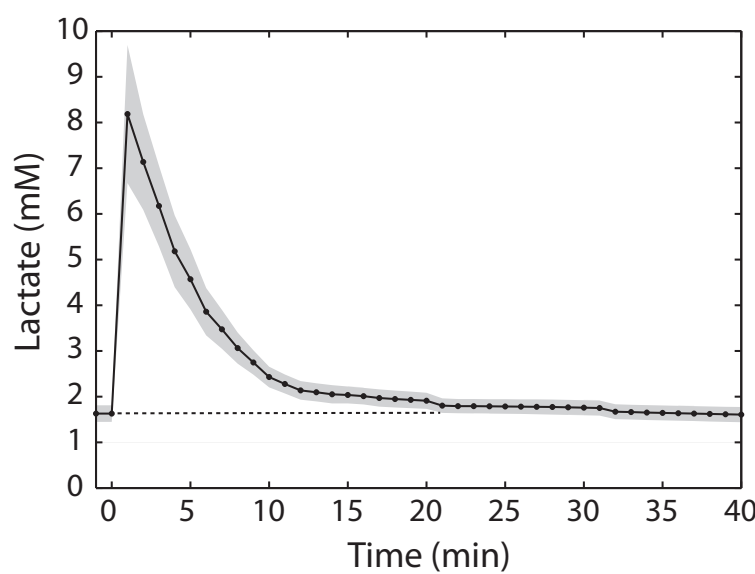


Figure 5.4: Lactate concentrations measured in arterial plasma samples extracted during experiments before and after a hyperpolarized ^{13}C labeled lactate injection. An average of interpolated lactate measurements is shown with the shaded grey area representing \pm standard deviation.

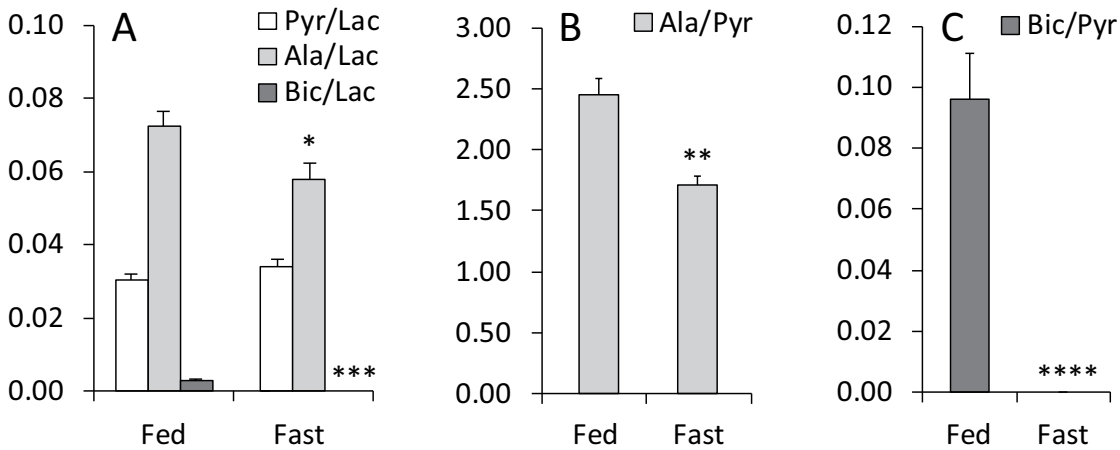


Figure 5.5: Signal ratios of pyruvate and bicarbonate relative to alanine. Asterisks denote statistical significant differences compared to the fed state between metabolite ratios where * $p<0.05$, ** $p<0.005$, *** $p<0.0005$, **** $p<0.00005$.

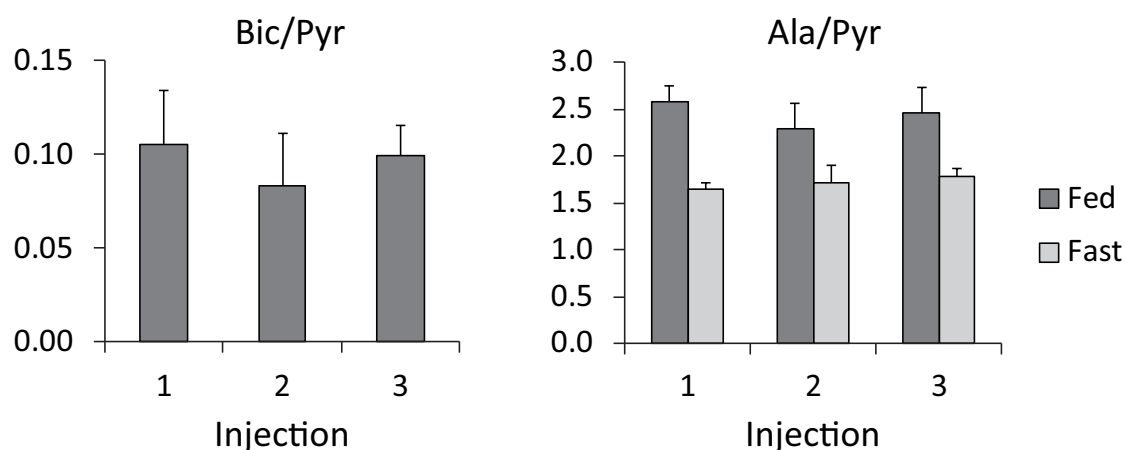


Figure 5.6: Influence of repeated injections of hyperpolarized lactate on observed metabolism. The signal ratios of bicarbonate relative to pyruvate are shown in the left panel. On the right the signal ratios of alanine relative to pyruvate are shown in both fed and fasted states. Bicarbonate was not observed in fasted animals and is therefore omitted.

pyruvate in the fed and fasted situation (Figure 5.6).

5.4 Discussion

In this study it was shown for the first time that lactate is readily taken up by resting skeletal muscle *in vivo* and quickly converted to pyruvate for subsequent oxidation in the mitochondrion. The metabolic conversion rate of lactate was sensitive to a simple alteration of nutritional state. Significant changes were observed in ^{13}C labeling of bicarbonate and alanine after an overnight fast. The absence of ^{13}C bicarbonate signal in the fasted group is a result of the inhibition of metabolic flux through PDH during fasting²⁰. Increases in the acetylCoA/CoA ratio or the NADH concentration further inhibit PDH. This is consistent with the reduction in PDH flux in the rat heart after a fasting period observed using hyperpolarized $[1-^{13}\text{C}]$ pyruvate²¹. In general, alanine attained higher ^{13}C signal intensities compared to pyruvate, as was also observed in the abdomen and the rat heart^{13;15}. This is attributed to the much larger pool size of alanine compared to pyruvate in both nutritional states^{22;23}. It also suggests that the fractional enrichment of the cellular pyruvate pool was high enough to ensure efficient ^{13}C label transfer into the cellular alanine pool. Contribution to the signal from surrounding organs was expected to be negligible and has been discussed previously²⁴.

It has been shown that, after administration of hyperpolarized pyruvate or lactate, there is a rapid exchange of ^{13}C label between the pyruvate and lactate pools, and that observed changes in ^{13}C labeling of lactate and pyruvate is representative of the metabolite's pool size at the time of the measurements rather than originating from a net enzymatic flux through lactate dehydrogenase (LDH)^{25–27}. Since, like LDH, alanine transaminase (ALT) is a reversible

enzyme, fast isotope redistribution between the pyruvate and alanine pools implies that the variation in alanine to pyruvate ^{13}C signal ratio is essentially a consequence of changes in the endogenous relative concentrations of both metabolites. The significant reduction of this ratio observed in fasted fed animals could result from an increased in pyruvate signal, a decrease in alanine signal or a combination of both.

An increase in endogenous pyruvate concentration in the fasted state could be due to inhibition of pyruvate oxidation²⁰, or due to increased NAD⁺ levels which shift the LDH-catalyzed reaction towards the formation of pyruvate²⁸. However, as mentioned above, the slight increase in pyruvate to lactate ^{13}C signal ratio observed in our experiments was not statistically significant ($p < 0.2$). The largely significant decrease in alanine to pyruvate ^{13}C signal ratio observed in the fasted state is thus most likely mainly a consequence of a decrease of the alanine pool size.

In previous studies where hyperpolarized $[1-^{13}\text{C}]$ pyruvate was used as a substrate, a decrease in the ^{13}C alanine signal was observed in a perfused liver model, the heart and in the liver in vivo after a fasting period and this reduction was ascribed to a cellular redox state change and a reduction in alanine transaminase activity respectively^{29–31}. However, a direct comparison with results obtained using pyruvate as a hyperpolarized substrate is challenging since different metabolite pools are enriched and the reaction pathways and directions probed are different. Moreover, the liver takes up alanine for gluconeogenic purposes while the muscle releases it.

There have been reports of decreased skeletal muscle tissue concentrations of alanine after a 24h fast³² and alanine concentrations were also diminished in overnight fasted animals in a different study conducted in our lab³³ based on ^1H NMR measurements of tissue extracts. Therefore, a decrease in ^{13}C alanine labeling can be most likely ascribed to a change in cellular alanine concentration. The endogenous alanine concentration is reduced in fasted muscles because of an enhanced alanine efflux^{34;35}.

It is known that during fasting conditions and other situations of negative nitrogen balance, muscle is the major source of carbon and nitrogen for the synthesis of glucose and urea in the liver^{36;37}. In such conditions, amino acid catabolism increases³⁸ and alanine is the principal amino acid released by skeletal muscle. Moreover, it was shown that the alanine release reflects the rate of de novo synthesis³⁹, and changes in alanine synthesis and release are related to pyruvate formation from amino acids⁴⁰, which increases during fasting. Although the formation and efflux of alanine is stimulated during fasting, the decreased hyperpolarized ^{13}C label transfer to alanine observed in this study is clearly not only dependent on the enzymatic flux through ALT but coupled with changes in fractional enrichments, pool sizes and formation of intermediate substrates. Since these factors are affected in several diseases, such as in diabetes where the release of lactate and alanine is increased^{22;39}, ketotic hypoglycemia where gluconeogenesis is impaired due to insufficient release of alanine⁴¹, or maple syrup urine disease where decarboxylation of amino acids is impaired and alanine levels are 3- to

10-fold lower⁴², the alanine-to-pyruvate ratio could be a sensitive biological marker for the detection of skeletal muscle metabolic disorders. The time evolution of the lactate resonance shows a buildup followed by decay and this is different from hyperpolarized acetate injections in skeletal muscle using an identical injection protocol²⁴. This difference could be attributed to a different uptake of both substrates. Acetate enters the cell via concentration gradient facilitated diffusion while lactate mainly enters via monocarboxylate transporters and also by free diffusion at concentrations >10 mM^{6;7}. Since the concentrations used in this study were 8 mM, lactate was assumed to enter the cell largely via MCT transport.

The hyperpolarized lactate injections resulted in a 5-fold elevation of endogenous lactate (8mM) compared to the resting state. Tissue concentrations of lactate can increase up to 10 - 50 mM in a state of exercise and our injected values are thus within physiological range^{43;44}. Lactate was cleared from the blood within minutes (Figure 5.4). The ability to uptake and process lactate at these concentrations is also reflected by the high K_M values for MCT across the cellular membrane which were found to be between 13 and 40 mM⁴⁵. MCT1 and MCT4 are the predominant isoforms expressed in skeletal muscle. No dose dependencies were observed in the metabolite-to-lactate ratios, which is indicative of lactate transport being proportional to blood lactate concentration and in agreement with the higher K_M value compared to the lactate concentrations.

Previous studies in the literature show that after a 24h and a 48h fast, plasma lactate concentrations decrease but the concentration of lactate in rat skeletal muscle tissue remains unchanged^{46;47}. In a study using overnight fasted rats, a 30 min infusion of lactate increased plasma lactate levels 4-fold but did not increase the plasma concentrations of free fatty acids and alanine⁴⁸. Infusing lactate up to 30 mM did not affect glucose uptake, pyruvate uptake/output, and alanine output in canine skeletal muscle¹². Therefore, we conclude that the observed changes in ^{13}C label propagation are a likely consequence of an actual shift in lactate metabolism in skeletal muscle upon fasting.

Conclusion

The significant changes observed in ^{13}C labeling of bicarbonate and alanine after an overnight fast were attributed to decreased PDH flux and a decrease in cellular alanine concentration, in agreement with previous ex vivo analysis of tissue extracts. We conclude that lactate can be administered at physiological concentrations without disturbing other oxidative processes and is readily oxidized in resting skeletal muscle. Moreover, the downstream metabolite pyruvate can be used as an intracellular reference. Therefore hyperpolarized $[1-^{13}\text{C}]\text{lactate}$ is well suited for studying carbohydrate metabolism in skeletal muscle in vivo. The ratio of alanine to pyruvate is not only dependent on the enzymatic flux through ALT, but also on changes in fractional enrichments and pool size of intermediates. It has potential to be a metric to probe skeletal muscle metabolic disorders

5.5 Metabolic flux analysis of alanine labeling

Alanine can be formed by transamination of pyruvate in a reaction catalyzed by the enzyme alanine transaminase, and the rate of efflux resembles that of alanine synthesis. This makes that the forward flux through ALT, V_{ALT} , is of the same order as the flux of alanine release from the muscle, V_{efflux} . The pool size of alanine (Ala) can be represented by the following equation:

$$\frac{d[Ala]}{dt} = V_{ALT} - V_{efflux} \quad (5.1)$$

Taking into account the ^{13}C label flow, indicated with * , the ^{13}C alanine pool can be described as follows:

$$\frac{d[Ala^*]}{dt} = V_{ALT} \frac{[Pyr^*]}{[Pyr]} - V_{efflux} \frac{[Ala^*]}{[Ala]} \quad (5.2)$$

It can be assumed that within each nutritional state the endogenous alanine pool is relatively constant, i.e. metabolic steady state, and therefore V_{ALT} equals V_{efflux} . Considering equal fluxes and equal ^{13}C enrichment of pyruvate between the fed and fasted state, Equation 5.2 shows clearly that a change in endogenous pool size of alanine has a direct effect on the rate of ^{13}C alanine formation. Note that when an isotopic steady state is reached, $d[Ala^*]/dt = 0$, the fractional enrichment of alanine cannot exceed that of pyruvate and thus a decreased pool size will result in a decrease of alanine that can be ^{13}C enriched and detected by NMR spectroscopy.

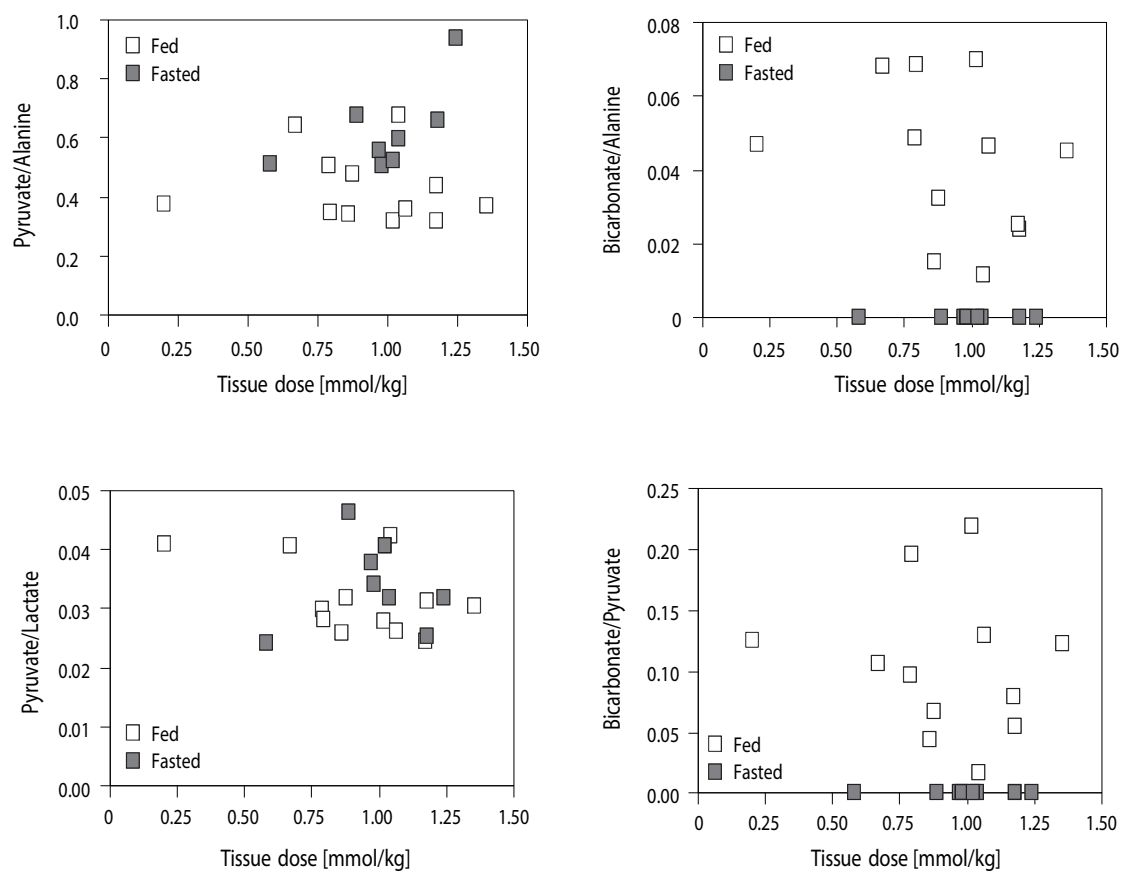


Figure 5.7: Pyruvate and bicarbonate ratios relative to alanine as function of the administered lactate dose in fed and fasted animals.

References

- [1] G. A. Brooks and J. Mercier. Balance of carbohydrate and lipid utilization during exercise - the crossover concept. *Journal of Applied Physiology*, 76(6):2253–2261, 1994.
- [2] G. A. Brooks. Mammalian fuel utilization during sustained exercise. *Comparative Biochemistry and Physiology B-Biochemistry and Molecular Biology*, 120(1):89–107, 1998.
- [3] D. A. Roth. The sarcolemmal lactate transporter - transmembrane determinants of lactate flux. *Medicine and Science in Sports and Exercise*, 23(8):925–934, 1991.
- [4] G. A. Brooks. Intra- and extra-cellular lactate shuttles. *Medicine and Science in Sports and Exercise*, 32(4):790–799, 2000.
- [5] L. B. Gladden. Lactate metabolism: a new paradigm for the third millennium. *Journal of Physiology-London*, 558(1):5–30, 2004.
- [6] C. Juel. Muscle lactate transport studied in sarcolemmal giant vesicles. *Biochimica Et Biophysica Acta*, 1065(1):15–20, 1991.
- [7] R. C. Poole and A. P. Halestrap. Transport of lactate and other monocarboxylates across mammalian plasma-membranes. *American Journal of Physiology*, 264(4):C761–C782, 1993.
- [8] L. A. Bertocci, J. G. Jones, C. R. Malloy, R. G. Victor, and G. D. Thomas. Oxidation of lactate and acetate in rat skeletal muscle: Analysis by c-13-nuclear magnetic resonance spectroscopy. *Journal of Applied Physiology*, 83(1):32–39, 1997.
- [9] L. A. Bertocci and B. F. Lujan. Incorporation and utilization of [3-c-13]lactate and [1,2-c-13]acetate by rat skeletal muscle. *Journal of Applied Physiology*, 86(6):2077–2089, 1999.
- [10] J. H. Ardenkjaer-Larsen, B. Fridlund, A. Gram, G. Hansson, L. Hansson, M. H. Lerche, R. Servin, M. Thaning, and K. Golman. Increase in signal-to-noise ratio of > 10,000 times in liquid-state nmr. *Proc Natl Acad Sci U S A*, 100(18):10158–10163, 2003.
- [11] Y. Yoshida, G. P. Holloway, V. Ljubicic, H. Hatta, L. L. Spriet, D. A. Hood, and A. Bonen. Negligible direct lactate oxidation in subsarcolemmal and intermyofibrillar mitochondria obtained from red and white rat skeletal muscle. *Journal of Physiology-London*, 582(3):1317–1335, 2007.
- [12] L. B. Gladden, R. E. Crawford, and M. J. Webster. Effect of lactate concentration and metabolic-rate on net lactate uptake by canine skeletal-muscle. *American Journal of Physiology*, 266(4):R1095–R1101, 1994.
- [13] A. P. Chen, J. Kurhanewicz, R. Bok, D. Xua, D. Joun, V. Zhang, S. J. Nelson, R. E. Hurd, and D. B. Vigneron. Feasibility of using hyperpolarized [1-c-13]lactate as a substrate for in vivo metabolic c-13 mrsi studies. *Magnetic Resonance Imaging*, 26(6):721–726, 2008.
- [14] B. W. C. Kennedy, M. I. Kettunen, D. E. Hu, and K. M. Brindle. Probing lactate dehydrogenase activity in tumors by measuring hydrogen/deuterium exchange in hyperpolarized l-[1-c-13,u-h-2]lactate. *Journal of the American Chemical Society*, 134(10):4969–4977, 2012.
- [15] D. Mayer, Y. F. Yen, S. Josan, J. M. Park, A. Pfefferbaum, R. E. Hurd, and D. M. Spielman. Application of hyperpolarized [1-13c]lactate for the in vivo investigation of cardiac metabolism. *Nmr in Biomedicine*, 25(10):1119–1124, 2012.
- [16] Yuhei Takado, T Cheng, B Lanz, J.A.M. Bastiaansen, M Mishkovsky, R Gruetter, and A Comment. Lactate brain metabolism in different mouse strains probed by hyperpolarized 13c

- mrs. *DNP Symposium 2013*, 2013.
- [17] A. Comment, B. van den Brandt, K. Uffmann, F. Kurdzesau, S. Jannin, J. A. Konter, P. Hautle, W. Th. Wenckebach, R. Gruetter, and J. J. van der Klink. Design and performance of a dnp prepolarizer coupled to a rodent mri scanner. *Concepts in Magnetic Resonance Part B: Magnetic Resonance Engineering*, 31B(4):255–269, 2007.
 - [18] Tian Cheng, Mor Mishkovsky, Jessica A. M. Bastiaansen, Olivier Ouari, Patrick Hautle, Paul Tordo, Ben van den Brandt, and Arnaud Comment. Method to minimize and monitor in situ the polarization losses in hyperpolarized biomolecules prior to in vivo mr experiments. *Nmr in Biomedicine - In Press*, 2013.
 - [19] R. Gruetter and I. Tkac. Field mapping without reference scan using asymmetric echo-planar techniques. *Magnetic Resonance in Medicine*, 43(2):319–323, 2000.
 - [20] P. B. Garland, P. J. Randle, and E. A. Newsholme. Regulation of glucose uptake by muscle .9. effects of fatty acids + ketone bodies + of alloxan-diabetes + starvation on pyruvate metabolism + on lactate/pyruvate + l-glycerol 3-phosphate/dihydroxyacetone phosphate concentration ratios in rat heart + rat diaphragm muscles. *Biochemical Journal*, 93(3):665–678, 1964.
 - [21] M. A. Schroeder, L. E. Cochlin, L. C. Heather, K. Clarke, G. K. Radda, D. J. Tyler, and R. G. Shulman. In vivo assessment of pyruvate dehydrogenase flux in the heart using hyperpolarized carbon-13 magnetic resonance. *Proceedings of the National Academy of Sciences of the United States of America*, 105(33):12051–12056, 2008.
 - [22] M. Berger, S. A. Hagg, M. N. Goodman, and N. B. Ruderman. Glucose-metabolism in perfused skeletal-muscle - effects of starvation, diabetes, fatty-acids, acetoacetate, insulin and exercise on glucose-uptake and disposition. *Biochemical Journal*, 158(2):191–202, 1976.
 - [23] B. M. Jucker, A. J. M. Rennings, G. W. Cline, and G. I. Shulman. C-13 and p-31 nmr studies on the effects of increased plasma free fatty acids on intramuscular glucose metabolism in the awake rat. *Journal of Biological Chemistry*, 272(16):10464–10473, 1997.
 - [24] J. A. M. Bastiaansen, T. Cheng, M. Mishkovsky, J. M. N. Duarte, A. Comment, and R. Gruetter. In vivo enzymatic activity of acetylcoa synthetase in skeletal muscle revealed by 13c turnover from hyperpolarized [1-13c]acetate to [1-13c]acetylcarnitine. *Biochimica Et Biophysica Acta*, 1830(8):4171–4178, 2013.
 - [25] S. E. Day, M. I. Kettunen, F. A. Gallagher, D. E. Hu, M. Lerche, J. Wolber, K. Golman, J. H. Ardenkjaer-Larsen, and K. M. Brindle. Detecting tumor response to treatment using hyperpolarized (13)c magnetic resonance imaging and spectroscopy. *Nat Med*, 13(11):1382–1387, 2007.
 - [26] M. E. Merritt, C. Harrison, C. Storey, F. M. Jeffrey, A. D. Sherry, and C. R. Malloy. Hyperpolarized 13c allows a direct measure of flux through a single enzyme-catalyzed step by nmr. *Proc Natl Acad Sci U S A*, 104(50):19773–7, 2007.
 - [27] M. I. Kettunen, D. E. Hu, T. H. Witney, R. McLaughlin, F. A. Gallagher, S. E. Bohndiek, S. E. Day, and K. M. Brindle. Magnetization transfer measurements of exchange between hyperpolarized [1-c-13]pyruvate and [1-c-13]lactate in a murine lymphoma. *Magnetic Resonance in Medicine*, 63(4):872–880, 2010.
 - [28] R. H. Houtkooper, C. Canto, R. J. Wanders, and J. Auwerx. The secret life of nad(+): An old metabolite controlling new metabolic signaling pathways. *Endocrine Reviews*, 31(2):194–223, 2010.
 - [29] S. Hu, A. P. Chen, M. L. Zierhut, R. Bok, Y. F. Yen, M. A. Schroeder, R. E. Hurd, S. J. Nelson,

- J. Kurhanewicz, and D. B. Vigneron. In vivo carbon-13 dynamic mrs and mrsi of normal and fasted rat liver with hyperpolarized c-13-pyruvate. *Molecular Imaging and Biology*, 11(6):399–407, 2009.
- [30] M. E. Merritt, C. Harrison, A. D. Sherry, C. R. Malloy, and S. C. Burgess. Flux through hepatic pyruvate carboxylase and phosphoenolpyruvate carboxykinase detected by hyperpolarized c-13 magnetic resonance. *Proceedings of the National Academy of Sciences of the United States of America*, 108(47):19084–19089, 2011.
- [31] Jessica A. M. Bastiaansen, A. Comment, and Matthew E Merritt. In vivo myocardial substrate competition using hyperpolarized 13c magnetic resonance. *Submitted*, 2013.
- [32] Christop J, J. Winand, and Hebbelin M. Amino acid levels in plasma, liver, muscle, and kidney during and after exercise in fasted and fed rats. *American Journal of Physiology*, 221(2):453–457, 1971.
- [33] Jessica A. M. Bastiaansen, J.M.N. Duarte, A. Comment, and R. Gruetter. Acetylcarnitine turnover in rat skeletal muscle measured in vivo using localized 13c nmr at 14.1 t. *Proc. Intl. Soc. Mag. Reson. Med.*, 21:120, 2013.
- [34] P. Felig. Glucose-alanine cycle. *Metabolism-Clinical and Experimental*, 22(2):179–207, 1973.
- [35] M. Macdonald, N. Neufeldt, B. N. Park, M. Berger, and N. Ruderman. Alanine metabolism and gluconeogenesis in rat. *American Journal of Physiology*, 231(2):619–626, 1976.
- [36] L. E. Mallette, J. H. Exton, and C. R. Park. Control of gluconeogenesis from amino acids in perfused rat liver. *Journal of Biological Chemistry*, 244(20):5713–5723, 1969.
- [37] N. B. Ruderman and M. Berger. Formation of glutamine and alanine in skeletal-muscle. *Journal of Biological Chemistry*, 249(17):5500–5506, 1974.
- [38] R. Odessey, Khairall.Ea, and A. L. Goldberg. Origin and possible significance of alanine production by skeletal-muscle. *Journal of Biological Chemistry*, 249(23):7623–7629, 1974.
- [39] I. E. Karl, A. J. Garber, and D. M. Kipnis. Alanine and glutamine synthesis and release from skeletal-muscle .3. dietary and hormonal-regulation. *Journal of Biological Chemistry*, 251(3):844–850, 1976.
- [40] A. J. Garber, I. E. Karl, and D. M. Kipnis. Alanine and glutamine synthesis and release from skeletal-muscle .2. precursor role of amino-acids in alanine and glutamine synthesis. *Journal of Biological Chemistry*, 251(3):836–843, 1976.
- [41] A. S. Pagliara, D. M. Kipnis, I. E. Karl, D. C. Devivo, and R. D. Feigin. Hypoalaninemia - concomitant of ketotic hypoglycemia. *Journal of Clinical Investigation*, 51(6):1440–1449, 1972.
- [42] J. Dancis, J. Hutzler, and M. Levitz. Metabolism of the white blood cells in maple-syrup-urine disease. *Biochimica Et Biophysica Acta*, 43(2):342–343, 1960.
- [43] P. W. Watt, P. A. MacIennan, H. S. Hundal, C. M. Kuret, and M. J. Rennie. L(+)-lactate transport in perfused rat skeletal-muscle - kinetic characteristics and sensitivity to ph and transport inhibitors. *Biochimica Et Biophysica Acta*, 944(2):213–222, 1988.
- [44] C. A. Gobatto, M. A. R. de Mello, C. Y. Sibuya, J. R. M. de Azevedo, L. A. dos Santos, and E. Kokubun. Maximal lactate steady state in rats submitted to swimming exercise. *Comparative Biochemistry and Physiology a-Molecular and Integrative Physiology*, 130(1):21–27, 2001.
- [45] C. Juel and A. P. Halestrap. Lactate transport in skeletal muscle - role and regulation of the monocarboxylate transporter. *Journal of Physiology-London*, 517(3):633–642, 1999.
- [46] M. N. Goodman, M. Berger, and N. B. Ruderman. Glucose-metabolism in rat skeletal-

- muscle at rest effect of starvation, diabetes, ketone-bodies and free fatty-acids. *Diabetes*, 23(11):881–888, 1974.
- [47] M. N. Goodman, R. Dietrich, and P. Luu. Formation of gluconeogenic precursors in rat skeletal muscle during fasted-refed transition. *American Journal of Physiology*, 259(4 Pt 1):E513–6, 1990.
- [48] R. Vettor, A. M. Lombardi, R. Fabris, C. Pagano, I. Cusin, F. RohnerJeanrenaud, G. Federspil, and B. Jeanrenaud. Lactate infusion in anesthetized rats produces insulin resistance in heart and skeletal muscles. *Metabolism-Clinical and Experimental*, 46(6):684–690, 1997.

Hyperpolarized acetylcarnitine as a probe for myocardial metabolism in vivo

6

Abstract

Acetylcarnitine is known to facilitate the influx and efflux of acetylgroups across the mitochondrial membrane and buffers an excess in acetylCoA in both cytosolic and mitochondrial compartments. Acetylcarnitine is a necessary intermediate for mitochondrial acetate metabolism. Since the detection of [5-¹³C]citrate and [5-¹³C]glutamate in the heart is hindered by the close proximity of the [1-¹³C]acetate resonance, acetylcarnitine could be an interesting substrate for hyperpolarized MR. Acetylcarnitine crosses the mitochondrial membrane easily, while acetate undergoes two enzymatic transformations in order to cross the membrane. Moreover, [1-¹³C]acetylcarnitine would not interfere with the detection of [5-¹³C]glutamate and [5-¹³C]citrate. The aim of the present study was to explore the use of hyperpolarized [1-¹³C]acetylcarnitine as a tracer myocardial substrate oxidation. [1-¹³C]Acetylcarnitine was successfully hyperpolarized and despite its short T_1 it was possible to detect the formation of [5-¹³C]glutamate in the heart *in vivo*. Due to the absence of the [5-¹³C]citrate resonance, we hypothesized the existence of an intricate relationship between reaction, transport and relaxation rates in the choice of hyperpolarized substrates.

Adapted from

Hyperpolarized [1-¹³C]acetylcarnitine as a tracer for cardiac metabolism.

Jessica AM Bastiaansen, Tian Cheng, Rolf Gruetter, Arnaud Comment

Presented at: Proc. Intl. Soc. Mag. Reson. Med. 21, 1936 (2013)

Manuscript in preparation

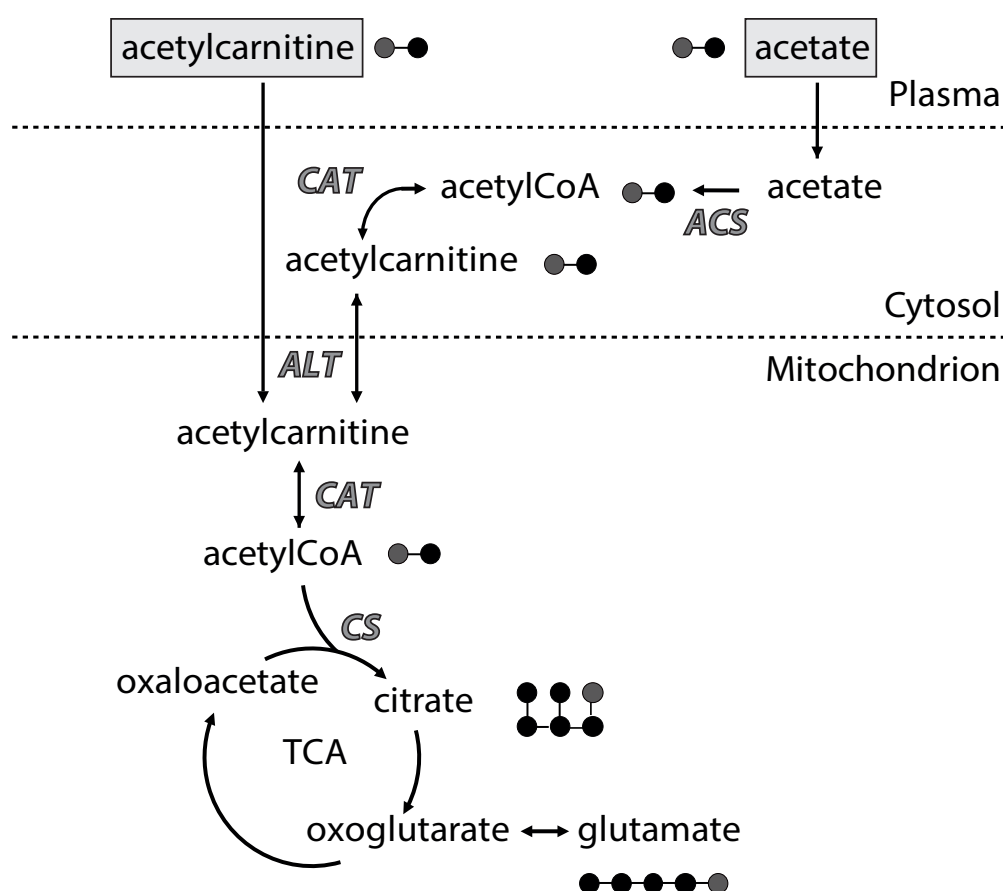


Figure 6.1: Illustration showing the metabolism of $[1-^{13}\text{C}]$ acetylcarnitine and $[1-^{13}\text{C}]$ acetate, both labeled at the C1 position, and the corresponding label propagation. Acetylcarnitine readily enters the mitochondrion and skips two biochemical transformations needed for acetate to enter.

6.1 Introduction

Acetylcarnitine is known to facilitate the influx and efflux of acetylgroups across the mitochondrial membrane and buffers an excess in acetylCoA in both cytosolic and mitochondrial compartments⁵. Acetylcarnitine is a necessary intermediate for mitochondrial acetate metabolism³ and has been shown to easily cross the blood brain barrier and act as a neuro-protective agent⁴. It is also being used for Alzheimer's disease treatment in humans².

The conversion of hyperpolarized acetate into acetylcarnitine, acetylCoA¹ and citrate (Chapter 3) have been observed *in vivo* in cardiac muscle and reflect the enzymatic activities of acetylCoA synthetase (ACS), citrate synthase (CS) and carnitine acetyltransferase (CAT). The ^{13}C labeling in these downstream metabolites appear with a time delay and typically decay corresponding to their T_1 . Following the injection of hyperpolarized $[1-^{13}\text{C}]$ acetate, the detection of $[5-^{13}\text{C}]$ citrate in the heart as described in Chapter 3 is hindered by the close proximity

of the $[1-^{13}\text{C}]$ acetate resonance, which also obscures the detection of $[5-^{13}\text{C}]$ glutamate.

In summary, acetylcarnitine could be an interesting substrate for myocardial oxidation, since it crosses the mitochondria easily, skipping two metabolic steps needed for acetate to cross the membrane (Figure 6.1). This would result in less signal losses compared to the use of acetate. Moreover, it does not interfere with the detection of $[5-^{13}\text{C}]$ glutamate and $[5-^{13}\text{C}]$ citrate, which could provide a reliable estimation of TCA cycle flux. The possibility to detect ^{13}C labeled acetylCoA would provide information about the flux through carnitine acetyl transferase (CAT).

The aim of the present study was to explore the use of hyperpolarized $[1-^{13}\text{C}]$ acetylcarnitine as a tracer myocardial substrate oxidation. Secondly, the use of hyperpolarized acetylcarnitine could help elucidate the backflux through the reaction from acetylcarnitine to acetylCoA to describe the entire system of enzymatic reactions in more detail.

6.2 Methods

Sample preparation and *in vitro* magnetic resonance spectroscopy

Acetyl- $1-^{13}\text{C}$ -L-carnitine hydrochloride (1.5M) solved in a 1:2 mixture of d_6 -EtOD/ D_2O containing 33mM TEMPO free radical were turned into frozen glassy beads and subsequently polarized in a custom-designed 5T DNP polarizer for 2 h. Following dissolution, the samples were transferred within 2 s into a home-built infusion pump located inside the magnet bore (9.4T) and connected to a catheter inserted into a D_2O filled phantom. The 5 s long infusion of 1 mL hyperpolarized $[1-^{13}\text{C}]$ acetylcarnitine solution was triggered 1 s later. The entire procedure was computer controlled in order to obtain an identical timing for all experiments. Series of single pulse acquisitions were recorded using 10° adiabatic RF pulses applied every 3 s starting with proton decoupling during the acquisition. MR acquisition started at the end of the infusion with a homebuilt surface coil with ^{13}C in quadrature mode.

In vivo magnetic resonance spectroscopy

The animal preparation ($n=3$) and *in vivo* MRS procedure are identical to the heart studies performed earlier and are described in Section 3.2.2.

Data analysis

A non-linear least-squares quantification algorithm, AMARES, as implemented in the jMRUI software package, was used to fit the ^{13}C NMR data. The spectra were corrected for the phases and DC offset. Soft constraints were imposed to peak frequencies (182.35 -182.45 ppm for glutamate and 173.85 -173.95 ppm for acetylcarnitine) and line widths ($\text{FWHM} = 10 - 30 \text{ Hz}$) and the relative phases were fixed to zero.

In vitro data were corrected for repeated RF excitations and fitted to the following equation to obtain the longitudinal relaxation time T_1 :

$$S \propto M_z = M_0 e^{-t/T_1} \cos \theta^{t/T_R} \quad (6.1)$$

6.3 Results and Discussion

[1- ^{13}C]acetylcarnitine was dynamically polarized with a buildup constant of 1390 s. After dissolution in a D₂O loaded phantom and data acquisition, the hyperpolarized time integrals were corrected for repeated adiabatic 10° excitations and the resulting decay was fitted to Equation 6.1. A T_1 value was obtained of 14.7 ± 1.0 s (Figure 6.2). This value is similar to the T_1 values of [1- ^{13}C]acetylcarnitine measured in blood plasma and D₂O as discussed in Section 2.5 and Table 2.1.

1 mL 100 mM [1- ^{13}C]acetylcarnitine was infused in healthy rats and the time evolution of substrate and metabolic products were measured in 3 animals (Figure 6.3). The linewidth of acetylcarnitine observed at 173.9 ppm was between 25 and 30 Hz. As expected given the relative short relaxation time, the acetylcarnitine signal could be observed during 20 to 40 seconds, exhibiting a mono-exponential decay of around 3 s regardless of the T_R (Figure 6.3). The uptake and enzymatic conversion of acetylcarnitine into [5- ^{13}C]glutamate was successfully detected in the heart *in vivo*. The resonance of [5- ^{13}C]glutamate appeared at 182.4 ppm (Figure 6.4).

The [5- ^{13}C]glutamate resonance cannot be observed using hyperpolarized [1- ^{13}C]acetate as a tracer because their resonances overlap (182.6 ppm vs. 182.4 ppm). Surprisingly [5- ^{13}C]citrate, resonating at 179.7 ppm was not observed in these experiments. The absence indicates that the disappearing polarization due to T_1 effects is relatively faster than the formation of citrate. An additional resonance appeared at 177.7 ppm. High resolution NMR on the infused solution revealed that this resonance originates from natural abundance ^{13}C in acetylcarnitine.

Conclusion

Despite its short T_1 it was possible to detect the formation of glutamate from hyperpolarized [1- ^{13}C]acetylcarnitine. [5- ^{13}C]citrate was not detectable in the current time frame. This study highlights the intricate relationship between reaction, transport and relaxation rates in the choice of hyperpolarized substrates.

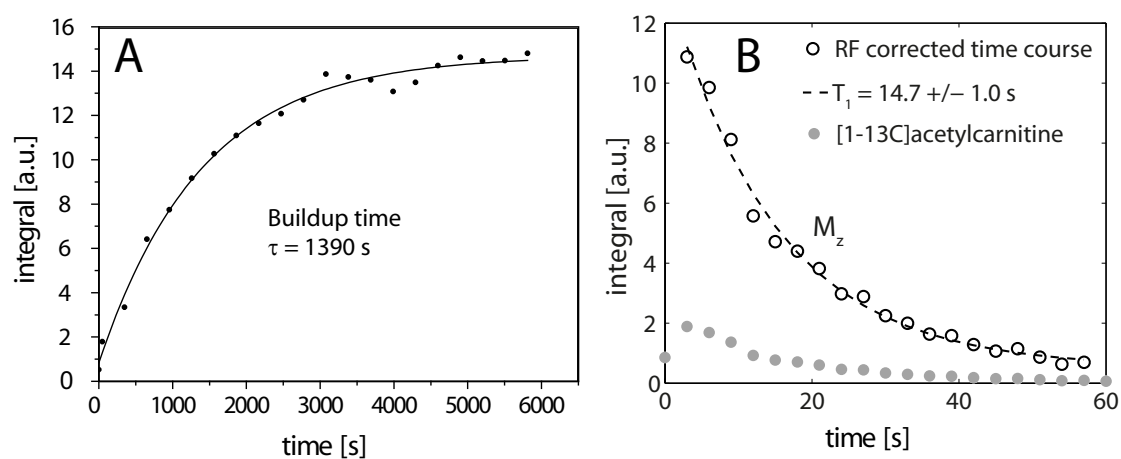


Figure 6.2: (A) Polarization buildup of $[1-^{13}\text{C}]$ acetylcarnitine with a time constant τ . (B) Following dissolution in a D_2O loaded sample, the decay of the hyperpolarized signal was measured. Data was corrected for repeated 10° RF excitations and was fitted to Equation 6.1 to obtain the longitudinal relaxation time T_1 .

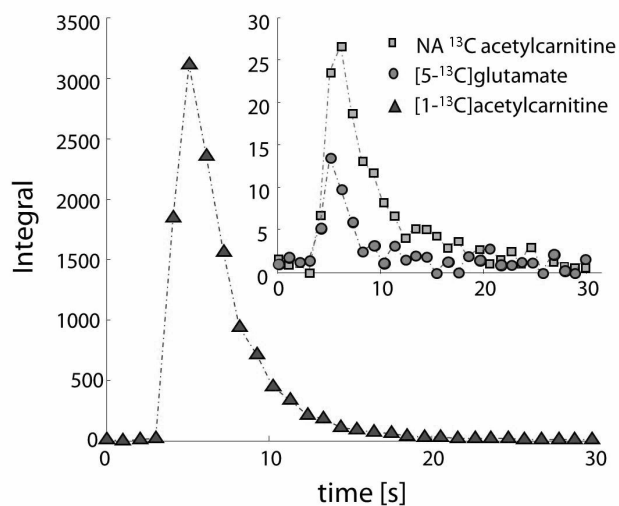


Figure 6.3: Integrated time course of cardiac NMR spectra following the infusion of 1 mL of 100 mM hyperpolarized $[1-^{13}\text{C}]$ acetylcarnitine.

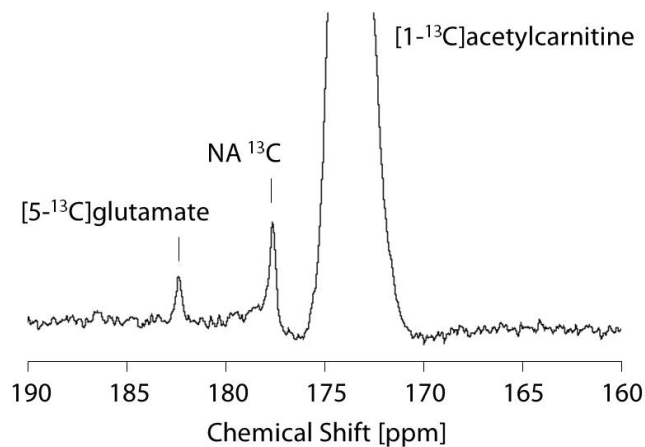


Figure 6.4: In vivo cardiac ^{13}C NMR spectrum at $t = 6$ s. $[5-^{13}\text{C}]$ Glutamate is observed at 182.4 ppm and a natural abundance ^{13}C resonance at 177.7 ppm.

References

- [1] P. R. Jensen, T. Peitersen, M. Karlsson, R. In 't Zandt, A. Gisselsson, G. Hansson, S. Meier, and M. H. Lerche. Tissue-specific short chain fatty acid metabolism and slow metabolic recovery after ischemia from hyperpolarized nmr in vivo. *Journal of Biological Chemistry*, 284(52):36077–82, 2009.
- [2] L. Parnetti, A. Gaiti, P. Mecocci, D. Cadini, and U. Senin. Pharmacokinetics of iv-acetyl-l-carnitine and oral acetyl-l-carnitine in a multiple-dose regimen in patients with senile dementia of alzheimer-type (vol 42, pg 89, 1992). *European Journal of Clinical Pharmacology*, 44(6):604–604, 1993.
- [3] P. A. Roberts, S. J. G. Loxham, S. M. Poucher, D. Constantin-Teodosiu, and P. L. Greenhaff. Acetyl-coa provision and the acetyl group deficit at the onset of contraction in ischemic canine skeletal muscle. *American Journal of Physiology-Endocrinology and Metabolism*, 288(2):E327–E334, 2005.
- [4] S. Scafidi, G. Fiskum, S. L. Lindauer, P. Bamford, D. Shi, I. Hopkins, and M. C. McKenna. Metabolism of acetyl-l-carnitine for energy and neurotransmitter synthesis in the immature rat brain. *Journal of Neurochemistry*, 114(3):820–31, 2010.
- [5] F. B. Stephens, D. Constantin-Teodosiu, and P. L. Greenhaff. New insights concerning the role of carnitine in the regulation of fuel metabolism in skeletal muscle. *J Physiol*, 581(Pt 2):431–44, 2007.

Acetylcarnitine turnover measurements in skeletal muscle *in vivo* using localized sensitivity enhanced ^{13}C MRS at 14.1 T

7

Abstract

Acetate has been widely used as a metabolic probe for measuring TCA cycle kinetics *in vivo* in skeletal muscle. In order to cross the mitochondrial membrane, acetate needs to be transformed into acetylcarnitine, which also functions as a storage for excess mitochondrial acetylCoA. Because of the relatively small pool sizes of acetylcarnitine in skeletal muscle, approximately one order of magnitude lower than glutamate, it has only been observed *in vivo* using hyperpolarized ^{13}C MRS techniques. Non-hyperpolarized ^{13}C MR studies of skeletal muscle are challenging because of large unwanted natural abundance ^{13}C lipid resonances. In this study, [2- ^{13}C]acetate was infused in healthy, fasted rats and metabolic data was acquired using localized ^{13}C MRS in combination with a heteronuclear ^1H - ^{13}C polarization transfer sequence to enhance the polarization level with a factor $\gamma_{1\text{H}}/\gamma_{13\text{C}}$. The choice of sequence in combination with the sensitivity increase at high field allowed for the first time the observation of [2- ^{13}C]acetylcarnitine *in vivo* at 21.5 ppm, and the determination of the metabolic turnover. The acetylcarnitine resonance assignment was confirmed by performing experiments infusing ^{13}C labeled glucose. Other metabolites such as glutamate (C2, C3 and C4), creatine (CH2 and CH3), taurine (C1 and C2) and citrate were also clearly observed, without lipid contamination. Localized ^{13}C NMR spectroscopy at high field enables an improved characterization of acetate oxidation in skeletal muscle *in vivo*, with sufficient time resolution for further modeling studies. Characterization of metabolic fluxes incorporating acetylcarnitine could give novel insights in metabolic disorders such as diabetes where carnitine deficiency occurs.

Adapted from

Acetylcarnitine turnover in rat skeletal muscle measured *in vivo* using localized ^{13}C NMR at 14.1 T

Jessica AM Bastiaansen, Joao MN Duarte, Arnaud Comment, Rolf Gruetter

Presented at: Proc. Intl. Soc. Mag. Reson. Med. 21, 0120 (2013)

Manuscript in preparation

7.1 Introduction

Acetate has been widely used as a metabolic probe for measuring TCA cycle kinetics *in vivo* in skeletal muscle¹⁻³. It has a relatively simple metabolism and enters the cells via facilitated diffusion^{4;5}. In order to cross the mitochondrial membrane for subsequent utilization in the TCA cycle, acetate needs to be transformed into acetylcarnitine⁶. Acetylcarnitine plays an important role in the transport of acetate across the mitochondrial membrane as well as for long chain fatty acids and acts as a storage for excess acetylgroups which are not needed for the tricarboxylic acid (TCA) cycle^{6;7}. It has relatively small poolsizes of in skeletal muscle, approximately one order of magnitude lower than glutamate^{8;9}. The tremendous gain in signal to noise ratio (SNR) and recent developments in hyperpolarized ^{13}C NMR spectroscopy *in vivo* allowed the visualization of acetylcarnitine after the infusion of hyperpolarized acetate in liver, skeletal and cardiac muscle^{10;11}.

Energy metabolism in skeletal muscle has been frequently studied by ^{13}C NMR *in vivo*. The conversion of ^{13}C labeled compounds can be measured using this method, since the ^{13}C label propagates through a cascade of enzymatic reactions from one biomolecule to the other. The rate at which other metabolites are labeled can be quantified by fitting the metabolite timecourses to mathematical models describing the biochemical pathways in differential equations^{12;13}.

^{13}C MR spectroscopy is hampered by a relative low sensitivity. Additionally, ^{13}C MR spectroscopy in skeletal muscle is challenging since the contamination of signals from naturally abundant ^{13}C in lipids, originating from subcutaneous fat tissue, hampers the detection of other compounds, such as glutamate and glutamine. A majority of skeletal muscle studies rely on subtraction schemes where a baseline ^{13}C spectrum is acquired, which is subtracted from the spectra acquired after the infusion of ^{13}C labeled substrates. This leads to SNR losses and potential errors due to subtraction. Those could be avoided by using localization schemes. In the past, several methods besides hyperpolarized techniques were introduced to increase the sensitivity by polarization transfer. While indirect Proton Observed Carbon Edited (POCE) spectroscopy generates the highest sensitivity, the direct ^{13}C acquisition by cross polarization¹⁴ or Distortionless Enhanced Polarization Transfer (DEPT)^{15;16} yields a larger chemical shift dispersion.

Polarization transfer sequences have been used in ^{13}C NMR studies *in vivo* for their gain in sensitivity. In the current study, a ^1H - ^{13}C polarization transfer sequence was used to enhance the SNR of the ^{13}C nucleus four fold. Additionally, a localization scheme was used to suppress subcutaneous fat resonances, thereby increasing the detectability of resonances in the 30 ppm region, and the inherent SNR was increased by performing the measurements at 14.1T.

The power of ^{13}C NMR to probe the TCA cycle and its intermediates was used to investigate whether acetylcarnitine could be observed *in vivo* by improving the detection method at thermal equilibrium polarization levels. To this end, [2- ^{13}C]acetate was infused in rat skeletal muscle using ^{13}C MR spectroscopy at 14.1T using localized DEPT, in order to enable improved

characterization and description of the system of enzymatic reactions involved in acetate oxidation.

7.2 Methods

7.2.1 Animal preparation

Male Sprague-Dawley rats ($n = 3$, obtained from Charles River Laboratoires, France) were fasted overnight. Animals were anesthetized using 2% isoflurane (Attane, Minrad, NY, USA) in 30% oxygen in air. Catheters were inserted into a femoral artery for monitoring blood gases, glucose, lactate, and arterial blood pressure, and into a femoral vein for infusion of saline solutions containing $[2-^{13}\text{C}]$ acetate (Isotec, Sigma-Aldrich, Basel, Switzerland).

Animals were immobilized in a homebuilt holder to minimize potential motion. Body temperature was maintained between 37.0 and 37.5°C with a warm water circulation system based on the feedback obtained from a homebuilt rectal temperature probe. Arterial blood pressure, heart rate, and respiratory rate were continuously monitored with an animal monitoring system (SA Instruments, NY, USA). Arterial pH and pressures of O_2 and CO_2 were measured using a blood gas analyzer (AVL Compact 3, Diamond Diagnostics, MA, USA). Plasma glucose and lactate concentrations were quantified with the glucose or lactate oxidase methods, respectively, using two multi-assay analyzers (GW7 Micro-Stat, Analox Instruments, London, UK).

7.2.2 Saline and $[2-^{13}\text{C}]$ acetate infusion procedure

During the preparation of the MR acquisition, such as the animal positioning, shimming and ^{13}C MR baseline acquisition, saline was infused at a rate of 0.2 mmol/kg/min. Infusing saline before the start of the actual $[2-^{13}\text{C}]$ acetate experiment greatly improved the preservation of the shim parameters. $[2-^{13}\text{C}]$ labeled acetate was dissolved to a concentration of 1.0 M in a saline solution with pH = 5. The saline infusion was stopped when the acetate infusion started with the same rate of 0.2 mmol/kg/min. This infusion rate was reduced during the experiment by 25% every hour on average. Plasma samples were taken at regular intervals throughout the experiments and were stored at -80°C for determination of substrate fractional enrichments (FE). Arterial pH and blood gases were maintained within the normal physiological range by adjusting respiratory rate and volume.

7.2.3 *In vivo* MR spectroscopy

All *in vivo* NMR experiments were carried out in a DirectDrive spectrometer (Agilent, Palo Alto, CA, USA) interfaced to a 14.1 T magnet with a 26-cm horizontal bore (MagneX Scientific, Abingdon, UK), using a homebuilt coil consisting of a ^1H quadrature surface coil and a ^{13}C linearly polarized surface coil. A glass sphere filled with ^{13}C formic acid placed in the centre of

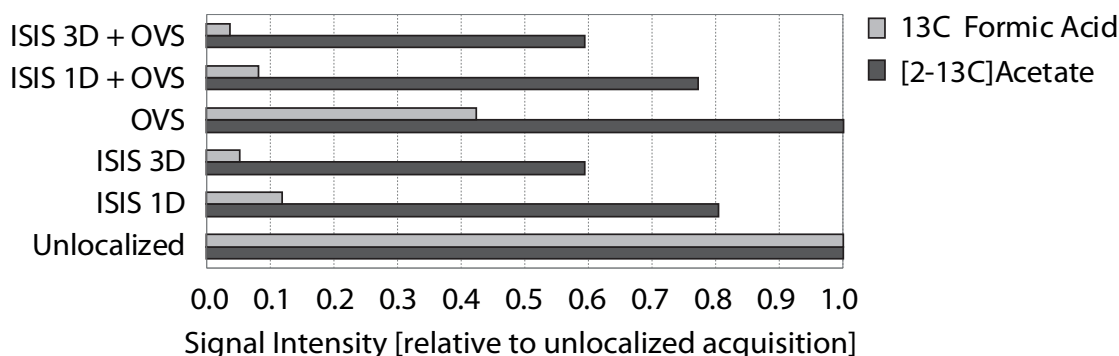


Figure 7.1: Measurements conducted on a $[2-^{13}\text{C}]$ labeled acetate phantom to investigate the effect of OVS and ISIS on signal localization.

the ^{13}C surface coil was used for pulse calibrations. The skeletal muscle was positioned in the isocenter of the magnet and fast-spin-echo images with repetition time of 5 s, echo time of 52 ms and echo train length of eight allowed to identify anatomical landmarks, which were used to place the volume of interest (VOI) of $6 \times 12 \times 10 \text{ mm}^3$ in the muscle. Shimming was performed with FASTESTMAP¹⁷ until a ^1H linewidth of 30 Hz was obtained. ^{13}C NMR spectra were acquired with 128 averages (5 min) using semi-adiabatic distortionless enhancement by polarization transfer (DEPT) combined with 3D-ISIS ^1H localization¹⁵ and outer volume suppression (OVS), and broadband ^1H decoupling using WALTZ-16 during the MR signal acquisition.

ISIS 3D in combination with OVS localization was chosen based on phantom calibrations. The localization method was tested on a phantom consisting of a syringe doped with $[2-^{13}\text{C}]$ acetate. A voxel was selected to include the syringe, and exclude the formic acid reference bubble. Results indicate that ISIS 3D in combination with OVS performs better in suppressing the formic acid signal (Figure 7.1).

Spectral analysis was carried out using LCModel (Stephen Provencher Inc., Oakville, ON, Canada) for ^{13}C NMR spectra. Simulation of basis spectra for the observable isotopomers was performed in Matlab (The MathWorks, Natick, MA, USA)¹⁸. *In vitro* ^{13}C NMR spectra from standard solutions including the metabolites of interest allowed correcting for the relative differences in signal enhancement by polarization transfer with DEPT. Then, relative intensities in ^{13}C NMR spectra were used to scale ^{13}C concentrations for all carbon resonances through all time courses.

7.2.4 *In vitro* MR spectroscopy

After each experiment, skeletal muscle tissue was excised and placed immediately in liquid nitrogen and rats were sacrificed. Skeletal muscle tissue was immediately stored at -80 C until extraction. Water-soluble metabolites from brain and plasma samples were extracted with 7%

(v/v) perchloric acid (PCA) as previously described¹⁹ and dried with a sample concentrator (SpeedVac DNA 120, Thermo Fisher Scientific, Wohlen, Switzerland). The dried extracts were dissolved in 2H₂O (99.9% 2H, Sigma-Aldrich) and 1.2 mmol sodium fumarate (Sigma-Aldrich) was added as internal standard for quantification by ¹H NMR spectroscopy. ¹H and ¹³C NMR spectra were acquired on a 14.1 T DRX-600 spectrometer equipped with a 5-mm cryoprobe (Bruker BioSpin SA, Fallanden, Switzerland) to determine the fractional enrichments and metabolite concentrations in the plasma and tissue samples. Peak areas were quantified by curve fitting.

7.2.5 Fractional enrichments and turnover calculations

Fractional ¹³C enrichments and absolute concentrations of acetate were determined from the ¹H NMR spectra taken from tissue extracts. The ratios of the acetate doublet to its singlet was used as a measure for fractional enrichment of [2-¹³C]acetate versus the natural abundance of acetate in plasma. A similar approach was used for the fractional enrichment calculation of lactate and alanine C3. The ¹³C acetate concentration measured in extracts was cross referenced with the ¹³C acetate signal in the last *in vivo* measurement and used as a scaling factor to determine time courses of the ¹³C concentrations of other metabolites *in vivo*, such as that of [2-¹³C]acetylcarnitine.

The FE of glutamate C2, C3 and C4 were determined by analysing the multiplets, or isotopomers of each resonance (see Figure 1.17 in Section 1.5). Using the ¹³C-¹³C J coupling induced splitting (Section 1.2.9) of the C4 resonance when the neighbouring C3 position is also ¹³C labeled, the FE of Glu C3 can be determined from the C4 isotopomers in ¹³C spectra of tissue extracts, with the following expression: $FE(C3) = C4D34 / (C4S + C4D34)$. Where $C4S + C4D34$ is the total area of the Glu C4 resonance. The last 8 scans of the *in vivo* time courses of Glu C2, C3 and C4 were scaled to the fractional enrichments determined in the tissue extracts.

Similarly, the FE of C2 acetylCoA, FE_{C2} , was determined using the following equation as described in²⁰:

$$FE_{C2} = \frac{C4D34}{C4} \frac{C4}{C3} \quad (7.1)$$

where C4D34 is the area of the doublet resonance of C4 glutamate and C4 and C3 the total areas of the C4 and C3 glutamate resonances respectively.

The concentrations of ¹³C labeled acetylcarnitine C2 were calculated based on the concentration of acetate C2, determined from high resolution ¹H and ¹³C MRS on tissue extracts. To determine the turnover time τ , the following equation was fitted to the time course of ¹³C labeling of acetylcarnitine C2:

$$[Acetylcarnitine]_{C2}(t) = [Acetylcarnitine]_{C2,max} * (1 - e^{-t/\tau}) \quad (7.2)$$

where $[\text{Acetylcarnitine}]_{\text{C2,max}}$ is the steady state acetylcarnitine C2 concentration. The turnover rate of the acetylcarnitine pool can be determined by dividing the total concentration of acetylcarnitine by the turnover time τ . The total concentration of acetylcarnitine, non-labeled plus labeled, can be determined by dividing the steady state concentration of acetylcarnitine C2 by its FE.

7.3 Results

The *in vivo* ^{13}C MR spectra demonstrated an excellent voxel localization using 3D ISIS in combination with OVS. The broad natural abundance ^{13}C lipid signals resonating around 30 ppm are suppressed without affecting the signals of natural abundance ^{13}C labeled creatine (Cre CH₂, CH₃) and taurine (Tau C1, C2), when using the localization module (Figure 7.2).

The specific protocol of ^{13}C -enriched acetate infusion raised plasma acetate to about 2.5 mM in 60 min and then remained constant. The plasma FE of acetate C2 reached a steady value of about 0.75 (Figure 7.3). In tissue extracts, prepared at the end of the experiment, the FE of acetate C2 was 0.55 and that of lactate C3 was 0.04. Signal contributions from lactate C3 were thus assumed to have a minor contribution to the labeling patterns observed in this study.

The *in vivo* spectral quality and sensitivity increase achieved at 14.1 T, in combination with the polarization transfer signal enhancement allowed the detection of ^{13}C labeling after [2- ^{13}C]acetate infusion in glutamate (Glu C2, C3, C4), citrate (Cit C2 C4), β -hydroxybutyrate (BHB C2, C4), glutamine (C2, C3, C4), acetate (Ace C2), with a time resolution of 5 min (Figure 7.4). The *in vivo* FE of glutamate C2, C3 and C4 were calculated after isotopomer analysis of ^{13}C spectra of the tissue extracts (Figure 7.5). Glutamate C4 is enriched at a faster rate compared with Glu C3 and C2. This is in agreement with the ^{13}C label flow of [2- ^{13}C]acetate metabolism, which dictates that Glu C4 is labeled in the first turn of the TCA cycle (Figure 1.16, Section 1.5). Glutamate C2 and C3 appeared more slowly than glutamate C4 as a consequence of the additional turns of the TCA cycle, which are necessary to scramble the C4 label into C2 and C3. Steady state isotopic enrichments in these metabolites were achieved in the experimental time frame.

Another metabolite was observed at 21.5 ppm and was tentatively assigned to that of acetylcarnitine C2 (Figure 7.4). Since the acetylcarnitine C2 resonance (21.5 ppm) is close to that of lactate C3 (21.0 ppm), the data obtained in this study was compared with that of data obtained in earlier brain studies by colleagues where [1,6- ^{13}C]glucose was infused. Since ^{13}C labeling in lactate and glutamate are generated from the metabolism of glucose, the chemical shifts of both could be compared (Figure 7.6).

When aligning both spectra using the glutamate resonances, the lactate C3 resonance does not correspond with that of acetylcarnitine C2. Since brain tissue is not equivalent to that of skeletal muscle tissue a similar glucose experiment was conducted in skeletal muscle. Since

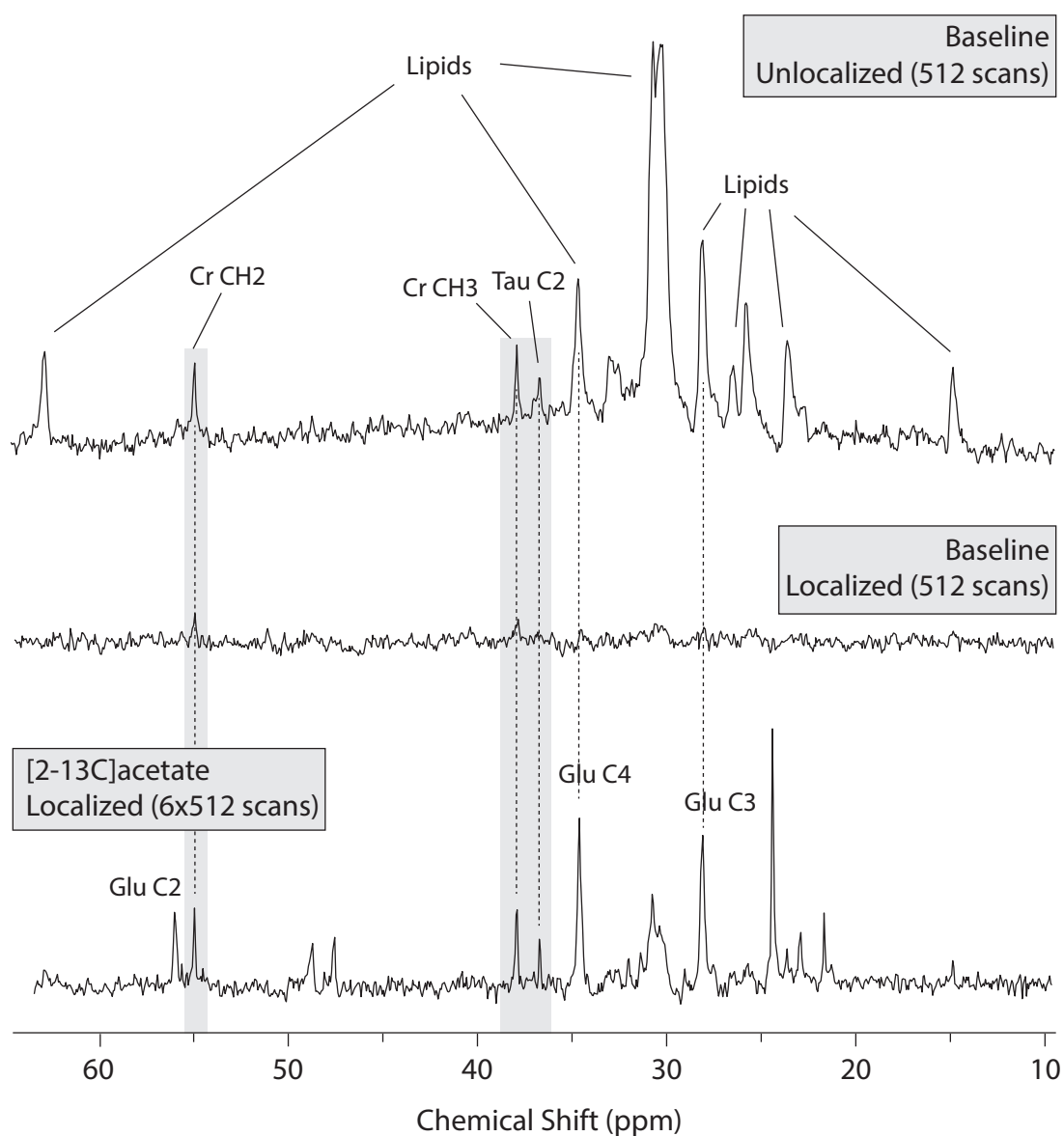


Figure 7.2: Difference between unlocalized and localized ^{13}C MR spectra in skeletal muscle. Baseline ^{13}C MR spectra were acquired without localization (top) and with localization via OVS and ISIS (middle). A plethora of lipid resonances are observed in the unlocalized baseline acquisition as indicated. The grey squares indicate natural abundance ^{13}C labeled (1%) creatine and taurine. By using ISIS and OVS localization (middle) the lipids are successfully suppressed. Comparison of the unlocalized baseline acquisition (top) with that of a $[2-^{13}\text{C}]$ acetate infusion (bottom) shows clearly that the detection of ^{13}C labeling in glutamate C3 and C4 is challenging due to overlapping lipid resonances. Spectra were apodized with 5 Hz for SNR enhancement.

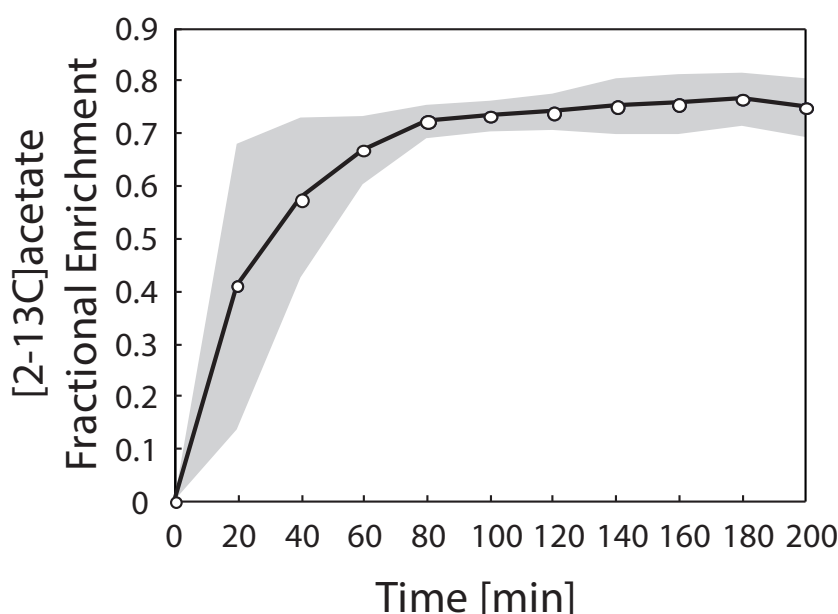


Figure 7.3: Fractional enrichment of ^{13}C in acetate C2 in plasma samples taken at regular intervals during the experiment. The FE was determined from high resolution ^1H NMR of extracted plasma metabolites.

the glutamate labeling was relatively low following glucose infusion, the chemical shifts of creatine were also used to align both spectra (Figure 7.7).

Again, it is clear that the lactate C3 resonance is not overlapping with the resonance of acetylcarnitine C2. Based on its chemical shift and the comparisons with $[1,6]\text{-}^{13}\text{C}_2\text{glucose}$ experiments in the brain and muscle, the resonance observed at 21.5 ppm was positively assigned to that of acetylcarnitine C2. The time evolution of the concentration of $[2\text{-}^{13}\text{C}]\text{acetylcarnitine}$ *in vivo* revealed a turnover time τ of 37 minutes (Figure 7.8). Assuming that the FE in acetylCoA C2 of 0.49, as determined with Equation 7.1, is similar to the FE of acetylcarnitine C2, the total acetylcarnitine pool size was $0.21\ \mu\text{mol/g}$. The resulting turnover rate of the acetylcarnitine pool was calculated to be $0.34\ \mu\text{mol/g/hr}$.

The high spectral resolution at 14.1 T enabled the distinction of all metabolites in the skeletal muscle, but was not sufficient to detect homonuclear $^{13}\text{C}\text{-}^{13}\text{C}$ J coupling induced multiplets in the glutamate C2, C3 and C4 resonances *in vivo*. NMR of tissue extracts revealed the presence of all metabolites observed *in vivo*, besides that of Cit C2-C4. Interestingly, the resonances of glutamine (C2, C3 and C4) which were of the same order of magnitude as the glutamate resonances (Figure 7.9) could be observed. Glutamine intensities in the *in vivo* ^{13}C spectra were too low to be reliably quantified.

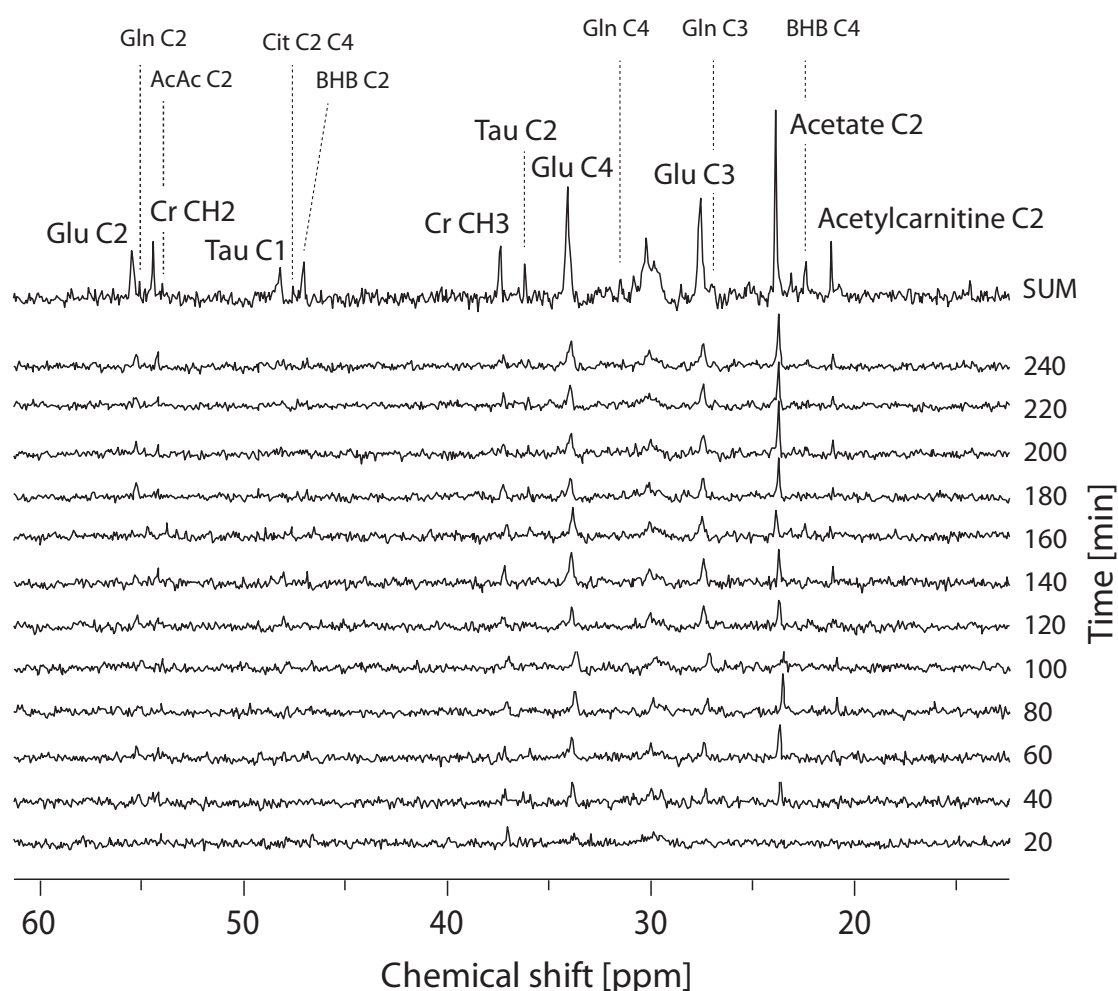


Figure 7.4: Typical time course of ^{13}C labeling of metabolites following $[2\text{-}^{13}\text{C}]\text{acetate}$ metabolism in skeletal muscle in vivo at 14.1T allowed the detection of the ^{13}C labeling in glutamate (Glu C2, C3, C4), citrate (Cit C2 C4), β -hydroxybutyrate (BHB C2, C4), glutamine (C2, C3, C4), acetate (Ace C2). ^{13}C MR spectra were acquired with a time resolution of 5 minutes and displayed with a 20 min time resolution for visual clarity. Spectra were apodized with 5 Hz for SNR enhancement.

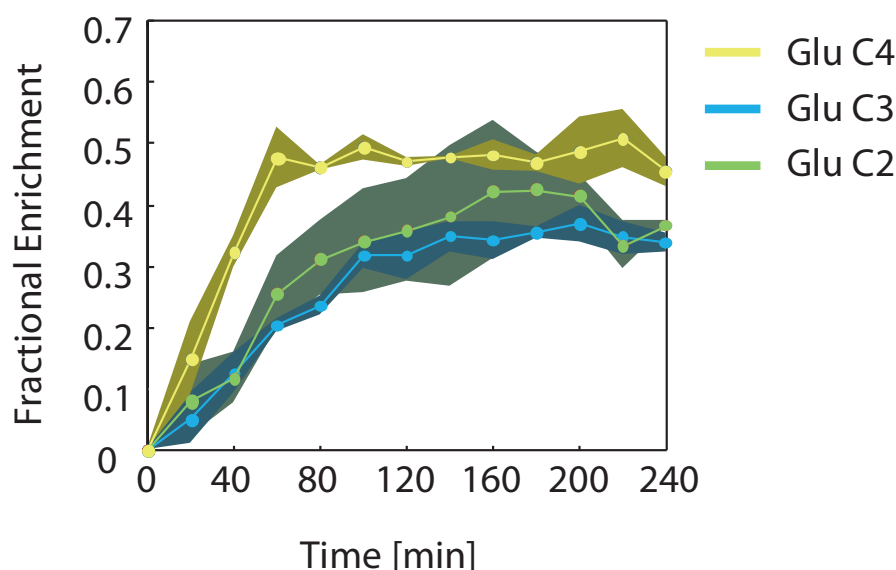


Figure 7.5: The time course of the fractional enrichment of the ^{13}C label in glutamate positions C2, C3, and C4 during the $[2\text{-}^{13}\text{C}]\text{acetate}$ infusion. The FE's were obtained from isotopomer analysis of the high resolution ^{13}C NMR of tissue extracts. These FE's were scaled with the last *in vivo* acquisition.

7.4 Discussion

In this study we showed improved detection of acetate metabolism in skeletal muscle *in vivo* by increasing the sensitivity using a polarization transfer sequence at high field. The technical challenge to suppress unwanted lipid resonances, which obscure the quantification of several metabolites, were adequately met using ISIS and OVS localization. Although a small fraction of lipid resonances are still visible around 30 ppm, it does not hinder with the quantification of metabolites present in that spectral region. An important advantage of the DEPT sequence is that the localization can be performed on protons. Namely, direct ^{13}C localization suffers from large chemical shift displacement errors especially at higher fields. Since the chemical shift range of all metabolite ^1H resonances are much less dispersed, ^1H localization minimizes the chemical shift displacement errors.

This allowed for the first time the *in vivo* visualization of $[2\text{-}^{13}\text{C}]\text{acetylcarnitine}$, an important intermediate metabolite in the oxidation of acetate. Also, the suppression of lipid resonances was sufficient to allow for an accurate determination of glutamate labeling in C4 and C3. The turnover time of acetylcarnitine was found to be $0.34\mu\text{mol/g/hr}$. Since acetylcarnitine is an intermediate of acetate oxidation, it is possible to make a comparison with the turnover of acetate. In human skeletal muscle, the flux from acetate to acetylCoA, which in fact has to pass through the acetylcarnitine pool, was determined to be $3\text{ nmol/g/min} = 0.18\mu\text{mol/g/hr}^{21}$. In another study, it was found that acetate was oxidized at a rate of $8.5\mu\text{mol/kg/min}$, which equals $0.51\mu\text{mol/g/hr}^{22}$. The values found in this study are comparable to the previously

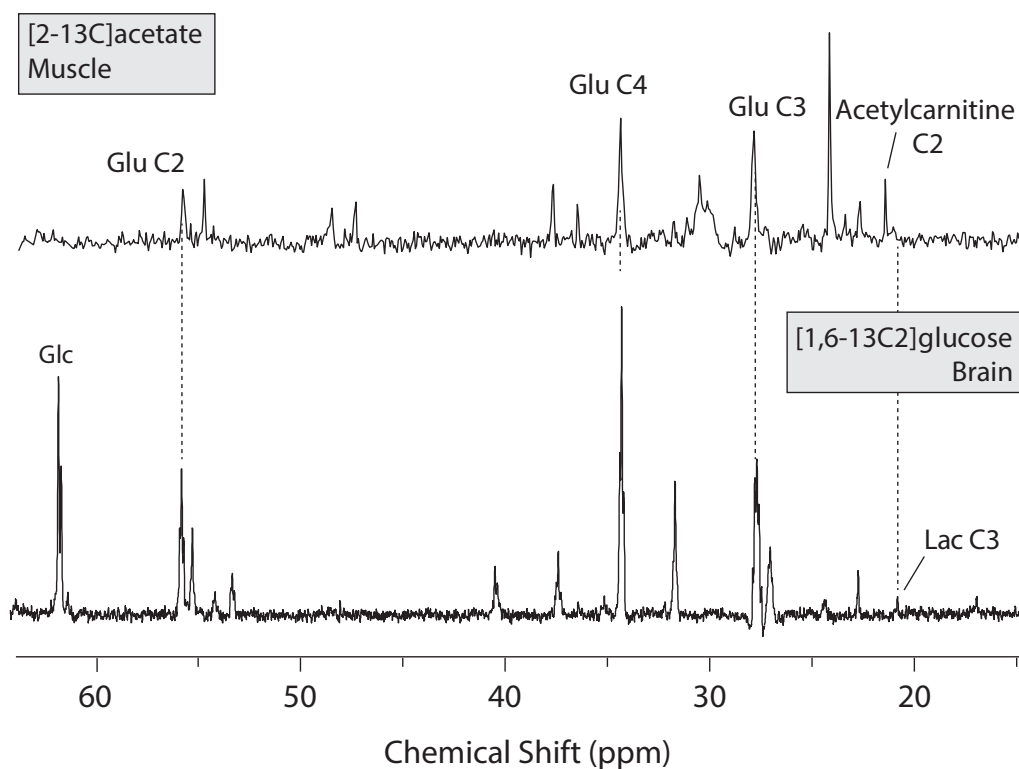


Figure 7.6: To verify the acetylcarnitine resonance assignment at 21.5 ppm, a comparison was made between ^{13}C spectra of a ^{13}C labeled glucose and acetate infusion in brain and muscle respectively. Top spectrum was apodized with 5 Hz and the bottom spectrum with 2 Hz for SNR enhancement.

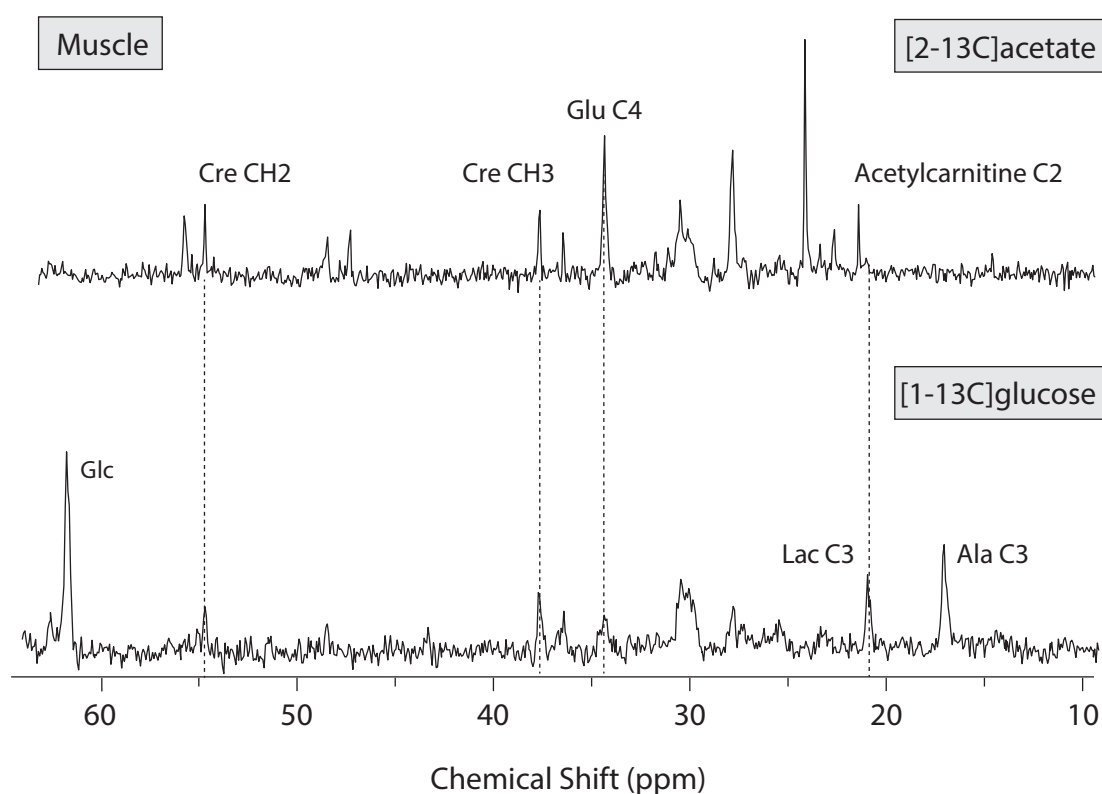


Figure 7.7: To verify the acetylcarnitine resonance assignment at 21.5 ppm, a comparison was made between ^{13}C spectra of a ^{13}C labeled glucose and acetate infusion in skeletal muscle. Spectra were apodized with 5 Hz for SNR enhancement.

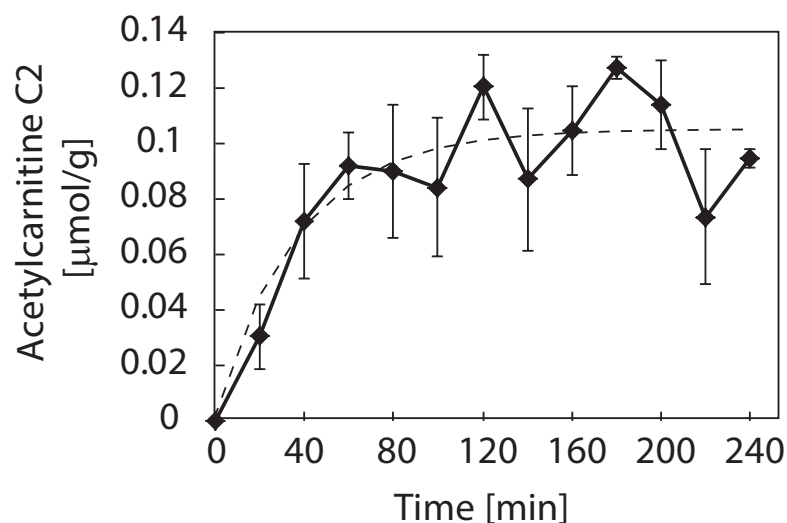


Figure 7.8: Concentration of acetylcarnitine C2 in skeletal muscle in vivo after the infusion of $[2-^{13}\text{C}]$ acetate was obtained by scaling with the acetate C2 signal which concentration was determined from the tissue extracts. The corresponding fit (dashed line) to Equation 7.2 was used to calculate the turnover time τ and the turnover rate.

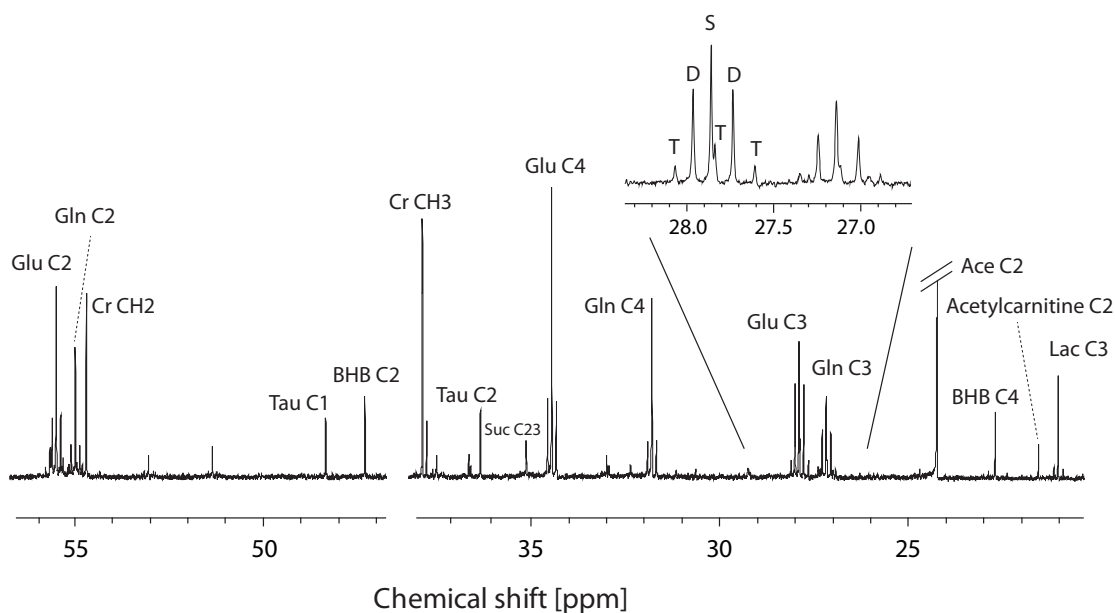


Figure 7.9: ^{13}C NMR of a skeletal muscle tissue extract. The presence of all metabolites observed in vivo was confirmed and fractional enrichments of glutamate C2, C3 and C4 could be calculated using the multiplet structures and isotopomer analysis. The inset shows the multiplet structure of Glu C3 and Gln C3, each of them consisting of a singlet (S), doublet (D) and a triplet (T). Spectra were apodized with 0.5 Hz for SNR enhancement.

reported values in the literature. In a study using ^{14}C acetate in guinea pig muscle, a combined turnover of acetylCoA and acetylcarnitine was found to be $8.23 \text{ nmol/g/min} = 0.49 \text{ }\mu\text{mol/g/hr}^{23}$.

The poolsize of acetylcarnitine in this study was calculated based on the fractional enrichment of acetylCoA, and the ^{13}C concentration of acetylcarnitine. AcetylCoA can be formed from other metabolic precursors, such as long chain fatty acid and carbohydrates, resulting in an influx of unlabeled acetylCoA. This would cause a reduction in the FE of acetylCoA compared to the FE in acetylcarnitine. Therefore the actual FE of acetylcarnitine might be higher. This would mean that the estimation of the total acetylcarnitine pool size of $0.21 \text{ }\mu\text{mol/g}$ could be overestimated. Previous studies in rat skeletal muscle, report acetylcarnitine concentrations of $0.13 \text{ }\mu\text{mol/g}$ at rest and up to $0.63 \text{ }\mu\text{mol/g}$ after fatty acid infusion in perfused rat skeletal muscle²⁴. Those values are in the range of the findings in this study.

It has been reported that acetylCoA rapidly equilibrates with acetylcarnitine, based on equal tracer incorporation in both acetylcanritine and acetylCoA after administration of ^{14}C labeled acetate²³. Therefore, for turnover rate calculations, acetylCoA and acetylcarnitine may be considered a single high energy acetyl pool, since acetylcarnitine must be converted to acetylCoA before entering metabolic pathways²³. Given that the measurements performed here require time averaging, allowing the pools of acetylcarnitine and acetylCoA to equilibrate, the assumption that the fractional enrichment in acetylcarnitine is similar to that in acetylCoA is valid.

Another interesting observation is that the resonance of glutamine is hardly visible *in vivo* while the intensities of the C2, C3 and C4 resonances of glutamine *in vitro* in respect to glutamate suggest sufficient ^{13}C labeling for *in vivo* detection. However, this remains to be further investigated. Also, the resonance of citrate (Cit C2 C4) was absent in the ^{13}C MRS spectra of tissue extract. The absence of citrate and presence of glutamine at similar levels compared with glutamate has been observed before in tissue extracts². To our knowledge, glutamine has not been observed *in vivo* in skeletal muscle.

Although these experiments were conducted at high field, it was not possible to detect the muliplet structures due to ^{13}C - ^{13}C homonuclear scalar coupling *in vivo*, unlike in brain studies. This was attributed to the extend at which the proton linewidth can be reduced in skeletal muscle. The minimum attainable proton linewidth was 30-34 Hz, compared to 22-27 Hz in the brain at 14.1T.

In this study it was shown that it is possible to monitor the time courses of ^{13}C enrichment in glutamate C2, C3 and C4 in skeletal muscle. The temporal data acquired in this study can be used as an index for TCA cycle flux. Together with the time courses obtained for acetylcarnitine, more detailed mathematical models can be constructed to enable the quantification of biochemical processes in skeletal muscle *in vivo*.

Conclusion

This study demonstrates for the first time, to our knowledge, the detection of [2- ^{13}C]acetylcarnitine *in vivo* and the acetylcarnitine turnover using localized ^{13}C NMR spectroscopy at high field. A major improvement was the increased sensitivity relative to lower fields and the use of a heteronuclear polarization transfer sequence. Sufficient time resolution was obtained for future modeling studies incorporating the metabolite acetylcarnitine. This allows for a more detailed characterization of acetate oxidation in skeletal muscle *in vivo* and in studies of metabolic disorders such as diabetes where carnitine deficiency occurs.

References

- [1] L. Szczepaniak, E. E. Babcock, C. R. Malloy, and A. D. Sherry. Oxidation of acetate in rabbit skeletal muscle: Detection by c- 13 nmr spectroscopy in vivo. *Magnetic Resonance in Medicine*, 36(3):451–457, 1996.
- [2] L. A. Bertocci, J. G. Jones, C. R. Malloy, R. G. Victor, and G. D. Thomas. Oxidation of lactate and acetate in rat skeletal muscle: Analysis by c- 13 -nuclear magnetic resonance spectroscopy. *Journal of Applied Physiology*, 83(1):32–39, 1997.
- [3] V. Mezzarobba, G. Bielicki, F. M. H. Jeffrey, M. Mignon, J. P. Renou, J. Grizard, and D. Meynial-Denis. Lack of effect of ageing on acetate oxidation in rat skeletal muscle during starvation: A c- 13 nmr study. *Journal of Experimental Biology*, 203(6):995–1001, 2000.
- [4] N. Karlsson, E. Fellenius, and K. H. Kiessling. The metabolism of acetate in the perfused hind-quarter of the rat. *Acta Physiol Scand*, 93(3):391–400, 1975.
- [5] B. Mittendorfer, L. S. Sidossis, E. Walser, D. L. Chinkes, and R. R. Wolfe. Regional acetate kinetics and oxidation in human volunteers. *American Journal of Physiology-Endocrinology and Metabolism*, 274(6):E978–E983, 1998.
- [6] P. A. Roberts, S. J. G. Loxham, S. M. Poucher, D. Constantin-Teodosiu, and P. L. Greenhaff. Acetyl-coa provision and the acetyl group deficit at the onset of contraction in ischemic canine skeletal muscle. *American Journal of Physiology-Endocrinology and Metabolism*, 288(2):E327–E334, 2005.
- [7] F. B. Stephens, D. Constantin-Teodosiu, and P. L. Greenhaff. New insights concerning the role of carnitine in the regulation of fuel metabolism in skeletal muscle. *J Physiol*, 581(Pt 2):431–44, 2007.
- [8] N. R. Marquis and I. B. Fritz. Distribution of carnitine acetylcarnitine and carnitine acetyltransferase in rat tissues. *Journal of Biological Chemistry*, 240(5):2193–2196, 1965.
- [9] M. Berger, S. A. Hagg, and N. B. Ruderman. Effects of starvation and diabetes on muscle glucose and alanine metabolism. *Diabetes*, 22:292–292, 1973.
- [10] P. R. Jensen, T. Peitersen, M. Karlsson, R. In 't Zandt, A. Gisselsson, G. Hansson, S. Meier, and M. H. Lerche. Tissue-specific short chain fatty acid metabolism and slow metabolic recovery after ischemia from hyperpolarized nmr in vivo. *Journal of Biological Chemistry*, 284(52):36077–82, 2009.
- [11] J. A. M. Bastiaansen, T. Cheng, M. Mishkovsky, J. M. N. Duarte, A. Comment, and R. Gruetter. In vivo enzymatic activity of acetylco synthetase in skeletal muscle revealed by ^{13}C turnover from hyperpolarized [1- ^{13}C]acetate to [1- ^{13}C]acetylcarnitine. *Biochimica Et Biophysica Acta*, 1830(8):4171–4178, 2013.
- [12] João M.N. Duarte, Bernard Lanz, and Rolf Gruetter. Compartmentalised cerebral metabolism of [1,6- ^{13}C]glucose determined by in vivo ^{13}C nmr spectroscopy at 14.1 t. *Frontiers in Neuroenergetics*, 3, 2011.
- [13] R Gruetter, E.R. Seaquist, and K Ugurbil. A mathematical model of compartmentalized neurotransmitter metabolism in the human brain. *Am J Physiol Endocrinol Metab*, 281:E100–E112, 2001.
- [14] D Artemov, Z. M. Bhujwalla, and J.D. Glickson. In vivo selective measurement of (1- ^{13}C) glucose metabolism in tumors by heteronuclear cross polarization. *Magnetic Resonance*

- in Medicine*, 33:151–155, 1995.
- [15] P. G. Henry, I. Tkac, and R. Gruetter. H-1-localized broadband c-13 nmr spectroscopy of the rat brain in vivo at 9.4 t. *Magnetic Resonance in Medicine*, 50(4):684–692, 2003.
 - [16] D.M. Doddrell and M.R. Bendall. Distortionless enhancement of mr signals by polarization transfer. *Journal of Magnetic Resonance*, 48:323–327, 1982.
 - [17] R. Gruetter and I. Tkac. Field mapping without reference scan using asymmetric echo-planar techniques. *Magnetic Resonance in Medicine*, 43(2):319–323, 2000.
 - [18] P. G. Henry, G. Oz, S. Provencher, and R. Gruetter. Toward dynamic isotopomer analysis in the rat brain in vivo: automatic quantitation of 13c nmr spectra using lmodel. *Nmr in Biomedicine*, 16(6-7):400–12, 2003.
 - [19] J. M. Duarte, R. A. Cunha, and R. A. Carvalho. Different metabolism of glutamatergic and gabaergic compartments in superfused hippocampal slices characterized by nuclear magnetic resonance spectroscopy. *Neuroscience*, 144(4):1305–13, 2007.
 - [20] C. R. Malloy, J. R. Thompson, F. M. H. Jeffrey, and A. D. Sherry. Contribution of exogenous substrates to acetyl coenzyme-a - measurement by c-13 nmr under non-steady-state conditions. *Biochemistry*, 29(29):6756–6761, 1990.
 - [21] D. E. Befroy, K. F. Petersen, S. Dufour, G. F. Mason, R. A. de Graaf, D. L. Rothman, and G. I. Shulman. Impaired mitochondrial substrate oxidation in muscle of insulin-resistant offspring of type 2 diabetic patients. *Diabetes*, 56(5):1376–1381, 2007.
 - [22] E. Pouteau, H. Piloquet, P. Maugeais, M. Champ, H. Dumon, P. Nguyen, and M. Krempf. Kinetic aspects of acetate metabolism in healthy humans using [1-13c] acetate. *Am J Physiol Endocrinol Metab*, 271:E58–E64, 1996.
 - [23] J. D. Erfle and F. Sauer. Acetyl coenzyme a and acetylcarnitine concentration and turnover rates in muscle and liver of ketotic rat and guinea pig. *Journal of Biological Chemistry*, 242(9):1988–1996, 1967.
 - [24] L. L. Spriet, D. J. Dyck, G. Cederblad, and E. Hultman. Effects of fat availability on acetyl-coa and acetylcarnitine metabolism in rat skeletal muscle. *Am J Physiol*, 263(3 Pt 1):C653–9, 1992.

This thesis focused on the development of magnetic resonance methods and applications to investigate energy metabolism in cardiac and skeletal muscle *in vivo*, using both DNP hyperpolarized and conventional ^{13}C spectroscopy. This ranged from development of the experimental frame work to mathematical tools to quantify the ^{13}C labeling time courses which are needed to characterize metabolic processes. This work presents novel metabolic information about skeletal and cardiac energy metabolism using the developed methods in hyperpolarized and non-hyperpolarized ^{13}C MRS. The results of these studies, which were mainly performed in healthy subjects, open the way for further investigations of carbohydrate and lipid oxidation in subjects where metabolic pathways are modified.

Initially, methods were developed to conduct hyperpolarized ^{13}C MR experiments in skeletal muscle *in vivo*. This enabled us to visualize the ^{13}C labeling kinetics of $[1-^{13}\text{C}]\text{acetylcarnitine}$ in resting skeletal muscle following the administration of hyperpolarized $[1-^{13}\text{C}]\text{acetate}$ (**Chapter 2**). With the aid of two different, novel, analytical approaches the kinetic rate constants could be determined. Although separated by two enzymatic reactions, it was shown that the conversion of acetate to acetylcarnitine was uniquely defined by the enzymatic activity of acetylCoA synthetase (ACS) and we were able to derive the Michaelis constants K_M and V_{max} of this reaction *in vivo*. ACS activity is altered in diseases such as diabetes and cancer. Therefore, the implemented protocols can be used to gain insight in those pathological processes.

While $[1-^{13}\text{C}]\text{acetate}$ can be used to quantify the enzymatic rates of ACS, $[1-^{13}\text{C}]\text{butyrate}$, also a short chain fatty acid, might give novel information about mitochondrial oxidation in resting skeletal muscle since the detection of $[5-^{13}\text{C}]\text{glutamate}$ is not hindered by its resonance, as is the case when using $[1-^{13}\text{C}]\text{acetate}$ as a substrate. Skeletal muscle shifts its metabolism towards carbohydrate oxidation with increasing exercise levels. In this context it would be interesting to probe substrate competition (as described in **Chapter 4**) in resting and exercising skeletal muscle while it undergoes a metabolic shift.

Cardiac ^{13}C MRS methods were developed and implemented, which enabled the first detection of $[5-^{13}\text{C}]\text{citrate}$ in the beating rat heart following the injection of hyperpolarized $[1-^{13}\text{C}]\text{acetate}$ (**Chapter 3**). Previously developed mathematical models were extended to

include the mitochondrial formation of citrate. Although the V_{ACS} could be derived from the observed ^{13}C labeling kinetics in the heart, the acetate signal mainly originates from the ventricular pool and appropriate scaling factors would be needed to obtain the fraction of acetate inside the tissue, and to estimate the actual V_{ACS} . Metabolic rates were fitted using the analytical solutions of the proposed model, taking into account the signal evolution of acetate, acetylcarnitine and citrate. Since only acetylcarnitine and citrate are located in the myocardium, it is currently investigated whether solving numerically the set of differential equations based on the flow scheme given in Equation 3.17, and using $[A.Car^*](t)$ as an input function, would give more reliable flux estimates for CAT and CS.

The results obtained in **Chapter 3** opened the way to further studies in cardiac ^{13}C MRS. The heart uses a variety of substrates in a well-balanced manner and a shift in substrate preference is observed at the onset of cardiac dysfunction and diseases such as left ventricular hypertrophy and heart failure. It was demonstrated that following the injection of two different hyperpolarized substrates, it is possible to estimate substrate competition in the rat myocardium *in vivo* (**Chapter 4**). ^{13}C labeled butyrate was used as a mimic for lipid oxidation and ^{13}C labeled pyruvate for carbohydrate oxidation. The sensitivity of the proposed protocol was successfully tested in a model where a metabolic shift was induced by a simple feed/overnight fast regime that produced significant changes in substrate selection. We presented a method which is sensitive and specific for simultaneous detection of the two primary oxidative pathways in the heart, glycolysis and β -oxidation. Hyperpolarization is an emerging technique for enhancing magnetic resonance sensitivity, and it has already undergone a successful phase 1 clinical trial in the investigation of prostate cancer. The method, which should be translatable to humans, could be used to assess the onset of metabolic changes associated with LVH or heart failure or to monitor the response of the heart to metabolic treatment.

Carbohydrate metabolism in healthy rat skeletal muscle at rest was studied in different nutritional states using hyperpolarized $[1-^{13}\text{C}]\text{lactate}$ (**Chapter 5**). Lactate was chosen since it can be administered at physiological concentrations leaving other metabolic process undisturbed, unlike pyruvate. ^{13}C labeling of bicarbonate was observed within seconds in fed animals, but was absent after an overnight fast, due to PDH inhibition. Also, significant decrease in $[1-^{13}\text{C}]\text{alanine}$ was observed comparing both groups, attributed to a change in cellular alanine concentration. Lactate, a carbohydrate, is not only a waste product in skeletal muscle, but an important metabolic intermediate. The controversy that muscle produces more lactate during exercise while conventional ^{13}C MRS studies did not observe changes in $[3-^{13}\text{C}]\text{lactate}$ metabolism in resting and exercising muscle, brings opportunities for hyperpolarized ^{13}C MRS which has the potential to sample the metabolic situation within a minute.

Besides detecting the metabolite acetylcarnitine after injecting suitable precursors, the use of acetylcarnitine as a substrate for myocardial oxidation was explored (**Chapter 6**). $[1-^{13}\text{C}]\text{Acetylcarnitine}$ was hyperpolarized and despite its short T_1 it was possible to detect the formation of $[5-^{13}\text{C}]\text{glutamate}$ in the heart *in vivo*. $[5-^{13}\text{C}]\text{citrate}$ detection was expected, since cetylcarnitine crosses the mitochondrial membrane easily, while skipping a few metabolic

steps needed for acetate to cross the membrane. Moreover, it does not interfere with the detection of [5-¹³C]glutamate and [5-¹³C]citrate. Due to the absence of the [5-¹³C]citrate resonance, we hypothesized the existence of intricate relationship between reaction, transport and relaxation rates in the choice of hyperpolarized substrates. Another hypothesis is that acetylcarnitine can cross the mitochondrial membrane, but not the cellular membrane easily, but this remains to be investigated.

Finally, it has been demonstrated that [2-¹³C]acetylcarnitine can be detected *in vivo* at 14.1T using a localized polarization transfer sequence (**Chapter 7**). The combination of the high magnetic field and the DEPT sequence increased the sensitivity of the ¹³C carbon nucleus to such extent that acetylcarnitine, which has relatively small poolsizes could be observed. So far, it has only been observed using hyperpolarized ¹³C MRS techniques, and it has not been possible to obtain reliable quantification of the metabolic turnover of acetylcarnitine *in vivo*. The acetylcarnitine turnover of 0.34 μmol/g/hr was in agreement with earlier reports in literature. Furthermore, the resonance assignment of acetylcarnitine was verified using ¹³C labeled glucose infusions in skeletal muscle. The measurement of the time courses of Glu C4 and C3 were also clearly observed, without lipid contamination and with sufficient time resolution. In combination with the time courses obtained for acetylcarnitine C2, more detailed mathematical models will be constructed to enable the quantification of biochemical processes in skeletal muscle *in vivo*, leading to an improved understanding of acetate oxidation. This is currently an ongoing project. Characterization of metabolic fluxes incorporating acetylcarnitine could give novel insights in metabolic disorders such as diabetes where carnitine deficiency occurs. Another interesting observation is the missing glutamine resonances in the *in vivo* data, however, this remains to be investigated.

Hyperpolarized [1-¹³C]acetate allowed for the visualization of citrate in the heart and acetylcarnitine in the muscle (**Chapter 3 and 2**). Performing the same experiments at higher fields, for example at 14.1 T, would increase the spectral resolution, meaning that the resonances of [5-¹³C]glutamate and [5-¹³C]citrate are better resolved. With the installment of a DNP polarizer at the 14.1 T at our laboratory, the first *in vivo* DNP experiments are currently scheduled to investigate the potential of skeletal muscle metabolism at high field using hyperpolarized ¹³C MRS. Since [2-¹³C]acetylcarnitine was also detected with conventional ¹³C MRS at the same system (**Chapter 7**), both techniques could be combined to give a full description of skeletal muscle metabolism in a single animal.

A.1 RF coil design for hyperpolarized ^{13}C NMR studies

A.1.1 Quadrature ^{13}C coil for cardiac muscle applications

Efficient excitation and detection of the hyperpolarized signal can be achieved by employing a quadrature surface coil design, as described by¹ and as well in Section 1.4. In quadrature mode, two orthogonal receiving surface coils, one with a 90° phase shift relative to the other, should increase the signal to noise ratio (SNR) of an experiment by $\sqrt{2}$. A quadrature coil can generate directly a circularly polarized field, which demands only half of the transmitter power to excite the magnetization². Combined with a better depth profile, the use of a quadrature carbon coil may achieve even higher sensitivity in hyperpolarized measurements. The tuning and matching circuit is set up in such a way that the RF coil can be adjusted to resonate at the Larmor frequency of the carbon nucleus at a field strength of 9.4 T. The two wire loops, from which the axes are at an angle of roughly 90° , act as a receiver and as a transmitter. A picture of the coil and its corresponding electrical circuit is given in figure A.1.

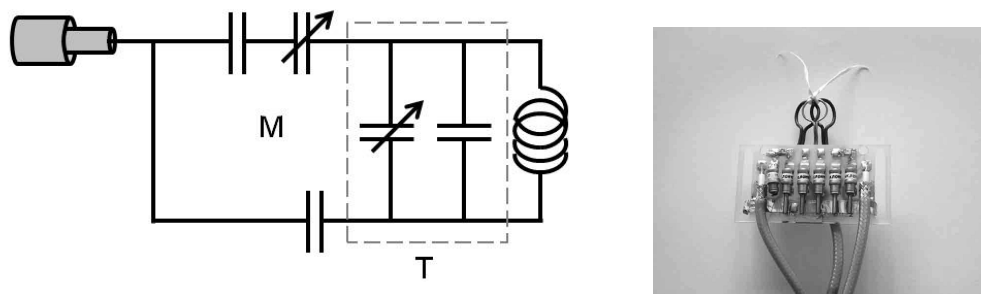


Figure A.1: Schematic representation of the tuning (T) and matching (M) circuit of the carbon coil (a). A picture of the quadrature carbon coil (b).

The quadrature properties of the constructed coil were tested initially by changing the resonance frequency of the coil to that of the ^{23}Na nucleus at 9.4 T (105.89 MHz). This because the ^{13}C nucleus has a low sensitivity and it takes longer measurement time for the same calibrations. The acquisition of ^{23}Na images (figure A.2) of a NaCl filled syringe with both surface coils connected in phase and anti-phase show that the coil has the right geometrical arrangement. One can see that when the surface coils are connected in phase, the sample is well excited compared to when the coils are connected anti phase, where the signal is clearly diminished. This excitation profile is distinct for quadrature coils.

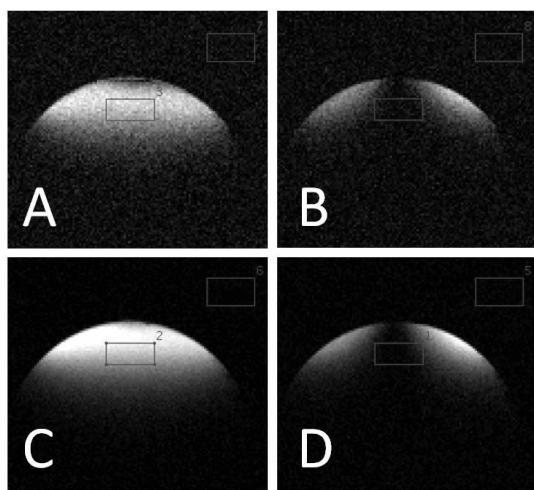


Figure A.2: Gradient echo ^{23}Na images of a NaCl phantom. Upper row without filters, bottom row with 100 MHz bandpass filters, left column quadrature connected, right column anti-quad. Signal to noise ratios are 21 (A), 8 (B), 79 (C) and 18 (D).

Using the same NaCl phantom, ^{23}Na spectra were taking by applying adiabatic 90° pulses. The SNR for the coil in quadrature mode was 2688, while the SNR for each separate loop was 1838 and 1971 (figure A.3). As a result, the gain in SNR is on average 1.41, which corresponds to $\sqrt{2}$. This is exactly the expected SNR gain for surface coils using quadrature detection.

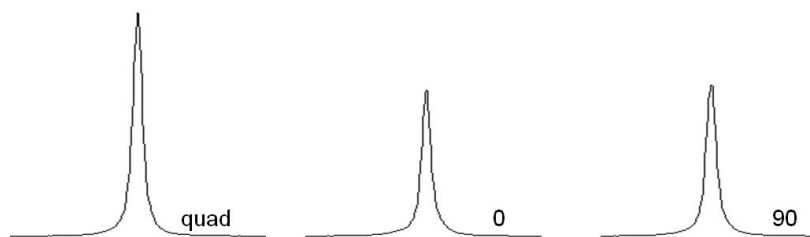


Figure A.3: ^{23}Na spectra of both surface coils in quadrature mode and each one separately.

Pulse bandwidth calibrations were performed on a [1-¹³C]acetate phantom for adiabatic 10° pulses (which are used in the DNP experiments) and the quadrature carbon coil shows the same profile as for single carbon coils. In these experiments, it is clearly shown that the noise level is strongly reduced comparing both coils (figure A.8). While increasing the power for the adiabatic 90° pulses an intensity plateau is reached at around 42 dB for the quadrature coil (figure A.4) compared to 46 dB for the conventional single surface coil. This decrease in transmit power is expected and desired in general for quadrature coils. The SNR of the quadrature coil compared to the standard coil is also higher, as expected.

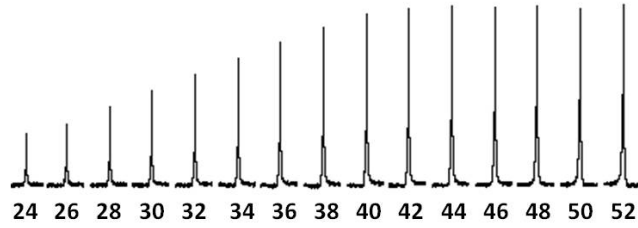


Figure A.4: Power calibration for an adiabatic 90° pulse on the quadrature coil

A.1.2 B_1 mapping

B_1 field maps (A.6) were acquired using a double flip angle method. Since the MR signal after an RF pulse with flip angle θ is proportional to $\sin\theta$, the flip angle θ can be determined by comparing the signals acquired by two flip angles, θ and 2θ , and can be calculated using,

$$\theta = \arccos \frac{I_2}{2I_1} \quad (\text{A.1})$$

A.1.3 Sensitivity comparison with a conventional design

A.2 Adiabatic RF pulse calibrations and simulations

Initial experiments indicated that the bandwidth of the 10° BIR4 pulse is not sufficient to excite acetate and acetylcarnitine in the same manner. It is important to know the excitation, or flip angle, to predict the magnetization behavior of the hyperpolarized substrates and their characteristic decay. Secondly it is important to assure that acetate does not receive a large flip angle excitation because this would destroy the hyperpolarized signal which can not be restored.

Bloch simulations of the used pulses were performed as well as experiments to look at the

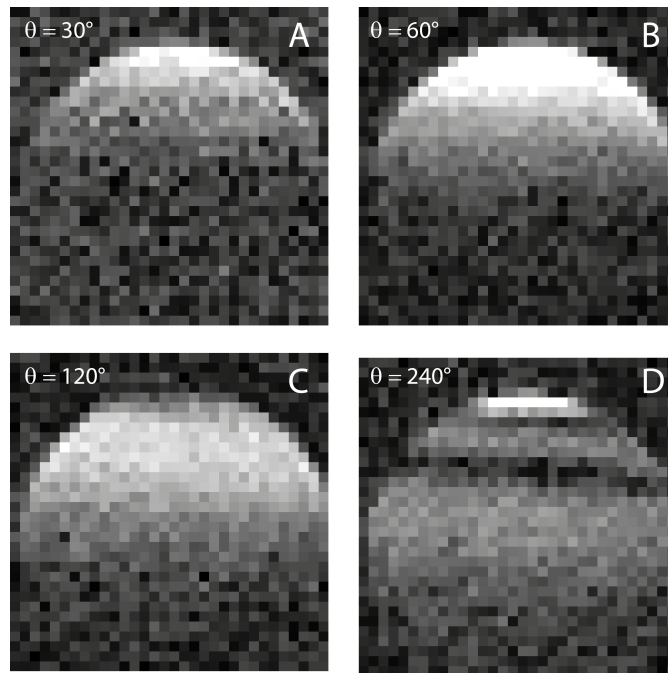


Figure A.5: ^{13}C images of a ^{13}C labeled acetate phantom with different nominal flip angles θ were acquired using a gradient echo sequence with a ^{13}C surface coil in quadrature mode. Image parameters: field of view = 2 cm x 2 cm, matrix = 32 x 32, T_R = 800 ms, T_E = 2.5 ms, slice thickness = 5 mm, averages = 1280, offset 6400 Hz. Gaussian pulse of 2 ms and 29.4 dB with nominal flip angle of 90° .

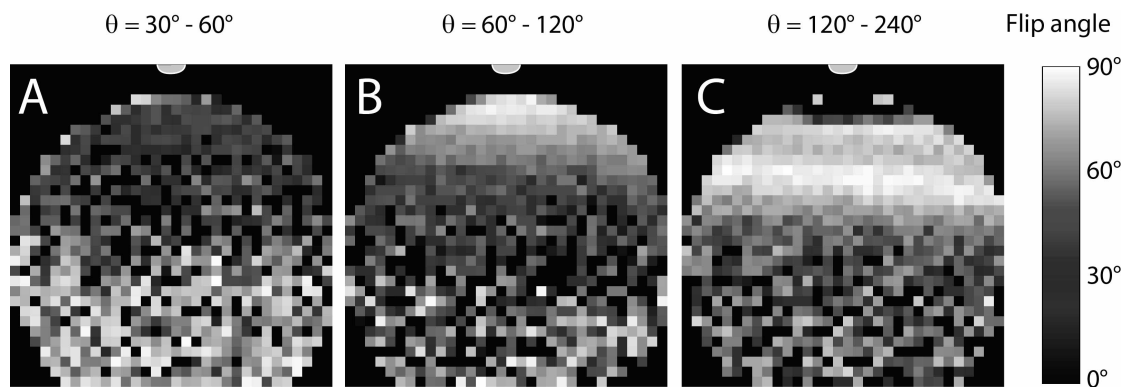


Figure A.6: B_1 maps were calculated after acquiring gradient echo images with different nominal flip angles θ .

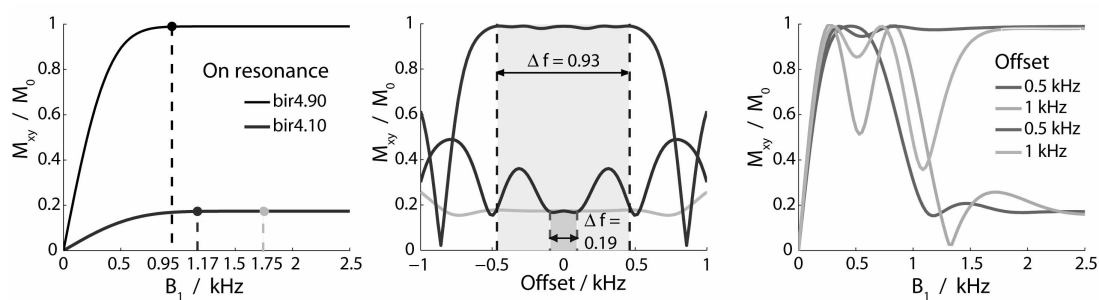


Figure A.7: Bloch simulation of the transversal M_{xy} magnetization as a function of the transmit power amplitude of a 10° and 90° adiabatic pulse, bir4.10 and bir4.90 respectively (A). After reaching a plateau, the simulated excitation bandwidth profiles for the transmit powers indicated by colored dots in A are displayed in (B). Off resonance simulation of M_{xy} magnetization (C)

behavior of the pulses. The simulations are shown in figure A.7. The left panel (A) shows the M_{xy} magnetization as function of the applied power for the adiabatic 10° and 90° pulses. The middle panel (B) shows the resulting excitation bandwidth while using the power value immediately after the plateau has been reached in (A). (B) shows that the bandwidth of the 10° pulse is not sufficient to excite the desired range of 10 ppm, which corresponds to 1000 Hz. The adiabatic 90° has an almost sufficient bandwidth after reaching a plateau. The right panel (C) depicts the M_{xy} magnetization of resonances which do not correspond with the resonance frequency of the applied pulse. It shows that when the power value is too low ($< 2 \text{ kHz}$), components which are 0.5 kHz or 1.0 kHz off-resonance receive a much higher flip-angle and this should certainly be avoided. It indicates that compared to the power value reached at plateau in (A), you need at least twice as much power for a bandwidth of 10 ppm. This means an addition of at least 6 dB at the console.

Adiabatic bir4.10 pulses

NMR experiments were performed on a $[1\text{-}^{13}\text{C}]\text{acetate}$ phantom with Omniscan to investigate the excitation bandwidth of the adiabatic 10° pulses. This experiment was done on the standard carbon coil and the new quadrature coil. It can be seen that a very large power is needed to assure a similar excitation over a bandwidth of 10 ppm. However, these plots show the absolute value of the complex signal so the influence of the phase is not visible. Taken the phase into account it is not possible to obtain the desired bandwidth with the pulses used in the DNP experiments performed until now, unless you increase the pulse duration from 3 ms to 5 ms.

Comparing the single loop carbon coil with the quadrature design it is visible that the excitation profiles are the same for both coils and the noise level is also reduced.

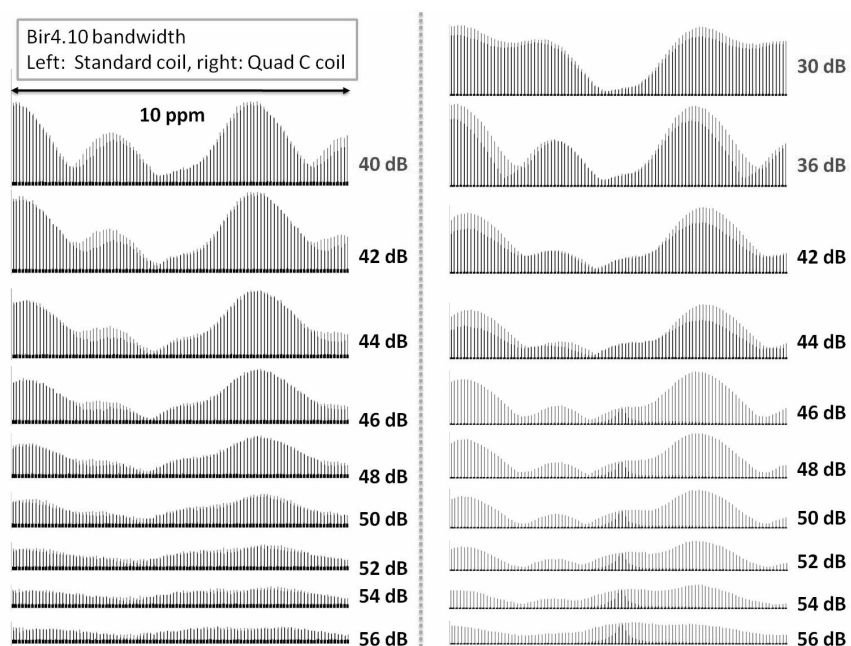


Figure A.8: Bandwidth calibrations for the adiabatic bir4.10 pulses on the standard quadrature proton coil and on the new quadrature carbon coil. Note that the difference in the noise level and the similarity of the bandwidth profiles.

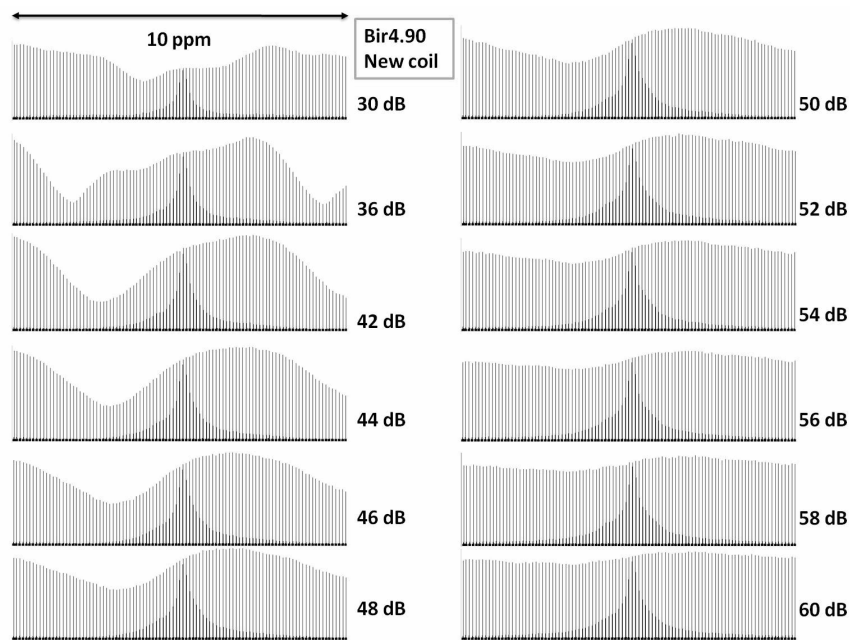


Figure A.9: Bandwidth calibrations for the adiabatic bir4.90 pulses on a quadrature carbon coil.

Adiabatic bir4.90 pulses

NMR experiments were performed on the same phantom to investigate the excitation bandwidth of the adiabatic 90° pulses. As expected from the simulations, less power is needed to reach the desired bandwidth.

Appendix References

- [1] G. Adriany and R. Gruetter. A half-volume coil for efficient proton decoupling in humans at 4 tesla. *J Magn Res*, 125:178–184, 1997.
- [2] D. I. Hoult, C. N. Chen, and V. J. Sank. Quadrature detection in the laboratory frame. *Magnetic Resonance in Medicine*, 1:339–353, 1984.

Curriculum Vitae

PERSONAL INFORMATION

Name: Jessica Bastiaansen
Given names: Josefina Adriana Maria
Date of birth: 28th of October 1982, The Netherlands
Nationality: Dutch

EDUCATION

- 2009-2013 **PhD Candidate in Physics**
Laboratory of Functional and Metabolic Imaging
Ecole Polytechnique Federale de Lausanne (EPFL), Switzerland.
- 2007-2008 **MSc Thesis**
Biological Imaging Center, Department of Bioengineering
California Institute of Technology, Pasadena, CA, USA
- 2006-2007 **Research Traineeship**
Gharib Research Group, Department of Bioengineering
California Institute of Technology, Pasadena, CA, USA
- 2002-2008 **Master of Science (MSc) in Biomedical Engineering**
Eindhoven University of Technology (TU/e), The Netherlands
- 1995-2001 **Gymnasium** (Secondary School)
Mencia de Mendoza Lyceum, Breda, The Netherlands. Cum Laude Honours

AWARDS

- 2010-2012 **Educational Stipend**, ISMRM 2010, 2011, 2012
- 2007-2008 **Special Student Award**, Scholarship, California Institute of Technology
- 2008 **New Entrand Stipend**, ISMRM 2008

TEACHING & OUTREACH EXPERIENCE

- 2009-2013 Teaching Assistant EPFL/CHUV
Physique Generale I and II, Lectures on CMR: principles and applications
- 2011 Tutor FENS-IBRO Training Center
Lausanne & Geneva, Switzerland
- 2007 Research Teaching Assistant, TU/e
Characterization of the mechanical properties of biomaterials
- 2006-2007 Member of the University Committee on Technology for Development, TU/e

- 2005-2007 Teaching Assistant, TU/e
Imaging Techniques (2x), Signal Analysis

- 2006 Study Case Project “Molecular Imaging in China”
Philips Medical Systems, Eindhoven

- 2005-2006 Chairwoman in the organizing committee “Wervingsdagen”
Annual career event, TU/e

- 2005-2006 Faculty Council member (elected)
Department of Biomedical Engineering, TU/e

- 2004-2005 Education Committee member (elected)
Department of Biomedical Engineering, TU/e